

# **Enhanced Oxidation Processes by Persulfate Activation and Microfluidics for Removal of Persistent and Emerging Contaminants**

by

**©Guihua Dong, B.Eng., M.Eng.**

A Thesis submitted to the School of Graduate Studies  
in partial fulfillment of the requirements for the  
Degree of Doctor of Philosophy

**Faculty of Engineering & Applied Science**

**Memorial University**

**May 2024**

**St. John's Newfoundland and Labrador Canada**

## ABSTRACT

The existence of persistent and emerging contaminants (e.g., polycyclic aromatic hydrocarbons, bisphenols) in the aquatic environment is a global issue. These contaminants received growing attention from environmental researchers, practitioners, and policy makers worldwide mainly because of our limited knowledge about their behaviors and adverse impacts on human beings and the environment as well as the lack of efficient treatment methods. Advanced oxidation processes (AOPs) have been regarded as one of the powerful technologies for the removal of recalcitrant organics due to their ability to generate reactive species and indiscriminately convert organics into non/less-toxic small molecules, and eventually into CO<sub>2</sub> and water, if ultimately mineralization can be achieved. There are some commonly used AOPs and enhancement methods, such as photocatalysis, UV/O<sub>3</sub>, and persulfate (PS) activation. Although these methods are approved and capable of reducing many organic pollutants to acceptable levels, some challenges have been widely recognized and limited their applications in treating persistent and emerging contaminants, such as relatively low efficiency, high energy consumption, and/or toxic intermediates or residues from incomplete mineralization, as well as the insufficient understanding of reaction mechanisms and transformation pathways. To address the challenges and gaps, the main goal of this dissertation research is, therefore, to develop novel, enhanced AOPs methods for removal of persistent and emerging contaminants and advance knowledge

about the associated degradation mechanisms and pathways. The major research achievements are from the following aspects: 1) A comprehensive review on AOP technologies and enhancement methods with – particular focus on PS activation and the rapidly emerging area of environmental microfluidics for the first time – This review offers a valuable insight for the recent advances of AOP enhancement methods and the future trend of AOPs development in environmental field. 2) Development of an enhanced technique of UV/O<sub>3</sub>/PS for marine oily wastewater treatment, exploration of its treatment mechanism, and assessment of the associated toxicity. The addition of PS could significantly shorten the treatment time which consequently reduces the energy consumption in the O<sub>3</sub>-based AOP. The research provided the scientific evidence and optimal treatment conditions for future scale-up demonstrations and applications. 3) Exploration of the enhanced degradation mechanisms of bisphenol A (BPA) in wastewater by UV/metal oxide activated PS process – The proposed synergetic PS activation process was proved to be a promising method for removal of BPA, a representative emerging contaminant, from wastewater. 4) Development of a new AOP-microreactor system integrated with UV LED-based PS activation by TiO<sub>2</sub>/g-C<sub>3</sub>N<sub>4</sub> nanosheet for removal of bisphenol S or BPS (a main substitute for BPA) and performance evaluation by comparing the developed microreactor with a conventional batch reactor – The AOP-microreactor system performed in higher efficiency with lower energy consumption than those of batch reactor. The approved AOP-microreactor method as a promising solution for removing emerging contaminants. This dissertation

not only helped build a scientific basis for the enhanced AOP methodologies, but also provided powerful techniques for advancement and potential applications in water and wastewater industry.

## ACKNOWLEDGEMENT

I would first like to express my sincere gratitude to my supervisory committee, Drs. Bing Chen, Stanislav R. Stoyanov (from Natural Resources Canada), and Helen Zhang for their attentive guidance and selfless help during my PhD program. My supervisor, Dr. Chen, is knowledgeable in his profession and generous and sincere in treating others. Whether I encountered setbacks in scientific research or life, I still remember that he always patiently guided and encouraged me to get out of trouble. I also sincerely thank my co-supervisors, Drs. Stanislav R. Stoyanov and Helen Zhang, for their insightful advice to help me conduct more meaningful research during my PhD program.

I would also acknowledge the Faculty of Engineering and Applied Science, the Memorial University (MUN), the Natural Sciences and Engineering Research Council of Canada (NSERC), the Canada Foundation for Innovation (CFI), the Fisheries and Oceans Canada (DFO) under the Multi-Partner Research Initiative (MPRI) program, and the PEOPLE Network by the NSERC Collaborative Research and Training Experience (CREATE) Program for their financial support.

Appreciate the lab manager Mrs. Lidan Tao from NRPOP for her kind help. Additional gratitude goes to my colleagues Dr. Bo Liu, Mr. Jingjing Ling, Dr. Zhiwen Zhu, Dr. Xiujuan Chen, Dr. Xing Song, Dr. Xudong Ye, Dr. Weiyun Lin, Dr. Xixi Li, Qiao Kang, Min Yang, Yunwen Tao, Miao Yu, Yuanmei Zhang, Jiabin Liu, and other NRPOP members. Also, special appreciation goes to Dr. Lindsay J. Hounjet from

Natural Resources Canada and Dr. Benjamin de Jourdan in Huntsman Marine Science Centre for their valuable suggestions in my research.

Last but not least, I must express my special appreciation to my husband Dr. Yiqi Cao for his understanding and support in my life. Thanks to my newborn baby, who has given me so much enthusiasm for the life ahead. My deepest thanks to my parents, sister, sister-in-law, and nephew for their endless love, support, and patience.

# TABLE OF CONTENTS

ABSTRACT.....	I
ACKNOWLEDGEMENT .....	IV
TABLE OF CONTENTS.....	VI
LIST OF FIGURES .....	XI
LIST OF TABLES.....	XVII
LIST OF ABBREVIATIONS.....	XVIII
LIST OF SYMBOLS .....	XX
CHAPTER 1 INTRODUCTION .....	1
1.1 Background .....	2
1.2 Statement of Problems .....	5
1.3 Objectives and Tasks.....	8
1.4 Co-Authorship Statement.....	12
CHAPTER 2 RECENT ADVANCES IN ENHANCEMENT METHODS FOR ADVANCED OXIDATION PROCESSES.....	14
2.1. Introduction .....	15
2.2. Persulfate Activation.....	16
2.2.1 Activation methods.....	17

2.2.2 Key factors influencing PS activation .....	24
2.2.3 Summary.....	25
2.3. Environmental Microfluidics .....	27
2.3.1 Hydrodynamic characteristics of microreactors .....	33
2.3.2. Applications of microreactor systems to AOPs.....	46
2.3.3. Challenges with the use of AOP-microreactors for environmental applications.....	79
2.3.4. Summary.....	86
 CHAPTER 3 DEGRADATION PERFORMANCE, TOXICITY EVALUATION, AND FLOCS ANALYSIS OF O <sub>3</sub> , UV/O <sub>3</sub> , AND UV/O <sub>3</sub> /PS PROCESSES FOR MARINE OILY WASTEWATER TREATMENT .....	 91
3.1. Introduction .....	92
3.2. Methods and Materials .....	95
3.2.1 Chemicals and materials .....	95
3.2.2 Experimental design .....	97
3.2.3 Extraction and analysis methods .....	99
3.2.4 Toxicity evaluation of treated water .....	100
3.2.5 Characterization and analysis of floating flocs.....	102

3.2.6 Statistical analysis.....	102
3.3. Results and Discussion.....	103
3.3.1 Degradation performance of three ozone-based processes.....	103
3.3.2 Acute toxicity assessment of both initial and treated water .....	131
3.3.3 Fate of oil flocs after O <sub>3</sub> -based AOPs .....	137
3.4. Summary .....	146
CHAPTER 4 UV STIMULATED MANGANESE DIOXIDE FOR THE	
PERSULFATE CATALYTIC DEGRADATION OF BISPHENOL A.....	148
4.1. Introduction.....	149
4.2. Materials and Methods.....	151
4.2.1 Chemicals and reagents .....	151
4.2.2 Degradation experiments.....	151
4.2.3 Analysis of water samples .....	152
4.2.4 Characterization and recovery of MnO <sub>2</sub> .....	152
4.2.5 Intermediates analysis.....	153
4.2.6 Toxicity evaluation .....	154
4.3. Results and Discussion.....	155
4.3.1 Degradation and mineralization of BPA .....	155

4.3.2 Effects of parameters on BPA degradation .....	161
4.3.3 Kinetic evaluation and reaction mechanism analysis .....	162
4.3.4 Infrared Spectra of MnO <sub>2</sub> and Mn leaching in different processes .....	170
4.3.5 Reusability of MnO <sub>2</sub> .....	173
4.3.6 Proposed degradation products and pathways.....	177
4.3.7 Acute toxicity evaluation.....	182
4.4. Summary .....	185
CHAPTER 5 UV LED-BASED PS ACTIVATION BY TiO <sub>2</sub> /G-C <sub>3</sub> N <sub>4</sub>	
NANOSHEETS IN A MICROREACTOR FOR BPS DEGRADATION .....	
5.1 Introduction .....	188
5.2 Materials and Methods .....	190
5.2.1 Chemicals and materials .....	190
5.2.2 Synthesis and characteristics of TiO <sub>2</sub> /g-C <sub>3</sub> N <sub>4</sub> nanosheets .....	190
5.2.3 System development and operations .....	191
5.2.4 Analysis of water samples .....	191
5.2.5 Acute toxicity evaluation.....	194
5.2.6 Statistical analysis.....	194
5.3 Results and Discussion.....	195

5.3.1 Nano photocatalysts characterization .....	195
5.3.2 Degradation performance in microreactor.....	200
5.3.3 Factorial-based performance analysis of microreactor .....	207
5.3.4 Performance comparison between a microreactor vs. a batch reactor .....	213
5.4 Summary .....	223
CHAPTER 6 CONCLUSION AND RECOMMENDATIONS .....	224
6.1 Conclusion.....	225
6.2 Research Contributions .....	228
6.3 Recommendations for Future Research .....	230
REFERENCES .....	232
APPENDIX.....	296

## LIST OF FIGURES

<b>Figure 1.1</b> The structure of the thesis.....	11
<b>Figure 2.1</b> Generation of sulfate radicals by persulfate activation. The dashed black line represents the fission position of O-O single band for the formation of sulfate radicals.....	26
<b>Figure 2.2</b> (a) Conventional photocatalytic reactor and (b) microreactor used for W/WWT.....	29
<b>Figure 2.3</b> Peer-reviewed publications on microfluidic processes over the last decade. Source: Web of Science. ....	32
<b>Figure 2.4</b> Relationships between characteristic length and mixing time for fluids of varying diffusion coefficients in micro-scale and conventional reactors (adapted from Ref. (Kockmann, 2007)).....	42
<b>Figure 2.5</b> Comparison of mass transfer parameters for conventional reactors and microreactors.....	45
<b>Figure 2.6</b> Main microreactor types used for photo(electro)catalytic degradation of aqueous-phase contaminants.....	48
<b>Figure 2.7</b> Electrochemical microreactors in flow-by and flow-through configurations. ....	65
<b>Figure 2.8</b> A novel microreactor developed and used by Díaz-Angulo et al. (2021) for a photo-Fenton AOP.....	70

<b>Figure 2.9</b> Different types of microreactors used for ozonation AOPs.....	74
<b>Figure 2.10</b> Schematic of a dielectric barrier discharge microfluidic plasma reactor.	78
<b>Figure 2.11</b> Numbering up and (selective) dimensional scaling up concepts of microreactors.....	84
<b>Figure 3.1</b> Schematic diagram of continuous flow UV/O <sub>3</sub> -based system.....	98
<b>Figure 3.2</b> Degradation performance of light (a) and heavy (b) crude oils under O <sub>3</sub> , UV/O <sub>3</sub> , and UV/O <sub>3</sub> /PS processes (O <sub>3</sub> dosage 10 mg/L, PS dosage 1 mM if used).....	104
<b>Figure 3.3</b> Significant analysis of crude oils degradation in different oxidation processes over time .....	109
<b>Figure 3.4</b> Effects of different parameters on light crude oil degradation in UV/O <sub>3</sub> /PS process: (a) initial oil concentration, (b) O <sub>3</sub> dosage, (c) PS dosage, (d) salinity, (e) pH level, and (f) temperature (O <sub>3</sub> dose 10 mg/L, PS dose 1 mM if not mentioned). In (a), the colors of line graph represent different initial concentrations and correspond to the colors in the bar graph (inset), in an ascending order. ....	114
<b>Figure 3.5</b> Effects of different parameters on heavy crude oil degradation in UV/O <sub>3</sub> /PS process: (a) initial oil concentration, (b) O <sub>3</sub> dosage, (c) PS dosage, (d) salinity, (e) pH level, and (f) temperature (O <sub>3</sub> dose 10 mg/L, PS dose 1 mM if not mentioned).....	115
<b>Figure 3.6</b> Pictures of initial light (a) and heavy (b) crude oils in reactor .....	120

<b>Figure 3.7</b> n-alkanes degradation performance in both light crude oil under (a) O <sub>3</sub> , (b) UV/O <sub>3</sub> , and (c) UV/O <sub>3</sub> /PS processes and heavy crude oil under (d) O <sub>3</sub> , (e) UV/O <sub>3</sub> , and (f) UV/O <sub>3</sub> /PS processes within 60 min .....	121
<b>Figure 3.8</b> PAHs degradation performance in both light crude oil under (a) O <sub>3</sub> , (b) UV/O <sub>3</sub> , and (c) UV/O <sub>3</sub> /PS processes and heavy crude oil under (d) O <sub>3</sub> , (e) UV/O <sub>3</sub> , and (f) UV/O <sub>3</sub> /PS processes within 60 min .....	124
<b>Figure 3.9</b> TOC removal efficiency after 1 h treatment of three processes in both light and heavy crude oils.....	127
<b>Figure 3.10</b> Performance of different processes (PS, UV, O <sub>3</sub> , UV/O <sub>3</sub> , and UV/O <sub>3</sub> /PS) for crude oil degradation .....	129
<b>Figure 3.11</b> Acute toxicity to <i>Vibrio fisheri</i> of oil compounds before and after 1 h three O <sub>3</sub> -based processes treatments of both light and heavy crude oils .....	132
<b>Figure 3.12</b> Contour maps of 3-D EEM fluorescence spectra of light and heavy crude oils and the mortality of <i>Artemia</i> before and after O <sub>3</sub> -based wastewater treatments. (a) Emission of untreated light crude oil and after O <sub>3</sub> , UV/O <sub>3</sub> , and UV/O <sub>3</sub> /PS processes; (b) Mortality of <i>Artemia</i> exposed to light crude oil; (c) Emission of untreated heavy crude oil and after O <sub>3</sub> , UV/O <sub>3</sub> , and UV/O <sub>3</sub> /PS processes; (d) Mortality of <i>Artemia</i> to heavy crude oil.....	134
<b>Figure 3.13</b> Optical microscope analysis of flocs under (a) O <sub>3</sub> , (b) UV/O <sub>3</sub> , and (c) UV/O <sub>3</sub> /PS processes in light crude oil .....	138
<b>Figure 3.14</b> The optical microscope analysis of the dried flocs in heavy crude oil ..	140

**Figure 3.15** SEM images and EDS of oil flocs before and after treatment for light crude oil: (a) initial, (b) O<sub>3</sub> process, (c) UV/O<sub>3</sub> process, (d) UV/O<sub>3</sub>/PS process and heavy crude oil: (e) initial, (f) O<sub>3</sub> process, (g) UV/O<sub>3</sub> process, (h) UV/O<sub>3</sub>/PS process..... 144

**Figure 3.16** FTIR characteristic of flocs which generated in (a) light and (b) heavy crude oils before and after three O<sub>3</sub>-based processes treatment..... 145

**Figure 4.1** BPA (a) and TOC (b) removal over time using the PS, MnO<sub>2</sub>, UV, UV/MnO<sub>2</sub>, MnO<sub>2</sub>/PS, UV/PS, and MnO<sub>2</sub>/UV/PS processes. Conditions at t = 0 min: [BPA] = 30 mg/L, [PS] = 1 mM, [MnO<sub>2</sub>] = 0.25 g/L, pH = 6.5, T = 22–25 °C ..... 156

**Figure 4.2** PS residual in MnO<sub>2</sub>/PS, UV/PS, and MnO<sub>2</sub>/UV/PS processes ..... 159

**Figure 4.3** Effects of (a) MnO<sub>2</sub> dosages, (b) PS concentration, and (c) pH level on BPA removal, and PS residual in different pH levels (d). Conditions at t = 0 min: [BPA] = 30 mg/L, pH in (a) and (b) = 6.5, [PS] in (a) and (c) = 1 mM, [MnO<sub>2</sub>] in (b) and (c) = 0.25 g/L. .... 160

**Figure 4.4** BPA degradation using MnO<sub>2</sub>/PS, UV/PS, and MnO<sub>2</sub>/UV/PS processes over 30 min. k = rate constant of pseudo-first-order kinetics. Conditions at t = 0 min: [BPA] = 30 mg/L, [PS] = 1 mM, [MnO<sub>2</sub>] = 0.25 g/L, pH = 6.5..... 164

**Figure 4.5** Effects of radical inhibitors on BPA concentrations over 30 min for UV/MnO<sub>2</sub>. Initial conditions: [BPA] = 30 mg/L, Ph = 6.5, [PS] = 1 mM, [MnO<sub>2</sub>] = 0.25 g/L. When inhibitor is used, initial [MeOH] = 1 M or [TBA]

= 1 M or [FFA] = 5 mM. ....	166
<b>Figure 4.6</b> Effects of radical inhibitors on BPA concentrations over 30 min for (a) MnO <sub>2</sub> /PS, (b) UV/PS, and (c) MnO <sub>2</sub> /UV/PS processes, and (d) effects these inhibitors on process rate constants. Initial conditions: [BPA] = 30 mg/L, pH = 6.5, [PS] = 1 mM, [MnO <sub>2</sub> ] = 0.25 g/L. When inhibitor is used, initial [MeOH] = 1 M or [TBA] = 1 M or [FFA] = 5 mM. ....	167
<b>Figure 4.7</b> ATR-FTIR spectra of MnO <sub>2</sub> particles (a) and the concentration of Mn leaching (b) after 2 h treatment via MnO <sub>2</sub> only, UV/MnO <sub>2</sub> , MnO <sub>2</sub> /PS, and MnO <sub>2</sub> /UV/PS processes .....	172
<b>Figure 4.8</b> MnO <sub>2</sub> recycles in MnO <sub>2</sub> /PS and MnO <sub>2</sub> /UV/PS processes.....	174
<b>Figure 4.9</b> XRD of MnO <sub>2</sub> before (a) and after (b) 2 h treatment in MnO <sub>2</sub> /UV/PS process .....	175
<b>Figure 4.10</b> SEM image and EDS analysis of MnO <sub>2</sub> before (a, b) and after (c, d) 2 h treatment in MnO <sub>2</sub> /UV/PS process .....	176
<b>Figure 4.11</b> Proposed main BPA degradation pathways with steps leading to the intermediates identified using GC-MS under the MnO <sub>2</sub> /UV/PS process	180
<b>Figure 4.12</b> Intermediates residue in MnO <sub>2</sub> /UV/PS process.....	183
<b>Figure 4.13</b> EC <sub>50</sub> of MnO <sub>2</sub> /UV/PS process mixtures determined after 4-fold dilution with the Microtox® Basic test. Initial conditions: [BPA] = 30 mg/L, [PS] = 1 mM, [MnO <sub>2</sub> ] = 0.25 g/L, with(out) phosphate buffer, pH = 6.5 .....	184
<b>Figure 5.1</b> Schematic diagram of the microfluidic reactor .....	193

<b>Figure 5.2</b> Characterization of g-C <sub>3</sub> N <sub>4</sub> , TiO <sub>2</sub> , and TiO <sub>2</sub> /g-C <sub>3</sub> N <sub>4</sub> nanosheets.....	198
<b>Figure 5.3</b> FTIR fingerprint regions of g-C <sub>3</sub> N <sub>4</sub> , TiO <sub>2</sub> , and TiO <sub>2</sub> /g-C <sub>3</sub> N <sub>4</sub> nanosheets	199
<b>Figure 5.4</b> Effects of parameters ((a) PS dose, (b) catalyst dose, (c) flow rate, (d) light distance, (e) pH level, and (f) inorganic salts) on BPS degradation in the microreactor (PS dose 1mM, catalyst 100 mg/L, light distance 3 cm if not mentioned) .....	201
<b>Figure 5.5</b> Residual graphs (a) normal probability plot for residuals, (b) histograms of residuals, (c) residuals vs. fitted values, and (d) residual vs. the run of the experiments .....	208
<b>Figure 5.6</b> (a) Main effect plot of impact factors in a microreactor, (b) Half-normal plot of effects to BPS degradation, and (c) 2-factor interaction plots for removal efficiency.....	212
<b>Figure 5.7</b> Comparison of BPS and TOC removal in micro- and batch reactors.....	214
<b>Figure 5.8</b> Comparison of reaction rate under batch and micro-reactors.....	216
<b>Figure 5.9</b> Comparison of the energy consumption in the (a) microreactor and (b) conventional reactors .....	219
<b>Figure 5.10</b> Acute toxicity of effluent from conventional and micro-reactors .....	222

## LIST OF TABLES

<b>Table 2.1</b> Key dimensionless parameters used in microfluidic mechanics. ....	35
<b>Table 2.2</b> Characteristics of photocatalytic microreactors reported over the last decade. .....	57
<b>Table 2.3</b> Characteristics of microreactors used for electrochemical AOPs. ....	66
<b>Table 2.4</b> Summary of AOP characteristics using conventional reactors and microreactors.....	87
<b>Table 3.1</b> Physicochemical properties of light and heavy crude oils at 15 °C .....	96
<b>Table 3.2</b> Kinetic parameters on crude oil degradation following first order rate law under three processes. ....	107
<b>Table 3.3</b> Kinetic parameters of different conditions on crude oil degradation following first order rate law under three processes.....	111
<b>Table 4.1</b> Parameters of BPA degradation following the pseudo-first-order kinetics with and without quenching (reaction time: 30 min; D: degradation efficiency) .....	169
<b>Table 4.2</b> Degradation products of BPA under the MnO <sub>2</sub> /UV/PS process identified using GC-MS .....	178
<b>Table 5.1</b> A 2 <sup>5</sup> full factorial design table .....	205
<b>Table 5.2</b> Significant factor effects and contributions.....	206

## LIST OF ABBREVIATIONS

ANOVA	One-way analysis of variance
ATR-FTIR	Fourier-transform infrared spectroscopy with attenuated total reflectance
AOPs	Advanced oxidation processes
BPA	Bisphenol a
BPS	Bisphenol s
BPs	Bisphenols
BSTFA	<i>N, o</i> -bis(trimethylsilyl)trifluoroacetamide
BTEX	Benzene, toluene, ethylbenzene, and xylenes
CNC	Computer numerical control
COD	Chemical oxidation demand
DBD	Dielectric barrier discharge
DCM	Dichloromethane
EC <sub>50</sub>	Effective concentration that given half-maximal response
EDS	Energy-dispersive x-ray spectroscopy
EEMs	Emission excitation spectra
FFA	Furfuryl alcohol
GC - MS	Gas chromatography - mass spectrometry
g-C <sub>3</sub> N <sub>4</sub>	Graphene carbon nitride
ICP-OES	Inductively coupled plasma optical emission spectrometer

IE	Inter-electrode
IS	Internal standards
ITO	Indium tin oxide
MeOH	Methanol
MnO <sub>2</sub>	Manganese dioxide
oxy-PAHs	Oxygenated pahs
PS	Persulfate
PAHs	Polycyclic aromatic hydrocarbons
PMS	Peroxymonosulfate
PEC	Photoelectrocatalysis
ROS	Reactive oxygen species
SEM	Scanning electron microscope
SIM	Selected ion monitoring
TBA	Tert-butyl alcohol
TMCS	Trimethylchlorosilane
TOC	Total organic carbon
UV	Ultraviolet
VSALLME	Vortex-shaker-assisted liquid-liquid microextraction
W/WWT	Water and wastewater treatment
XRD	X-ray diffraction

## LIST OF SYMBOLS

$a$	Effective interfacial area
$[A]$	Instant concentration
$Bo$	Bond number
$Ca$	Capillary number
$C$	Bulk concentrations
$C_{eq}$	Equilibrium concentrations
$C_{A,surf}$	Concentration of compound a at the water/catalyst surface
$C_{A,bulk}$	The concentration of compound a in the bulk aqueous phase
C10-C19	Short-chain $n$ -alkanes
C20-C29	Middle-chain $n$ -alkanes
C30-C35	Long-chain $n$ -alkanes
$Da_{II}$	Damköhler number
$D$	Molecular diffusivity
$Ha$	Hatta number
$k_{La}$	Volumetric mass transfer coefficient
$k_L$	Mass transfer coefficient
$k$	Intrinsic rate constant
$K_{a,d}$	Adsorption-desorption equilibrium constant
$k_g$	Global mass transfer coefficient
$L$	Diffusion path length

$\bullet\text{OH}$	Hydroxyl radical
$^1\text{O}_2$	Singlet oxygen
$-\text{OH}$	Hydroxyl group
$Pe$	Péclet number
$Re$	Reynolds number
$R$	Interfacial mass transfer rates
$r$	Instantaneous reaction rate
$\text{SO}_4^{\bullet-}$	Sulfate radical
$Sh$	Sherwood number
$Sc$	Schmidt number
$\%S$	Synergy value
$t_m$	Characteristic mixing time
$\mu\text{PBRs}$	Micro-packed bed reactors
$We$	Weber number

**CHAPTER 1**  
**INTRODUCTION**

## 1.1 Background

The presence of persistent and emerging organic contaminants has been growing concern worldwide and poses deleterious effects on human and environmental health, even at trace levels (Najam & Alam, 2023). For example, the persistent toxic organic compounds polycyclic aromatic hydrocarbons (PAHs) in marine oily wastewater could result in disastrous impacts on marine ecosystems due to oil production and transportation, oil spill responses, and other human activities near the coasts (Liu et al., 2021a; Song et al., 2021a). One of the emerging contaminants, bisphenols (BPs) such as bisphenol A (BPA), and its alternatives have become a globally recognized problem for environmental and public health in the last decade (Guo et al., 2023b). Exposure to persistent and emerging contaminants above a specific limit can lead to severe consequences for humans and aquatic life, and hence, pollutants need to be removed properly (Deyris et al., 2023). Therefore, developing effective technologies to treat these pollutants to acceptable levels is on the agenda.

As conventional wastewater treatment processes are insufficient in reducing trace concentrations of toxic and/or recalcitrant organic substances to below acceptable levels, there is an urgent need to develop more effective wastewater treatment technologies (Honarmandrad et al., 2023). Advanced oxidation processes (AOPs) based on the production of hydroxyl radical ( $\bullet\text{OH}$ ), which acts as a powerful oxidant, have been regarded as highly promising for the effective degradation of various

organic pollutants unselectively (Dong et al., 2021). Although various AOP-based technologies can reduce aqueous pollutant concentrations to within acceptable levels, their limited process efficiencies and high energy consumption rates remain the foremost concerns for extensive applications (Miklos et al., 2018). To overcome this drawback, emerging technologies, such as persulfate-based AOPs and environmental microfluidics, have been proposed for the highly effective degradation of recalcitrant organic pollutants (Lee et al., 2020; Liu et al., 2023).

Persulfate-based AOPs have drawn considerable attention in recent years due to their high efficiency in generating sulfate radical ( $\text{SO}_4^{\bullet-}$ ), which has more positive redox potential (2.6–3.1 V) than  $\bullet\text{OH}$  (1.9–2.7 V), to degrade recalcitrant organic pollutants (Wang & Wang, 2018). Persulfate (PS) is one of the main precursors for generating  $\text{SO}_4^{\bullet-}$ . PS can be activated by transition metal catalysts, nonmetal catalysts, ultraviolet (UV) and visible light, ultrasound, alkaline, heat, and strong oxidants to produce  $\text{SO}_4^{\bullet-}$  and other radicals for the removal of organic pollutants (Petala et al., 2020). Due to its low cost and high efficiency, most attention has been paid to the applications of transition metals or their oxides (*e.g.*, iron, copper, and cobalt) for PS catalytic activation (Pan et al., 2019; Wang et al., 2020a). Manganese dioxide ( $\text{MnO}_2$ ) is widely used as a catalyst or activator in various heterogeneous reaction systems due to its high natural abundance, low toxicity, and low environmental impact (Huang et al., 2019a; Huang et al., 2022). Ozonation or UV processes have been used to eliminate recalcitrant contaminants due to their ability to efficiently degrade recalcitrant organics

reliably via direct reaction with ozone molecules or the generation of  $\bullet\text{OH}$  with strong oxidizing capabilities (Liu et al., 2021a). All the above metal oxides and oxidants have been applied as activators for PS activation for organics removal (Wang & Wang, 2022). However, single activators are considered to have limited process efficiency, and synergetic persulfate activation was recently demonstrated with enhanced recalcitrant contaminants removal (Chen et al., 2024).  $\text{MnO}_2$  is a promising candidate for photocatalyst application due to its narrow bandgap (1–2 eV) and ability to absorb light under solar energy (Huang et al., 2019a). Previous reports indicated that the simultaneous use of  $\text{MnO}_2$  and UV light for PS activation has been considered for more generation of free radicals (Eslami et al., 2018). The efficiency of ozone in degrading organics is improved when combined with UV (254 nm) radiation. As one of the powerful AOPs, the UV/ $\text{O}_3$  process has been proven to have a strong ability to treat oily wastewater, such as n-alkanes and PAHs (Ji et al., 2024). It is reported that both  $\text{O}_3$  and UV can activate persulfate to form  $\text{SO}_4^{\bullet-}$  and  $\bullet\text{OH}$  simultaneously (Zou et al., 2021).

Microfluidic devices are state-of-the-art systems that manipulate chemical reactions and fluid behavior through the use of microchannels with lateral dimensions ranging from micron to millimeter scales. Microfluidics has attracted considerable attention over the last few decades in diverse fields, such as chemical synthesis, biological processes, control systems, and environmental applications (Cao et al., 2021e; Kim et al., 2021). For example, microreactors have been widely employed to synthesize organic compounds, nanoparticles, polymers, and pharmaceuticals (Gioria et al., 2020a;

Siguemoto et al., 2020). Recently, there has been a growing interest in utilizing microreactors for photocatalytic degradation because of their numerous advantages over conventional reactors (Liu et al., 2023). The interior structure of microreactors exhibits comparatively higher surface area-to-volume ratios, which reduces reactant diffusion distances, increases process efficiencies, and minimizes energy consumption (Bojang & Wu, 2020a). Microchannel reactors, with their small transverse dimensions, possess extremely high surface-to-volume ratios and consequently exhibit enhanced mass transfer rates. Some studies have reported that AOPs in microreactors overcome the shortcomings of conventional reactors. For example, a microreactor is considered one of the efficient solutions to enhance mass transfer and photocatalytic efficiency (Kim et al., 2022; Yu & Wang, 2020). However, detailed studies of the advantages and mechanism analysis of AOPs in microreactors for emerging contaminants removal are still limited (Shukla et al., 2021b).

## **1.2 Statement of Problems**

The emergence of more complicated persistent and emerging contaminants has brought many negative impacts on human life. For example, petroleum aromatic hydrocarbon (PAH) in marine oily wastewater, as one of the common persistent contaminants, can endanger marine ecosystems and affect human health. For emerging contaminants, we can take bisphenols as examples. Bisphenols (like bisphenol A and bisphenol S) can be found everywhere, such as in plastics, receipt paper, and containers.

Growing evidence has shown the long-term adverse effects of bisphenols on aquatic life and human health. Although various AOP-based technologies can be used to reduce these persistent and emerging contaminants from water or wastewater streams to within acceptable levels, their limited process efficiencies remain the foremost concerns for extensive applications. Therefore, exploring AOP enhancement methods is needed to remove trace levels of these contaminants.

Persulfate activation has emerged to be a promising AOP technique to abate a wide range of organic pollutants in water (Yan et al., 2023). Synergetic PS activation has been proven more effective than single activation (Zhang et al., 2021b). It is reported that both O<sub>3</sub> and UV can activate PS to form SO<sub>4</sub><sup>•-</sup> and •OH simultaneously. Qin et al. (2020) have indicated that the pseudo-first-order rate constants of atrazine degradation in the UV/O<sub>3</sub>/PS process increase by 3.3 times compared to that in the UV/O<sub>3</sub> process. While these findings suggest that SO<sub>4</sub><sup>•-</sup> could decrease energy consumption and enhance degradation efficiency, such a hypothesis has not been validated for treating marine oily wastewater. Oily wastewater can cause ecological disturbances, including alteration of the aquatic community structure and food chains, through physical and chemical means. However, the detailed toxicity evaluation of ozonation-based AOPs treated oily wastewater is rare. It is worth noting that the treatment of oily wastewater by ozonation can produce some flocs that can be suspended in water, stick to reactor walls, or float on the water surface. To our best knowledge, few studies have been reported on their properties (e.g., components and surface characteristics) and fate.

MnO<sub>2</sub> is a promising candidate for photocatalyst application due to its narrow bandgap (1–2 eV) and ability to absorb light under solar energy. However, to our best knowledge, synergistic use of MnO<sub>2</sub> and UV has never been applied for PS activation. Recently, Eslami et al. (2018) confirmed that the synergistic use of MnO<sub>2</sub> and UV is a promising hybrid activator for peroxymonosulfate (PMS) activation. Accordingly, there are many distinctive differences during the activation of PS and PMS, especially in reactivity toward radicals and responses to different pH levels. Furthermore, the synergistic mechanism for PS catalytic activation, especially the interactions between MnO<sub>2</sub> and UV, remains unknown and deserves further investigation.

The advantages of microreactors, including their continuous-flow processing capabilities, large specific surface areas, rapid heat, and mass transfer, and reduced safety hazards, have fostered the development of AOPs for water and wastewater (W/WWT) treatment at the microscale (Russo, 2021). To date, some studies have mainly focused on enhancing photocatalytic, electrochemical, Fenton, ozonation, and plasma-phase AOPs by exploiting microfluidic technologies. Results indicate that the unique hydrodynamic features and greater range and tunability of process conditions offered by microfluidic devices enable AOPs that are safer, more effective for the degradation of aqueous organic pollutants, and have superior energy efficiency when compared with conventional reactors (Lin et al., 2021c). Some researchers reviewed the application of photochemical and photocatalytic microreactors for wastewater treatment (Heggo & Ookawara, 2017). However, these reviews lack an in-depth

discussion of the effects of reactor dimension on AOPs. The opportunities and challenges of various AOP types (e.g., photocatalytic, electrochemical, Fenton, ozonation, and plasma-phase processes) for W/WWT treatment have not yet been comprehensively reviewed. In recent years, there has been a growing interest in utilizing microreactors for photocatalytic degradation because of their numerous advantages over conventional reactors. Microreactors' interior structures exhibit comparatively higher surface area-to-volume ratios, which reduce reactant diffusion distances, impart high process efficiencies, and minimal energy consumption. Microchannel reactors, with their small transverse dimensions, possess extremely high surface-to-volume ratios and consequently exhibit enhanced mass transfer rates. Some studies have reported that AOPs in microreactors overcome the shortcomings of conventional reactors, but detailed studies are still limited (Dong et al., 2022).

### **1.3 Objectives and Tasks**

The objectives of this dissertation are the exploration and enhancement of AOPs for bisphenols and PAHs removal. The main enhancement methods involve synergetic persulfate activation and microreactor design. Some synergetic PS activation strategies and key impact factors will be summarized as reference for practical application. The advantages of microreactors over the use of conventional reactors to enhance the performance of AOPs will be illustrated to provide theoretical support for future research and development of AOPs in microreactors. In addition, the oxidation

mechanism, degradation pathway, and acute toxicity studies of persistent and emerging contaminants will provide a strong basis for future policy formulation. The main tasks of this dissertation are listed below.

Chapter 2 gives an in-depth literature review of recent advances in two enhancement methods of AOPs: Synergetic persulfate activation and AOP-microreactor design. Various synergetic persulfate activation strategies and their advantages are discussed. Key impact factors are discussed to provide data support on the application of PS-based AOPs. Special attention is paid to the rapidly emerging area of environmental microfluidics in Part II, in which recent advances in the development and application of microreactors in AOPs for water and wastewater treatment are described and discussed in detail. Chapter 3 develops a bench-scale O<sub>3</sub> reactor and examines the degradation and toxicity of on-site treatment of marine oily wastewater by three AOP (O<sub>3</sub>, UV/O<sub>3</sub>, UV/O<sub>3</sub>/PS) technologies. Furthermore, the flocs characterization reveals the fate of insoluble components during oxidation. Chapter 4 investigates an enhanced MnO<sub>2</sub>/UV/PS process for efficient BPA removal and explores the degradation mechanism, degradation pathway, and toxicity reduction of BPA in this synergetic persulfate activation process. Chapter 5 designs a UV light based photocatalytic-microreactor system for BPS degradation. The main impact factors in a photocatalytic-based AOP-microreactor are explored by full factorial design. The degradation performance, energy consumption, and toxicity evaluation in both

microreactor and batch reactor are examined/compared thoroughly. Finally, Chapter 6 presents general conclusions and recommendations for future work.

The structure of the thesis is displayed below (**Fig. 1.1**). Chapter 1 introduces the general research background, gap, objectives, and structure of the PhD dissertation. Chapter 2 provides a literature review on the two emerging AOP enhancement methods, including 1) Persulfate-based enhancement method and 2) Microfluidics-based method. Chapter 3 develops a lab-scale reactor and applies the synergetic persulfate-based process (UV/O<sub>3</sub>/PS) for marine oily wastewater treatment. Chapter 4 investigates an enhanced catalyst-based persulfate activation method (MnO<sub>2</sub>/UV/PS) for BPA removal. Chapter 5 designs an AOP-microreactor system, examines its degradation efficiency for BPS, and compares it with conventional reactors. Chapter 6 concludes the thesis with summarized contributions and recommendations for future research.

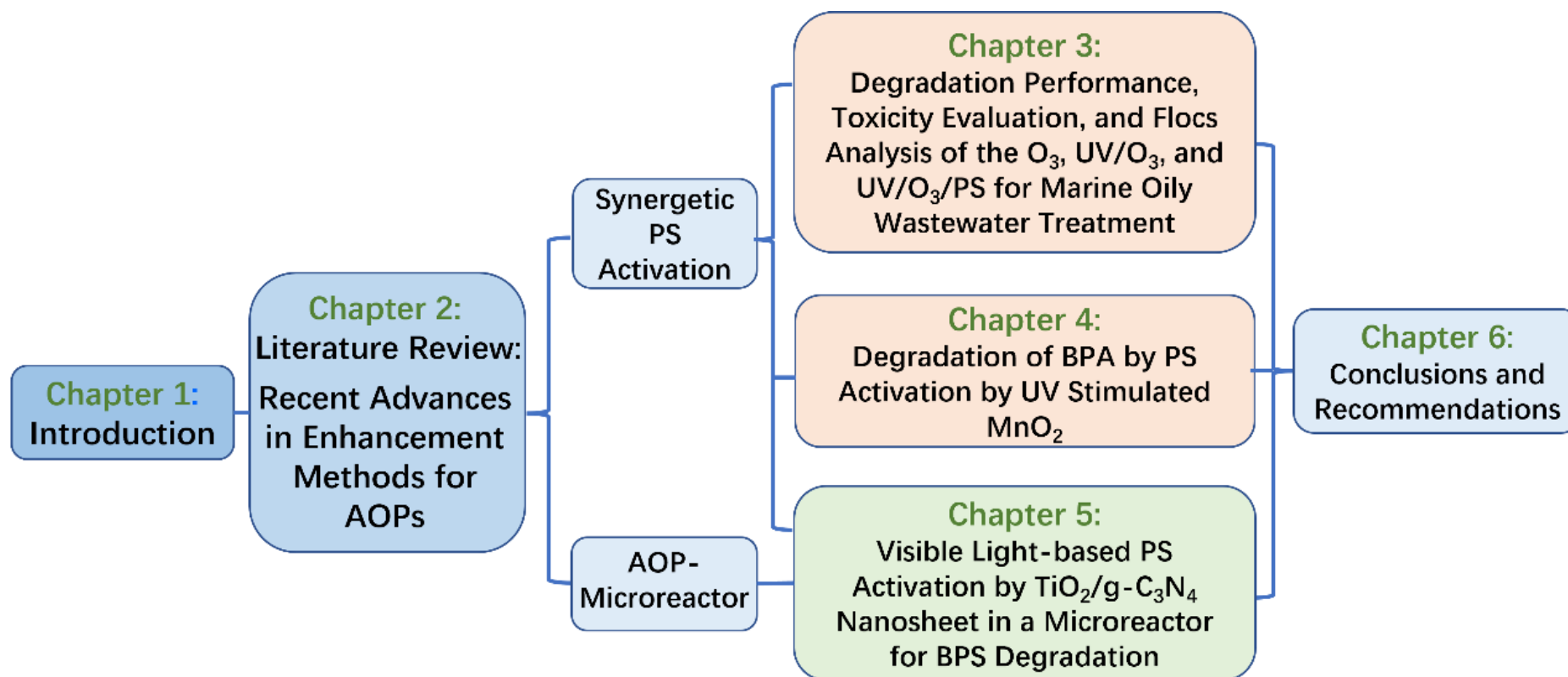


**Figure 1.1** The structure of the thesis

## 1.4 Co-Authorship Statement

I am the primary author of this dissertation under the supervision of Dr. Bing Chen and the co-supervision of Dr. Stanislav R. Stoyanov and Dr. Baiyu (Helen) Zhang. This dissertation comprises one literature review and three research papers in Chapters 2 to 5. Chapter 2 is based and expanded on the paper “Advanced Oxidation Processes in Microreactors for Water and Wastewater Treatment: Development, Challenges, and Opportunities,” published in *Water Research*. In this Chapter, I wrote the first draft of the literature review under the supervision of Dr. Bing Chen and Dr. Bo Liu and subsequently revised it based on the valuable comments from co-authors. Chapter 3 is based on the paper “Comparison of O<sub>3</sub>, UV/O<sub>3</sub>, and UV/O<sub>3</sub>/PS Processes for Marine Oily Wastewater Treatment: Degradation Performance, Toxicity Evaluation, and Flocc Analysis” published in *Water Research*. In this Chapter, I developed the experimental plan and designed the reactor under the supervision of Dr. Bing Chen. I conducted all the experiments and prepared the manuscript with the assistance of co-authors. To achieve the best outcomes, I have collaborated with Dr. Benjamin de Jourdan from Huntsman Marine Science Centre to complete the toxicity analysis. Chapter 4 is based on “UV stimulated manganese dioxide for the persulfate catalytic degradation of bisphenol A” published in *Catalysts*. In this Chapter, I was the primary author under the direct supervision of Dr. Bing Chen. I performed the experiments and wrote the first draft of the manuscript. I also revised and polished the manuscript based on all the co-

authors' edits and suggestions. In Chapter 5, I was the primary author, contributing to the conceptualization, methodology, experiment design, and manuscript preparation. Details of the contributions of each author in each paper are listed at the beginning of the below Chapters.

# CHAPTER 2

## RECENT ADVANCES IN ENHANCEMENT METHODS FOR ADVANCED OXIDATION PROCESSES

---

The contents of this chapter are based and expanded on the following publication:

**Dong, G.**, \*Chen, B., Liu, B., Hounjet, L., Cao, Y., \*Stoyanov, S. R., Yang, M., & Zhang, B. (2022). Advanced Oxidation Processes in Microreactors for Water and Wastewater Treatment: Development, Challenges, and Opportunities. *Water Research*, 118047. <https://doi.org/10.1016/j.watres.2022.118047>

**Authorship contribution statement:**

**Guihua Dong:** *Conceptualization, Methodology, Investigation, Visualization, Writing – original draft.*

**Bing Chen:** *Conceptualization, Supervision, Writing – review & editing.* **Bo Liu:** *Methodology, Investigation, Visualization, Writing – original draft.* **Lindsay J Hounjet:** *Writing – review & editing.*

**Yiqi Cao:** *Visualization, Writing – original draft.* **Stanislav R Stoyanov:** *Supervision, Writing – review & editing.* **Min Yang:** *Visualization, Writing – original draft.* **Baiyu Zhang:** *Supervision, Writing – review & editing.*

## 2.1. Introduction

Increasing water consumption to meet agricultural, industrial, and municipal needs threatens global water security (Alemu & Dioha, 2020). Water and wastewater treatment has, therefore, been emphasized as critical measures needed to alleviate increasing water scarcity (Huang & Fan, 2020). Conventional primary and secondary wastewater treatment processes often fail to reduce trace concentrations of toxic and/or recalcitrant organic substances to below acceptable levels. Therefore, there is an urgent need for the development of more effective wastewater treatment technologies (Stasinakis et al., 2013). Under these circumstances, AOPs have attracted considerable attention owing to their use of reactive oxygen species (ROS) that unselectively convert various aqueous contaminants into relatively nontoxic substances (Dong et al., 2021; Liu et al., 2021a). Although various AOP-based technologies can be used to reduce aqueous pollutant concentrations to within acceptable levels, their limited process efficiencies and high energy consumption rates remain foremost concerns for extensive applications (Miklos et al., 2018).

Exploring new enhancement methods for advanced oxidation technology is one of the key strategies to solve the above problems. Persulfate-based AOP has attracted increasing attention due to its economic, effective, practical, safety and stability characteristics. PS is not easy to react directly with organic pollutants and usually needs to be activated to produce active species such as  $\text{SO}_4^{\bullet-}$  and  $\bullet\text{OH}$  to degrade them (Wang

& Wang, 2022). The summary and comparison of various activation methods will provide method reference and support for determining the optimum technologies for organic pollutants degradation in practical applications. Microfluidics has emerged as a promising solution for AOP enhancements in water treatment because it enables faster more efficient mass transfer, improves treatment efficiency, and decreases the energy consumption (Santana et al., 2020b). While the AOP in microreactor technology remains in an early stage of development, the summary and exploration of more AOP-microreactor methods offer valuable insight for future research and development of AOPs in microreactors for environmental practice.

In this work, recent advances in AOP enhancement methods primarily focus on synergetic persulfate activation and environmental microfluidics will be summarized. Some persulfate activation methods and their combination strategies will be discussed to optimize the performance of sulfate radical-based AOPs. As microfluidics is the state-of-art technology in the environmental field and is growing rapidly, and there are few studies in this topic, more attention in this work will be placed on the microfluidics, especially for the application of AOPs in microreactors.

## **2.2. Persulfate Activation**

The conventional AOPs presented good performance for the removal of persistent and emerging contaminants, mainly depending on the generation of hydroxyl radicals. Over the past decades, sulfate radical-based AOPs have been receiving increasing

attention due to their high efficiency for generating  $\text{SO}_4^{\bullet-}$ . Persulfate originally was introduced for soil and groundwater remediation in the late 1990s to overcome the limitations of  $\text{H}_2\text{O}_2$  (Lee et al., 2020). In general, sulfate radicals are produced by cleaving the peroxide bond in the persulfate molecule via energy and electron transfer reactions (**Fig. 2.1**). Sulfate radicals possess equal or even more positive redox potential (2.5–3.1 V) than hydroxyl radicals (1.9–2.7 V) (Wang & Wang, 2018). Therefore, sulfate radical-based AOPs are expected to exhibit better capacity for degrading persistent and emerging contaminants.

### **2.2.1 Activation methods**

Persulfate is not easy to react directly with organic pollutants and must be activated to produce active species. Most academic research focuses on developing various persulfate activation strategies (Zawadzki, 2022). In general, PS can be activated by physical and chemical methods to produce  $\text{SO}_4^{\bullet-}$ ,  $\bullet\text{OH}$ , singlet oxygen ( $^1\text{O}_2$ ), and other reactive species to remove organic pollutants.

#### ***2.2.1.1 Physical activation methods***

The common physical activation methods include thermal activation, cavitation activation (e.g., ultrasonic, hydrodynamic), electromagnetic radiation activation (e.g., UV light, visible light, microwave, Gamma-ray), and discharge plasma activation.

Persulfate can be induced by thermal activation at temperatures above 40°C, which will speed up the reaction and greatly reduce the need for oxidants (Li et al., 2022).

Thermal heating, microwave heating, and photo heating can all be applied as the typical thermal driving force to activate PS for organics removal. Thermal activation is less influenced by the color of the wastewater and has been applied in small-scale wastewater treatment, such as hospital effluents (Ghauch & Tuqan, 2012).

Ultrasonic (US) refers to the use of the cavitation effect to make the liquid locally generate high temperature and pressure and generate stirring through vibration. Under the joint interaction, PS is activated to produce radicals to degrade organic pollutants (Gujar et al., 2023; Zhang et al., 2015). Hydrodynamic cavitation can produce instantaneous local high pressure and temperature in water. One example of hydrodynamic cavitation activation is the microbubble-activated PS that can effectively degrade organic matter (Miruka et al., 2021).

Electromagnetic radiation activation methods such as UV light are one of the popular activation systems. Studies showed that the wavelength of UV light at 254 nm has the highest effect on the activation of PS (Yang et al., 2018). The UV/PS process has been considered economical and safe. It has a better treatment effect and stronger oxidation capacity than UV/H<sub>2</sub>O<sub>2</sub> for the treatment of slightly polluted water (Matzek & Carter, 2016). Visible light, also known as sunlight or simulated sunlight, can activate PS at room temperature but is less efficient. It can be used in combination with other methods, such as catalysts, to better activate PS in the degradation of organics (Saha & Bagdi, 2022). Microwave is another well-known PS activation method due to the advantages of reducing the activation energy of the reaction, shortening the reaction

time, and enhancing the selectivity. Gao et al. (2020) carried out the reaction at the power of 500 W to achieve 99.4% tetracycline hydrochloride degradation for only 5 min. However, energy consumption and its harmful effects on humans limit the large-scale application of microwave-based PS activation. Gamma radiation has a high energy and penetrating ability and can generate many active substances such as  $\bullet\text{OH}$ , hydrated electrons, and hydrogen atoms, which directly contribute to the degradation of organic pollutants. On the other hand, gamma radiation can play a role in activating PS. Zhang et al. (2021c) investigated the triclosan degradation by using gamma radiation. It turns out that the addition of PS could significantly save reaction time. However, high cost, the requirement of instruments, and their harmful to human body limit their large-scale application.

Discharge plasma can produce various active species (e.g.,  $\text{H}_2\text{O}_2$ ,  $\text{O}_3$ ,  $\bullet\text{OH}$ ,  $\text{HOO}\bullet$ ) to directly degrade organic matter. When plasma is applied as the PS activator, more reactive substances are generated (Shilin et al., 2023). Several works proved the high efficiency of plasma-activated PS process for various recalcitrant contaminants removal (Fang & Huang, 2018; Liang et al., 2021; Wang et al., 2021). However, in comparison with other activation methods, discharge plasma would increase the PS consumption due to the complex plasma reaction and activation process (Wang et al., 2022).

### ***2.2.1.2 Chemical activation methods***

Chemical activation methods involve alkaline activation, electrochemistry activation, and catalyst activation (e.g., carbon-based catalyst, transition metal and metal oxide).

The pH plays a key role in the PS activation. PS can be decomposed into sulfate radicals under alkaline conditions, and sulfate radicals can further transform into hydroxyl radicals. Previous studies have attempted the use of alkaline activation methods for the treatment of organics polluted groundwater and soil (Santos et al., 2018). Although alkaline activation methods were considered as an effective way for organic contaminants degradation, the strict pH limits their wide application.

Electrochemistry activation has the advantages of longer life of radicals, wide adaptability to external conditions, and a high removal rate of pollutants. The mechanism of the electrochemistry activation method is the loss of electrons from the metal anode and the conversion of persulfate ions. Ding et al. (2020) investigated the performance of electrolysis activated PS in different electrode materials. They found that the boron-doped diamond (BDD) anode is better than the dimensional stable anode (DSA) anode under the same conditions for bisphenol A degradation.

One of the research hotspots for PS activation is the application of various carbon-based materials, including activated carbon, biochar, and so on. It has been reported that the oxygen-containing groups in carbon-based materials played a key role in PS

activation. The mechanism of PS activation by carbon-based materials is based on the electron transfer, generation of free radicals, and singlet oxygen (Devi et al., 2016). Active carbon is one of the popular carbon materials because it has the advantages of developed microporous structures and excellent absorption performance. It provides lots of surface active sites for PS activation and reduces the activation energy and shortens the reaction time. Lee et al. (2013) investigated the degradation of PFOA under the active carbon activated PS system, and they found that the PFOA removal rate was 12 times higher than that in PS only system. As an environmentally friendly material, biochar has gained increasing attention from researchers in the field of pollutants removal as the catalyst. Guo et al. (2020) applied the biochar activated PS system to remove benzo(a)pyrene (BaP) in sewage water and achieved nearly 90% of remove rate. Various other carbon-based materials, such as graphene, carbon nanotube, and heteroatom doping, have also been used as activators in a wide pH range and showed excellent performance for different kinds of organic pollutants removal (Hou et al., 2023; Liu et al., 2022b; Wu et al., 2022).

Transition metal and metal oxide have been widely used to activate PS to degrade various organic contaminants based on previous reports (Zheng et al., 2022). Transition metal activation of PS is based on the chemical reaction between transition metal and PS to generate oxidative free radicals. Iron, manganese, and their oxides are the most studied metals due to their excellent properties, such as being environmentally friendly, relatively non-toxic, and cost-effective compared to other transition metals (Karim et

al., 2021; Zhu et al., 2018). Various transition metal ions (e.g.,  $\text{Fe}^{2+}$ ,  $\text{Mn}^{2+}$ ,  $\text{Ag}^+$ ,  $\text{Cu}^{2+}$ ,  $\text{Co}^{2+}$ , and  $\text{Zn}^{2+}$ ) have been proven to be effective in activating PS in the aquatic environment, while the difficulty in removing those ions from water bodies limits their wide application (Li et al., 2021). Fe-based heterogeneous materials (e.g., zero-valent iron,  $\text{Fe}_2\text{O}_3$ ,  $\text{Fe}_3\text{O}_4$ , and  $\text{FeOOH}$ ) are considered the most used transition metal catalysts for PS activation its abundant reserves, non-toxicity, and environmental friendliness (Li et al., 2021). The most frequently studied  $\text{Fe}_3\text{O}_4$  has drawn substantial attention due to its cubic inverse spinel crystal structure that plays an active role in PS activation (Pervez et al., 2020). Manganese dioxide ( $\text{MnO}_2$ ) is one of the most ubiquitous minerals and is regarded as a feasible material due to its low cost, natural abundance, high stability, and unique  $\text{Mn}^{2+}/\text{Mn}^{3+}/\text{Mn}^{4+}$  redox cycles (Yuan et al., 2020). Zhu et al. (2018) found that  $\text{MnO}_2$  could act as the PS activator to generate non-radical singlet oxygen from decomposition of manganese intermediate.

### ***2.2.1.2 Synergetic activation methods***

Single activation methods have been verified to have some unavoidable shortcomings. For example, thermal will lead to high energy consumption, and transition metal activation will generate metal ions, which cause secondary pollution. The advantages of different activation methods can be complementary; therefore, the combination of different activation methods becomes common. Numerous studies have verified that synergetic persulfate activation has become popular due to their thorough

degradation of organic contaminants and energy saving (Yan et al., 2023). For physical activations, thermal activation itself is limited due to the temperature range, which can be combined with other activation methods such as ultrasonic or UV light. During this synergetic activation process, both energy saving and high efficiency could be achieved with less persulfate dosage and low ultrasonic frequency (Gujar et al., 2023). Compared with the above-mentioned physical synergetic activation methods, most attention has been paid to the combination of chemical activation methods. Among them, the synergetic use of transition metals or their oxides (e.g., iron, manganese, copper, and cobalt) and UV have been recognized as one of the cheapest and most powerful hybrid activators for persulfate activation (Pan et al., 2017; Pan et al., 2019; Wang et al., 2020a). For the synergetic use of electrochemistry and metal catalysts, persulfate activation can be promoted by adding a variety of transition metal elements to the electrode or adding transition metal oxides and ions. Meanwhile, the formation of toxic intermediates and by-products can be inhibited during this combination process (Lei et al., 2020; Qi et al., 2021). Strong oxidizing active substances is another useful catalyst for persulfate activation.  $O_3$  itself has a certain ability to directly oxidize organic pollutants and is one of the powerful active substances for persulfate activation. Qiao et al. (2019) carried out a reaction under  $O_3/PS$  oxidation process, and over 90% of nitrobenzene was removed within 30 min. Zou et al. (2021) achieved 99.8% of Meta-cresol removal in 30 min under the conditions of less  $O_3$  dosage and the assistance of UV irradiation. This

indicated that the combination of UV/O<sub>3</sub> is conducive to the improvement of the persulfate activation for the production of reactive species.

## **2.2.2 Key factors influencing PS activation**

### ***2.2.2.1 Effect of pH value***

The pH value plays an important role in almost all reactions among the widely investigated activation methods. In general, PS activation has a wide pH range of applications, although the oxidation potential changes with acidity and alkalinity (Gujar et al., 2023). The main oxidation active substance is SO<sub>4</sub><sup>•-</sup> under acidic conditions, becomes •OH in alkaline conditions, and will be converted into O<sub>2</sub><sup>•-</sup> under strongly alkaline conditions. Usually, the pH should be adjusted to >7 in an alkaline activation system, while the pH will remain neutral or acidic in a cavitation activation system such as UV or plasma (Guo et al., 2023a). For the metal oxide activation method, pH has also been found to have a dramatic effect on the surface charge of metal oxide, which significantly enhances its activation performance (Mani et al., 2021). In some specific activation methods, especially in the presence of catalysts or metal ions, the pH needs to be adjusted to avoid catalyst deactivation or metal ion precipitation (Wang & Wang, 2022).

### ***2.2.2.2 Effect of water matrix***

The water matrix may affect the generation of reactive oxygen species during PS activation. In some cases, the common anions such as Cl<sup>-</sup>, HCO<sub>3</sub><sup>-</sup>, CO<sub>3</sub><sup>2-</sup>, and SO<sub>4</sub><sup>2-</sup>

can inhibit the activation of PS and the degradation of different pollutants due to their ability to quench  $\text{SO}_4^{\bullet-}$  and  $\bullet\text{OH}$  from the aquatic environment. For example, it was reported that  $\text{Cl}^-$  has certain levels of promoting degradation in some pesticides (Khan et al., 2021; Lebig-Elhadi et al., 2020). The degradation effect of  $\text{Cl}^-$  on the same substance is also related to the concentration of  $\text{Cl}^-$  itself. When the  $\text{Cl}^-$  concentration is low ( $<10$  mmol/L), the degradation of 2,4-D can be slightly promoted, but when the  $\text{Cl}^-$  concentration is high (50 mmol/L), the degradation of 2,4-D is affected to a certain extent by inhibition.

### **2.2.3 Summary**

In general, different activation methods have their own advantages and limitations. Synergetic persulfate activation is believed to trend toward the direction of high efficiency, aiming to fully activate persulfate and minimize energy consumption and environmental effects. The pH value and the ions contained in the wastewater play a key role in the PS activation and degradation of organic pollutants. It's necessary to find the appropriate combination of different activation methods to overcome shortcomings and increase the process efficiency in real practical applications.

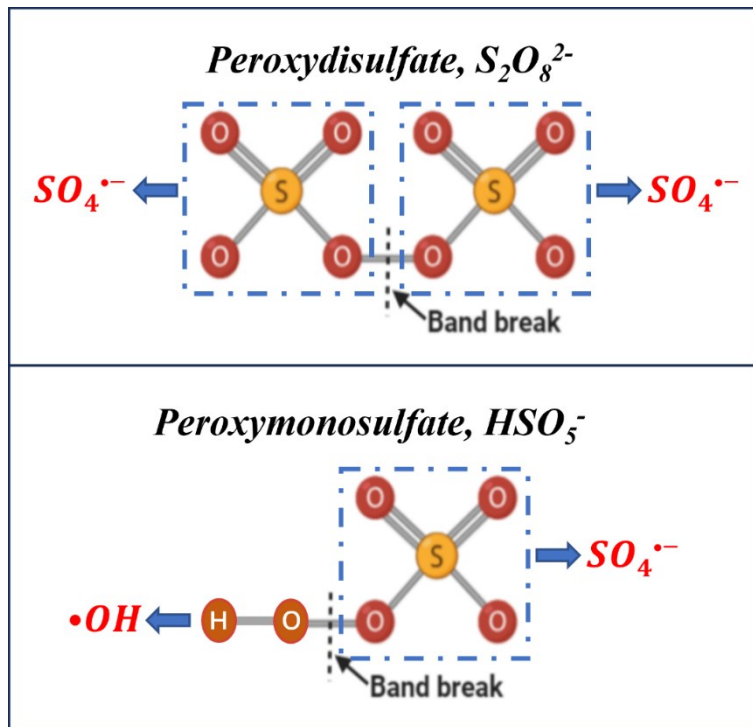


**Figure 2.1** Generation of sulfate radicals by persulfate activation. The dashed black line represents the fission position of O-O single band for the formation of sulfate radicals.

### 2.3. Environmental Microfluidics

Microreactors, or microfluidic devices, are state-of-art systems that manipulate both chemical reactions and the behavior of fluids by using microchannels with lateral dimension measuring from micrometer through millimeter scales (1  $\mu\text{m}$  to 1 mm). Microreactors offer many advantages over conventional reactors; their small size and high interfacial surface areas give rise to short diffusion and conduction paths for laminar flow and enhanced mass transfer. Microreactors can also be made of transparent materials to enable visual observations of reaction processes in real time, and the use of external light sources for photocatalytic AOPs (Cambié et al., 2016). **Fig. 2.2** illustrates differences between a conventional stirred-tank photocatalytic reactor and a microreactor for W/WWT. Over the last few decades, considerable attention has been given to applications of microreactor technologies in diverse fields, such as chemical synthesis, biological processes, control systems, and environmental applications (Cao et al., 2021d; Kim et al., 2020; Wong et al., 2020; Yao et al., 2015; Yew et al., 2019). For instance, microreactors have been widely employed to synthesize organic compounds, nanoparticles, polymers, and pharmaceuticals (Gioria et al., 2020b; Siguemoto et al., 2020; Su et al., 2020). The extreme temperature and pressure conditions, toxicity of chemicals, and reaction kinetics of the organic synthetic processes are the main aspects researchers have been concerned about (Suryawanshi et al., 2018). In such situations, owing to their inherent operational safety, ease-of-use,

and high process efficiencies, microreactors have been proven to achieve high product yields and selectivities with minimal energy consumption (Ashikari et al., 2020; Suryawanshi et al., 2018). Many studies have also demonstrated the utility of microfluidic devices for environmental applications, including sample component separation and extraction, contaminant detection/quantification, and water purification (Santana et al., 2020a; Wang et al., 2020c). The advantages of microreactors, including their continuous-flow processing capabilities, large specific surface areas, rapid heat and mass transfer, and reduced safety hazards, have fostered the development of AOPs for W/WWT at the microscale (Cambié et al., 2016; Russo, 2021).

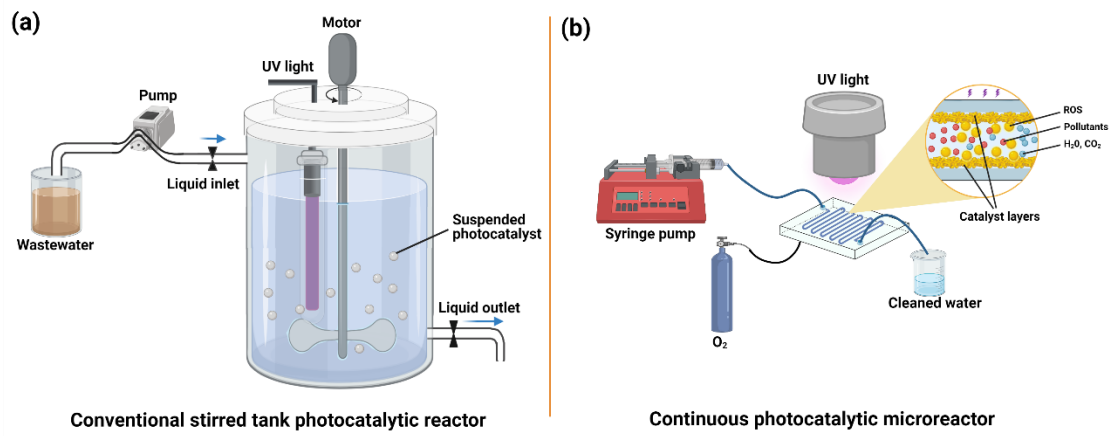


**Figure 2.2** (a) Conventional photocatalytic reactor and (b) microreactor used for

W/WWT

Efforts to adapt and employ microfluidic processes to intensify and precisely control chemical reactions for various industrial applications have increased appreciably over the last few decades (Cambié et al., 2016; Nge et al., 2013). We present strong evidence to suggest that a new area of “environmental microfluidics” has emerged and is growing rapidly, especially in its applications to water-related research. Based on the results of a Web of Science database search (see **Fig. 2.3**), over the past decade, there has been an increasing number of publications related to microfluidics and their applications to water treatment. The slight decrease of publications in 2020 may be due to COVID-19. These results show that although microfluidics research is growing steadily (approximately 3400-5750 articles per year from 2011-2020), only a small portion of microfluidic studies is related to water treatment (30-90 articles per year). To date, such studies have mainly focused on enhancing photocatalytic, electrochemical, Fenton, ozonation, and plasma-phase AOPs by exploiting microfluidic technologies. Results indicate that the unique hydrodynamic features, and greater range and tunability of process conditions offered by microfluidic devices, enable AOPs that are safer, more effective for the degradation of aqueous organic pollutants, and have superior energy efficiency when compared with conventional reactors (Lin et al., 2021b; Russo, 2021). Tanimu et al. (2017) reviewed the manufacturing of catalytic microreactors and their applications in photochemical and pharmaceutical synthesis. Heggo and Ookawara (2017) provided a general overview of different types of photocatalytic microreactors. Das and Srivastava (2016) and Shukla et al. (2021a)

highlighted the fabrication and application of photochemical and photocatalytic microreactors for wastewater treatment. However, these reviews lack in-depth discussion of the effects of reactor dimension on AOPs. The opportunities and challenges of various AOP types (*e.g.*, photocatalytic, electrochemical, Fenton, ozonation, and plasma-phase processes) for W/WWT have not yet been comprehensively reviewed.

This work provides an in-depth discussion of recent advances in AOP-microreactor systems for W/WWT by reviewing the unique hydrodynamic characteristics of microfluidic devices, their component materials, and fabrication techniques. The merits of using variously designed microreactors to carry out photocatalytic, electrochemical, Fenton, ozonation, and plasma-phase AOPs for W/WWT are discussed in detail. Further, impact factors, kinetic modeling, scale-up strategies, and cost-reduction of AOP-microreactor systems are also considered.

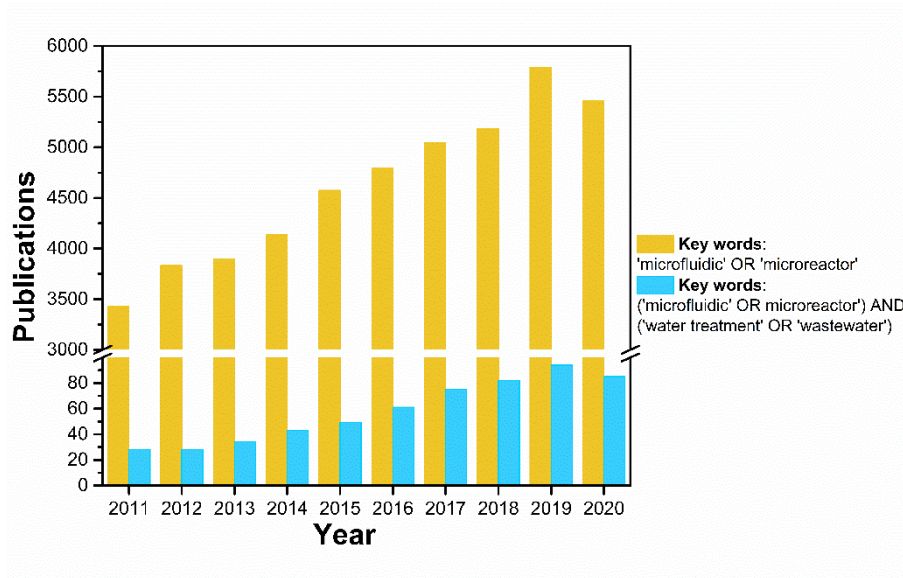


**Figure 2.3** Peer-reviewed publications on microfluidic processes over the last decade.

Source: Web of Science.

### **2.3.1 Hydrodynamic characteristics of microreactors**

Understanding of microfluidic hydrodynamic characteristics is needed to successfully apply microreactor technology to AOPs. Compared with larger, bulk reactors, an essential advantage of microreactors is their ability to significantly accelerate mass transfer processes. Within microreactors, the presence of microchannels having high surface area-to-volume ratios that impart short diffusion lengths improves both mass and heat transfer (Sattari-Najafabadi et al., 2018). Previous reports have demonstrated that, compared with conventional reactors, microreactors can increase overall mass transfer coefficients by more than one order of magnitude, making them powerful tools for enhancing reaction rates (Dessimoz et al., 2008; Sattari-Najafabadi et al., 2018). In fluid mechanics, several dimensionless parameters are commonly used to quantify mass transfer rates that affect intrinsic reaction kinetics (Song et al., 2018a). Mass transfer phenomena occurring in microreactors can be described by the characteristic mixing time and the volumetric mass transfer coefficient in single and multi-phase systems (Su et al., 2014).

#### ***2.3.1.1 Dimensionless parameters relevant to microfluidic processes***

The most important type of mass transfer occurring in a microreactor is diffusion, the predominance of which distinguishes such a system from a conventional reactor. Within the latter, inertial force dominates the flow behavior, and the predominant mass transfer type is advection. As the reactor scale decreases to the microscale, effects of

reactor capillaries, surfaces and interfaces, as well as those attributable to fluid properties, e.g., viscosity and surface tension, become increasingly important (Song et al., 2018b). In the field of microfluidics, some important dimensionless parameters, such as Reynolds number, Weber number, Capillary number, Bond number, second Damköhler number, Péclet number, Schmidt number, Sherwood number, and Hatta number, have been used to describe flow regimes, study mass transfer mechanics, and develop theoretical models of microfluidic processes (Geng et al., 2020; Russo, 2021). The formulation and significance of each parameter in the capillary or microchannel environment of a microreactor are presented in **Table 2.1**.

**Table 2.1** Key dimensionless parameters used in microfluidic mechanics ((Banerjee et al., 2019; Fischer et al., 2010; Geng et al., 2020; Kakaç et al., 2010; Russo, 2021; Su et al., 2014)).

<b>Dimensionless parameter</b>	<b>Formulation</b>	<b>Conceptual expression</b>	<b>Relationship to mass transfer</b>	<b>Significance to fluid mechanics</b>
Reynolds number	$Re = \mu\rho L/\eta$	$\frac{\text{Inertial force}}{\text{Viscous force}}$	Mixing time ( $t_m$ ) decreases when $Re$ increases.	Distinguishes laminar flow from turbulent flow
Weber number	$We = \frac{\rho\mu^2L}{\gamma}$	$\frac{\text{Inertial force}}{\text{Interfacial tension}}$	–	Describes fluid flow in multiphase systems
Capillary number	$Ca = \frac{\mu\eta}{\gamma}$	$\frac{\text{Viscous force}}{\text{Interfacial tension}}$	–	Describes the dynamic contact angle of a flowing droplet at an interface
Bond number	$Bo = \frac{\rho gL}{\gamma}$	$\frac{\text{Gravitational force}}{\text{Interfacial tension}}$	–	Determines behaviors of bubbles and droplets

<b>Dimensionless parameter</b>	<b>Formulation</b>	<b>Conceptual expression</b>	<b>Relationship to mass transfer</b>	<b>Significance to fluid mechanics</b>
Second Damköhler number	$Da_{II} = \frac{k_r CL}{D}$	$\frac{\text{Reaction rate}}{\text{Diffusive mass transfer rate}}$	$\ll 1$ , reaction-limited; $\gg 1$ , diffusion-limited	Represents a key factor in determining chemical reaction efficiency
Péclet number	$Pe = \frac{\mu L}{D}$	$\frac{\text{Advective mass transfer rate}}{\text{Diffusive mass transfer rate}}$	$< 1$ , diffusion dominates; $> 1$ , advection dominates	Relates to the mass/heat transfer in a continuum
Schmidt number	$Sc = \frac{\mu}{\rho D}$	$\frac{\text{Viscous diffusivity}}{\text{Mass diffusivity}}$	For high $Sc$ , concentration gradients continue much longer than velocity gradients	Describes the relative thickness of the mass transfer boundary layer
Sherwood number	$Sh = \frac{k_L L}{D}$	$\frac{\text{Interfacial mass transfer}}{\text{Diffusivity mass transfer}}$	Depend on $Re$ and $Sc$ numbers	Estimates the interfacial mass transfer

<b>Dimensionless parameter</b>	<b>Formulation</b>	<b>Conceptual expression</b>	<b>Relationship to mass transfer</b>	<b>Significance to fluid mechanics</b>
Hatta number	$Ha = \frac{\sqrt{k_r D}}{k_L}$	$\frac{\text{Mass transfer time}}{\text{Reaction time}}$	< 0.3, no mass transfer limitation; 0.3 < $Ha$ < 3, weakly mass transfer limitation; > 3, strong mass transfer limitation	Characterizes the relationship between reaction and mass transfer

Note:  $\mu$  is flow velocity;  $\rho$  is fluid density;  $L$  is characteristic length of microchannel;  $\eta$  is fluid dynamic viscosity;  $\gamma$  is interfacial tension;  $g$  is gravitational acceleration;  $k_r$  is surface reaction constant;  $C$  is initial reactant concentration;  $D$  is diffusive mass transfer rate;  $k_L$  is mass transfer coefficient.

The Reynolds number can be used to distinguish the flow regime of a fluid in a microreactor from that in a conventional, continuous-flow reactor (Kakaç et al., 2010). The Reynolds number describes the relationship between inertial force and viscous force. As the reactor's characteristic length (internal volume divided by internal surface area) decreases to within the microfluidic range, the viscous force begins to exceed the inertial force. Fluid flow in a cylindrical tube is considered turbulent if the Reynolds number is above 4,000 and is considered laminar if the Reynolds number is below about 2,300. In microchannels, fluid flow has a very small Reynolds number ( $\sim 1 < Re < \sim 100$ ), well within the laminar flow regime (Banerjee et al., 2019; Zhang et al., 2016). Theoretically, the mixing time should decrease by around 2 orders of magnitude when the Reynolds number increases from 1 to 100 (Falk & Commenge, 2010). Yusuf and Palmisano (2021) used a three-dimensional (3D) computational fluid dynamic model to predict the performance of a microfluidic process for photodegradation of 4-nitrophenol, wherein the Reynolds number was estimated to be 21, concluding that the flow within the photocatalytic parallel-channel microreactor employed for this process was laminar. The Weber number, showing the relationship between inertial force and interfacial tension, is usually used to characterize fluid flow in a multiphase system. The Capillary number, which is defined as the ratio of the Weber number to the Reynolds number, is a characteristic parameter of droplets (Geng et al., 2020). The large surface area-to-volume ratio of a microreactor creates smaller droplets that give

rise to higher capillary numbers and enhanced mass transfer. The Bond number describes the relative importance of interfacial tension and body force, which characterizes the behaviors of bubbles and droplets. Other dimensionless numbers described in **Table 2.1** (second Damköhler, Péclet, Schmidt, Sherwood, Hatta, *etc.*) are related to diffusivity, mass transfer, and reaction rates (Kockmann, 2007; Su et al., 2014).

The ratio of chemical reaction rate to the diffusive mass transfer rate is reflected by the second Damköhler number ( $Da_{II}$ ), which is one of the critical indicators determining mass transfer effects within a microreactor (Su et al., 2014). The process kinetics are diffusion-limited for  $Da_{II} \gg 1$  and become reaction-limited for  $Da_{II} \ll 1$  (Kockmann, 2007). Gorges et al. (2004) evaluated  $Da_{II}$  to estimate mass transfer limitations within a photocatalytic microreactor containing  $TiO_2$ -coated micropores. Their estimates were in the range of  $Da_{II} = 0.33\text{--}3.83$ , indicating that there was no mass transfer limitation within the microreactor-based process. The Péclet number ( $Pe$ ) is the ratio of advection to diffusion. Usually, when  $Pe < 1$ , diffusion dominates, whereas if  $Pe > 1$ , advection dominates (Elvira et al., 2013). Since the flow in a microfluidic system is not turbulent, the fluid mixing by advection is less important than that by diffusion. de Sá et al. (2018) evaluated the Reynolds, Damköhler, and Péclet numbers to better understand the photocatalytic degradation of pollutants in meso- and micro-scale reactors. The values of Damköhler and Péclet numbers in the microreactor were  $1.6 \times 10^{-3} \leq Da_{II} \leq 2.1 \times 10^{-2}$  and  $0.9 \leq Pe \leq 46.2$ . Their results showed that the kinetics

of diffusion processes were more important than those of the chemical reactions and highlighted that the performance of the photodegradation process carried out in a microreactor was superior to that in a meso-reactor. To evaluate the extent of mass transfer limitation in gas/liquid and liquid/liquid biphasic reaction systems, an important parameter, Hatta number (Ha), can be considered (Fischer et al., 2010). Usually, the process is reaction-controlled, and the mass transfer limitation is negligible when  $Ha < 0.3$ . Weakly-limited mass transfer occurs when  $0.3 < Ha < 3$ . There are strong mass transfer limitations if  $Ha > 3$ .

### **2.3.1.2 Mixing efficiency**

High mixing efficiency, consistent residence time, and nearly isothermal control are among the main advantages of microreactors over conventional reactor systems (Bojang & Wu, 2020b). The mixing time in a conventional reactor depends on many factors, such as viscosity, reactor internal volume, energy dissipation rate, diffusivity, *etc.* As the flow in microchannels is strictly laminar, the mixing in one dimension is driven by molecular diffusion. The characteristic mixing time ( $t_m$ ) in microreactors can be calculated by the Einstein–Smoluchovski equation:

$$t_m = \frac{L^2}{D}$$

where L is the diffusion path length or hydraulic diameter, and D is the molecular diffusivity (Kockmann, 2007). To account for differences in the structures, mixing, and flow regimes characteristic of microreactors, some researchers have also proposed

relationships to describe the mixing time based on the Reynolds and Péclet numbers (Fath et al., 2019; Kockmann et al., 2006). The relationships between characteristic length and time scales for mixing in both conventional and microscale devices, which account for differing fluid diffusion coefficients, are displayed in **Fig. 2.4**. According to this representation, processes having shorter diffusion lengths require shorter mixing times. In a conventional reactor, the characteristic mixing time is longer than 1 ms for gases and is on the order of 1 s for liquids, whereas in a microstructured device, the mixing time decreases to less than 100  $\mu\text{s}$  for gases and to approximately 1 ms for liquids. Since microreactors impart shorter diffusion distances, complete mixing occurs much faster in these systems to accelerate chemical reactions.

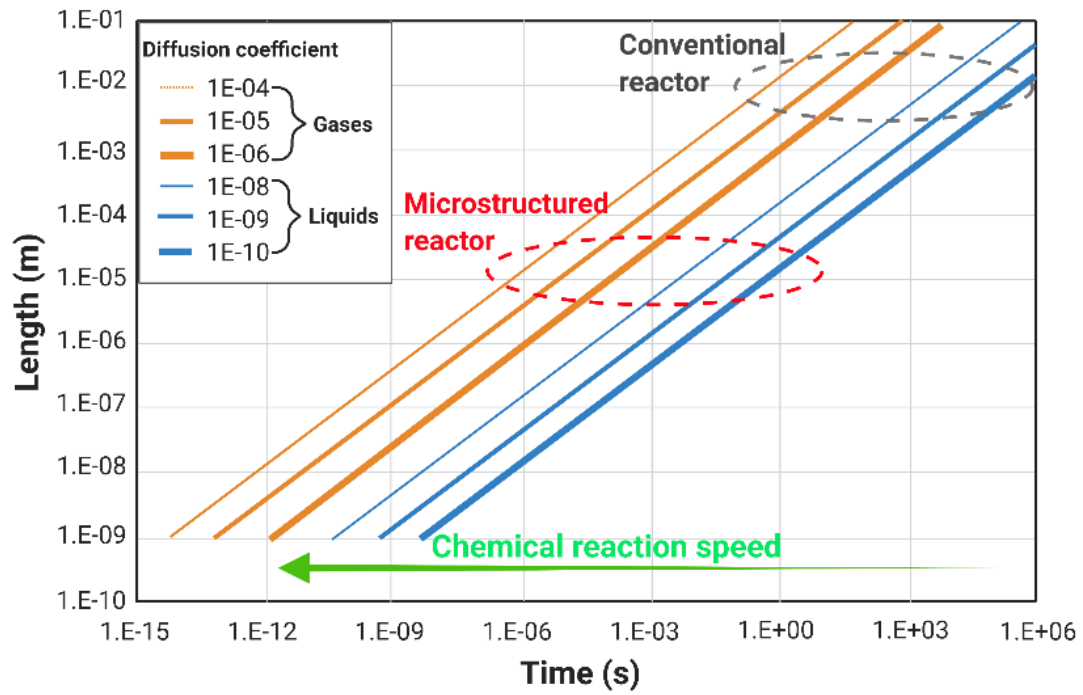


**Figure 2.4** Relationships between characteristic length and mixing time for fluids of varying diffusion coefficients in micro-scale and conventional reactors (adapted from Ref. (Kockmann, 2007)).

### ***2.3.1.3 Volumetric mass transfer coefficient and reaction rate constant***

In multiphase processes, mainly gas/liquid, liquid/solid, and gas/liquid/solid in many types of AOPs, chemical reactions can occur either at the interfaces between different phases or in the bulk phase, with their rates depending both on mass transfer of reactive compounds and on reaction kinetics. The interfacial mass transfer rates ( $R$ ) depend on the difference between bulk ( $C$ ) and equilibrium concentrations ( $C_{eq}$ ), and the volumetric mass transfer coefficient ( $k_La$ ), which is the product of the mass transfer coefficient in water phase ( $k_L$ ) and the effective interfacial area ( $a$ ).

$$R = k_L a (C_{eq} - C)$$

Compared to a conventional reactor, the effective interfacial area of a microreactor is much higher owing to their greater surface area-to-volume ratio, which restricts droplet/bubble sizes. The microreactor's relatively short interphase mixing time also ensures effective diffusion of reactants from interface to bulk phase (Sattari-Najafabadi et al., 2018).

The values of  $k_La$  and  $a$  for both conventional reactors or contactors and microfluidic reactors were collected from the literature and are compared in **Fig. 2.5**. The results clearly show that the mass transfer increases as reactor scale decreases. It is worth noting that both the  $k_La$  and  $a$  values for micro-scale reactors (e.g., micro-capillary reactor, micro packed-bed reactor, microchannel reactor) are at least 1–2 orders of magnitude higher than those associated with conventional reactors or

contactors (*e.g.*, packed column and spray column). Such high mass transfer rates can be rationalized by considering the large interfacial areas, arising from a microreactor's fine internal structure and characteristically small dimensions. The specific interfacial area of a microreactor can reach up to 20,000 m<sup>2</sup>/m<sup>3</sup>, which is uncharacteristically high for conventional reactors (Yao et al., 2015).

In studies of heterogeneous catalytic reactions that occur during the photodegradation of contaminants in the aqueous phase, the Langmuir-Hinshelwood kinetic equation is applied to describe the reaction rate ( $r$ ) (Charles et al., 2011; Corbel et al., 2012; Krivec et al., 2013; Matsushita et al., 2008):

$$r = \frac{kK_{a,d}C_{A,surf}}{1 + K_{a,d}C_{A,surf}} = k_g a (C_{A,bulk} - C_{A,surf})$$

where  $k$  is the intrinsic rate constant,  $K_{a,d}$  is the adsorption-desorption equilibrium constant,  $C_{A,surf}$  and  $C_{A,bulk}$  represent the concentration of compound A at the water/catalyst surface and in the bulk aqueous phase, respectively. The global mass transfer coefficient,  $k_g$ , can be expressed by a semi-empirical correlation between the non-dimensional  $Sh$ ,  $Sc$ , and  $Re$  numbers (Russo, 2021). In microchannels, the high mass transfer rate and large specific interfacial area give rise to a high concentration of reactants at the liquid/solid interface, resulting in a higher reaction rate (Su et al., 2014).

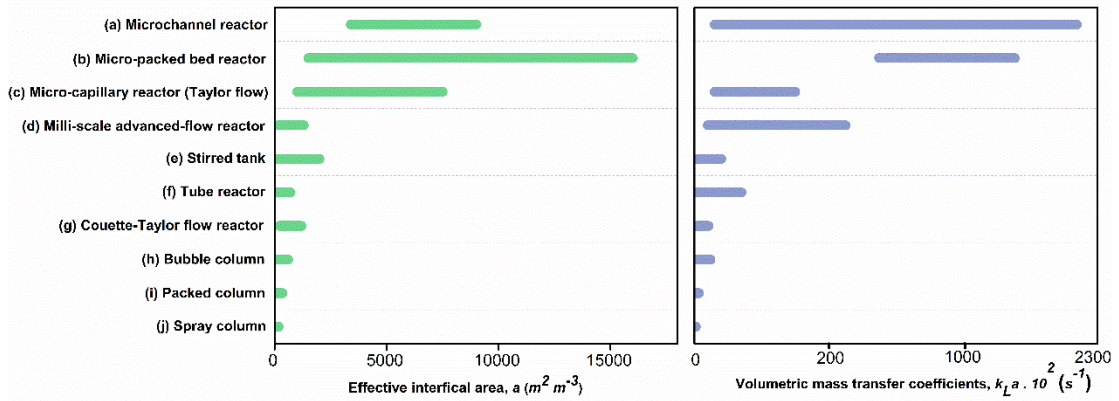


**Figure 2.5** Comparison of mass transfer parameters for conventional reactors and microreactors (a, (Kayahan et al., 2021; Yue et al., 2007); b, (Cao et al., 2021a; Losey et al., 2001); c, (Shao et al., 2010); d, (Nieves-Remacha et al., 2013); e, (Cao et al., 2021a); f, (Charpentier, 1981); g, (Dłuska et al., 2004); h, (Kayahan et al., 2021); i, (Charpentier, 1981); j, (Kies et al., 2004))

### **2.3.2. Applications of microreactor systems to AOPs**

Applications of micro-structured reactors have been expanded in recent years due to their inherent safety, sustainability, compactness, effectiveness, minimal waste output, low operating and capital costs, and reduced energy demand (Kakaç et al., 2010; Nge et al., 2013). An increasing number of studies have used AOP- microreactors to degrade pollutants in W/WWT (Cambié et al., 2016). In this section, applications of microreactors for photocatalytic, electrochemical, Fenton, ozonation, and plasma-phase AOPs are discussed.

#### ***2.3.2.1 Photocatalytic oxidation***

As a green and sustainable process, the photocatalytic AOP has received significant attention for its widespread applicability to industrial, hospital, municipal, and landfill leachate W/WWT (Ahmed & Haider, 2018; Yang et al., 2020; Zhu & Zhou, 2019). The main factors affecting photocatalytic process efficiency are mass transfer, photon transfer, and concentrations of dissolved oxygen (Chong et al., 2010). Mass transfer sometimes limits the reaction rates and is related to the system's surface area-to-volume ratio. Photon transfer is affected by interference of the light beam from its source to the photocatalytic semiconductor. Uniform irradiation of a photocatalytic surface benefits the utilization of photons by the photocatalytic process (Wang et al., 2014d). The availability of dissolved oxygen is also necessary for photocatalytic AOPs (Yu & Wang, 2020). In terms of their physical states, catalysts used in conventional

photocatalytic reactors may exist either within a slurry or may be immobilized upon interior reactor surfaces (Wang et al., 2014d). The slurry reactors employ solid catalyst particles suspended in a liquid medium, whereas in solid-state photocatalytic reactors, the catalytically-active material is coated onto the interior reactor wall. While the slurry system offers high catalytic surface area, it suffers drawbacks of limited light transparency and consumption of photocatalysts. On the other hand, the lower interfacial surface area of the immobilized-catalyst system limits the effective external mass transfer (Shukla et al., 2021a).

Emerging microfluidic reactor systems offer many advantages over conventional reactors for photochemical transformations. Due to the smaller sizes of their interior channels, microreactors offer volumetric mass transfer coefficients that are at least two orders of magnitude higher than those of traditional photocatalytic reactors (Wang et al., 2014d). As a result, significantly enhanced reaction rates can be achieved with microreactors. In a microfluidic device, the most effective means of enhancing photodegradation of aqueous-phase contaminants is to deposit the catalysts within the microchannels in the form of a thin coating, monolith, or packed bed (Munirathinam et al., 2015). Microreactor design has been a hot topic in photocatalytic process research for several decades. Presented in **Fig. 2.6** are the main photo(electro)catalytic microreactor types, each of which operates via externally supplied radiation and for which the most recent applications to W/WWT are subsequently described.

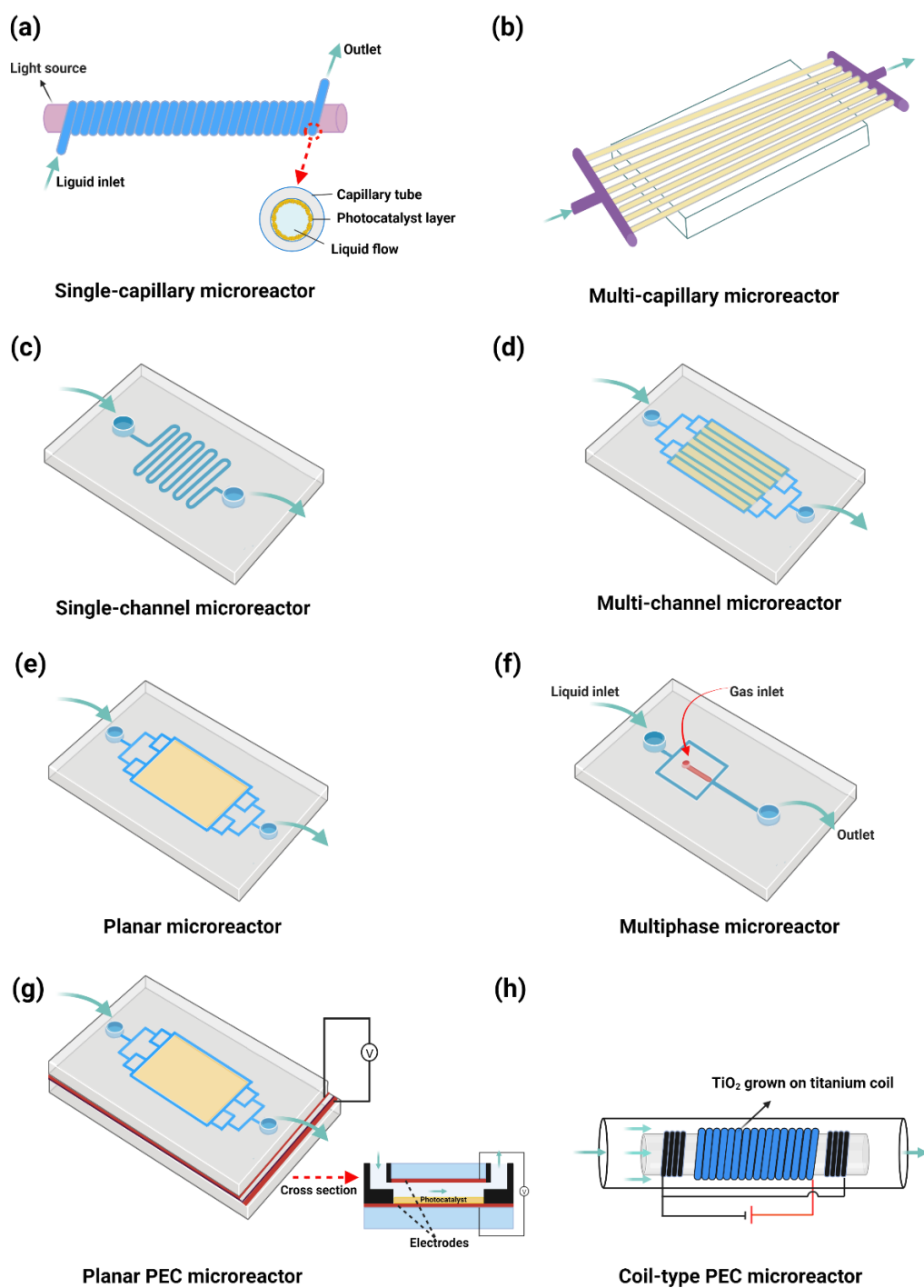


**Figure 2.6** Main microreactor types used for photo(electro)catalytic degradation of aqueous-phase contaminants

### *2.3.2.1.1 Single-capillary microreactors*

In a capillary microreactor, a chemical reaction occurs as the feed solution flows through a capillary tube. Several researchers have reported on the use of single-capillary microreactors for photochemical conversion of organics (Hurtado et al., 2016; Li et al., 2003; Ramos et al., 2014b; Russo et al., 2020; Russo et al., 2016) (**Fig. 2.6a**). Single-capillary UV/H<sub>2</sub>O<sub>2</sub> microreactors have recently been adopted to efficiently remove emerging contaminants, including benzoylecgonine, isoxazole, and isothiazolinones, the photodegradation products of which were then analyzed (Russo et al., 2020; Russo et al., 2016). This UV/H<sub>2</sub>O<sub>2</sub> microcapillary reactor-based technique represents an environmentally friendly, economical, highly efficient, and time-saving homogeneous AOP for W/WWT. For the photocatalytic process, the catalytically-active materials are coated on the inner wall of the capillary, and the catalytic reaction occurs when external radiation passes through the wall to interact with the catalytic material layer. Li et al. (2003) designed a single-capillary microreactor with TiO<sub>2</sub>/SiO<sub>2</sub> adsorbed to the inner wall. The addition of hexagonal SiO<sub>2</sub> arrays onto the walls increased the effective surface area, which in turn increased the amount of coated TiO<sub>2</sub>. In this case, microcapillary provided a higher surface area-to-volume ratio to enhance the degradation of methylene blue, which is 150 times faster than a bulk reactor.

### *2.3.2.1.2 Multi-capillary microreactors*

Multi-capillary microreactors use several capillaries in parallel to improve contact

surface area, light utilization efficiency, and process throughput capacity (He et al., 2010; Zhang et al., 2013) (**Fig. 2.6b**). He et al. (2010) described a photocatalytic device, consisting of a circular array of parallel capillaries containing ZnO/TiO<sub>2</sub> nanorod arrays. A tubular UV lamp, situated at the center of the circular array and parallel to capillary axes provided sufficient and uniform illumination. This rapid, continuous-flow process offers commercialization potential and exemplifies use of a multi-capillary microreactor for the degradation of aqueous organic pollutants.

#### *2.3.2.1.3 Single-channel microreactors*

Single-channel microreactors may contain straight-, serpentine-, or spiral-shaped channels within glass, ceramic, polymers, or other material substrates. These systems have been used to demonstrate the feasibility of photocatalytic microreactor-based AOPs for the removal of aqueous organic substances (Eskandarloo et al., 2015; Krivec et al., 2013; Matsushita et al., 2008; Yu & Wang, 2020) (**Fig. 2.6c**). Serpentine-shaped microchannels were developed to increase the residence time of pollutants as a means of enhancing process efficiency (Eskandarloo et al., 2015). Krivec et al. (2013) developed a microreactor consisting of a single, serpentine-shaped microchannel containing immobilized TiO<sub>2</sub> nanoparticles on the bottom and sidewalls of the channel, which was sealed with UV-transparent Plexiglas. Poorly designed single-channel microreactors may suffer from large empty spaces that reduce process efficiency.

#### *2.3.2.1.4 Multi-channel microreactors*

Several groups have carried out photocatalytic reactions using multi-channel microreactors, wherein parallel channels provide greater and more uniform photo-exposure (Gorges et al., 2004; Renault et al., 2012; Takei et al., 2005) (**Fig. 2.6d**). Such microreactor systems have been widely used in chemical synthesis, owing to their ability to more accurately control and maintain reaction process conditions while enabling high product yields (He et al., 2020; Takei et al., 2005). Gorges et al. (2004) used a 19-parallel-channel microreactor, having channel cross-sections of  $200 \times 300 \mu\text{m}$ , for the degradation of 4-chlorophenol within a W/WWT process. Their results showed that the illuminated specific surface area of this micro-structured reactor is 4–400 times higher than that of a conventional photocatalytic reactor.

#### *2.3.2.1.5 Planar microreactors*

A planar microreactor contains a wide and shallow channel within the substrate through which the reaction mixture flows. It has been suggested that, compared to capillary or channel-based microreactors, planar microreactors could further increase surface contact with the reaction mixture and enhance its exposure to radiation (Lei et al., 2010; Wang et al., 2014d) (**Fig. 2.6e**). Many studies have demonstrated the utility of planar microreactors (Li et al., 2018; Wang et al., 2014c). Li et al. (2018) used a  $\text{TiO}_2$  nanorod array-based, dual-film optofluidic planar microreactor, demonstrating its efficient light-harvesting capability and high durability during a photocatalytic

application. Wang et al. (2014b) used a planar microreactor containing a BiVO<sub>4</sub>-coated layer for visible light photocatalysis and confirmed that this device could make use of both heat and light energy to degrade organic compounds.

Despite the evident utility of planar microreactors, uneven liquid flow throughout the wide channel presents a major drawback. Bifurcation of the upstream reactor zone has therefore been used to provide a more uniform flow through more separate channels instead of one (Heggo & Ookawara, 2017). Liao et al. (2016) designed and compared the performance of planar microreactors with and without-bifurcated channels for photocatalytic applications. Their results showed that bifurcation of the planar channel increases methylene blue degradation efficiency by 68%. The increased reaction efficiency was attributed to greater flow velocity fluctuation in the bifurcated microreactor.

#### *2.3.2.1.6 Multiphase microreactors*

Photocatalytic W/WWT processes need sufficient oxygen input to effect degradation of organic contaminants (Heggo & Ookawara, 2017; Lindstrom et al., 2007). Many researchers have used microreactors containing channels fitted with air/oxygen intake ports for this purpose (Li et al., 2013; Zhu et al., 2016) (**Fig. 2.6f**). Aran et al. (2011) have developed a porous photocatalytic membrane microreactor, which provides a continuous supply of gaseous reactants and a shorter light path length for multiphase reactions. In this device, TiO<sub>2</sub> is immobilized onto the surface of porous

aluminum oxide on the interior walls of channels. Ports permit the introduction of oxygen gas into the reactor chambers to improve the efficiency of this multiphase process. Yu and Wang (2020) developed a tunable, spiral-channel photocatalytic microreactor, which provides a high surface area for interactions of gaseous and liquid reactants with the solid surface, thereby enhancing reaction kinetics and process efficiency for photodegradation of methylene blue. These authors calculated reaction rate constants ( $k$ ) both with and without the application of oxygen bubbles and found that oxygen bubbling increases the photocatalytic degradation rate by a factor of 2.4. They also provided insight into the design of industrial-scale photocatalytic reactors for W/WWT that are inspired by the designs of multiphase microreactors.

#### *2.3.2.1.7 Planar photoelectrocatalytic (PEC) microreactors*

Photoelectrocatalysis is a process whereby an electrified semiconductor is further excited by radiation to accelerate a chemical reaction (Wang et al., 2020f; Wu & Hu, 2020). PEC microreactors offer promising applicability to AOPs for W/WWT because electrification of the photocatalyst suppresses recombination of photo-generated electron-hole pairs, which enhances photocatalytic process efficiency (Wang et al., 2012). Wang et al. (2012) designed and used a planar PEC microreactor to decompose methylene blue. This microreactor consisted of a substrate coated with a porous, photocatalytic BiVO<sub>4</sub> film, which was then sandwiched between indium tin oxide (ITO) glass plates. An external bias potential was then applied across the two ITO plates as

the methylene blue solution was passed through the reactor (**Fig. 2.6g**). These researchers carried out a series of experiments and found that this PEC microreactor offers many advantages, such as high photon utilization rate, easy control over the oxidation pathway, and sufficient oxygen supply. Their follow-up study further demonstrated that this PEC microreactor could simultaneously degrade organic contaminants in seawater while reducing or even eliminating chlorine generation (Wang et al., 2017).

#### *2.3.2.1.8 Coil-type PEC microreactors*

Suhadolnik et al. (2017) designed a coil-type PEC microreactor to degrade caffeine under various process conditions (**Fig. 2.6h**). They compared process performance under photocatalytic, electrocatalytic, and PEC conditions, noted that the best performance was achieved using the latter, and upscaled the reactor to the macroscale for application to degradation of organic compounds. Owing to its superior mass and photon transfer, and control over oxidative pathways compared to either photocatalytic or electrocatalytic processes, the PEC process may represent the most efficient type of AOP for applications to W/WWT.

#### *2.3.2.1.9 Other research highlights of photocatalytic oxidation*

Hot topics in the design of photocatalytic microreactors include the selection of catalytically-active materials, sources and distribution of light, and combination processes (**Table 2.2**).

The currently popular photocatalysts used in photocatalytic microreactors include TiO<sub>2</sub>, ZnO, CuO, *etc.* The rapid recombination of photo-generated electron-hole pairs can impact the efficacy of semiconductors as photocatalysts. Preferred catalysts for photocatalysis should exhibit slow recombination rates, high surface area, and permit effective mass transfer. The traditional catalysts usually have high recombination rates leading to relatively low efficiency, which has been regarded as a key factor limiting the application of photocatalytic technology. Zhang et al. (2013) constructed a Pt/ZnO nanorod array-modified catalyst to achieve rapid and highly efficient photocatalytic activity in a capillary microreactor. When this microreactor was repeatedly used for 110 h, the degradation efficiency of phenol was still higher than 85%, showing excellent durability. The development of new catalysts (doped metal oxides, perovskite, g-C<sub>3</sub>N<sub>4</sub>, and metal-organic frameworks, *etc.*) with low recombination rates offers great potential for microfluidic technology applications (Wang et al., 2020e). However, to our best knowledge, there are currently no reports of such emerging photocatalysts used with AOP-microreactors for environmental applications, suggesting that this may represent a new research and development opportunity.

To optimize light distribution within this photocatalytic system, internal light sources with a waveguide or optical fibers have been employed (Sohrabi et al., 2020; Zhu et al., 2016). Özbakır et al. (2021) developed a compact hydrophobic composite material, which functions both as a photocatalyst and light-guide. Based on experiments and a quantitative theoretical model, these authors demonstrated that a photocatalytic

microreactor employing this composite is well suited for the degradation of dissolved organic and inorganic compounds in water under a wide range of operating conditions.

The combination of photocatalysis with other AOP types (*e.g.*, thermolysis, plasma-phase, and sulfate radical-based processes) has been attempted to enhance the process efficiency (Hafeez et al., 2021b; Lumbaue et al., 2021; Wang et al., 2014b). The combination of photocatalysis and a sulfate radical-based AOP has been reported to minimize carrier recombination since persulfate has a high electron affinity and easily captures photo-generated electrons (Ike et al., 2018). The recent interest in sulfate radical-based AOPs has inspired their integration with photocatalysis in microreactors. Lumbaue et al. (2021) applied a tube-in-tube membrane microreactor to boost the efficiency of a persulfate-based AOP by combining it with a photocatalytic (UV/TiO<sub>2</sub>) process. The microreactor's design facilitates transportation of persulfate to the photocatalyst's surface and improves the distribution of reactants across the microreactor's length.

**Table 2.2** Characteristics of photocatalytic microreactors reported over the last decade.

<b>Casing material</b>	<b>Catalyst material</b>	<b>Thickness of catalyst layer (<math>\mu\text{m}</math>)</b>	<b>Channel size (mm)</b>	<b>Light source (<math>\lambda</math>, nm)</b>	<b>Flow rate (<math>\mu\text{L}/\text{min}</math>)</b>	<b>Residence time (s)</b>	<b>Pollutant(s) converted</b>	<b>Concentration (mM)</b>	<b>Conversion efficiency (%)</b>	<b>Ref.</b>
PDMS	TiO <sub>2</sub>	20–30	1 × 0.1	UV (352–368)	5–20	80–20	<i>p</i> -Chlorophenol	0.1–6.0	95	(Yoon et al., 2011)
Polymer	TiO <sub>2</sub>	5 ± 1	1–2 × 0.5	UV LED	42–167	320–40	Salicylic acid	0.072	20-80	(Charles et al., 2011)
$\alpha$ -Al <sub>2</sub> O <sub>3</sub>	TiO <sub>2</sub>	–	1 × 0.5	UV-365	10–50	198–18	Methylene blue	0.07	35-90	(Aran et al., 2011)
Glass	TiO <sub>2</sub>	0.2–2	50 × 18 × 0.1	UV-365	75	72	Methylene blue	0.03	55	(Wang et al., 2011)
Silica	TiO <sub>2</sub>	3	0.66 × 0.53	UV LED	–	–	Several dyes	0.05	–	(Tsuchiya et al., 2012)
ITO glass	BiVO <sub>4</sub>	1.5	10 × 10 × 0.1	Blue LED	75–200	3–8	Methylene blue	0.03	27-53	(Wang et al., 2012)
Quartz	TiO <sub>2</sub>	2–5	150 × 0.32	UV (253.7)	1000	4,800	Azo dye	0.03–0.15	91.7	(Zhang et al., 2012)
PDMS and glass	TiO <sub>2</sub>	0.3	20 × 10 × 0.25	UV (310–400)	66.6	45	Methylene blue	0.02	90.5	(Li et al., 2013)

Caseing material	Catalyst material	Thickness of catalyst layer ( $\mu\text{m}$ )	Channel size (mm)	Light source ( $\lambda$ , nm)	Flow rate ( $\mu\text{L}/\text{min}$ )	Residence time (s)	Pollutant(s) converted	Concentration (mM)	Conversion efficiency (%)	Ref.
PDMS and glass	electrospun nanofibrous $\text{TiO}_2$	30	$0.5 \times 0.1$	UV light	25–100	53–12.43	Methylene blue	0.03	56-99	(Meng et al., 2013)
Silica glass	Pt/ZnO nanorods	1–2	0.53	UV LED	–	180	Phenol	0.053	93	(Zhang et al., 2013)
Titanium foil	$\text{TiO}_2$	10	$390 \times 0.5 \times 0.5$	UV LED	20–100	292.5–58.5	Caffeine	0.013–0.129	40-85	(Krivec et al., 2013)
ITO glass	$\text{BiVO}_4$	1.5	$10 \times 10 \times 0.1$	Blue LED	75	8	Methylene blue	0.03	–	(Wang et al., 2013a)
Polymer	$\text{TiO}_2$	1.5–4	0.25–1	UV LED	–	1,680	Phenol	1.0	75	(Ramos et al., 2014b)
Serpentine	$\text{TiO}_2$	10	$390 \times 0.5$	UV	300	14	Dichloroacetic acid	1–1.5	75	(Krivec et al., 2014)
FTO glass and PDMS	$\text{TiO}_2$	–	$20 \times 10 \times 0.2$	Simulated sunlight	100	12	Methylene blue	0.01–0.04	23.7-83.9	(Li et al., 2014)
Pyrex glass	–	–	$500 \times 0.1 \times 0.04$	UV LED	–	–	Methylene blue	10	–	(Ramos et al., 2014a, 2014c)

<b>Casing material</b>	<b>Catalyst material</b>	<b>Thickness of catalyst layer (<math>\mu\text{m}</math>)</b>	<b>Channel size (mm)</b>	<b>Light source (<math>\lambda</math>, nm)</b>	<b>Flow rate (<math>\mu\text{L}/\text{min}</math>)</b>	<b>Residence time (s)</b>	<b>Pollutant(s) converted</b>	<b>Concentration (mM)</b>	<b>Conversion efficiency (%)</b>	<b>Ref.</b>
PMMA	TiO <sub>2</sub>	–	800 × 0.4 × 0.05	UV LED	10–150	96–6.4	4-Nitrophenol	0.036–0.216	19-100	(Eskandarloo & Badieli, 2015)
Stainless steel	Ag/TiO <sub>2</sub>	–	540 × 0.4 × 0.05	UV LED	10.22	63	Terephthalic acid	0.078	98.8	(Eskandarloo et al., 2015)
Glass	ZnO/Zn(OH)F nanofibers	40	530	UV	25	40	Methylene blue	0.016	>90	(Zhao et al., 2016a)
PDMS	TiO <sub>2</sub> nanotubes	15	7 × 2.5 × 0.125	UV	5	60,000	Methylene blue	0.469	88	(Zhu et al., 2016)
Glass and foil	titania nanotubes	8	30 × 15 × 0.6	Sunlight	25	12,000	Methylene blue	18	46	(Jayamohan et al., 2016)
Stainless steel	Cu–CuO nanocomposite	0.01	0.04	UV	20,000	3,000	Methylene blue	0.031	98.5	(Xu et al., 2017)
Silicon	ZnO nanowires	1.5	7 × 7 × 0.15	UV LED	250	<5	VOCs	2,000	Up to 95	(Azzouz et al., 2018)

<b>Casing material</b>	<b>Catalyst material</b>	<b>Thickness of catalyst layer (<math>\mu\text{m}</math>)</b>	<b>Channel size (mm)</b>	<b>Light source (<math>\lambda</math>, nm)</b>	<b>Flow rate (<math>\mu\text{L}/\text{min}</math>)</b>	<b>Residence time (s)</b>	<b>Pollutant(s) converted</b>	<b>Concentration (mM)</b>	<b>Conversion efficiency (%)</b>	<b>Ref.</b>
PDMS	TiO <sub>2</sub>	6.4	–	UV LED	–	–	Several dyes	0.015–0.03	90-100	(de Sá et al., 2018)
FTO glass	TiO <sub>2</sub> nanorods	1–10	20 × 20 × 0.2	UV (365)	30–120	80–20	Methylene blue	0.02	48-90	(Li et al., 2018)
Glass	TiO <sub>2</sub> films	0.65–2.7	58 × 20 × 0.18	UV (365)	15-330	840-40	Clofibric acid	0.093	50-100	(Satuf et al., 2019)
Glass	Ce-doped TiO <sub>2</sub>	–	58 × 20 × 0.18	Simulated sunlight	15	840	17- $\alpha$ -Ethinylestradiol	0.03	86	(Martin et al., 2019)
PDMS	TiO <sub>2</sub>	1	0.06	Sunlight	–	–	Methylene blue	–	–	(Yu & Wang, 2020)
Carbon foam	TiO <sub>2</sub>	–	< 0.1	Sunlight	–	7,200	Rhodamine B	0.025	90	(Lu et al., 2020)
PDMS	ZnO	–	40 × 25 × 5	UV (365)	20000	15	Tetracycline	0.045	73.2	(Chen et al., 2020a)
SiO <sub>2</sub> –TiO <sub>2</sub> aerogels	TiO <sub>2</sub>	1100	41 × 1.1	Femtosecond-UV pulses (366)	3.6–28.3	649.4–82.6 1	Phenol	0.33	36-93	(Özbakır et al., 2021)

*Note: FTO is fluorine-doped tin oxide; LED is light-emitting diode; VOCs are volatile organic compounds.*

### ***2.3.2.2 Electrochemical oxidation***

During an electrochemical AOP,  $\cdot\text{OH}$  is generated by the application of current, which initiates the unselective, oxidative degradation of aqueous organic contaminants. The high efficiency, mild operating conditions, ease of automation, and versatility of electrochemical AOPs are among their most useful aspects for W/WWT applications (Rao & Venkatarangaiah, 2014; Sirés et al., 2014; Wu et al., 2014). Moreover, the operating cost of highly efficient electrochemical processes can be reduced if powered directly by renewable, *i.e.*, wind or solar, energy sources (Martínez-Huitle et al., 2015; Mook et al., 2014). Despite their many advantages, electrochemical AOPs do have some intrinsic drawbacks. Electrochemical process tends to have lower surface area-to-volume ratios, which manifest as AOP mass transfer limitations, low space-time yield, reduced reaction efficiency, and increased energy consumption (Radjenovic & Sedlak, 2015). Due to the high reactivity of  $\cdot\text{OH}$ , it can only exist within a narrow zone adjacent to the electrode surface ( $<1.0\ \mu\text{m}$ ). Oxidation reactions occur mainly within a diffusion region of  $100\ \mu\text{m}$  around the electrode surface (Chaplin, 2014). Therefore, the dimensions of a microreactor chamber greatly affect the process efficiency of electrochemical AOP. An electrochemical AOP's energy consumption is directly related to the ohmic drop, which is influenced by the size of the inter-electrode (IE) gap. The low electrical conductivity of the reaction mixture or feed may exacerbate the ohmic drop, thereby increasing energy consumption. In this case, the addition of electrolytes

to improve conductivity is both costly and often leads to secondary pollution. Therefore, reactors used for electrochemical AOPs should have optimized IE gaps to enhance pollutant conversion efficiency and reduce process energy consumption. In this context, microreactors have been explored due to their miniature and small IE gaps (Santana et al., 2020a; Wang et al., 2020b).

A typical electrochemical reactor adopts one of two configurations: flow-by and flow-through (**Fig. 2.7**). Reported electrochemical microfluidics experiments and their operating parameters are summarized in **Table 2.3**. Scialdone et al. (2010) were the first to develop an electrochemical flow-by microreactor and found that the abatement of oxalic acid and the electric current efficiency strongly depended on the IE gap (**Fig. 2.7a**). Although shortening the IE gap significantly enhanced pollutant conversion efficiency, it also constricted the flow, thereby reducing process throughput such that longer processing time was required. These authors later studied the effects of various experimental parameters on the oxidation of formic acid at microreactor anodes, both with respect to pollutant degradation and current efficiency (Scialdone et al., 2011). They then developed and experimentally validated a simple theoretical model of this electrochemical microreactor and used it to effectively balance high pollutant degradation and current efficiencies with minimal processing time. Scialdone et al. (2012) tested the feasibility of utilizing a microreactor containing a silver cathode and a boron-doped diamond anode for the electrochemical oxidation of 1,1,2,2-

tetrachloroethane. Experiments were performed without added electrolyte, under various conditions of flow rate (0.1–0.4 mL/min), current density (3–15 mA/cm<sup>2</sup>), and IE gap (50–75 μm) to achieve impressive pollutant abatements approaching 100% in various cases. These authors provided two explanations for the improved performance of this electrochemical AOP: (1) The charge passing from the anode to the cathode accumulates on surfaces to more efficiently convert pollutants; (2) Pollutant conversion occurs at the surfaces of both electrodes, making the microreactor's active surface area-to-volume ratio significantly higher, which also helps to accelerate mass transfer. Obviously, traditional reactors used for high-throughput AOPs require wider channels and in turn, larger IE gaps that do not allow for an overlap of anode and cathode diffusion layers. In follow-up studies, these authors explored organics abatement by electrochemical AOP variants, including direct anodic oxidation, electro-Fenton, electro-chlorination, and coupled processes at both macro- and micro-scales (Scialdone et al., 2014a; Scialdone et al., 2014b). Numerous process features, such as electrode material composition, flow rate, current density, and IE gap were varied to optimize the removal of pollutants by these electrochemical AOPs (Scialdone et al., 2014a; Scialdone et al., 2014b). Khongthon et al. (2016) conducted a series of experiments to investigate diuron degradation kinetics via an electrochemical microreactor. Their results suggested that the rate constant for the process was 1–2 orders of magnitude higher than that observed using a conventional reactor. High removal of total organic carbon (TOC; up to 90%) was achieved in microfluidic cells without supporting

electrolyte. Meanwhile, the energy consumption per unit of TOC converted was also comparatively low. High TOC removal efficiency using microreactors has been also reported by others (Ma et al., 2018).

Electrochemical flow-through reactors are theoretically superior to flow-by reactors in terms of mass transfer (Ma et al., 2016). Pérez et al. (2017) designed a flow-through microreactor that exhibits low ohmic resistance and high mass transfer (**Fig. 2.7b**). The results showed that this flow-through microreactor more efficiently degrades organics compared to a flow-by reactor. The flow-through microreactor requires only 2.3 Ah/dm<sup>3</sup> for the total mineralization of 100 mg/dm<sup>3</sup> of clopyralid, whereas a commercially-available flow-by microreactor requires 11.4 Ah/dm<sup>3</sup> to achieve the same result. The specific energy consumed by the flow-through microreactor is *ca.* 6 times less than that of the flow-by microreactor (12.5 vs. 75 kWh/m<sup>3</sup>), due to the faster degradation kinetics achieved with the former. These authors therefore concluded that the flow-through microreactor represents a more promising approach to electrochemical AOPs.

Although the development of microreactors-based electrochemical AOPs for W/WWT is still in its infancy, the promising results reported from lab studies offer much promise and insight for the development of extensive, low-cost electrochemical W/WWT processes. The observation that these AOPs can be effectively conducted in the absence of added electrolyte is also promising for the elimination of a potential secondary pollution source and minimization of operating costs.

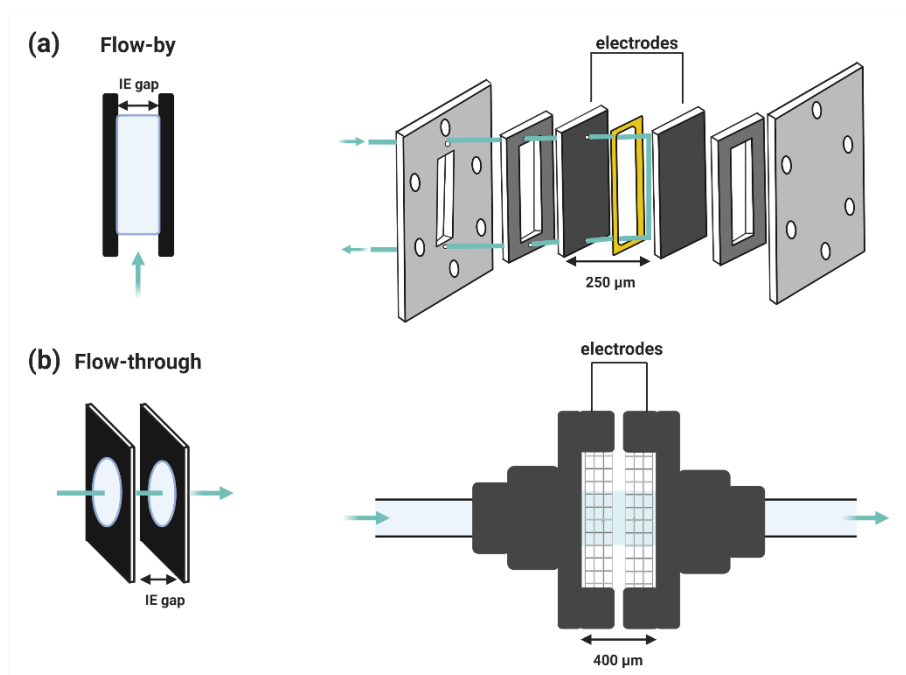


**Figure 2.7** Electrochemical microreactors in flow-by and flow-through configurations

(adapted from Refs.(Khongthon et al., 2016; Pérez et al., 2018)).

**Table 2.3** Characteristics of microreactors used for electrochemical AOPs.

<b>Configu- ration</b>	<b>Anode material</b>	<b>Cathode material</b>	<b>IE gap (<math>\mu\text{m}</math>)</b>	<b>Current density (<math>\text{A}/\text{m}^2</math>)</b>	<b>Flow rate (<math>\text{mL}/\text{min}</math>)</b>	<b>Energy consumption (<math>\text{kWh}/\text{g}</math>)</b>	<b>Pollutant(s) converted</b>	<b>Conversion efficiency (%)</b>	<b>Ref.</b>
<b>Flow-by</b>	BDD	Nickel	50	20	0.1–0.5	–	Oxalic acid	80–96	(Scialdone et al., 2010)
	BDD	Silver	50–75	30–150	0.1–0.4	–	1,1,2,2-Tetrachloroethane	99.4	(Scialdone et al., 2012)
	Ti/IrO <sub>2</sub> Ta <sub>2</sub> O <sub>5</sub>	Graphite	50–240	20–40	0.05–0.4	–	Acid orange 7	>90	(Scialdone et al., 2013)
	BDD	Graphite	50	50–200	0.3–0.5	–	Chloroacetic acid	86–100	(Scialdone et al., 2014a)
	BDD	Graphite	50	100–200	0.1–0.3	–	Acid orange 7	90–98	(Sabatino et al., 2016)
BDD	Carbon felt	500	40	1	0.18	Acetaminophen	84	(Mousset et al., 2019)	

<b>Configuration</b>	<b>Anode material</b>	<b>Cathode material</b>	<b>IE gap (μm)</b>	<b>Current density (A/m<sup>2</sup>)</b>	<b>Flow rate (mL/min)</b>	<b>Energy consumption (kWh/g)</b>	<b>Pollutant(s) converted</b>	<b>Conversion efficiency (%)</b>	<b>Ref.</b>
	BDD	Nickel	50	160	0.1–0.5	0.15	TOC of real wastewater	60–90	(Ma et al., 2018)
	Graphite	Stainless steel	250–750	1.57–6.37	0.032–0.127	0.16–0.35	Diuron, TOC	90 (diuron), 60 (TOC)	(Bumroongsakulsawat et al., 2020; Khongthong et al., 2016)
<b>Flow-through</b>	3D-mesh	Stainless steel	400	100	1667	12.5	Clopyralid	≤ 100	(Pérez et al., 2017)
	Diachem® diamond	steel							
	BDD mesh	Stainless steel	400	10–100	1667	12.5–115.0	Clopyralid	≤ 100	(Pérez et al., 2018)
	BDD	CB/PTFE-Al	400	200	1167	0.02	Clopyralid	≤ 100	(Pérez et al., 2019)

Note: BDD is boron doped diamond; CB/PTFE is carbon black/polytetrafluoroethylene; TOC is total organic carbon.

### ***2.3.2.3 Fenton oxidation***

Fenton AOPs—among the most effective and rapid types—use  $\text{Fe}^{2+}$  and  $\text{H}_2\text{O}_2$  as reagents to generate strongly oxidizing  $\cdot\text{OH}$  (Babuponnusami & Muthukumar, 2014; Zhang et al., 2019). Process variants include photo-, electro-, photo-electro-Fenton, and Fenton catalytic AOPs. Among the most significant advantages of Fenton AOPs is their relative simplicity. These systems do not require complicated reactor designs. They do, however, rely on the input of relatively inexpensive chemical reagents. Reported Fenton AOPs carried out in batch reactors require, relatively long mixing times to effectively convert pollutants (Saien et al., 2012). The use of microreactors for such processes is, however, anticipated to greatly reduce required mixing times and the consumption of reagents.

Rahimi et al. (2014) introduced a Y-shaped microreactor for the decolorization of azo dye-contaminated solutions via a continuous-flow Fenton AOP. These authors reported an azo dye conversion efficiency of 86 % over a residence time of only 4.2 s, showcasing the advantageous use of a microreactor for the continuous-flow decolorization AOP.

The photo-Fenton process variant applies UV/visible radiation along with  $\text{H}_2\text{O}_2$  and  $\text{Fe}^{2+}$  to accelerate  $\cdot\text{OH}$  generation, thereby further increasing the pollutant degradation rate (Parsons, 2004). Shinozawa et al. (2019) compared photo-Fenton AOPs for degradation of carbofuran under visible light both in a conventional batch reactor and in a microreactor. The batch scale process was conducted in a 250 mL beaker, while the microscale process was performed in a PTFE tube with an inner diameter of 500  $\mu\text{m}$ . Results showed that the process carried out in the microreactor was 7.5 times faster than that in the batch reactor. The microreactor's

shortened light path reduced visible light attenuation by the precipitation of ferric ions. To further overcome ferric ion light absorption, Díaz-Angulo et al. (2021) adopted a tube-in-tube membrane microreactor to continuously titrate the contaminated feed with a ferrous solution (**Fig. 2.8**). When low concentrations of ferrous solution are continuously introduced into the feed, a uniform reagent concentration is ensured to permit effective photo-exposure. More importantly, acidic aqueous ferric ions near the membrane shell side may be effectively regenerated into ferrous ions by UV irradiation, to minimize precipitation of light absorbing ferric species while regenerating  $\cdot\text{OH}$  using less ferrous solution. Compared to batch reactors, this microreactor design offers controlled delivery of Fenton reagents to improve AOP efficiency in terms of pollutant degradation.

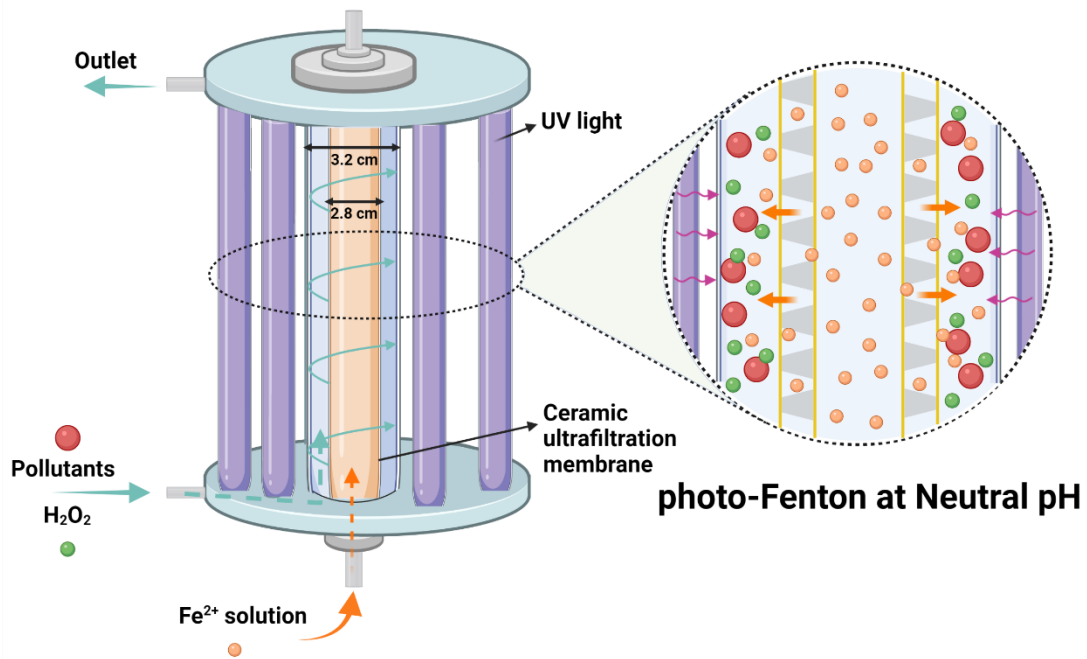


**Figure 2.8** A novel microreactor developed and used by Díaz-Angulo et al. (2021) for a photo-Fenton AOP

The electro-Fenton process is another promising AOP type for W/WWT, whereby  $\cdot\text{OH}$  is generated both by the combination of Fenton reagents and by anodic oxidation to degrade organic pollutants (Brillas et al., 2009; Nidheesh & Gandhimathi, 2012). Scialdone et al. (2013) constructed a microreactor used to demonstrate for the first time that organic pollutants can be degraded by both electro-generated  $\text{H}_2\text{O}_2$  and Fenton-generated  $\cdot\text{OH}$ . These authors found that the concentration of  $\text{H}_2\text{O}_2$  generated at the microreactors' cathode was one order of magnitude higher than that in a batch reactor. Moreover, the chemical oxygen demand of water released from the microreactor was much lower than that released from the batch reactor. These authors further tested the feasibility of applying high flow rates to a cascade of microreactors used to reduce high concentrations of organic pollutants (Sabatino et al., 2016). Their results confirmed that a tandem AOP, involving electro-Fenton followed by electrochemical oxidation, could achieve a high abatement of both organics and total organic carbon, while simultaneously reducing energy consumption. A single microreactor that coupled electro-Fenton and anodic oxidation processes was applied to the direct treatment of soil washing wastes (Vilar et al., 2020). The high efficiency and short treatment time enabled by use of this tandem AOP microreactor offer potential applicability to W/WWT.

During heterogeneous photo-Fenton AOPs, catalysts can destroy the formed inactive  $\text{Fe}^{3+}$  complexes by assisting the UV irradiation, allowing the regeneration of active  $\text{Fe}^{2+}$  within the Fenton catalytic cycle (Kasiri et al., 2008). Catalysts, such as metal-organic frameworks, perovskites, and zero-valent iron, are likely to be highly effective within microreactors given their ability to reduce the generation of sludge, which may clog microreactors. Hao et al. (2020)

developed a miniaturized, five-loop, spiral-shaped microreactor containing rod-like, multi-stacked, zero-valent iron catalytic nano-assemblies, to degrade organic dyes via a Fenton AOP. Compared with conventional batch reactors, use of this microreactor significantly shortened the degradation process duration (from hours to seconds).

#### **2.3.2.4 Ozonation**

Ozonation is another very effective AOP type for W/WWT whereby organic pollutants are degraded either by their direct reaction with ozone or indirectly by their reaction with ozone-generated radicals (Loeb et al., 2012). Ozone gas is produced by exposing oxygen to an electrical discharge. Limited mass transfer of gaseous ozone to the aqueous phase is a challenge for its application to AOPs, which can lead to low ozone utilization rates and high operating costs (John et al., 2020; Mehrjouei et al., 2015). Compared to conventional gas-liquid contactors, microchannels within microreactors offer short transport paths that facilitate gas/liquid contact to dramatically enhance mass transfer (Lee et al., 2011; Wang et al., 2020d). Various designs of microreactors, which have been proposed for ozonation AOPs, are shown in **Fig. 2.9** (Cao et al., 2020a; He et al., 2016; Shirke et al., 2014; Sun et al., 2014).

The Y-shaped microreactor has separate inlets for ozone gas and contaminated water in order to ensure efficient gas-liquid mixing (**Fig. 2.9a**). This microreactor was effectively used to disinfect *E. coli* (Shirke et al., 2014). Gao et al. (2012) were the first to use a microporous tube-in-tube microchannel reactor to enhance the ozonation of an azo dye (**Fig. 2.9b**). In this reactor, two coaxial tubes provide an annular microchannel. Ozone gas is passed through the inner tube while the wastewater stream is passed in the same direction through the outer tube.

Micropores in the inner tube allow ozone gas to diffuse into the wastewater stream. Compared to the use of a conventional reactor, experimental results showed that the use of this microreactor significantly enhances mass transfers of gaseous ozone into the wastewater stream. It was also observed that the ozone utilization within the microreactor was significantly increased when the width of the annular microchannel (*i.e.*, the distance between the exterior surface of the inner tube to the interior surface of the outer tubes) was decreased from 1500 to 250  $\mu\text{m}$ .

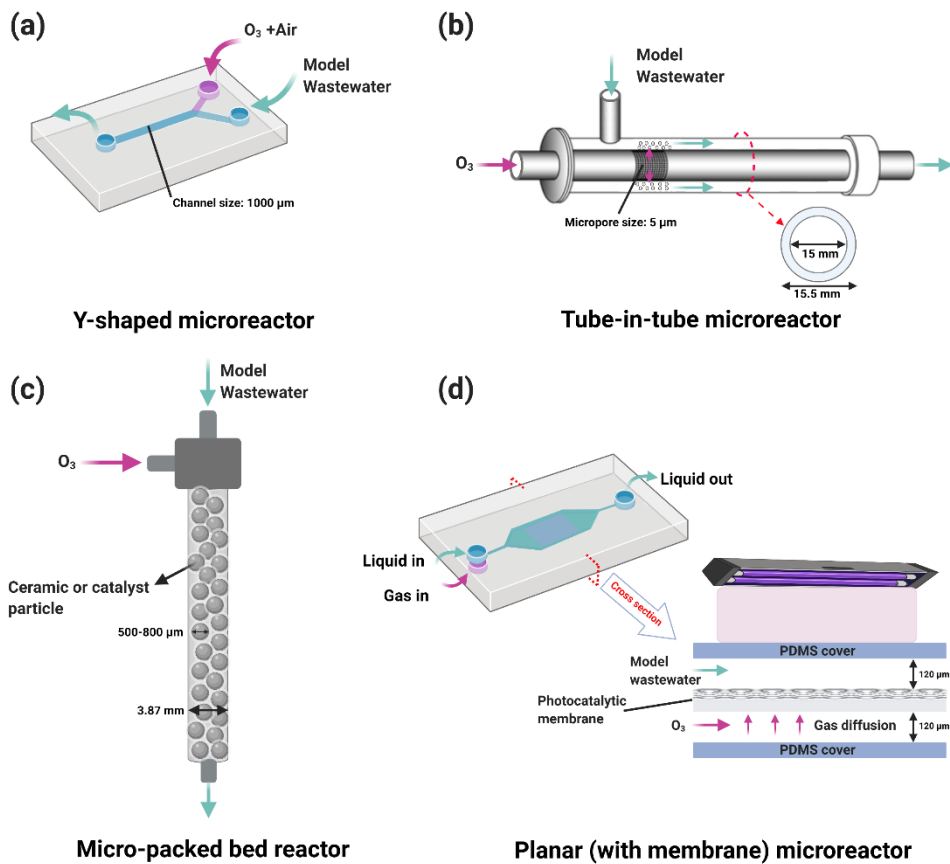


**Figure 2.9** Different types of microreactors used for ozonation AOPs (adapted from

Refs.(Cao et al., 2020a; Gao et al., 2012; He et al., 2016; Shirke et al., 2014)).

Recently, micro-packed bed reactors ( $\mu$ PBRs) have been proposed for use in ozonation AOPs owing to their high surface areas, which encourage gas-liquid contact to accelerate mass transfer and multiphase mixing (Sang et al., 2020; Tu et al., 2019; Zhang et al., 2018). The first continuous ozonation AOPs based on the use of  $\mu$ PBRs were developed by Cao et al. (2020a) to degrade the refractory organic pollutants in wastewater with high efficiency (**Fig. 2.9c**). The fully wetted, packed particles of zirconia ceramic beads or  $\gamma$ -Al<sub>2</sub>O<sub>3</sub> pellets provide a high interfacial area that minimizes the thickness of the liquid film and maximizes gas-liquid mixing, thereby enhancing the interfacial mass transfer and the dissolution of ozone. Moreover, these authors compared the water treatment performance of  $\mu$ PBRs with those of several conventional reactors. To achieve a high pollutant removal efficiency, the residence time of reaction mixtures within  $\mu$ PBRs should be in the range of 20–71 s, whereas that within conventional reactors should be 0.5–2 hours. The chemical oxidation demand (COD) removal efficiency reached up to 86% within 71 s using this microreactor. The apparent rate constant for degradation of refractory organic pollutants via ozonation AOPs conducted using  $\mu$ PBRs is 1–2 orders of magnitude higher than those carried out in conventional reactors. These results revealed that  $\mu$ PBRs improve ozone utilization efficiency and offer much insight toward the development of industrial-scale ozonation AOPs for the degradation of refractory contaminants during W/WWT.

The use of ozonation catalysts within a microreactor can further enhance the efficiency of an ozonation AOP (Wang & Chen, 2020). Specific approaches to this end include adding catalyst pellets to  $\mu$ PBRs (Cao et al., 2020a), coating nanoparticles on the inner wall of a

microreactor (Da Silva et al., 2016), and the incorporation of photocatalytic membrane within a microreactor used for ozonation AOPs (He et al., 2016). He et al. (2016) designed and employed a novel optofluidic membrane-based microreactor to degrade methylene blue via a photocatalytic ozonation AOP (**Fig. 2.9d**). The photocatalytic membrane was prepared by coating TiO<sub>2</sub> onto carbon paper, which was then treated with hydrophobic PTFE. The carbon paper of 0.28 mm thickness was placed within a planar reaction chamber having dimensions of 1 cm × 1 cm × 120 μm. AOPs carried out under varying conditions were then compared to reveal that photocatalysis and ozonation processes synergistically enhance process efficiency, demonstrating the usefulness of this new membrane-based microreactor for W/WWT.

The fabrication of microreactors designed for ozonation AOPs has enabled in-depth studies of the ozonation reaction mechanisms and kinetics occurring in microchannels. Ongoing development of innovative microreactor designs and fundamental studies of their applicability to ozonation AOPs will together support microreactor commercialization initiatives.

### ***2.3.2.5 Plasma-phase oxidation***

With its emerging applicability to AOPs, plasma technology has attracted considerable attention due to its environmental compatibility and high efficiency toward degradation of organic pollutants (Jiang et al., 2014). The use of plasma within an AOP is considered as a process feature or enhancement, rather than as the defining operating characteristic. Within the plasma phase, various fleeting ROS, including radicals (H·, O·, OH·, O<sub>2</sub><sup>-·</sup>, HOO·) and other reactive molecules (H<sub>2</sub>O<sub>2</sub>, O<sub>3</sub>, *etc.*) are generated and applied, often along with UV radiation,

to affect the oxidization or mineralization of organic pollutants (Jiang et al., 2014). However, major drawbacks arising from sub-optimal conditions and long required residence times have limited the applicability of conventional plasma reactors to AOPs (Foster, 2017). Considering that plasma-based AOPs tend to be most effective when performed using continuous-flow reactors with high internal surface area-to-volume ratios, the use of microreactors for this purpose offers a promising solution (Lin et al., 2021b; Malik, 2010; Patinglag et al., 2021). Recently, Patinglag et al. (2019) have fabricated a dielectric barrier discharge (DBD) microfluidic plasma reactor and evaluated its performance at atmospheric pressure for the degradation of methylene blue in water (**Fig. 2.10**). They optimized the reactor's parameters and verified that lower liquid flow rates, thinner dielectric barriers, and shallower channel could enhance the degradation of organic pollutants. Moreover, Hafeez et al. (2021a) constructed a multiplexed plasma microreactor to enhance both ozone formation and AOP efficiency for W/WWT. This new system containing six corona-DBD hybrid packed-bed plasma microreactors, overcomes the drawbacks of less ozone production due to low input power and large bubble formation in conventional domestic ozonator-based corona reactors. This multiplex microreactor's enhanced ozone generation and high density of microbubbles allow it to treat 1 L of wastewater in less than 10 min, making this system an effective replacement for conventional ozone generators.

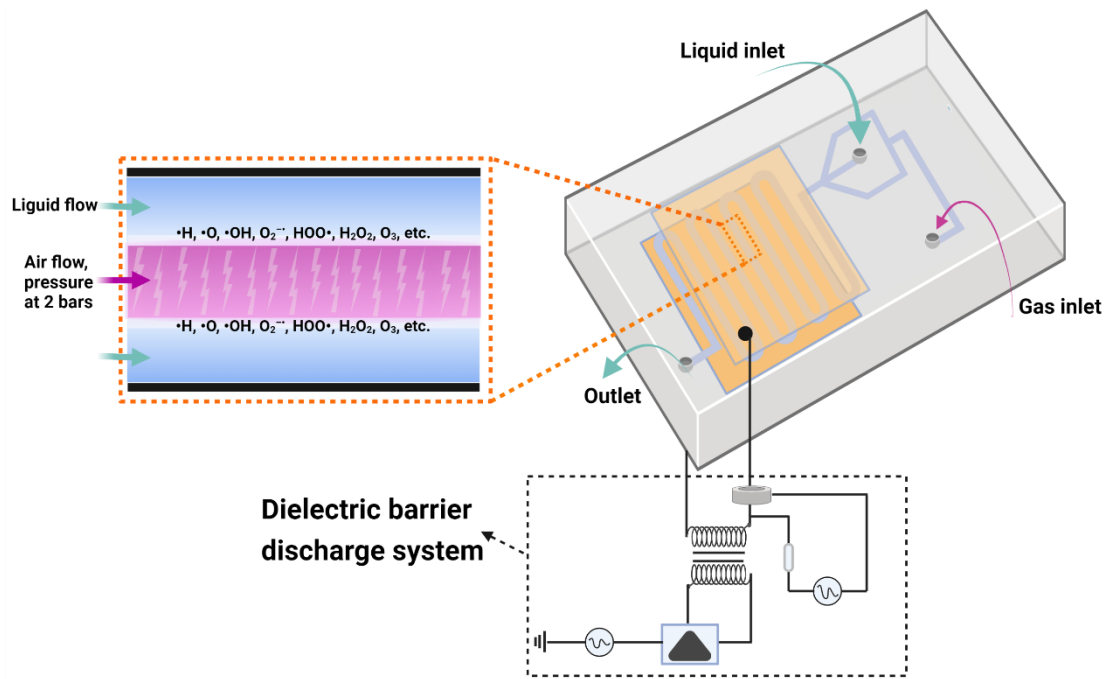


**Figure 2.10** Schematic of a dielectric barrier discharge microfluidic plasma reactor (adapted from Ref. (Patinglag et al., 2019))

### **2.3.3. Challenges with the use of AOP-microreactors for environmental applications**

When used to carry out AOPs for W/WWT, microreactors provide numerous advantages over conventional reactors. Their larger internal specific surface areas enable processes with faster heat and mass transfer, more precise flow control, and lower energy consumption for more efficient degradation of pollutants. Despite their advantages, there are still some challenges that should be addressed before its real-world applications. These entail (1) factors affecting AOPs efficiency in microreactors, (2) scale-up strategies, and (3) cost-saving methods.

#### ***2.3.3.1 Factors affecting AOPs efficiency in microreactors***

In a microreactor, AOPs performance can be affected by several parameters, such as microreactor internal dimensions (*i.e.*, channel size/length), feed flow rate, pH, water matrix, *etc.*

It has been demonstrated that increasing channel length extended the residence time leading to more contact opportunities between targeted pollutants and catalysts, and consequently, enhanced degradation performance. Eskandarloo and Badiei (2015) reported that dye degradation efficiency improved from 19 to 70% by lengthening the channel of their photocatalytic microreactor from 10 to 70 cm. Smaller channel diameter also has the positive effect on AOPs efficiency. Scialdone et al. (2010) found that a smaller IE gap increased abatement of oxalic acid using their flow-by electrochemical microreactor.

The flow rate, another critical factor affecting AOP process efficiency, is generally in the range of microliters to milliliters per minute, but can reach up to liters per minute in flow-

through electrochemical microreactors (Das & Srivastava, 2016; Pérez et al., 2017). Lower flow rates tend to increase pollutants degradation efficiency due to the extended residence times. For example, in a microreactor used for Fenton AOP, decreasing the flow rate from 250 to 10  $\mu\text{L min}^{-1}$ , which correspondingly extended residence time from 1.5 to 37.6 s, improved methylene blue removal efficiency from around 20 to 100% (Hao et al., 2020).

It is well known that the water pH plays an important role in the degradation of aqueous pollutants by various oxidation processes. A study by Khongthon et al. (2016) showed that degradation of diuron in an electrochemical microreactor was more effective under acidic conditions due to the generation of hydroxyl radicals via water discharge reaction (Khongthon et al., 2016). Using an ozonation microreactor AOP, Gao et al. (2012) showed that dye decolorization efficiency increased when a dye solution's initial pH was increased from 2 to 9, while further increasing the initial pH from 9 to 12 decreased dye decolorization efficiency. The latter observation was explained by considering that ozone decomposition, which generates ROS necessary for dye degradation, peaks at slightly alkaline pH values, whereas at  $\text{pH} > 9$  the rate of ROS self-quenching exceeded that of the reaction between ROS and dye.

The water matrix (containing dissolved inorganic ions and organic matter, for example) may affect the generation of ROS during a photocatalytic AOP. Matrix components may reduce light- transmittance and/or scavenge hydroxyl radicals (Miklos et al., 2018). Castellanos et al. (2020) concluded that the water matrix was responsible for a 2-fold decrease in the organic's removal efficiency. In this case both organic and inorganic matrix components acted as UV filters and hydroxyl radical scavengers. Sun et al. (2014) investigated the effects of inorganic

salts on the  $k_{La}$  of  $O_3$  and decolorization of acid dye with an ozonation AOP using a microporous tube-in-tube microreactor. Interestingly, their results showed that both  $k_{La}$  of  $O_3$  and decolorization efficiency of acid dye were improved with increasing salts (*e.g.*,  $NaNO_3$ ,  $NaCl$ ,  $Na_2SO_4$ ,  $Na_2CO_3$ , and  $NaHCO_3$ ) concentrations.

### **2.3.3.2 Scale-up strategies**

The limited throughput capacity of microreactors is the biggest challenge to their applicability for industrial-scale W/WWT. Therefore, the upscaling of microreactor technology, for instance, to include the use of capillaries and microchannels within conventional continuous-flow reactors, presents both a significant opportunity and challenge to improve the performance of AOPs for W/WWT.

Important reactor scale-up strategies that have been studied and applied to pharmaceutical and fine chemical production include parallel numbering up and dimensional scaling-up (Zhang et al., 2017) (**Fig. 2.11**). In the infancy stage of microreactor development, numbering up was considered an easy way to overcome throughput limitations and meet pilot or industrial-scale needs (Saber et al., 2010) (**Fig. 2.11a**). Microreactor numbering up involves placing multiple microchannels or microreactors in parallel to increase the total reactor internal volume. The main advantage of this strategy is that it aims to retain the hydrodynamic characteristics and excellent performance of microreactors. As expected, however, the use of multiple microchannels or microreactors greatly increases not only the complexity of system monitoring and control, but also the energy consumption and equipment costs (Saber et al., 2010; Zhang et al., 2017). On the other hand, scaling up a microreactor's internal volume, which can increase

its characteristic dimensions from micrometer to millimeter scales or beyond, has become the preferred way to resolve the inherently low throughput to meet industrial needs (Wang et al., 2020d) (**Fig. 2.11b**). However, as channel dimensions increase, the fluid flow pattern gradually transforms from a surface-force driven into gravity driven. Thus, it may be unreasonable to simply increase the channel size to enhance throughput capacity, as doing so may significantly reduce the microreactor's inherently high process efficiency (Javornik et al.). Some have proposed selective-dimension enlarging as a compromising scale-up strategy, which increases reactor throughput while retaining its high internal surface area-to-volume ratio for excellent mass and heat transfers and high process efficiency.

Little has been reported on the effects of microreactor scale-up on process parameters in W/WWT field. Yang et al. (2016) investigated the effect of upscaling a liquid–solid mini-fluidized bed reactor on a photocatalytic AOP by increasing the tube inner diameter from 1 to 3 mm. With the increased inner diameter, many parameters such as radiation flux density, specific surface area, and mass transfer distance had changed significantly. These authors determined that the photocatalytic reactor with a mini-fluidized bed combines the advantages of micro- with macro-scale photocatalytic reactors to overcome the drawbacks of limited microreactor throughput and substantial light attenuation within macro-scale reactors. Suhadolnik et al. (2019) designed a scaled-up PEC reactor for the large-capacity treatment of dye-contaminated wastewater. The inner volume of this PEC reactor was 714 times larger than that of a microreactor, and the residence time required for complete degradation of the dye was approximately 18 h. de Sá et al. (2018) developed and employed a new scale-up method that

enables both external and internal numbering up of meso- and micro-scale reactors to investigate photodegradation of methylene blue, rhodamine B, and phenol. In this study, multiple upscaled micro-units were connected in parallel to enlarge the reactor's volume, while retaining the benefits of a microstructured reactor. This demonstration may offer a favorable means of improving microreactor design to meet industrial-scale W/WWT throughput needs.

Which scale-up methods can retain the processing advantages of microreactors while meeting the high-throughput requirements for commercial applications? More research is needed to answer this important question. True upscaling of microreactor technology for AOPs requires that microfluidic features are incorporated within larger reactors, to intensify process conditions, and accelerate chemical reactions, and enable high process efficiency and performance. Finally, it is necessary to balance reactor fabrication costs, energy consumption, and operational AOP performance for W/WWT.

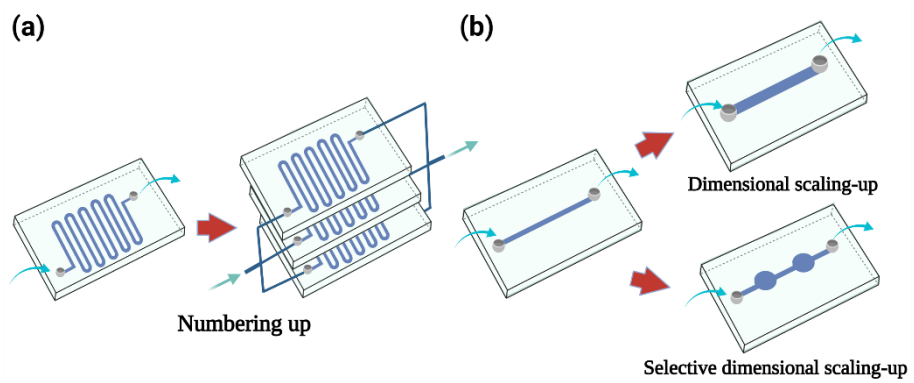


**Figure 2.11** Numbering up and (selective) dimensional scaling up concepts of microreactors

### 2.3.3.3 Costs analysis

The costs associated with applying emerging microfluidic technology to environmental challenges, including W/WWT, have not yet been considered within published reports and evidently require further investigation. Possible options to reduce the fabrication and operating costs of microreactors used for AOPs are considered below.

Fabrication costs can be reduced in two ways: 1) selecting less expensive microreactor component materials, *e.g.*, inexpensive polymers for capillary microreactors, nanoscale TiO<sub>2</sub> or ZnO as photocatalysts for photo-induced microreactors, and finding alternative cheap electrodes for electrochemical microreactors; and 2) application of cost-efficient fabrication methods (*e.g.*, soft lithography and 3D printing for chip-like microreactors) (Das & Srivastava, 2016; Mousset et al., 2019).

AOP energy consumption represents a major operating cost, which can be minimized by: 1) improving light utilization in UV-based AOPs, *e.g.*, by adjusting the position of the light source to shorten the light path (Miklos et al., 2018), choosing low-cost, uniformly-radiating, visible-light emitting diodes as light sources (Shinozawa et al., 2019), or increasing illumination coverage through an internal optical fiber (Özbakır et al., 2021); 2) enhancing energy utility efficiency, *e.g.*, by using an electrochemical flow-through microreactor instead of a commercial flow-by system (Pérez et al., 2017), choosing  $\mu$ PBR for ozonation AOPs to achieve excellent multiphase mixing (Cao et al., 2021b), adopting a tube-in-tube ceramic membrane microreactor to minimize consumption of titration reagent during Fenton AOPs (Vilar et al., 2020).

#### **2.3.4. Summary**

This review presents an overview of the hydrodynamic characteristics, designs, emerging applications, scale-up opportunities and challenges associated with applying AOP-microreactors for W/WWT. This work also reveals the fast growth of an emerging area of environmental microfluidics. Fundamental microscale hydrodynamic characteristics pertaining to mass transfer, mixing efficiency, and reaction kinetics are presented. Factors and considerations influencing microreactor designs, and the appropriate selection of their construction materials and fabrication techniques are discussed. An overview and in-depth discussion of emerging applications of microreactor systems to AOPs for the removal of aquatic pollutants are also provided. Several important microreactor designs are presented to showcase the merits of microfluidic technology for various AOP applications. Lastly, key strategies and recommendations for microreactor scale-up are discussed, with particular emphasis on the retention of microfluidic features that accelerate chemical processes within high-throughput reactors offering improved utility for environmental industry.

**Table 2.4** Summary of AOP characteristics using conventional reactors and microreactors.

<b>AOP type</b>	<b>Challenges in conventional reactors</b>	<b>Advantages of microreactors</b>
Photocatalytic oxidation	Uneven light distribution and hindered transmission; low mixing and mass transfer; deficiency of dissolved oxygen; catalysts loss and difficult for recovery (Chong et al., 2010; Shukla et al., 2021a)	Enhanced mass transfer; large surface area; short diffusion length; uniform irradiation and residence time; easy to control (Das & Srivastava, 2016; Wang et al., 2014d)
Electrochemical oxidation	Low surface area-to-volume ratios; low space-time yield; high IE gap; low electrical conductivity; high energy consumption (Radjenovic & Sedlak, 2015)	Charge passing between electrodes accumulates on surfaces to more efficiently convert pollutants; high surface area-to-volume ratio within narrow IE gap accelerates mass transfer; minimal electrolyte demand (Scialdone et al., 2012)
Fenton oxidation	Long mixing time; uneven light distribution in photo-Fenton; water pH restrictions (Zhang et al., 2019)	Continuous dosing to minimize Fe <sup>3+</sup> precipitation; short light path; amenable to a wide range of water pH (Díaz-Angulo et al., 2021; Shinozawa et al., 2019)

<b>AOP type</b>	<b>Challenges in conventional reactors</b>	<b>Advantages of microreactors</b>
Ozonation	Poor ozone utilization efficiency; high operating cost; low specific surface area; low partial pressure of ozone; poor multiphase mixing performance (John et al., 2020)	High ozone utilization efficiency; high volumetric mass transfer coefficients and gas/liquid interfacial areas (Cao et al., 2021b; Gao et al., 2012)
Plasma-phase oxidation	Difficult to implement at the macroscale; high operating cost; long residence time (Foster, 2017)	Large plasma/liquid interfacial area for enhancing mass transfer and reducing transfer distance of reactive species in plasma to liquid; better process control; low fabrication and operation cost (Patinglag et al., 2019)

With their high internal specific surface areas, which impart high process efficiencies, and minimal energy consumption, microreactors overcome many of the shortcomings of conventional reactors used for photocatalytic, electrochemical, Fenton, ozonation, and plasma-phase AOPs (**Table 2.4**). Furthermore, strategies toward the scale-up of microreactors for industrial-scale AOP applications to W/WWT are discussed. Although much progress has already been made to this end, continued research efforts are needed to address knowledge and technological gaps pertaining to the enhancement of chemical reaction kinetics and process outputs using microreactors for AOPs that degrade waterborne pollutants.

Currently, microfluidic studies mainly focus on the optimization of reactor designs and process parameters. We recommend that future research focuses on the following aspects:

(1) Improving theoretical understanding of microfluidic processes: Theoretical models of processes occurring at the microscopic scale are incomplete and require further development to better inform microreactor process design and scale-up. Although the hydrodynamic characteristics of microreactors have been well studied, the kinetic models of chemical reactions that occur during AOPs carried out in microreactors require further development.

(2) Integrated analysis of recalcitrant organic pollutants degradation occurring during AOPs carried out using microreactor systems: Most of the model contaminants used to study AOP performance are artificial dyes, such as methylene blue, azo compounds, *etc.* However, the chemical structures of such dyes, which are quite reactive and predisposed to photo-degradation and are poorly representative of the wide variety of organic contaminants that may persist in wastewater. Future research endeavors ought to expand upon the range of model

contaminant analytes (including antibiotics, perfluoroalkyl compounds, microplastics, *etc.*) used to gauge AOP process performance, by examining the degradation of more representative and/or recalcitrant molecular species. Thus, degradation reaction mechanisms and kinetic models for an expanded array of analytes are needed to inform the practical applicability of microreactor-based AOPs in the industry.

(3) Retaining microfluidic AOP performance enhancements during microreactor scale-up for practical water applications: Much of the microfluidic research currently underway remains limited to microscale applications. However, there remain ample opportunities to effectively employ microfluidic technology at much larger scales that enable higher-throughput AOPs for practical needs in the water treatment sector. Research efforts should focus on scaling-up and feasibility demonstrations of microreactor-inspired AOPs for industrial applications to W/WWT at various scales (*e.g.*, households, small communities, towns, and cities).

(4) Development of microreactor applications for emerging and innovative AOP types: Microfluidic technology may eventually be exploited for other novel AOP types, including those that employ supercritical water, ultrasonication, microwave, and electron beam irradiation to affect the oxidative degradation of pollutants. However, such systems have not yet been reported to the authors' knowledge.

Although microfluidic technology remains in an early stage of development, it is important to note that limited evidence and efforts made so far from this emerging area offer profound implications for improving contemporary practices in environmental industry.

# CHAPTER 3

## DEGRADATION PERFORMANCE, TOXICITY EVALUATION, AND FLOCS ANALYSIS OF O<sub>3</sub>, UV/O<sub>3</sub>, AND UV/O<sub>3</sub>/PS PROCESSES FOR MARINE OILY WASTEWATER TREATMENT

---

This chapter has been published in the Journal “*Water Research*”.

**Dong, G.**, \*Chen, B., Liu, B., Cao, Y., de Jourdan, B., \*Stoyanov, S. R., Ling, J., Ye, X., Lee, K., & Zhang, B. (2022). Comparison of O<sub>3</sub>, UV/O<sub>3</sub>, and UV/O<sub>3</sub>/PS Processes for Marine Oily Wastewater Treatment: Degradation Performance, Toxicity Evaluation, and Flocculation Analysis. *Water Research*, 119234. <https://doi.org/10.1016/j.watres.2022.119234>

### Authorship contribution statement:

**Guihua Dong:** Conceptualization, Methodology, Investigation, Visualization, Writing – original draft. **Bing Chen:** Conceptualization, Supervision, Writing – review & editing. **Bo Liu:** Methodology, Investigation, Writing – original draft. **Yiqi Cao:** Investigation, Writing – original draft. **Benjamin de Jourdan:** Investigation, Writing – review & editing. **Stanislav R Stoyanov:** Supervision, Writing – review & editing. **Jingjing Ling:** Writing – original draft. **Xudong Ye:** Writing – original draft. **Baiyu Zhang:** Supervision, Writing – review & editing

### 3.1. Introduction

Marine oily wastewater refers to the oil-contaminated water from offshore petroleum and marine shipping operations (*e.g.*, bilge water, ballast water, and offshore produced water), accidental oil spill response (*e.g.*, decanted water), and other wastewater streams containing oil from the harbor and coastal activities (Isaacson, 1979; Jing et al., 2015). The discharge and exposure of marine oily wastewater could result in disastrous impacts on marine ecosystems (Jing et al., 2015; Jing et al., 2018a; Li et al., 2016; Song et al., 2021b). A variety of physical, chemical, and biological treatment methods have been developed and geared toward the recovery/removal of oil impurities from water (Cao et al., 2022; Chen et al., 2020b; Liu et al., 2020b; Zhu et al., 2022). Among all the existing treatment methods, ozonation and its integration with other oxidation techniques have been among the most effective AOPs to eliminate the recalcitrant contaminants unselectively in various water matrices (Dong et al., 2022; Jing et al., 2018b; Wen et al., 2022). Ozonation or UV processes have been used to eliminate recalcitrant contaminants due to their ability to efficiently degrade recalcitrant organics in a reliable manner, via direct reaction with ozone molecules or the generation of  $\bullet\text{OH}$  that with strong oxidizing capabilities (Coha et al., 2021; Liu et al., 2021a). The efficiency of ozone in degrading organics is improved when combined with UV (254 nm) radiation (Gassie & Englehardt, 2019). As one of the powerful AOPs, the UV/O<sub>3</sub> process has been proven to have strong ability to treat oily wastewater, such as *n*-alkanes and PAHs (Lin et al., 2014).

Sulfate radical, as a strong one electron oxidant with a redox potential of 2.5-3.1 V, has an extremely high reactivity toward a variety of organic substances, which is comparable with

that of  $\bullet\text{OH}$ . It is reported that both  $\text{O}_3$  and UV can activate PS to form  $\text{SO}_4^{\bullet-}$  and  $\bullet\text{OH}$  simultaneously (Dong et al., 2021; Zou et al., 2021). Qin et al. (2020) have indicated that the pseudo-first-order rate constants of atrazine degradation in the UV/ $\text{O}_3$ /PS process increase by 3.3 times compared to that in the UV/ $\text{O}_3$  process. While these findings suggest that  $\text{SO}_4^{\bullet-}$  could decrease energy consumption and enhance the degradation efficiency, such a hypothesis has not been validated for treating marine oily wastewater.

Oily wastewater can cause ecological disturbances, including alteration of the aquatic community structure and food chains, through physical and chemical means. Toxic components of oily wastewater, specifically benzene, toluene, ethylbenzene, and xylenes (BTEX) and alkylated/non-alkylated PAHs have been observed to exhibit potential toxicity to both marine organisms and human health (Baird et al., 2007; Kponee et al., 2015). On the other hand, oxidation byproducts or excessive oxidants may also increase the toxicity level during the treatment process, which calls for the needs for better understanding of the mechanisms and control of the treatment process to ensure the quality/toxicity of effluent in compliance with standards (Liu et al., 2021a; Wang et al., 2013b). Therefore, toxicity assessment of marine oily wastewater treated by ozone-based processes with respect to aquatic organisms becomes important. Microtox<sup>®</sup> test for monitoring the acute toxicity of oily wastewater and the treatment efficacy has been widely adopted in research and practice as a rapid, sensitive, and cost-effective method and recommended by many regulators (Lee et al., 2003). This bioassay is based on the measurement of changes in light emission by a nonpathogenic bioluminescent marine bacterium (*Vibrio fischeri*) upon exposure to the test samples. Brine shrimp (*Artemia*

*franciscana*), one of the best-studied species of crustaceans, plays a key role in the marine food chain and is a suitable organism for bioassay and toxicity studies (Khoshnood et al., 2017). These two species were selected to evaluate and compare the toxicity of the raw and treated water in this study.

It is worth noting that the treatment of oily wastewater by ozonation can produce some flocs that can be suspended in water, stick to reactor walls, or float on the water surface (Khalifa et al., 2021; Sun et al., 2020). In detail, flocs generation may suppress the O<sub>3</sub> bubble interactions with oil and reduce the transmission of the UV light during the UV-induced oxidation process, limiting the production of free radicals for wastewater treatment. Flocs can also cause clogging and make system cleaning difficult. To our best knowledge, although the generation of flocs during O<sub>3</sub>-based processes is a common and important phenomenon, few studies have been reported on their properties (*e.g.*, components and surface characteristics) and fate (de Araujo et al., 2020). To fill this gap and provide practical strategies for the on-site O<sub>3</sub>-based treatment of oily wastewater, it is necessary to explore the physical and chemical properties of flocs and their fate during different approaches.

In this study, a lab-scale O<sub>3</sub> reactor was developed to explore the degradation of marine oily wastewater from synthetic seawater. Two oils and three types of ozonation processes were compared, and some key parameters such as initial oil concentration, O<sub>3</sub> dosage, PS dosage, salinity, pH level, and temperature were studied to determine the optimal conditions. The degradation kinetics of *n*-alkanes, PAHs and TOC were investigated to reveal the degradation performance of three processes. Bioassays with luminous bacterium and brine shrimp were

performed to evaluate the reduction in toxicity of the treated water. Microscopic and spectroscopic techniques were employed to investigate the characteristics of flocs generated in three O<sub>3</sub>-based processes.

## **3.2. Methods and Materials**

### **3.2.1 Chemicals and materials**

Sodium persulfate (PS), dichloromethane (DCM), PAH Mix 3, C8-C40 alkanes calibration standard, Internal Standards (IS), and sea salts were purchased from Sigma-Aldrich (Ontario, Canada). Two commonly used light and heavy crude oils, produced in Canada, were compared thoroughly. The physicochemical properties of both light and heavy crude oils including gravity, density, viscosity, sulphur content, and SARA (saturates, aromatics, resin, and asphaltene) fractions were obtained from Environment Canada and displayed in **Table 3.1**. It can be seen that the SARA fractions of light crude oil and heavy crude oil are significantly different. Heavy crude oil is low in saturates and aromatics but very high in resins and asphaltenes.

**Table 3.1** Physicochemical properties of light and heavy crude oils at 15 °C

Oil type	API	Density (kg/m <sup>3</sup> )	Viscosity (mPa s)	Sulphur (mass%)	SARA (% wt.)			
					Saturates	Aromatics	Resins	Asphaltenes
Light crude oil	33.3	853	12	0.5	69	25	4	2
Heavy crude oil	20.7	929.0	205	3.61	20	10	52	18

### 3.2.2 Experimental design

Different AOP experiments were carried out in a lab-scale reactor with a continuous supply of ozone at atmospheric temperature, as shown in the schematic diagram in **Fig. 3.1**. The ozone reactor comprises a glass column, in which 1 L of synthetic seawater with dissolved crude oil was introduced. A UV-254 nm (UVP 90-0012-01 Model) source (Krackeler Scientific) was inserted from the upper part as light source. An ozone diffuser (micropore size: 500  $\mu\text{m}$ ) was set at the bottom of the reactor. Ozone was produced in the lab using an ozone generator (OzoneLab<sup>TM</sup> OL80A Model). A flow meter (REG 5404-R, flows: 0-4 L/min) was used to provide a constant oxygen flow of 0.25 L/min into the ozone generator.

To better adjust the experimental conditions and operational parameters and explore the reaction mechanisms, we chose to use synthetic water in this study. Synthetic seawater was prepared by dissolving 35 g sea salt in 1 L distilled water with a magnetic stirrer. Marine oily wastewater was prepared by adding 1 mL crude oil in 1 L synthetic seawater (oil-to-water ratio 1:1000) followed by homogenization (Fisherbrand<sup>TM</sup> 850 Homogenizer) for 5 min in 15,000 rpm at room temperature (22–25 °C). All experiments were also conducted with real seawater in comparison, and all the results were similar. Each experiment was conducted at least three times since the dilution of crude oils in the seawater was not completely homogenous throughout the study.

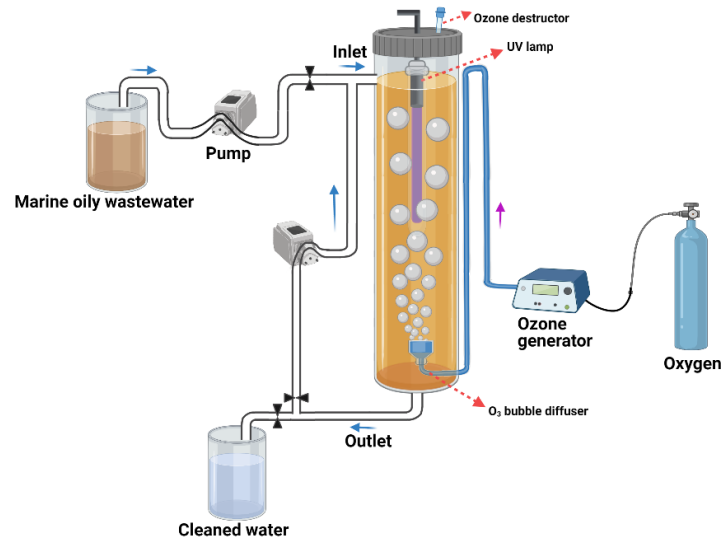


**Figure 3.1** Schematic diagram of continuous flow UV/O<sub>3</sub>-based system

### **3.2.3 Extraction and analysis methods**

#### ***3.2.3.1 Extraction procedure***

The water samples were first pre-treated by a vortex-shaker-assisted liquid-liquid microextraction (VSALLME) method modified from that reported by Zheng et al. (2015). For PAHs detection, ten milliliters of the treated solution were collected in a 15 mL glass screw-top tube, and 1 mL of DCM was added. The tube was well sealed and vortexed for 1 min, then, stood for 10 min to allow the separation of the organic and aqueous phases. A hundred microliters of the organic phase were transferred to a 150  $\mu$ L micro-vial. Ten microliters of IS (10  $\mu$ g/mL) were added before instrumental analysis. For the detection of *n*-alkanes, the procedure was same as above, except that the organic phase DCM was replaced with hexane.

#### ***3.2.3.2 Determination of total crude oil concentration***

The UV–Vis spectrophotometer (Thermo Fisher, GENESYS 10S) was applied to estimate the total oil concentration. All the components were dissolved in DCM in the same proportions, and then the absorbance measurements were recorded at wavelengths of 340, 370, and 400 nm (Cao et al., 2021c; Yang et al., 2021). The total organic carbon (TOC) concentrations were measured by the burning oxidation-non-dispersive infrared absorption method using a Shimadzu TOC-L analyzer (Shimadzu, Tokyo, Japan). A few drops of phosphoric acid were added before measuring TOC to maintain the sample pH < 1. Additional fluorometric analysis (Horiba Aqualog) was performed during the toxicity studies to estimate the concentration of crude oils in water.

### **3.2.3.3 Determination of *n*-alkanes and PAHs using GC-MS**

Both the normal alkanes (*n*-alkanes) and PAHs analysis were performed using an Agilent 7890A/5975C gas chromatography - mass spectrometry (GC - MS) equipped with an Agilent 7693 autosampler. Two microliters of analytes were injected into GC and separated by a 30 m × 0.25 mm id × 0.25 μm DB-5MS UI fused silica capillary column. For *n*-alkanes analysis, the oven was programmed to hold the initial temperature at 40 °C for 8 min, then ramp from 7 °C/min to 295 °C for 10 min. The injection mode was split at 300 °C with a split ratio of 10:1. For PAHs analysis, the oven program was set as the initial temperature at 65 °C for 1 min, then ramped 65–300 °C at 4 °C/min and held at 300 °C for 1 min. The injection mode was splitless at 300 °C. The PAH analyses were performed in the selected ion monitoring (SIM) mode with an electron energy of 70 eV. The ion-source was set at 300 °C. The methods detection limit was 0.3–1 ng/L. The variance of the analytical method was 5%, based on duplicate measurements.

### **3.2.4 Toxicity evaluation of treated water**

#### **3.2.4.1 *Vibrio fischeri* acute toxicity evaluation**

Acute toxicity tests of the solution before and after 1 h O<sub>3</sub>, UV/O<sub>3</sub>, and UV/O<sub>3</sub>/PS processes treatment were carried out using a Microtox® (Model 500) analyzer, whose primary indicator was the luminous bacterium (*Vibrio fischeri*). The acute toxicity test relied on bacterial luminescence via cellular respiration. Inhibition of cellular activity (caused by exposure to toxicants, acidic or alkaline conditions, *etc.*) decreased the respiratory rate, leading to a corresponding decrease in luminosity. The EC<sub>50</sub> referred to the percentage of water samples

that cause a 50% decrease of luminous intensity. The pH range of 6.0–8.5 was recommended as standard since *Vibrio fischeri* is pH-sensitive (Fang et al., 2019). Fifteen minutes of nitrogen was conducted to remove the residual ozone before the tests.

#### **3.2.4.2 *Artemia* acute toxicity evaluation**

The *Artemia* toxicity tests were conducted at Huntsman Marine Science Centre (St. Andrews, NB, Canada). *A. franciscana* cysts were sourced from Aquamerik Inc. (Levis, QC, Canada). Decapsulated cysts were hatched 24 h prior to exposure in an aerated flask at  $25 \pm 3$  °C. Hatched *A. franciscana* nauplii at the II and III instar stages were used for all exposures and 20 individuals were imaged to confirm the developmental stage. Exposures were performed at room temperature ( $25 \pm 2$ °C) with a 16:8 h light: dark photoperiod with LED light.

The acute toxicity of *Artemia* was evaluated based on the mortality rate at 48 h exposure to the marine oily wastewater before and after 1 h O<sub>3</sub>-based AOPs. All solutions were tested in triplicate, with 10 organisms per vial (4 mL glass GC vial). After 48 h exposure to the samples, organisms that were no longer able to swim within 15 seconds after gentle agitation with flowing water from a pipette were considered dead. Water quality parameters including dissolved oxygen (%DO), pH, salinity (PSU), and temperature (°C) were measured in the test solutions at the beginning and end (48 h) of the exposure. A test was considered valid if the control survival was greater than 80%, dissolved oxygen remained over 60% saturation, and the test solution temperature remained within 1.5 °C for the duration of the trial. Tests were performed and data collected consistent with Good Laboratory Practice standards. To better

understand what the organisms were exposed to, fluorometric readings (Horiba Aqualog® excitation-emission range: 220–600 nm) were collected to detect the relative differences in key components in crude oils before and after the O<sub>3</sub>-based AOPs. All contour maps were generated using Origin 2021 software.

### **3.2.5 Characterization and analysis of floating flocs**

The flocs formed in three O<sub>3</sub>-based AOPs (*i.e.*, O<sub>3</sub>, UV/O<sub>3</sub> and UV/O<sub>3</sub>/PS) after 1 h were collected on a glass slide and dried in a vacuum oven (Fisherbrand Isotemp Model 281A, Fisher Scientific, set at 50 °C, 10 h) for further analysis. Oil flocs were observed under a Leica DM2500 M optical microscope (Leica Microsystems, Buffalo Grove, IL, USA). The surface morphology of crude oil flocs before and after treatment was measured by the scanning electron microscope (SEM, Quanta 400 MLA) equipped with energy-dispersive X-ray spectroscopy (EDS). The surface functional groups of floating flocs were characterized using Fourier-transform infrared spectroscopy with attenuated total reflectance (ATR-FTIR). The spectra were taken in the range of 4000–650 cm<sup>-1</sup>.

### **3.2.6 Statistical analysis**

All experiments were conducted in triplicate for quality control. Error bar and error area represented each standard deviation from the means of independent experiment. The significant differences were determined by one-way analysis of variance (ANOVA) with *F*-tests using Minitab 18 software. The  $P < 0.05$  (\*) was considered as statistically significant and  $P < 0.001$  (\*\*) as statistically highly significant.

### **3.3. Results and Discussion**

#### **3.3.1 Degradation performance of three ozone-based processes**

##### ***3.3.1.1 PS addition enhanced the overall degradation of crude oils***

Changes in total oil concentration over time were examined to compare the treatment performance of O<sub>3</sub>, UV/O<sub>3</sub>, and UV/O<sub>3</sub>/PS processes for both light and heavy crude oils (**Fig. 3.2**). Under the same oil-to-water ratio (1:1000), the initial concentration of light crude oil measured by the spectrophotometer was about 380~430 ppm, and that of heavy crude oil was about 190~230 ppm.

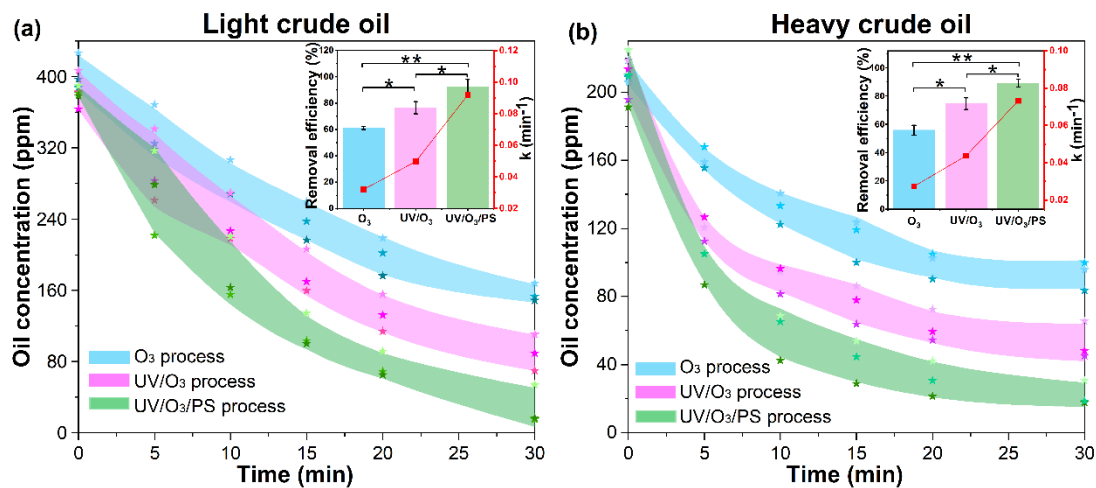


**Figure 3.2** Degradation performance of light (a) and heavy (b) crude oils under  $\text{O}_3$ , UV/ $\text{O}_3$ , and UV/ $\text{O}_3$ /PS processes ( $\text{O}_3$  dosage 10 mg/L, PS dosage 1 mM if used)

It was found that, in the first 5 min, three oxidation processes showed no significant difference on the light crude oil degradation (**Fig. 3.3**). After 10 min of reaction, the UV/O<sub>3</sub>/PS process showed significant degradation performance in comparison with O<sub>3</sub> process. After that, these three processes started to show significant differences on light crude oil degradation. After 30 min treatment, the concentrations of light crude oil in O<sub>3</sub>, UV/O<sub>3</sub>, and UV/O<sub>3</sub>/PS processes were 156.63, 90.03, and 28.76 ppm, respectively. Correspondingly, the removal efficiencies of O<sub>3</sub>, UV/O<sub>3</sub>, and UV/O<sub>3</sub>/PS processes were 61.22%, 76.57%, and 92.49%, respectively (**Fig. 3.2a**). The results indicated that the addition of PS showed little effect on the first 5 min, but the degradation efficiency gradually increased afterward. This could be due to the activation of PS, and generation of more SO<sub>4</sub><sup>•-</sup> after 5 min (**Fig. 3.2a**) (Lee et al., 2020). The crude oil degradation could be fitted with the pseudo-first-order kinetic model. The rate constant of the UV/O<sub>3</sub>/PS process was 0.092 min<sup>-1</sup>, which was significantly higher than both O<sub>3</sub> (0.032 min<sup>-1</sup>) and UV/O<sub>3</sub> (0.050 min<sup>-1</sup>) processes, showing that the addition of persulfate could substantially improve the oxidation performance within 30 min.

The degradation performance of these three processes for heavy crude oil was displayed in **Fig. 3.2b**. It would be worth noting that, unlike light crude oil, the degradation of heavy crude oil in three oxidation processes showed a significant difference in the first 5 min (**Fig. 3.3**). Since then, the degradation performance improved significantly from O<sub>3</sub> to UV/O<sub>3</sub> and UV/O<sub>3</sub>/PS processes. It could be due to more hydroxyl radicals being generated when O<sub>3</sub> was irradiated by UV light, and more sulfate radicals being produced, when persulfate was activated under the dual action of UV light and hydroxyl radicals (Soubh & Mokhtarani, 2016; Wang et

al., 2019). The concentrations of heavy crude oil in O<sub>3</sub>, UV/O<sub>3</sub>, and UV/O<sub>3</sub>/PS decreased to 93.07, 53.04, and 22.41 ppm after 30 min treatment, respectively. The average removal efficiencies of heavy crude oil were slightly lower than those of light crude oil degradation, which were 55.91%, 74.64%, and 89.26% in O<sub>3</sub>, UV/O<sub>3</sub>, and UV/O<sub>3</sub>/PS processes, respectively. The rate constants of the O<sub>3</sub>, UV/O<sub>3</sub>, and UV/O<sub>3</sub>/PS process were 0.027, 0.044, 0.073 min<sup>-1</sup>, respectively (**Table 3.2**). All the above results indicated that the addition of only a small amount of persulfate can significantly improve the UV/O<sub>3</sub> treatment performance of crude oil containing wastewater

**Table 3.2** Kinetic parameters on crude oil degradation following first order rate law under three processes.

Oil type	Process	Parameter	First-order kinetic equation	Rate constant k (min <sup>-1</sup> )	Correlation coefficient (R <sup>2</sup> )	
crude oil	O <sub>3</sub>	1	$y = -0.0317x - 0.0065$	0.0317	0.9964	
		2	$y = -0.0308x - 0.0257$	0.0308	0.9957	
		3	$y = -0.0337x - 0.0532$	0.0337	0.972	
	Light	UV/O <sub>3</sub>	1	$y = -0.0453x + 0.0157$	0.0453	0.9926
			2	$y = -0.0563x - 0.0376$	0.0563	0.9946
			3	$y = -0.0475x - 0.0161$	0.0475	0.996
	UV/O <sub>3</sub> /PS		1	$y = -0.0698x + 0.0531$	0.0698	0.9871
			2	$y = -0.1023x + 0.0855$	0.1023	0.9744
			3	$y = -0.1035x + 0.1565$	0.1035	0.9868

Oil type	Process	Parameter	First-order kinetic equation	Rate constant k (min <sup>-1</sup> )	Correlation coefficient (R <sup>2</sup> )
		1	$y=-0.0259x-0.1357$	0.0259	0.8696
	O <sub>3</sub>	2	$y=-0.0306x-0.1458$	0.0306	0.8801
		3	$y=-0.0254x-0.0959$	0.0254	0.9272
Heavy		1	$y=-0.0364x-0.2932$	0.0364	0.8104
crude oil	UV/O <sub>3</sub>	2	$y=-0.0467x-0.2593$	0.0467	0.8851
		3	$y=-0.048x-0.209$	0.048	0.9272
		1	$y=-0.0624x-0.3403$	0.0624	0.8991
	UV/O <sub>3</sub> /PS	2	$y=-0.0784x-0.4129$	0.0784	0.8665
		3	$y=-0.0788x-0.2398$	0.0788	0.962

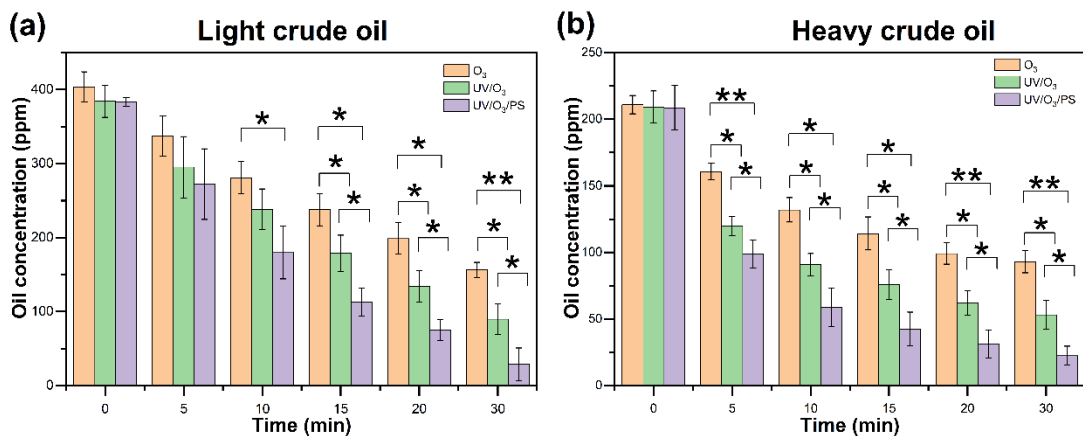


**Figure 3.3** Significant analysis of crude oils degradation in different oxidation processes over time

### ***3.3.1.2 Factors affecting degradation of crude oils***

Parameters including initial crude oil concentration, O<sub>3</sub>, PS, salinity, pH level, and temperature were further investigated to test UV/O<sub>3</sub>/PS process on the degradation of crude oils. Six different light crude oil concentrations from 200 ppm to 500 ppm were prepared to test the effect of initial crude oil concentrations on UV/O<sub>3</sub>/PS process. The results showed that regardless of the initial oil concentrations, the remaining crude oil concentrations were relatively close (20~70 ppm), and around 85~91% of the crude oil could be removed after 30 min treatment (**Fig. 3.4a**). Increased initial concentration (from 202.02 ppm to 513.20 ppm) resulted in a slight decrease in process efficiency (from 90.95% to 86.40%) and rate constants (from 0.080 to 0.067 min<sup>-1</sup>). More than 80.00% of the heavy crude oil was removed within 30 min at initial concentration of less than 200 ppm (**Fig. 3.5a**). However, a lower removal rate (less than 60.00%) occurred at increased heavy crude oil concentration (> 200 ppm). This could be due to the low UV penetration in wastewater with high heavy crude concentrations, resulting in decreased free radical production. The degradation performance of the crude oils under UV/O<sub>3</sub>/PS process followed the first order kinetic equation. The corresponding parameters were collected in **Table 3.3**. This indicated that the initial concentrations had little effect on the degradation performance of this process.

**Table 3.3** Kinetic parameters of different conditions on crude oil degradation following first order rate law under three processes.

Oil type	Process	Parameter	First-order kinetic equation	Rate constant k (min <sup>-1</sup> )	Correlation coefficient (R <sup>2</sup> )
Light crude oil	Initial concentration	1	$y = -0.0716x + 0.0615$	0.0716	0.992
		2	$y = -0.0776x - 0.0099$	0.0776	0.9987
		3	$y = -0.0804x + 0.0713$	0.0804	0.9926
		4	$y = -0.0698x + 0.0531$	0.0698	0.9871
		5	$y = -0.0665x + 0.0337$	0.0665	0.987
		6	$y = -0.0679x + 0.036$	0.0679	0.9909
	O <sub>3</sub> dose	0	$y = -0.0164x + 0.0021$	0.0164	0.9973
		2 ppm	$y = -0.0352x + 0.0217$	0.0352	0.994
		5 ppm	$y = -0.0514x - 0.0009$	0.0514	0.9937
		10 ppm	$y = -0.0693x + 0.0416$	0.0693	0.9887
		PS dose	0	$y = -0.0453x + 0.0157$	0.0453
0.5 mM	$y = -0.0514x - 0.0009$		0.0514	0.9937	

		1 mM	$y = -0.0705x + 0.0016$	0.0705	0.9751
		2 mM	$y = -0.0902x - 0.0325$	0.0902	0.9765
		0	$y = -0.0427x + 0.0732$	0.0427	0.9804
	Salinity	15‰	$y = -0.0552x + 0.0563$	0.0552	0.9875
		35‰	$y = -0.0698x + 0.0531$	0.0698	0.9871
		50‰	$y = -0.088x - 0.0419$	0.088	0.972
		1	$y = -0.0617x - 0.0378$	0.0617	0.9602
		2	$y = -0.0715x - 0.0377$	0.0715	0.9595
	Initial	3	$y = -0.0652x - 0.2139$	0.0652	0.9519
	concentration	4	$y = -0.0462x - 0.1949$	0.0462	0.9327
		5	$y = -0.0287x - 0.0343$	0.0287	0.9947
		6	$y = -0.0278x - 0.0095$	0.0278	0.995
Heavy	crude	0	$y = -0.0071x + 0.0174$	0.0071	0.9559
oil	O <sub>3</sub> dose	2 ppm	$y = -0.0361x - 0.0386$	0.0361	0.9716
		5 ppm	$y = -0.053x - 0.0195$	0.053	0.9975
		10 ppm	$y = -0.0878x + 0.0145$	0.0878	0.9871

	0	$y = -0.0109x - 0.0144$	0.0109	0.9883
PS dose	0.5 mM	$y = -0.0169x - 0.0039$	0.0169	0.9918
	1 mM	$y = -0.0363x + 0.0427$	0.0363	0.9926
	2 mM	$y = -0.0514x + 0.1269$	0.0514	0.9688
	0	$y = -0.025x - 0.0256$	0.025	0.9265
Salinity	15‰	$y = -0.0374x - 0.0767$	0.0374	0.961
	35‰	$y = -0.0878x + 0.0145$	0.0878	0.9871
	50‰	$y = -0.1167x + 0.0376$	0.1167	0.9955

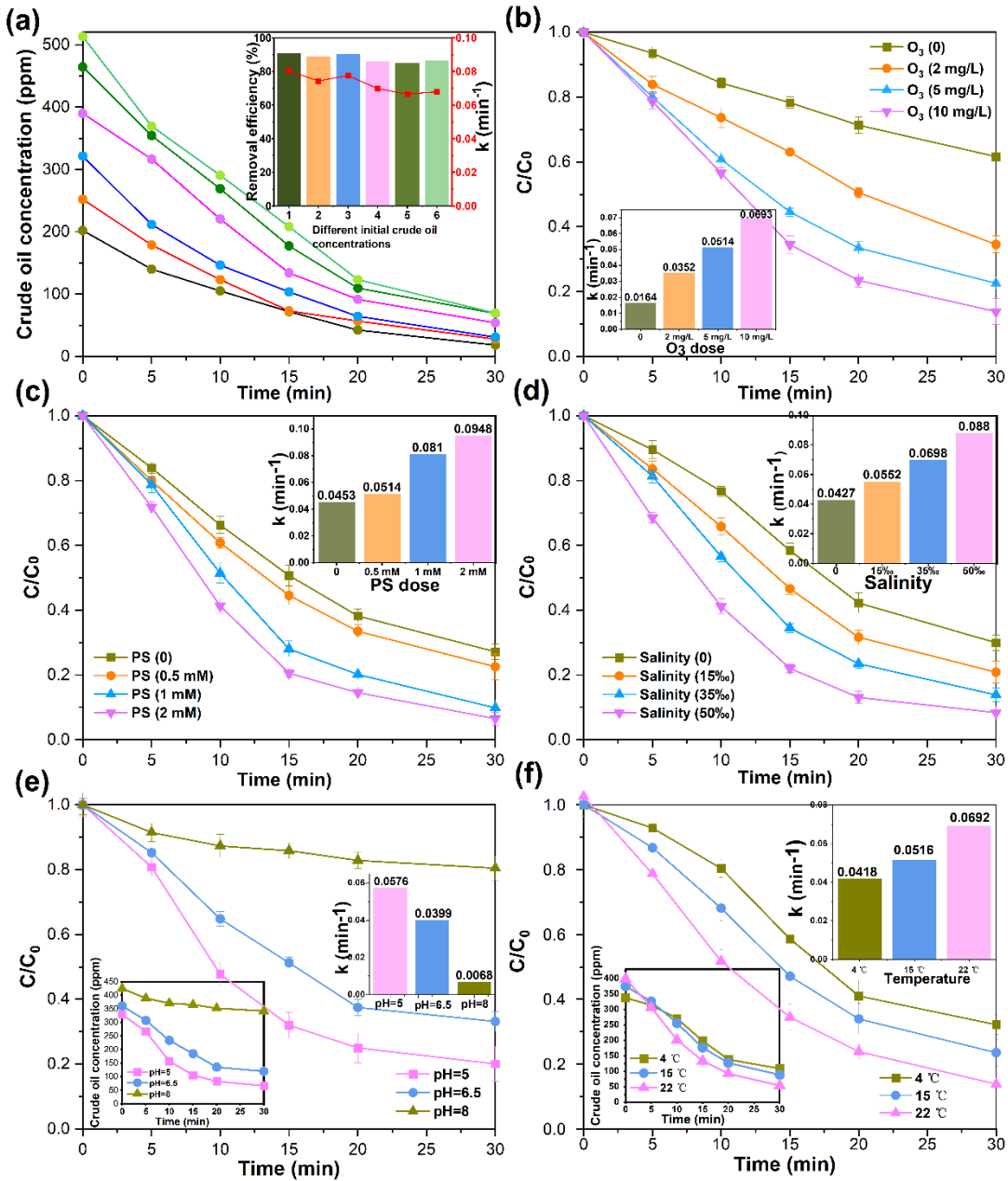


**Figure 3.4** Effects of different parameters on light crude oil degradation in UV/O<sub>3</sub>/PS process: (a) initial oil concentration, (b) O<sub>3</sub> dosage, (c) PS dosage, (d) salinity, (e) pH level, and (f) temperature (O<sub>3</sub> dose 10 mg/L, PS dose 1 mM if not mentioned). In (a), the colors of line graph represent different initial concentrations and correspond to the colors in the bar graph (inset), in an ascending order.

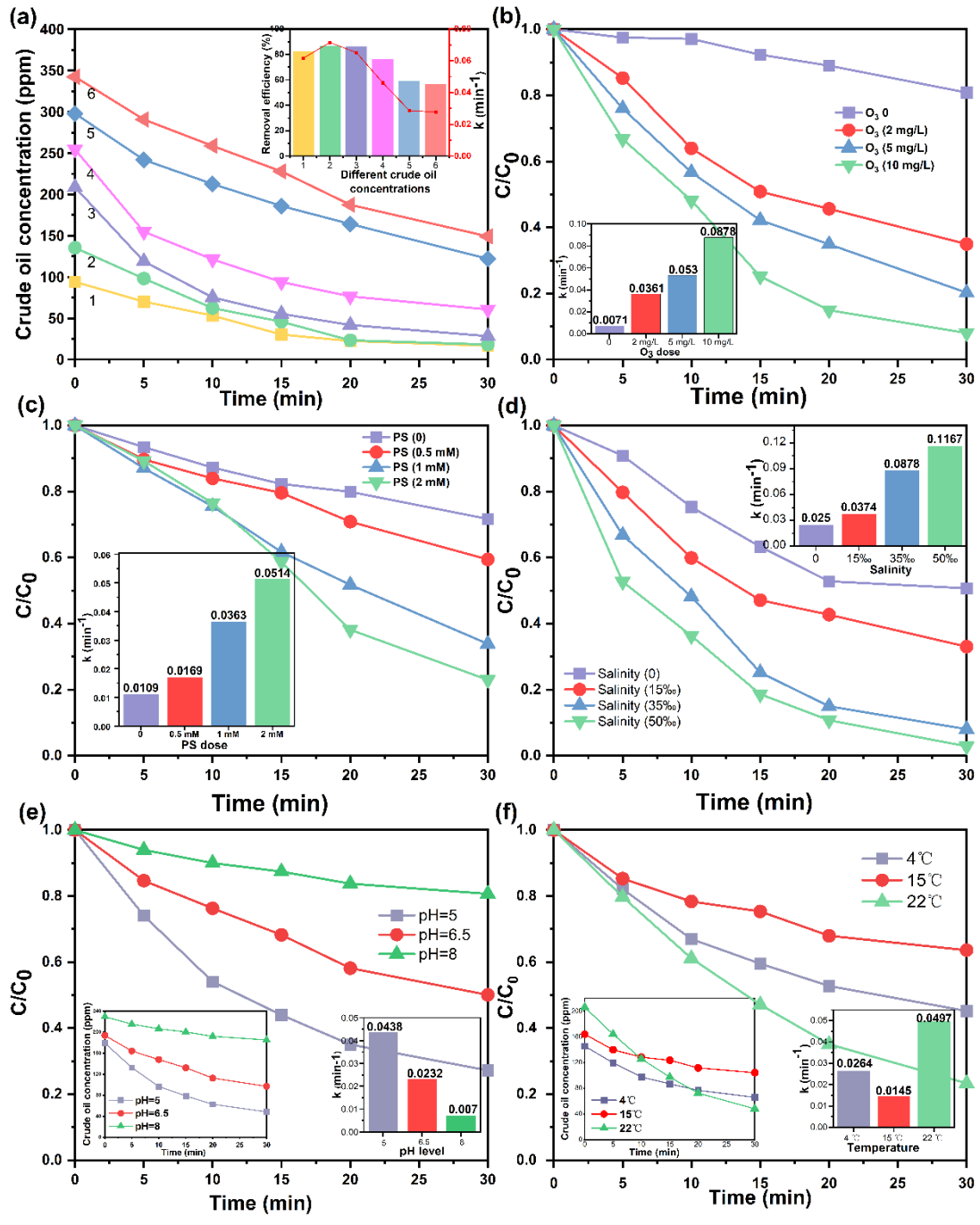


**Figure 3.5** Effects of different parameters on heavy crude oil degradation in UV/O<sub>3</sub>/PS process: (a) initial oil concentration, (b) O<sub>3</sub> dosage, (c) PS dosage, (d) salinity, (e) pH level, and (f) temperature (O<sub>3</sub> dose 10 mg/L, PS dose 1 mM if not mentioned).

The ozone dose had a significant impact on crude oil removal. Only 38.34% of light crude oil could be removed in 30 min in UV/PS process (**Fig. 3.4b**). An addition of 2 mg/L of ozone could enhance the removal efficiency up to 65.44% comparing with no ozone input. And when the blown ozone reached 10 mg/L, more than 90% of crude oil could be eliminated in 30 min, showing the great effect of ozonation. The calculated rate constant increased from 0.016 to 0.069 min<sup>-1</sup>, corroborating that the ozone dosage played a key role in this combined oxidation process. Only 19.13% of heavy crude could be removed in 30 min without propagating O<sub>3</sub> (**Fig. 3.5b**). When ozone was injected, the results were similar to light crude oil.

It was reported that an appropriate dosage of persulfate was conducive to the degradation of organic pollutants (Sharma & Ruparelia, 2017). The dosage exceeding the optimal limit would not only cause an excessive use of chemicals but also may act as a scavenger and reduce the treatment effectiveness (Sharma & Ruparelia, 2017). To find the optimum persulfate dosage, different PS dosages were selected to test their effects on the light crude oil degradation (**Fig. 3.4c**). It was found that the removal efficiency could be improved from 72.81% to 77.47%, when 0.5 mM persulfate was added. The removal efficiency was further increased to 90.17% and 93.47%, when increasing the concentration of persulfate to 1 mM and 2 mM, respectively. The trend was similar to that seen in heavy crude oil (**Fig. 3.5c**). Given that increasing the persulfate dosages above 1 mM did not significantly improve the process efficiency, the concentration of 1mM was then selected for the remainder of the study.

As indicated in **Figs. 3.4d** and **3.5d**, the crude oil removal efficiency was improved significantly with the increase of salinity. The corresponding reaction rate constants in light

crude oil were 0.043, 0.055, 0.070, and 0.088 min<sup>-1</sup> under the salinity of 0, 15‰, 35‰, and 50‰, respectively (**Fig. 3.4d**). The rate constant reached 0.117 min<sup>-1</sup> when the solution salinity was set as 50‰, showing an impressive removal efficiency of heavy crude oil (**Fig. 3.5d**). These indicated that salinity played a key role on crude oil degradation in the UV/O<sub>3</sub>/PS process. Our result has been in line with previous results, which demonstrated that salinity played a critical role in the degradation of oily pollutants (Cao et al., 2020b; Zhang et al., 2020). It may be due to the low amount of chloride that would react with •OH to produce Cl•, which had a high redox potential of 2.4 V, to further degrade organics as active species (Xu et al., 2018). Further, the existence of salts (Na<sub>2</sub>SO<sub>4</sub> or NaCl) accelerated the mass transfer of ozone at the gas-liquid interface and as a result the removal efficiency of organic pollutants enhanced significantly (Liu et al., 2021b).

An investigation on the effect of pH on the degradation of crude oils by UV/O<sub>3</sub>/PS process was conducted at the pH values of 5, 6.5, and 8. As seen in the inset chart of **Fig. 3.4e**, the initial light crude oil concentrations increased with the elevated pH, reaching 329.25 ppm, 360.76 ppm, and 425.27 ppm, at pH 5, 6.5, and 8, respectively. This trend was also observed in heavy crude oil. Under the same oil-to-water ratio, the concentration of light and heavy crude oils under alkaline pH was higher than in neutral and acidic conditions (**Figs. 3.4e** and **3.5e**, inset chart). This could be due to the alkaline reaction of the organic acids in the crude oils, producing an in-situ surfactant, which reduced the interfacial tension and thus increased the concentration of crude oil in water (Sheng, 2015). As seen in **Fig. 3.4e**, the efficiency of light crude oil removal increased from 66.85% to 79.89% as the pH was decreased from 6.5 to 5;

while the removal efficiency was significantly reduced to 19.59% when the pH reached up to 8. Similar results were displayed in **Fig. 3.5e** for heavy crude oil degradation. Thus, the UV/O<sub>3</sub>/PS process would be more suitable for light and heavy crude oils degradation in acidic rather than alkaline conditions. It was reported that molecular ozone, sulfate radicals, and hydroxyl radicals were the dominant reactive species at pH < 7 in UV/O<sub>3</sub>/PS process (Izadifard et al., 2017). Indirect ozonation, usually by hydroxyl radicals, played a major role in alkaline conditions because of the decomposition of molecular ozone (Ji et al., 2018). Besides, more sulfate radicals reacted with OH<sup>-</sup> forming hydroxyl radicals, which were the primary reactive species under basic conditions (Izadifard et al., 2017). Ji et al. (2018) reported that direct ozonation was the predominant process for the oxidation of some oil compounds, such as *n*-alkanes and PAHs. Therefore, the reduced sulfate radicals and the decomposition of molecular ozone could result in inhibited degradation of crude oil in alkaline conditions.

**Figs. 3.4f** and **3.5f** presented the degradation of light and heavy crude oils at various temperatures (4 °C, 15 °C, and 22 °C) under the UV/O<sub>3</sub>/PS process. The initial crude oil concentrations in water at 4 °C, 15 °C, and 22 °C were 337.88 ppm, 375.23 ppm, and 399.70 ppm, respectively, showing an increasing trend. It was seen that low temperature decreased the concentration of initial crude oil in water and inhibited the degradation of total crude oil in this combined process (**Fig. 3.4f**). With the temperature rising from 4 to 22 °C, the total light crude oil removal increased from 67.82% to 86.12%. The reason could be that the rising temperature accelerated the solubility of ozone in water and speeded up the production of hydroxyl radicals. The lowest removal rate for heavy crude oil occurred at 15 °C instead of 4 °C, which could be

attribute to the significantly different initial heavy crude oil concentrations (**Fig. 3.5f**).

### ***3.3.1.3 Removal of *n*-alkanes and PAHs during three ozone-based processes***

Chronic and acute exposure to hydrocarbons from crude oil such as *n*-alkanes and PAHs could cause detrimental health disorders to both aquatic and human beings (Rajasekhar et al., 2021). It is necessary to monitor the concentration change of *n*-alkanes and PAHs during three ozone-based processes.



**Figure 3.6** Pictures of initial light (a) and heavy (b) crude oils in reactor

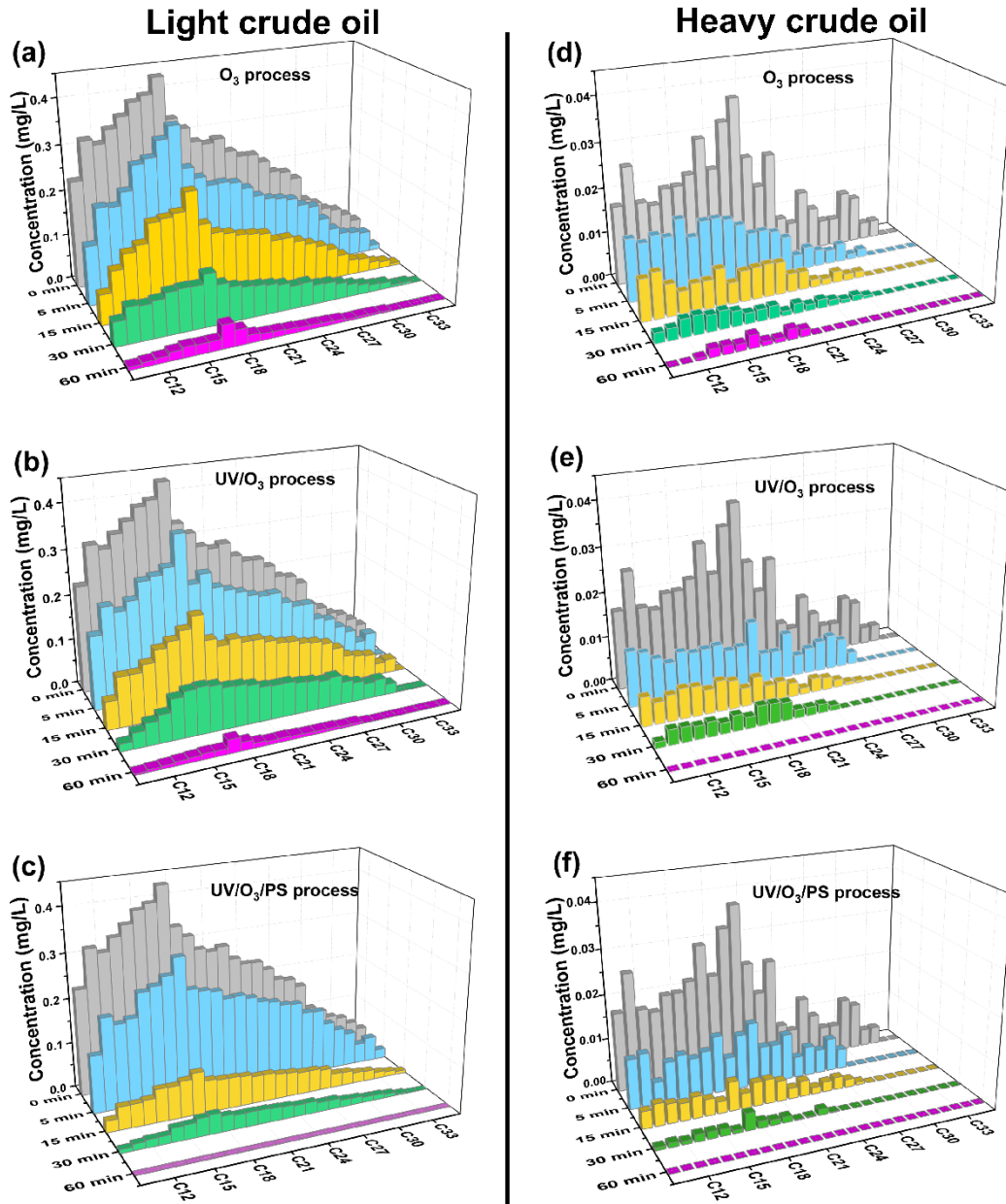


**Figure 3.7** *n*-alkanes degradation performance in both light crude oil under (a) O<sub>3</sub>, (b) UV/O<sub>3</sub>, and (c) UV/O<sub>3</sub>/PS processes and heavy crude oil under (d) O<sub>3</sub>, (e) UV/O<sub>3</sub>, and (f) UV/O<sub>3</sub>/PS processes within 60 min

As displayed in the reactors of **Figs. 3.6a** and **b**, the color of homogenized light and heavy crude oils are yellow and dark brown, respectively. The abundance of the *n*-alkane peaks in light crude oil was observed to be much higher than that in heavy crude oil, as shown in the GC-MS chromatogram (**Fig. 3.7**). This result was consistent with the crude oil properties given in **Table 3.1**, *i.e.*, the concentration of saturates in light crude oil was significantly higher than in heavy crude oil. In comparison with heavy crude oil, the initial total *n*-alkanes concentration in light crude oil (6.24 mg/L) is 15 times higher than in heavy crude oil (0.41 mg/L) (**Fig. 3.7**). In both light and heavy crude oils, short-chain (*i.e.*, C10-C19) *n*-alkanes are the most abundant, accounting for more than half of the total *n*-alkanes. The content of long-chain (*i.e.*, C30-C35) *n*-alkanes was the lowest, accounting for only about 7.31% of total *n*-alkanes in both light and heavy crude oils.

For light crude oil, after 30 min treatment, the O<sub>3</sub> process could remove 69.41% of the *n*-alkanes, the UV/O<sub>3</sub> process reached up to 73.23%, and 90% removal could be achieved with the UV/O<sub>3</sub>/PS process (**Fig. 3.7a-c**). It would be noteworthy that, after 1 h treatment, small amounts of *n*-alkanes still can be detected in both O<sub>3</sub> and UV/O<sub>3</sub> processes, but none can be found in UV/O<sub>3</sub>/PS process, which indicated that the UV/O<sub>3</sub>/PS process had an impressive efficiency for *n*-alkanes removal (**Fig. 3.7a-c**). After 1 h O<sub>3</sub> process treatment, the removal efficiencies of short-chain, middle-chain (*i.e.*, C20-C29), and long-chain *n*-alkanes were 93.65%, 96.30%, and 99.29%, respectively. In the UV/O<sub>3</sub> process, 96.59%, 97.66%, and 100% of efficiencies could be reached for short-chain, middle-chain, and long-chain *n*-alkanes degradation, respectively. Therefore, we concluded that the longer the carbon chain of the *n*-

alkanes, the easier these were to remove. It was possible that the long-chain *n*-alkanes were cleaved into short-chain before being completely removed under the O<sub>3</sub>-based processes.

For heavy crude oil, 96.45% of the total *n*-alkanes removal efficiency could be observed in O<sub>3</sub> process, and these were completely removed in both UV/O<sub>3</sub> and UV/O<sub>3</sub>/PS AOPs. This confirmed that both UV light and persulfate had positive effect on the degradation of *n*-alkanes. It would be worth noting that 97.88% of *n*-alkanes could be removed in only 30 min in the UV/O<sub>3</sub>/PS process, showing excellent degradation performance. Different *n*-alkane fractions showed different results. It only took 5 to 15 min to remove all long-chain *n*-alkanes in these three O<sub>3</sub>-based AOPs. However, it took longer to degrade short-chain *n*-alkanes than both middle- and long-chain *n*-alkanes. This was consistent with the degradation performance in light crude oil.

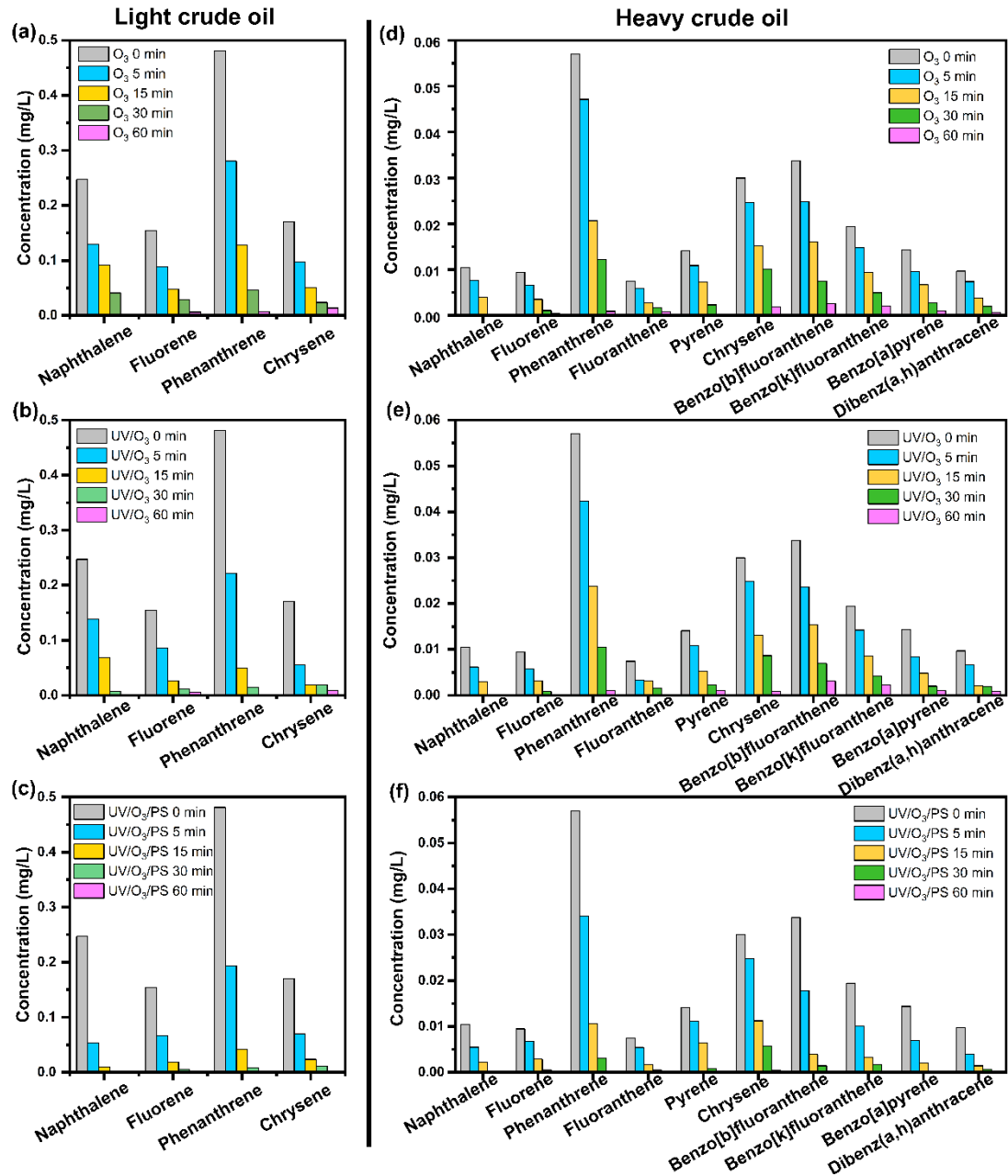


**Figure 3.8** PAHs degradation performance in both light crude oil under (a) O<sub>3</sub>, (b) UV/O<sub>3</sub>, and (c) UV/O<sub>3</sub>/PS processes and heavy crude oil under (d) O<sub>3</sub>, (e) UV/O<sub>3</sub>, and (f) UV/O<sub>3</sub>/PS processes within 60 min

The 16 priority PAHs were classified by the U.S. Environmental Protection Agency based on the wide range of toxicological effects on humans (Ambade et al., 2022). Therefore, the main PAHs in both light and heavy crude oils were detected and their degradation performance under three O<sub>3</sub>-based processes were monitored and displayed in **Fig. 3.8**. The main detected PAHs in light crude oil were naphthalene, fluorene, phenanthrene, and chrysene, and the total PAHs concentration was 1.05 mg/L. In contrast, as many as 10 PAHs were detected in heavy crude oil, including naphthalene, fluorene, phenanthrene, fluoranthene, pyrene, chrysene, benzo[b]fluoranthene, benzo[k]fluoranthene, benzo[a]pyrene, and dibenz(a,h)anthracene. Their total concentration of about 0.21 mg/L was 5 times lower than the total PAHs concentration in light crude oil. The concentration of phenanthrene was the highest in both light and heavy crude oils.

Although the concentration of total PAHs in light crude oil was higher than in heavy crude oil, these were easy to remove unselectively under the three AOPs (**Fig. 3.8a**). The results showed that 86.72%, 95.09%, and 97.46% of total PAHs in light crude oil could be removed in only 30 min under O<sub>3</sub>, UV/O<sub>3</sub>, and UV/O<sub>3</sub>/PS processes, respectively. Both UV/O<sub>3</sub> and UV/O<sub>3</sub>/PS processes could improve the removal efficiency. After 60 min, 97.28% and 98.67% of PAHs in O<sub>3</sub> and UV/O<sub>3</sub> processes could be removed, respectively, and no PAHs could be detected in UV/O<sub>3</sub>/PS process. For heavy crude oil, the degradation efficiencies of the total PAHs in O<sub>3</sub>, UV/O<sub>3</sub>, and UV/O<sub>3</sub>/PS AOPs after 30 min were 78.36%, 81.21%, and 92.91%, respectively (**Fig. 3.8b**). After 1 h of heavy crude oil treatment, the removal efficiencies in the O<sub>3</sub>, UV/O<sub>3</sub>, and UV/O<sub>3</sub>/PS processes were 94.79%, 94.97%, and 100%, respectively.

Overall, the addition of persulfate could achieve more than 90% of degradation efficiency for both *n*-alkanes and PAHs within 30 min, and the degradation rate was significantly higher than that of O<sub>3</sub> and UV/O<sub>3</sub> processes.

#### **3.3.1.4 TOC removal**

The TOC concentrations of crude oils before and after treatment were further evaluated to explore the mineralization of the treated water in the above three O<sub>3</sub>-based AOPs. The average TOC concentrations of initial light and heavy crude oils were 135.08 mg/L and 207.93 mg/L, respectively. It was found that the TOC removal efficiencies of the O<sub>3</sub>, UV/O<sub>3</sub>, UV/O<sub>3</sub>/PS processes after 1 h of treatment were 85.33%, 89.89%, and 90.33%, respectively (**Fig. 3.9**), indicating that these three AOPs had very positive effects on crude oil mineralization. Similar results were obtained for heavy crude oil degradation. After 1 h of treatment, the TOC removal efficiencies of heavy crude oil in O<sub>3</sub>, UV/O<sub>3</sub>, and UV/O<sub>3</sub>/PS processes were 89.56%, 91.58%, and 92.40%, respectively. The TOC analysis showed that these three processes had no significant difference in the mineralization of crude oil after one hour of treatment. This result was consistent with both *n*-alkanes and PAHs degradation, which showed no significant difference in degradation after 1 h treatment under these three processes.

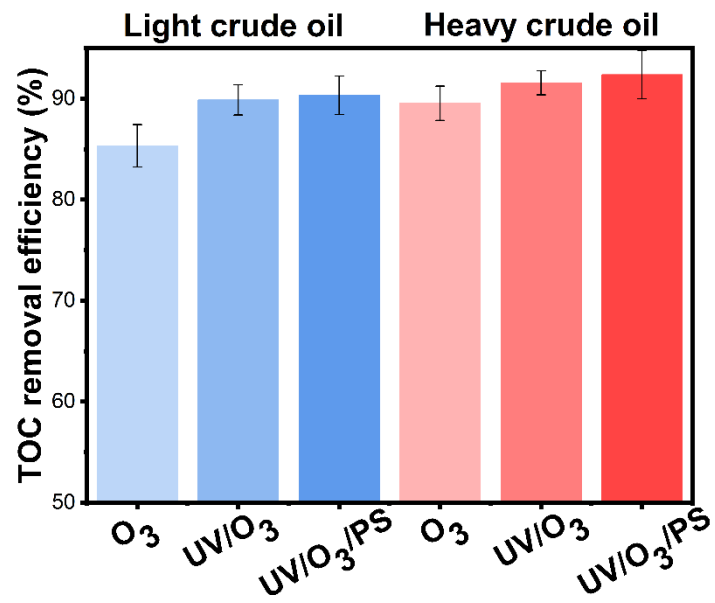


**Figure 3.9** TOC removal efficiency after 1 h treatment of three processes in both light and heavy crude oils

Overall, in the first 30 min of the reaction, the three AOPs showed significant differences in crude oil degradation. The UV/O<sub>3</sub>/PS process showed superior degradation performance regardless of total crude oil content, *n*-alkanes, or PAHs. When the reaction was run for 60 min, the effects of the three processes on the two crude oils were not significantly different. For AOPs technique, the high process efficiency and short processing time can reduce electrical cost and energy consumption. Therefore, the addition of persulfate to UV/O<sub>3</sub> process may be a promising hybrid AOP system for marine oily wastewater treatment.

#### ***3.3.1.5 Mechanisms and cost analysis of UV/O<sub>3</sub>/PS process***

The degradation performance of light crude oil obtained via the 5 oxidation processes (PS, UV, O<sub>3</sub>, UV/O<sub>3</sub>, and UV/O<sub>3</sub>/PS) within 30 min was further investigated. The pseudo-first-order kinetic behaviors of the above processes were displayed in **Fig. 3.10a**. The rate constants of different processes showed that the combined process could enhance the removal performance in comparison with a single process (**Fig. 3.10b**). The degree of synergy between PS, UV, and O<sub>3</sub> was calculated from the rate constants according to Eq. 1. The rate constant of UV/O<sub>3</sub>/PS process was 0.0698 min<sup>-1</sup>, a value much higher than the sum of the rate constants achieved by the independent PS (0.0005 min<sup>-1</sup>), UV (0.0072 min<sup>-1</sup>), and O<sub>3</sub> (0.0317 min<sup>-1</sup>) processes. The calculated degree of synergy value (%S) for the UV/O<sub>3</sub>/PS process was 43.6%, reflecting the great synergistic effect of the combined process. The main reaction equations in UV/O<sub>3</sub>/PS process were provided below (Eqs. 2-8).

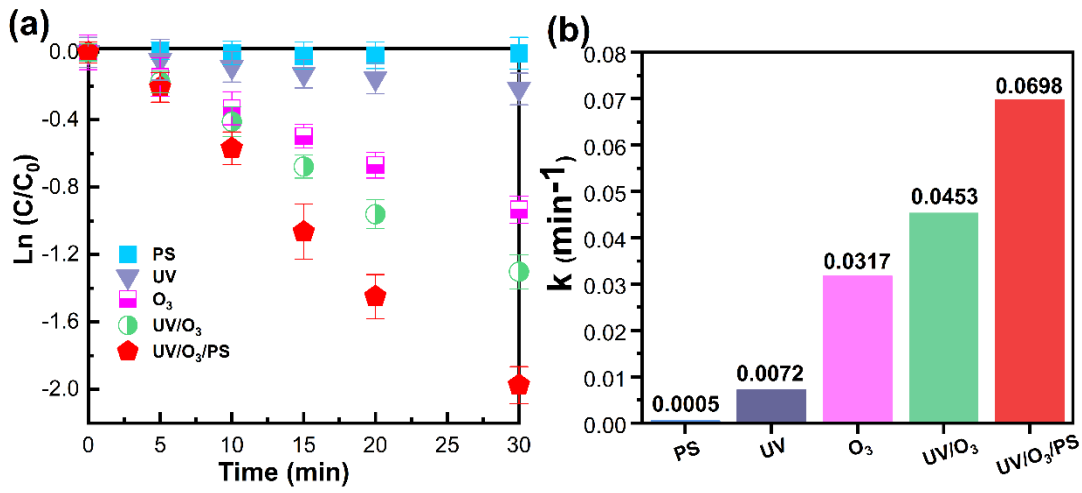
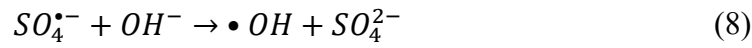
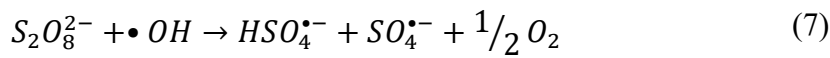
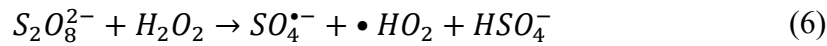
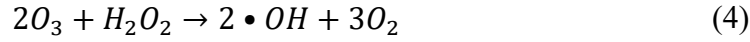


**Figure 3.10** Performance of different processes (PS, UV,  $O_3$ ,  $UV/O_3$ , and  $UV/O_3/PS$ ) for crude oil degradation

$$\%S = \frac{k_{UV/O_3/PS} - (k_{PS} + k_{UV} + k_{O_3})}{k_{UV/O_3/PS}} \times 100 \quad (1)$$



It was reported that the activation of persulfate resulted in high reactive sulfate radicals, leading to enhanced interactions with organics via hydrogen abstraction, addition on double bond, and electron transfer (Dong et al., 2021; Neta et al., 1977). In UV/O<sub>3</sub> involved system, ozonation could proceed via two routes: direct molecular ozone reactions and indirect ozone decomposition to generate hydroxyl radicals (Izadifard et al., 2017). Direct ozonation was the predominant process for the oxidation of some oil compounds (*e.g.*, *n*-alkanes and PAHs) (Ji et al., 2018). Based on the literature and the results obtained from the effects of pH values on crude oil degradation (**Fig. 3.4e**), molecular ozone, sulfate radicals, and hydroxyl radicals were the dominant reactive species at pH < 7 in UV/O<sub>3</sub>/PS process (Izadifard et al., 2017). The sulfate radicals react with OH<sup>-1</sup> forming hydroxyl radicals which were the primary reactive species under basic conditions (Eq. 8).

We estimated the operating costs of the O<sub>3</sub>, UV/O<sub>3</sub>, and UV/O<sub>3</sub>/PS processes based on the experiments carried out in the bench-scale reactor (1 L). The costs included the energy

consumption of UV irradiation and ozone generation and usage of oxidants (oxygen and sodium persulfate). The calculations revealed the costs of around US \$ 34, 25, and 16 to achieve 90% removal of total oil concentration per cubic meter of water by using O<sub>3</sub>, UV/O<sub>3</sub>, and UV/O<sub>3</sub>/ PS processes, respectively. This indicated that the UV/O<sub>3</sub>/PS was the most economical option.

### **3.3.2 Acute toxicity assessment of both initial and treated water**

Since the marine oily wastewater treated by AOP technology would eventually be discharged back into the ocean, it was necessary to pay attention to its acute toxicity to bacteria and aquatic species in the sea. In this section, we chose the luminescent bacteria (*Vibrio fischeri*) and brine shrimp (*Artemia franciscana*) as targets to evaluate the toxicity of marine oily wastewater before and after treatment. All the treated water samples were bubbled using nitrogen for 15 min to remove residual O<sub>3</sub> from the water.

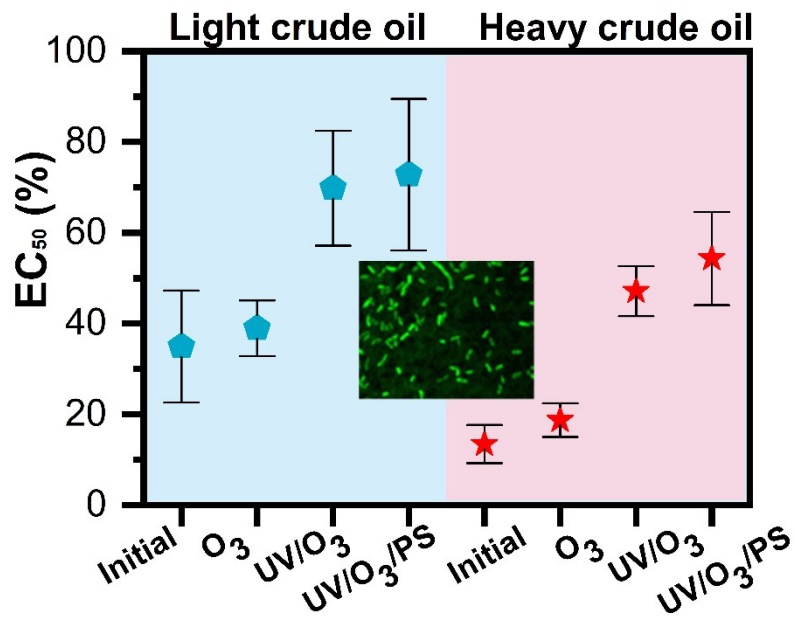


**Figure 3.11** Acute toxicity to *Vibrio fisheri* of oil compounds before and after 1 h three O<sub>3</sub>-based processes treatments of both light and heavy crude oils

### 3.3.2.1 Acute toxicity of marine oily wastewater to *Vibrio fischeri*

The acute toxicity of solution with light and heavy crude oils before and after three treatments was monitored by Microtox®, and the results were shown in **Fig. 3.11**. The control solutions, *i.e.*, seawater and seawater with PS addition, have been shown to be non-toxic to *Vibrio fischeri*. For light crude oil, the EC<sub>50</sub> increased slightly from the initial value of 34.91% to 38.94% after O<sub>3</sub> process treatment. The EC<sub>50</sub> value increased around 2-fold in both UV/O<sub>3</sub> and UV/O<sub>3</sub>/PS process, indicating that the enhanced oxidation processes could reduce the toxicity of treated water. Similar trend was found for the heavy crude oil. The initial EC<sub>50</sub> value of heavy crude oil was 13.44%, which was much lower than that of light crude oil, indicating the higher toxicity of heavy crude oil. That could be due to the presence of more diverse PAHs in heavy crude oil and its higher sulfur content, as shown in **Fig. 3.8** and **Table 3.1**. After O<sub>3</sub> treatment, the EC<sub>50</sub> value of heavy crude oil increased to 18.71%, showing a slight toxicity reduction. The UV/O<sub>3</sub> process could increase the EC<sub>50</sub> value to 47.16%. The EC<sub>50</sub> value of UV/O<sub>3</sub>/PS process treated sample increased as much as 4-fold from 13.44% to 54.31%. This indicated that the combined UV, O<sub>3</sub> and PS process could effectively remove toxicity products from water. To verify and compare the differences in the toxicity of wastewater to bacteria and aquatic species, we further studied its effect on brine shrimp.

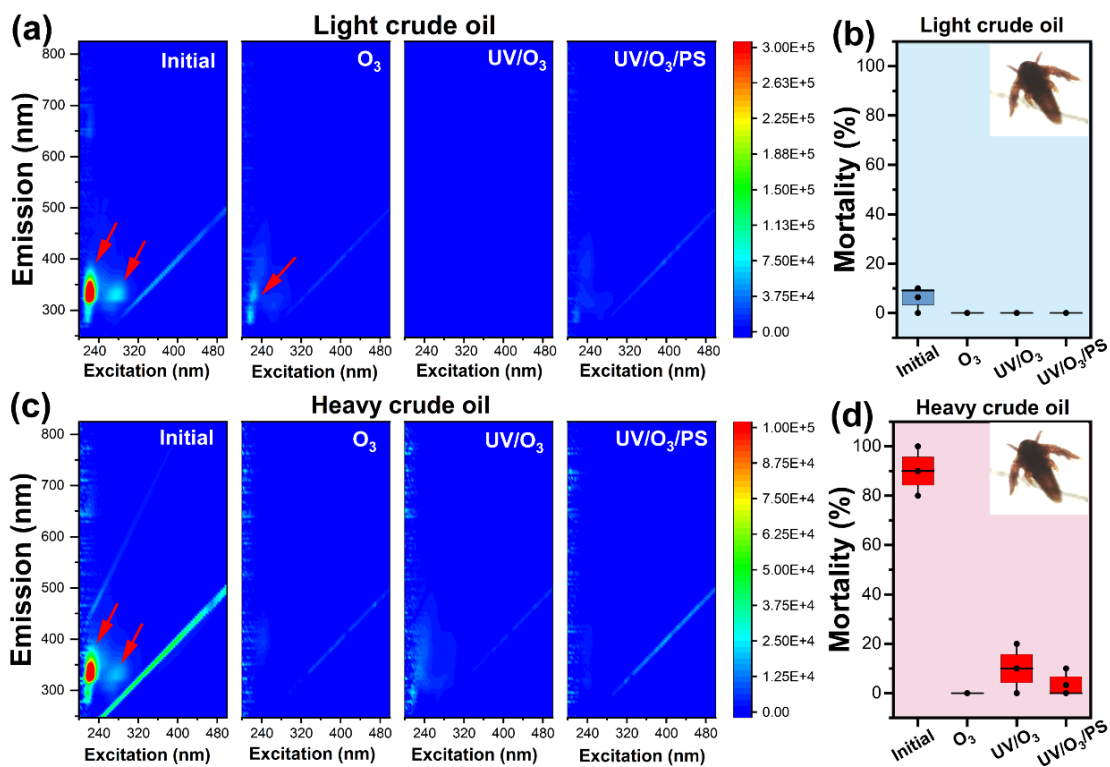


**Figure 3.12** Contour maps of 3-D EEM fluorescence spectra of light and heavy crude oils and the mortality of *Artemia* before and after  $O_3$ -based wastewater treatments. (a) Emission of untreated light crude oil and after  $O_3$ , UV/ $O_3$ , and UV/ $O_3$ /PS processes; (b) Mortality of *Artemia* exposed to light crude oil; (c) Emission of untreated heavy crude oil and after  $O_3$ , UV/ $O_3$ , and UV/ $O_3$ /PS processes; (d) Mortality of *Artemia* to heavy crude oil.

### 3.3.2.2 *Acute toxicity of marine oily wastewater to Artemia franciscana*

Three-dimensional fluorescence emission excitation spectra (EEMs) of both light and heavy crude oils before and after 1 h of treatment showed distinct fluorescence characteristics (**Fig. 3.12a** and **c**). The fluorescence intensity of light crude oil was around 3 times stronger than that of heavy crude oil. This observation was similar to that from UV–Vis spectrophotometry (**Fig. 3.2**). Light crude oil had its maximum fluorescence intensity centered on Ex/Em 224/340 nm (**Fig. 3.12a**). Another fluorescence component of the crude oil had an emission maximum located at 320 nm over the excitation wavelength range of 260–280 nm, which coincided with the fluorescence peak identified for other crude oils by previous reports (Bugden et al., 2008; Zhou et al., 2013). The oblique lines may be due to scattering effects (Ludmerczki et al., 2019; Yin et al., 2020). This weak fluorescence component at an emission wavelength of 320 nm showed no signal after three O<sub>3</sub>-based processes treatment, demonstrating that the emission was strongly quenched, and the oil was degraded. A significant decrease of the maximum fluorescence intensity peak at Ex/Em 224/340 nm occurred after 1 h O<sub>3</sub> treatment, indicating that most of the oil was degraded. Further weakened and even disappeared fluorescence emission was observed in UV/O<sub>3</sub> and UV/O<sub>3</sub>/PS processes, respectively, showing enhanced degradation performance. For heavy crude oil, the main fluorescence intensities were also observed on Ex/Em 224/340 nm and Ex 260–280/Em 310–330 nm (**Fig. 3.12c**). Interestingly, only extremely weak fluorescence intensity could be observed in UV/O<sub>3</sub> treated sample. Almost no peak signal could be found in O<sub>3</sub> and UV/O<sub>3</sub>/PS processes.

The mortality rate of *Artemia* to both initial crude oil emulsions and the treated water was evaluated to further explore the feasibility of three O<sub>3</sub>-based processes (**Figs. 3.12b and d**). The control samples, *i.e.*, seawater and seawater with PS addition, showed no obvious intensity signal on EEMs and zero mortality to *Artemia*. The 48 h mortality rate of untreated light crude oil to *Artemia* was between 0 and 10%, showing that it was less toxic (**Fig. 3.12c**). The mortality rate of 0 was observed in three O<sub>3</sub>-based AOPs. This indicated that the light crude oil treated with the three O<sub>3</sub>-based processes was not toxic to *Artemia*. The mortality of *Artemia* exposed to untreated heavy crude oil was considerably higher (80–100%) than that in initial light crude oil (0–10%) (**Fig. 3.12d**). This result is aligned with the results of the Microtox analysis, which also had high toxicity in untreated heavy crude oil. The *Artemia* mortalities were 0, 0-20%, and 0-10% after 1 h of O<sub>3</sub>, UV/O<sub>3</sub>, and UV/O<sub>3</sub>/PS treatments, respectively (Fig. 7d). The increased toxicity of heavy crude oil in UV/O<sub>3</sub> process may be related to a greater variety of PAHs compared to light crude oil. Some previous studies reported that some PAHs were more likely oxidized to form oxygenated PAHs (oxy-PAHs), which were sometimes more toxic than their parent compounds (Lundstedt et al., 2007). PS addition reduced the mortality from 0-20% to 0-10% in comparison with the UV/O<sub>3</sub> process. That could be due to further oxidation results in ring cleavage and the release of ketones, aldehydes, and carboxylic acids, which were more biodegradable than aromatics as reported by our previous work (Liu et al., 2022a; Liu et al., 2021a). Further studies on the relationship between toxicity and byproducts were needed and would help better elucidate this point.

### **3.3.3 Fate of oil flocs after O<sub>3</sub>-based AOPs**

Oil flocs were produced and found floating on the water surface during gas-related treatment processes, such as gas floatation and ozonation (Khalifa et al., 2021; Saththasivam et al., 2016). Actually, the generated oil flocs could affect the penetration of light and increase the burden of the cleaning work of the device. However, few studies investigated the floating flocs that form during O<sub>3</sub>-based treatment. It was necessary to conduct a detailed study of flocs characteristics and fate after the reaction in order to subsequently optimize the O<sub>3</sub>-based marine oily wastewater treatment technology. This section further provides an in-depth understanding of the marine oily wastewater treatment process by analyzing the dried flocs from the morphology (optical microscope and SEM) and surface functional group (FTIR) perspectives.

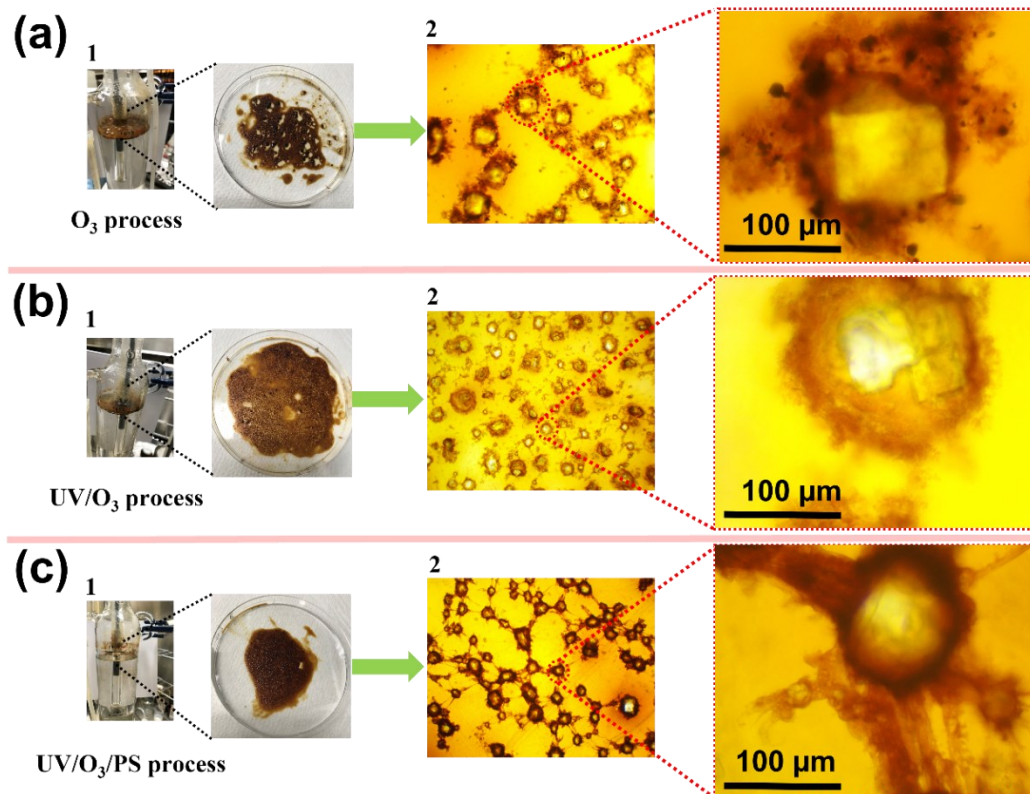


**Figure 3.13** Optical microscope analysis of flocs under (a)  $O_3$ , (b) UV/ $O_3$ , and (c) UV/ $O_3$ /PS processes in light crude oil

### ***3.3.3.1 Optical microscope analysis of flocs***

The morphology of oil flocs in light crude oil were observed under an optical microscope, as displayed in **Fig. 3.13**. The dried flocs were centered on sea salt under different processes. With the enhancement of the treatment processes from O<sub>3</sub>, UV/O<sub>3</sub> to UV/O<sub>3</sub>/PS, the volume of flocs decreased visually (**Figs. 3.13a1, b1, and c1**). The morphology of sea salt particles and adhered surface flocs was quite different in these three processes. It was observed that the flocs produced by the O<sub>3</sub> process had a very rough surface (**Fig. 3.13a2**). The clear shape of salt crystal indicated a lack of amphiphilic groups between salt and flocs. There were some darker droplets around the salt surface that could need to be further degraded. During the UV/O<sub>3</sub> process, the morphology of flocs in the plate was a little sticky (**Fig. 3.13b**). Under the optical microscope, the flocs were tidy and loosely adhered to the salt surface, which indicated that the flocs were further degraded with the presence of UV light (**Fig. 3.13b2**). During the UV/O<sub>3</sub>/PS process, the volume of the flocs was significantly reduced than that of the other two processes (**Fig. 3.13c1**). Moreover, the flocs produced by this process were very viscous and there were bonds between the salt particles (**Fig. 3.13c2**). This indicated that the flocs were gradually decomposed in order to enhance the treatment processes. The optical microscopy analysis for heavy crude oil was also observed and displayed in **Fig. 14**. In comparison with light crude oil, the flocs in heavy crude oil were darker and stickier. And the irregular shape of sea salt particles was found in each process. To understand their surface characteristics, SEM was applied to further examine the flocs in two crude oils and three processes.

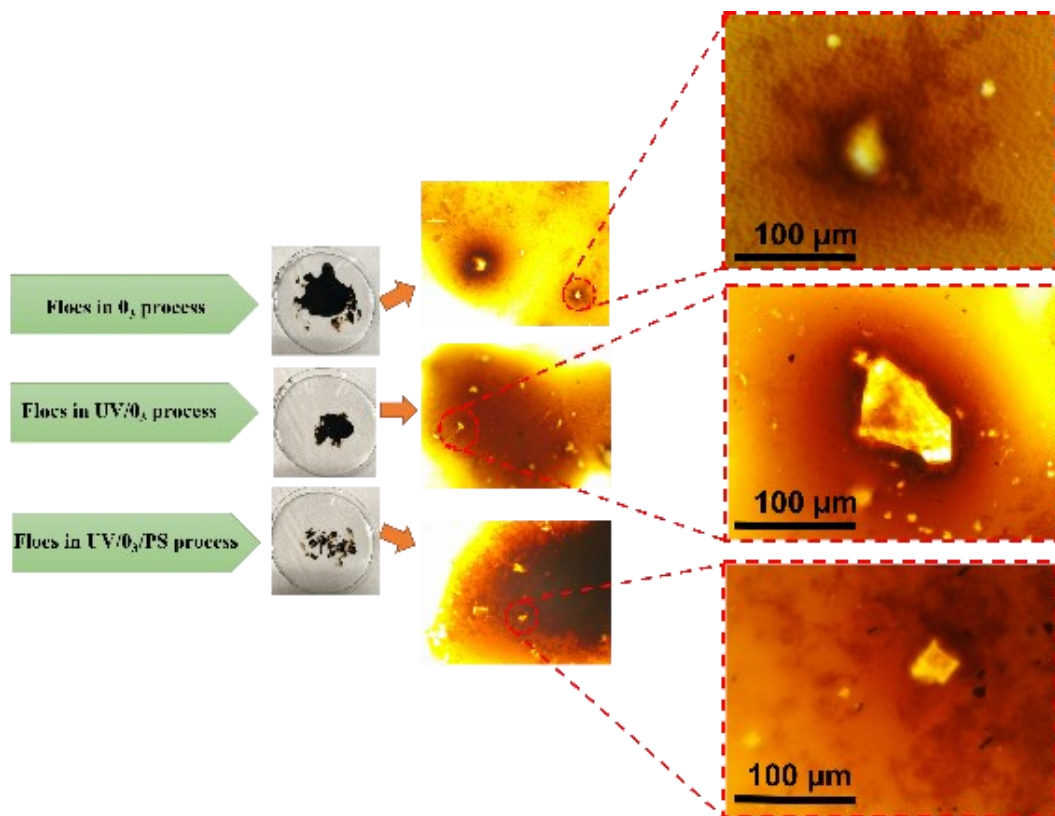


**Figure 3.14** The optical microscope analysis of the dried flocs in heavy crude oil

### 3.3.3.2 SEM analysis of flocs

The morphology and EDS analysis of both untreated crude oils and flocs generated in three O<sub>3</sub>-based oxidation processes were studied and displayed in **Fig. 3.15**. All samples were coated with gold before SEM analysis. **Fig. 3.15a** presented the morphology and elemental analysis of untreated light crude oil. The surface of untreated light crude oil was smooth, and its main component (96.82%) was carbon. After 1h O<sub>3</sub> process treatment, flocs with wrinkles were generated, and some crystalline salts could be seen on the surface (**Fig. 3.15b**). The carbon content was reduced from 96.82 to 71.82% after the reaction, indicating that the degradation of organics occurred in oil flocs surface. When UV light was added in O<sub>3</sub> process (**Fig. 3.15c**), more sea salts were found on the flocs surface. The carbon contents were decreased to 58.19% and some oxygen was introduced. In the UV/O<sub>3</sub>/PS process, the floc surfaces became rough, and more salts embedded into the flocs, showing further oxidation (**Fig. 9d**). The reduced carbon and increased NaCl contents confirmed these results. Similar behavior was found in heavy crude oils. The surface of initial heavy crude oil was somewhat rough compared to light crude oil (**Fig. 3.15e**). Compared with light crude oil, the heavy crude oil had high sulfur content (7.28% versus 2.33% in light crude oil), consistent with the information given in **Table 1**. After O<sub>3</sub> and UV/O<sub>3</sub> treatment, the flocs clustered together with some salt particles appearing on the surface (**Fig. 3.15f and g**). It would be worth noting that, after UV/O<sub>3</sub>/PS treatment, the flocs became coarser and their surface sea salt content was high, showing further oxidation (**Fig. 3.15h**). The EDS results showed that the contents of O, Na, and Cl increased with the enhancement of the treatment process. The above results concluded that with the strengthening

of the oxidation process, the carbon content in the flocs gradually decreased, and the oxygen content gradually increased. The addition of persulfate accelerated the degradation of the flocs.

### 3.3.3.3 FTIR analysis of flocs formed in O<sub>3</sub>-based processes

FTIR analysis was performed to observe the changes in the functional groups of initial crude oils and flocs after three O<sub>3</sub>-based processes (**Fig. 3.16**). In light crude oil, the large wavenumber bands found at about 2953, 2921 and 2852 cm<sup>-1</sup> were associated with C-H stretching vibration, specifically C-H in-phase stretch in CH<sub>2</sub>, and C-H out-of-phase stretch in CH<sub>2</sub> (Akmaz et al., 2011) (**Fig. 3.16a**). The broad peak between 3100-3600 cm<sup>-1</sup> represented the hydroxyl groups (O-H) that could be related to hydrogen bonds (Dong et al., 2018). There were no notable O-H functional groups in the FTIR of the initial light crude oil. However, the peak area at 3100-3600 cm<sup>-1</sup> increased significantly with the enhancement of the oxidation processes. The peak at around 1706 cm<sup>-1</sup> contributed to the C=O vibration stretching in the ketones and/or carboxylic acids. It had been reported that ozone could oxidize alkanes, cleaving carbon-carbon double bonds to give ketones or carboxylic acids (Soriano Jr et al., 2003). With the duration of ozone and further enhancement of oxidation processes by the addition of UV light and persulfate, the C=O stretching peak area became larger, suggesting an increased concentration of new carbonyl compounds. The production of more oxygen-containing functional groups indicated that the flocs were gradually oxidized, and this phenomenon was more pronounced with the addition of persulfate.

In heavy crudes, the same oxygen-containing groups (*i.e.*, O-H and C=O) and enhanced

peak intensities were observed with the enhancement of the treatment processes (from O<sub>3</sub> and UV/O<sub>3</sub> to UV/O<sub>3</sub>/PS processes) (**Fig. 3.16b**). Besides, unlike light crudes, heavy crude oil featured some low-wavenumber functional groups. For example, the asymmetric stretching of C-O-C in ethers give rise to bands in the region between 1300 and 1200 cm<sup>-1</sup>, and the C-H out-of-plane bending (wagging) vibration of aromatic rings was the main contributor in the region between 900 and 700 cm<sup>-1</sup> (Asemani & Rabbani, 2020). It had been reported by previous researchers that these two bands belonged to the asphaltenes and resins (Akmaz et al., 2011; Asemani & Rabbani, 2020). These two bands were absent in light crude oil, probably because of its low asphaltene and resin content. After the three oxidation processes, the peak area of these two bands gradually decreased, showing that the asphaltene and resin contents in flocs were decreased.

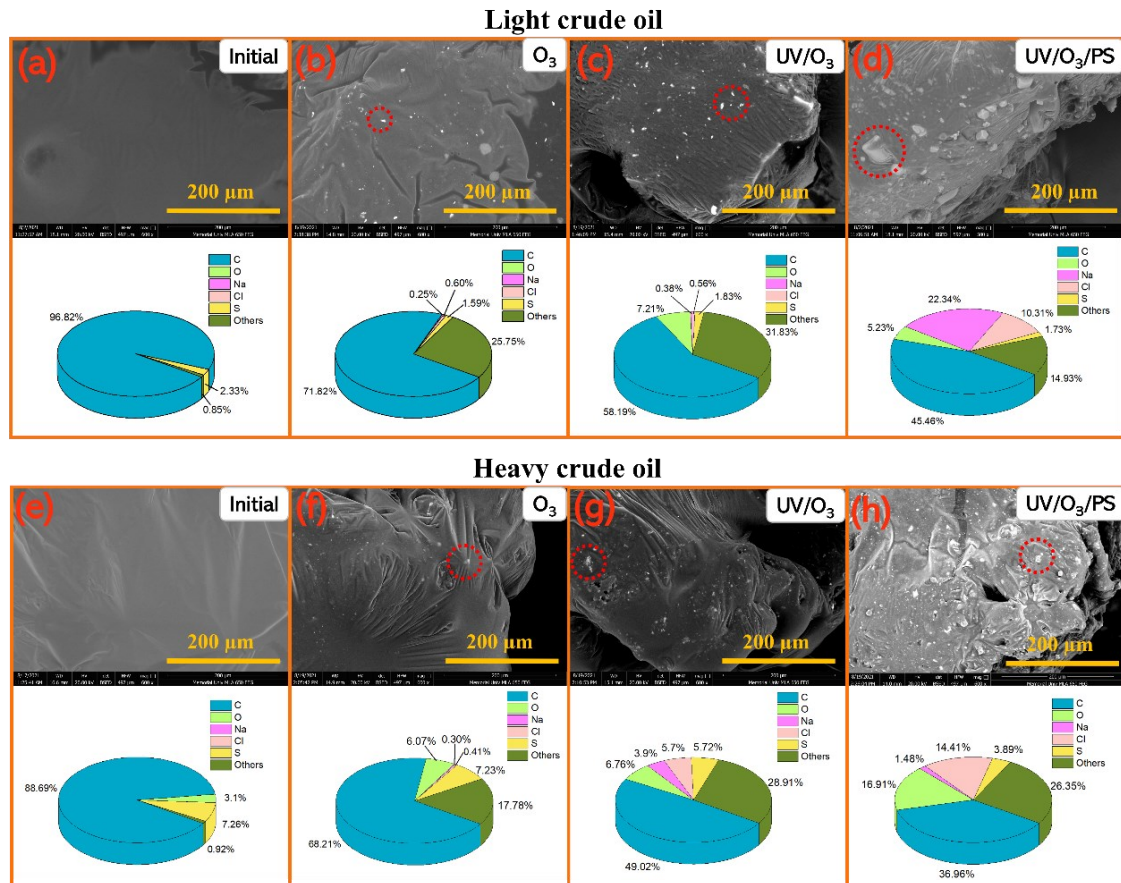


**Figure 3.15** SEM images and EDS of oil flocs before and after treatment for light crude oil:

(a) initial, (b) O<sub>3</sub> process, (c) UV/O<sub>3</sub> process, (d) UV/O<sub>3</sub>/PS process and heavy crude oil: (e)

initial, (f) O<sub>3</sub> process, (g) UV/O<sub>3</sub> process, (h) UV/O<sub>3</sub>/PS process

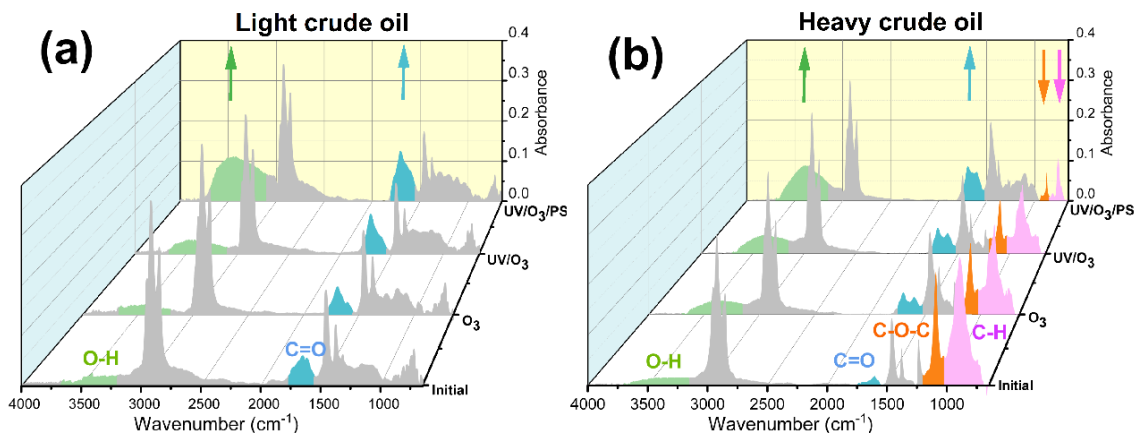


**Figure 3.16** FTIR characteristic of flocs which generated in (a) light and (b) heavy crude oils before and after three O<sub>3</sub>-based processes treatment.

### 3.4. Summary

Marine industries (transportation, petroleum and energy, fishing and aquaculture, ports, etc.) generate a tremendous quantity of wastewater (*e.g.*, offshore produced water, bilge water, ballast water, and decanted water) which contains complex organic contaminants especially including toxic and recalcitrant hydrocarbons, leading to significant challenges on marine wastewater treatment (usually requires high efficiency, mobile and small footprint) and sustainable development. Ozonation-based AOP is one of the highly effective solutions to achieve a rapid and feasible on-site treatment method for marine oily wastewater to meet the more stringent standards.

Our study thoroughly compared the degradation performance, toxicity assessment, and floc formation of three ozone-based processes (*i.e.*, O<sub>3</sub> only, UV/O<sub>3</sub>, and UV/O<sub>3</sub>/PS) for light and heavy crude oils. The results showed that, in comparison with O<sub>3</sub> and UV/O<sub>3</sub> processes, the addition of PS could significantly shorten the treatment time of marine oily wastewater to 30 min, which would potentially reduce the energy consumption. This provided the scientific evidence for the value of addition of PS in O<sub>3</sub>-based AOP, gained the in-depth understanding of the mechanisms, and recommended the optimal operational conditions for scale-up to an operational system of marine oily wastewater treatment. Two types of marine species (bacteria and crustacean species) were chosen to systematically evaluate the toxicity of marine oily wastewater. The acute toxicity to *Vibrio fischeri* was significantly reduced in UV/O<sub>3</sub> and UV/O<sub>3</sub>/PS processes than in O<sub>3</sub> process. The mortality of *Artemia* from marine oily wastewater was significantly reduced in all three processes, confirming the significance of the treatment

processes on reducing the negative ecological impacts of oily wastewater. The flocs are a tough nut but receive limited investigations. It was found that the flocs generated by different O<sub>3</sub>-based processes have different fates. Morphology and surface functional groups analysis confirmed that the flocs issue could be alleviated by the enhanced oxidation process and extended reaction time, especially in the UV/O<sub>3</sub>/PS process. Therefore, the results in this paper demonstrated a more energy-effective and low environmental impact approach to treating marine oily wastewater by O<sub>3</sub>-based processes.

Overall, this study added new scientific knowledge to improve the understanding of oxidation mechanisms of heavy and light crude oil in seawater and support the practical operations and policy making as well as sustainable development of marine industry. The UV/O<sub>3</sub>/PS process was further approved to be a promising option for marine oily wastewater treatment in a more cost-efficient way with potential of applications in the other relevant areas. Meanwhile, future efforts are still needed to address some limitations in the current study. For example, more in-depth mechanistic analysis (*e.g.*, generation of free radicals and fate and impact of byproducts) can help gain comprehensive understanding and optimize the system design and operation; toxicity to different species, the chronic toxicity assessment of many marine organisms (*e.g.*, microbes, crustaceans, vertebrates) scaling up and field demonstration are desired for further performance evaluation and improvement under operational conditions for large-scale implementation.

# CHAPTER 4

## UV STIMULATED MANGANESE DIOXIDE FOR THE PERSULFATE CATALYTIC DEGRADATION OF BISPHENOL A

---

This chapter has been published in the Journal “*Catalysts*”.

**Dong, G.**, \*Chen, B., Liu, B., \*Stoyanov, S. R., Cao, Y., Yang, M., & Zhang, B. (2021). UV Stimulated Manganese Dioxide for the Persulfate Catalytic Degradation of Bisphenol A. *Catalysts*, 11(4), 502. <https://doi.org/10.3390/catal11040502>

**Authorship contribution statement:**

**Guihua Dong:** *Conceptualization, Methodology, Resources, Visualization, Writing – original draft.* **Bing Chen:** *Methodology, Supervision, Writing – review & editing.* **Bo Liu:** *Conceptualization, Methodology, Writing – original draft.* **Yiqi Cao:** *Writing – original draft.* **Stanislav R Stoyanov:** *Supervision, Writing – review & editing.* **Min Yang:** *Writing – original draft.* **Baiyu Zhang:** *Supervision, Writing – review & editing.*

## 4.1. Introduction

Bisphenol A (BPA) is a high-production-volume industrial chemical used as a precursor in synthetic polycarbonate plastics and epoxy resins, as well as many consumer products, including food containers, paper products, toys, medical equipment, and electronics (Ouada et al., 2018). Growing evidence has shown the long-term negative effects of BPA on aquatic life and human health (Xiao et al., 2020). Several studies have reported on the potential adverse effects of BPA exposure to humans during critical stages of neonatal or early development (Fisher et al., 2020). Meanwhile, BPA was ubiquitously detected in river water and soil at microgram levels (Ana & Espino, 2020). Moreover, the highest BPA concentrations were found in landfill leachate in Japan (up to 17.2 mg/L) and Germany (4.2–25 mg/L) (Xiao et al., 2020; Yamamoto et al., 2001). Growing concerns have been raised on the associated environmental risks caused by BPA as sole and co-contaminant, leading to the urgent demands for effective remediation techniques towards contaminated waters (McBean, 2019).

AOPs based on the production of  $\bullet\text{OH}$ , which acts as a powerful oxidant, have been regarded as highly promising for the degradation of BPA (Ghernaout & Elboughdiri, 2020). Persulfate-based AOPs, have drawn considerable attention in recent years due to their high efficiency for generating  $\text{SO}_4^{\bullet-}$ , which has more positive redox potential (2.6–3.1 V) than  $\bullet\text{OH}$  (1.9–2.7 V), to degrade recalcitrant organic pollutants (Lin et al., 2019). PS is one of the main precursors for the generation of  $\text{SO}_4^{\bullet-}$  (Li et al., 2020). PS could be activated by transition metal catalysts (such as iron oxides and manganese oxides), nonmetal catalysts, UV and visible light, ultrasound, alkaline, heat, and strong oxidants to produce  $\text{SO}_4^{\bullet-}$  and other radicals for removal

of organic pollutants (Petala et al., 2020; Wang & Wang, 2018).

Synergetic PS activation was recently demonstrated with enhanced contaminants removal. Most attention has been paid to the applications of transition metals or their oxides (e.g., iron, copper, cobalt) and UV as hybrid activators for PS activation (Pan et al., 2017; Pan et al., 2019; Wang et al., 2020a). In fact,  $\text{MnO}_2$  is widely used as a catalyst or activator in various heterogeneous reaction systems due to high natural abundance, low toxicity, and low environmental impacts (Dong et al., 2018; Huang et al., 2019a; Mazloomi et al., 2016). However, to our best knowledge, synergetic use of  $\text{MnO}_2$  and UV has never been applied for PS activation. Recently, Eslami et al. (2018) confirmed that the synergetic use of  $\text{MnO}_2$  and UV is a promising hybrid activator for PMS activation. Accordingly, there are many distinctive differences during activation of PS and PMS, especially in reactivity toward radicals and responses to different pH levels (Lee et al., 2020). Furthermore, the synergistic mechanism for PS activation, especially the interactions between  $\text{MnO}_2$  and UV, remains unknown and deserves further investigations.

Therefore, in this study, we first developed an enhanced  $\text{MnO}_2$ /UV-activated PS process for efficient BPA removal and mineralization. The optimum activation performance of UV irradiation and  $\text{MnO}_2$  in various conditions was examined in detail. The mechanism of enhanced BPA degradation in the hybrid activation process was then explored using quenching studies for ROS. More importantly, the effect of UV irradiation on the  $\text{MnO}_2$  surface in this process was substantially investigated. Moreover, the complex BPA degradation mechanism was presented in terms of the predominant reaction pathways, supported by intermediates

identified using GC-MS. Finally, the acute toxicity due to the BPA removal through the MnO<sub>2</sub>/UV/PS process was evaluated.

## **4.2. Materials and Methods**

### **4.2.1 Chemicals and reagents**

BPA (2, 2-bis (4-hydroxyphenyl) propane, purity > 99%), MnO<sub>2</sub> (particle size = 10 µm), sodium persulfate (PS, purity > 99%), methanol (MeOH), tert-butyl alcohol (TBA), furfuryl alcohol (FFA), sodium acetate, acetic acid, sodium monohydrogen phosphate, disodium hydrogen phosphate, sodium carbonate, bicarbonate, toluene, and phosphoric acid were purchased from Sigma-Aldrich (Canada). *N, O*-bis(trimethylsilyl)trifluoroacetamide with trimethylchlorosilane (BSTFA+TMCS) for gas chromatography derivatization, LiChropur™, contains 1% TMCS, 99% (excluding TMCS) was purchased from Sigma-Aldrich (Canada), as well.

### **4.2.2 Degradation experiments**

All degradation experiments were conducted in 200 mL glass bottles placed on a room temperature shaker (280 r/min). A 30 mg/L sample of the BPA solution prepared with deionized water was placed in each glass bottle. PS (1 mM) and MnO<sub>2</sub> (0.25 g/L) were added into each glass bottle. A UV-254 nm (UVP 90-0012-01 Model) source (Krackeler Scientific) was used to treat the solutions. In evaluation of solution pH impacts, different buffers were adopted with sodium acetate and acetic acid for pH 3.6 and 5.0, sodium dihydrogen phosphate and disodium hydrogen phosphate for pH 6.5 and 8.0, and sodium carbonate and bicarbonate for pH 10.0.

### 4.2.3 Analysis of water samples

The water samples were collected by syringe and first filtered through 0.22  $\mu\text{m}$  membrane filters, and the BPA concentrations were analyzed using a high-performance liquid chromatography (HPLC) instrument with a C18 column (Agilent 1260 Infinity II). An acetonitrile/water (50:50, v/v) mixture was used as the mixed mobile phase at a flow rate of 1 mL/min. The detection wavelength was 276 nm. Under these conditions, the BPA peak in the chromatogram corresponds to an elution time of 6.24 min. The TOC concentrations were measured by the burning oxidation-non-dispersive infrared absorption method using a Shimadzu TOC-L analyzer (Shimadzu, Japan). Phosphoric acid was added into the samples before measuring TOC to maintain the solution pH < 1. The pH was measured using a pH meter (EL20, Mettler Toledo®). The PS concentrations were detected following a modified spectrophotometric methods (Lee et al., 2015). In detail, 0.5 M potassium iodide with bicarbonate buffer ( $\text{NaHCO}_3$ , 0.05 M) was prepared, and then 0.3 mL filtered sample was mixed with the above iodide solution (4.7 mL). Shaking well, and after 20 min reaction, the water sample was detected by spectrophotometer (UV-Vis) at  $\lambda = 352$  nm. The leached Mn concentrations in different processes were measured using an inductively coupled plasma optical emission spectrometer (ICP-OES, PerkinElmer, America).

### 4.2.4 Characterization and recovery of $\text{MnO}_2$

The surface functional groups of  $\text{MnO}_2$  before and after degradation reaction in  $\text{MnO}_2$ , UV/ $\text{MnO}_2$ ,  $\text{MnO}_2$ /PS, and  $\text{MnO}_2$ /UV/PS processes were characterized using ATR-FTIR. An

X-ray powder diffractometer (XRD, Rigaku XtaLAB Synergy-S) was applied to determine the crystallographic structure of MnO<sub>2</sub> particles before and after treatment in MnO<sub>2</sub>/UV/PS process. The surface morphology of MnO<sub>2</sub> particles before and after treatment in MnO<sub>2</sub>/UV/PS process was measured by the s SEM ( Quanta 400 MLA) equipped with EDS. MnO<sub>2</sub> particles were recovered and dried in a vacuum oven (Fisherbrand Isotemp Model 281A, set at 60 °C, 12 h).

#### **4.2.5 Intermediates analysis**

To analyze the BPA degradation intermediates in the MnO<sub>2</sub>/UV/PS process, the reaction solutions (at 0, 5, 15, 30, 60, 90, and 120 min) were analyzed using Agilent 7890 GC coupled with an Agilent 5975 MS. The details of BPA extraction, derivatization, and GC-MS analysis methods were based on previous studies (Lin et al., 2009; Sharma et al., 2015). We prepared six identical mixtures, each containing: 200 mL of water containing 30 mg/L BPA, 1 mM of PS, and 0.25 g/L MnO<sub>2</sub>. Samples (30 mL) of each were taken from different flasks after 0, 5, 15, 30, 60, 90, and 120 min of UV treatment. Each sample was transferred into a separatory funnel, and 15 mL methylene chloride was immediately added to extract the BPA and its degradation intermediates. After agitation, the mixture was allowed to settle for 30 min, and the underlying organic phase was separated from the aqueous phase. A second 15 mL aliquot of methylene chloride was then used to recover any organic matter remaining in the separatory funnel. The extract was dehydrated with anhydrous sodium sulfate, filtered, and concentrated to near dryness on a vacuum rotary evaporator. The residue was redissolved in 1 mL of toluene and transferred to a 1.5 mL brown vial, from which a 100 µL aliquot was analyzed directly, and the remaining sample was derivatized before analysis. For derivatization, toluene was first

removed from the remaining sample by evaporation to dryness under a gentle nitrogen stream, then 150  $\mu\text{L}$  of BSTFA+TMCS were added to silylate the polar degradation products in the residue. The silylation reaction was conducted by heating the mixture in a water bath for 2 h at 60  $^{\circ}\text{C}$ . Toluene (350  $\mu\text{L}$ ) was added to the vial to dissolve the silylated products. Both the silylated and non-silylated aliquots were analyzed using gas chromatography. Chromatographic separation of analytes was carried out using a DB-5MS UI fused silica capillary column (30 m  $\times$  0.25 mm  $\times$  0.25  $\mu\text{m}$ ). The inlet and detector temperatures of the gas chromatograph were set to 260 and 320  $^{\circ}\text{C}$ , respectively. The oven temperature was initially set to 80  $^{\circ}\text{C}$  and held for 3 min, then increased to 300  $^{\circ}\text{C}$  at 3  $^{\circ}\text{C}/\text{min}$  and held for 30 min. Helium was used as the carrier gas at the flow rate of 1.0 mL/min. The sample (2  $\mu\text{L}$ ) was injected in the pulsed splitless mode. The temperatures of the transfer line, ion source, and mass spectrometry detector were 280, 230, and 150  $^{\circ}\text{C}$ , respectively. Qualitative analysis was performed in the electron impact mode at 70 eV using the full scan mode in the m/z range of 40–1000 (Lin et al., 2009; Sharma et al., 2015).

#### **4.2.6 Toxicity evaluation**

Acute toxicity tests of the  $\text{MnO}_2/\text{UV}/\text{PS}$ -treated samples were carried out using a Microtox<sup>®</sup> Model 500 (M500) analyzer, whose primary indicator is the luminous bacterium *Vibrio fischeri*. The acute toxicity test relies on bacterial luminescence via cellular respiration. Inhibition of cellular activity (caused by exposure to toxins, acidic or alkaline conditions, etc.) decreases the respiratory rate, leading to a corresponding decrease in luminosity. The pH range of 6.0–8.5 is recommended as standard since *V. fishery* is pH-sensitive (Johnson, 2005). The

toxicity testing of BPA and its intermediates were conducted both with and without phosphate buffer (pH = 6.5). In addition to BPA, the presence of MnO<sub>2</sub> particles, PS, etc. would affect the light-emitting bacteria, so each sample was diluted before testing. To ensure consistency, the first sample was quickly obtained in the presence of MnO<sub>2</sub> and PS. Therefore, the measured effective concentration that given half-maximal response (EC<sub>50</sub>) of the original BPA might differ from the value given in the literature (Chiang et al., 2004). The samples were diluted 4-fold before testing to concentrations that help provide a consistent instrumental response.

### **4.3. Results and Discussion**

#### **4.3.1 Degradation and mineralization of BPA**

To evaluate and compare BPA degradation and mineralization performance of the MnO<sub>2</sub>/UV/PS process with those of its component processes, seven different processes (namely PS, MnO<sub>2</sub>, UV, UV/MnO<sub>2</sub>, MnO<sub>2</sub>/PS, UV/PS, or MnO<sub>2</sub>/UV/PS) were tested (**Fig. 4.1**).

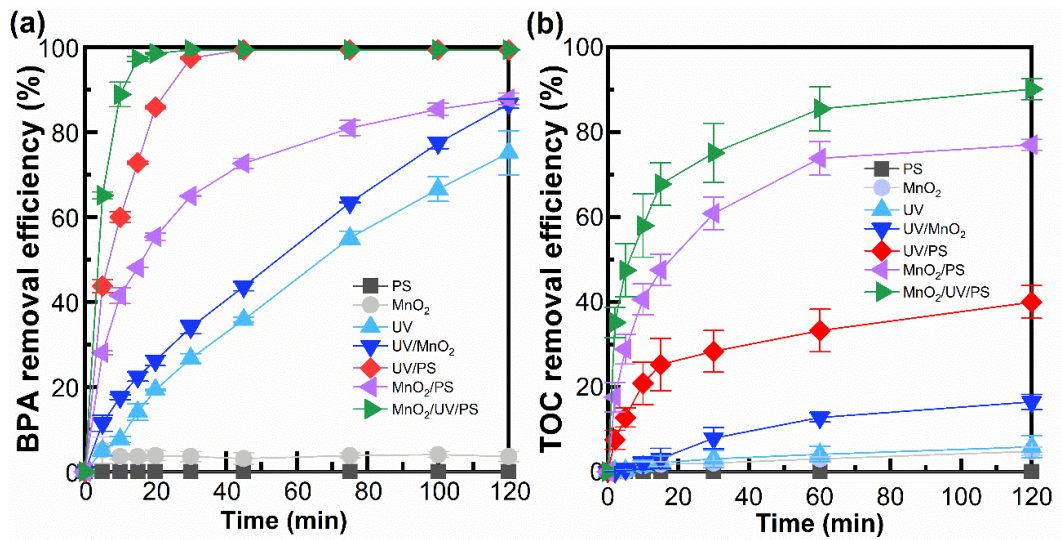


**Figure 4.1** BPA (a) and TOC (b) removal over time using the PS, MnO<sub>2</sub>, UV, UV/MnO<sub>2</sub>, MnO<sub>2</sub>/PS, UV/PS, and MnO<sub>2</sub>/UV/PS processes. Conditions at t = 0 min: [BPA] = 30 mg/L, [PS] = 1 mM, [MnO<sub>2</sub>] = 0.25 g/L, pH = 6.5, T = 22–25 °C

The PS process alone had no effect on BPA removal, while only 3.6% of BPA could be removed by the MnO<sub>2</sub> process after 2 h (**Fig. 4.1a**). Lin et al. (2009) reported the relatively high efficacy of BPA removal from a 4.4 μM solution using a high concentration of 800 μM MnO<sub>2</sub> over 10 min. The low BPA removal efficiency effected by our MnO<sub>2</sub> process might be due to its relatively low concentration of MnO<sub>2</sub> compared to BPA. The individual applications of MnO<sub>2</sub> and PS were ineffective, presumably due to slow (or no) free radical generation. Both UV and UV/MnO<sub>2</sub> processes degraded 75.0% and 85.0% of BPA in 2 h, respectively. In the MnO<sub>2</sub>/PS process, the removal efficiency of 87.8% was observed after 2 h, while the UV-activated PS process could effectively remove all BPA in 45 min. The synergetic PS activation by MnO<sub>2</sub>/UV could entirely remove BPA within 30 min. Apparently, both the UV/PS and MnO<sub>2</sub>/UV/PS processes had better performances than the MnO<sub>2</sub>/PS process, and the concurrent presence of UV and MnO<sub>2</sub> further enhanced the PS activation, and consequently, the BPA degradation.

A TOC analyzer was employed to explore the mineralization of BPA in the above-noted seven processes. **Fig. 4.1b** showed that the TOC removal efficiencies of these seven processes were quite different. The TOC removal efficiencies of the PS, MnO<sub>2</sub>, and UV processes after 2 h of treatment were 0, 4.8, and 5.8%, respectively, indicating the sole processes could barely mineralize BPA from aqueous phase. The TOC removal efficiency in the UV/MnO<sub>2</sub> process was enhanced to 16.4%, which implied the combination of UV irradiation and MnO<sub>2</sub> had a positive effect on BPA mineralization. The MnO<sub>2</sub>/PS process further increased the removal efficiency to 77.0%. Huang and Zhang (2019) suggested that MnO<sub>2</sub> activated PS could promote

the generation of radicals (such as  $\text{SO}_4^{\cdot-}$  and  $\cdot\text{OH}$ ) to remove organic pollutants. The results of UV/PS process showed that BPA could be removed entirely in 45 min, but the TOC value remained high, even after 2 h of treatment (40.0% of the mineralization rate). By comparing with the  $\text{MnO}_2/\text{PS}$  process, the UV-activated PS process exhibited improved performance for BPA removal but was less effective for BPA mineralization. Remarkably, the  $\text{MnO}_2/\text{UV}/\text{PS}$  process could achieve more than 90.0% of TOC removal efficiency in 2 h, demonstrated that PS activation by the combination of UV and  $\text{MnO}_2$  could effectively improve the TOC removal from water. PS residuals in the  $\text{MnO}_2/\text{PS}$ , UV/PS, and  $\text{MnO}_2/\text{UV}/\text{PS}$  processes (**Fig. 4.2**) suggested the UV irradiation was the main factor on the acceleration of PS decomposition. The synergetic effect of UV and  $\text{MnO}_2$  could also be observed. The high PS consumption but the low TOC removal rate in the UV/PS process may be because the process can convert BPA and cannot fully mineralize it.

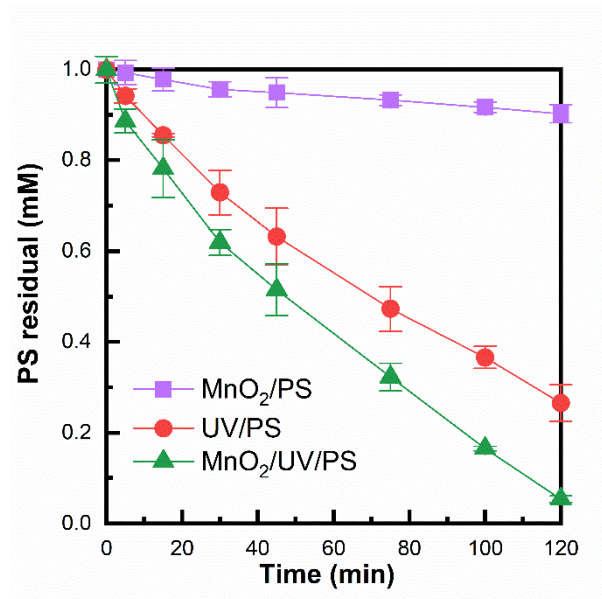


**Figure 4.2** PS residual in MnO<sub>2</sub>/PS, UV/PS, and MnO<sub>2</sub>/UV/PS processes

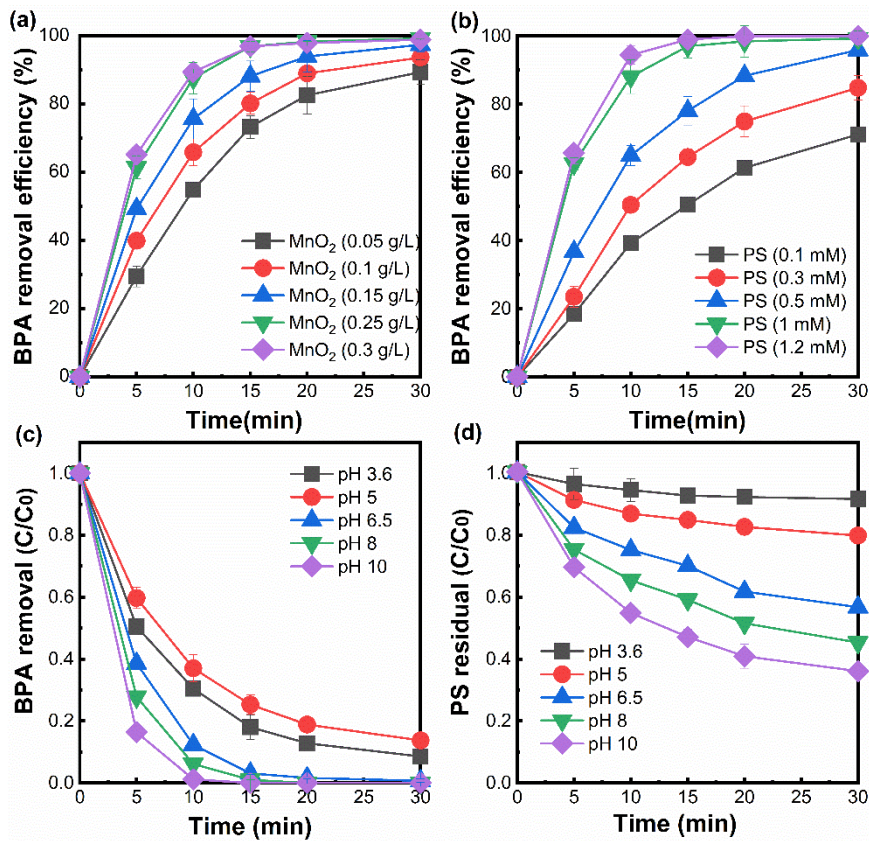


**Figure 4.3** Effects of (a)  $MnO_2$  dosages, (b) PS concentration, and (c) pH level on BPA removal, and PS residual in different pH levels (d). Conditions at  $t = 0$  min:  $[BPA] = 30$  mg/L, pH in (a) and (b) = 6.5,  $[PS]$  in (a) and (c) = 1 mM,  $[MnO_2]$  in (b) and (c) = 0.25 g/L.

### 4.3.2 Effects of parameters on BPA degradation

We further evaluated the effects of the MnO<sub>2</sub> dosages, PS concentrations, and pH levels on BPA degradation using the MnO<sub>2</sub>/UV/PS process within 30 min. **Fig. 4.3a** showed that the extent of BPA degradation gradually promoted with the increased MnO<sub>2</sub> dosages (0.05–0.30 g/L) due to more surface sites for PS activation. Complete BPA degradation was observed with a MnO<sub>2</sub> dosage of 0.25 g/L, while further increasing dosages had a slight improvement. The effects of PS concentrations were then evaluated under the conditions of 0.25 g/L MnO<sub>2</sub> and UV irradiation (**Fig. 4.3b**). Compared with the effect of MnO<sub>2</sub>, increasing PS concentration enhanced BPA degradation to a greater extent, leading to a complete BPA removal at 1 mM PS. The further increase of PS dosages only promoted the removal rate slightly, indicating that the concentration of 1 mM was sufficient for BPA degradation. Therefore, 0.25 g/L MnO<sub>2</sub> and 1 mM PS were optimized for the efficient degradation of BPA in our study.

As can be seen, BPA could be effectively degraded with efficiency over 80% in a wide range of pH levels (3.6 to 10.0) (**Fig. 4.3c**). The degradation rate was relatively low under acidic conditions (pH 3.6 and 5.0). That might be because Mn dissolution occurred in acidic conditions, which was relatively inactive for PS activation (Zhu et al., 2018). It was confirmed by the PS residual results (**Fig. 4.3d**), where the PS was less decomposed under acidic conditions. The lowest reaction rate occurred at pH 5.0. According to the reports by Criquet and Leitner (2009), this phenomenon was caused by the increased consumption of SO<sub>4</sub><sup>•-</sup> by acetic acid in buffer at pH 5.0 compared to other pHs. At pH 6.5, the improved BPA degradation was achieved comparing with acidic conditions. At pHs 8.0 and 10.0, a slight improvement of

BPA degradation could be the additional PS activation by alkaline conditions (Lominchar et al., 2018). Lee et al. (2020) suggested that the main oxidants may change from  $\text{SO}_4^{\cdot-}$  to  $\cdot\text{OH}$  under alkaline conditions, leading to the abatement of organics that persisted in PS activation. From **Fig. 4.3d**, the PS decomposition rate was gradually increased along with the increased pH value. Differently, the contaminant degradation was significant in acidic (pH 4.0) condition while decreased at neutral (pH 7.0) and alkaline (pH 10.0) conditions in PMS activation process (Eslami et al., 2018). The high efficiency of the  $\text{MnO}_2/\text{UV}/\text{PS}$  oxidation process in a wide range of pH levels (pH from 3.6 to 10.0) suggested its robust capacity in treating wastewater with broad pH ranges.

### 4.3.3 Kinetic evaluation and reaction mechanism analysis

#### 4.3.3.1 Synergetic effect of $\text{MnO}_2$ and UV as a hybrid activator

Batch tests of three processes ( $\text{MnO}_2/\text{PS}$ ,  $\text{UV}/\text{PS}$ , and  $\text{MnO}_2/\text{UV}/\text{PS}$ ) were implemented within 30 min to explore the synergetic effect of  $\text{MnO}_2$  and UV as the hybrid activator of PS. The pseudo-first-order kinetic behaviors of the three processes were shown in **Fig. 4.4**. The rate constants of both the  $\text{MnO}_2/\text{PS}$  process ( $k_{\text{MnO}_2/\text{PS}} = 0.0334 \text{ min}^{-1}$ ) and the  $\text{UV}/\text{PS}$  process ( $k_{\text{UV}/\text{PS}} = 0.1177 \text{ min}^{-1}$ ) were found to be lower than that of the  $\text{MnO}_2/\text{UV}/\text{PS}$  process ( $k_{\text{MnO}_2/\text{UV}/\text{PS}} = 0.2196 \text{ min}^{-1}$ ). The degree of synergy between  $\text{MnO}_2$  and UV as the hybrid activator was calculated from the rate constants according to Eq. 1 (Frontistis et al., 2012). The calculated degree of synergy value (%S) of 31.2% for the hybrid  $\text{MnO}_2/\text{UV}/\text{PS}$  process reflected the synergetic PS activation by  $\text{MnO}_2$  and UV, which accelerated BPA removal

beyond the sum of the rates achieved by the independent MnO<sub>2</sub>/PS and UV/PS processes. To explore the mechanism of the MnO<sub>2</sub>/UV/PS process, quenching experiments were conducted as discussed in the following section.

$$\%S = \frac{k_{MnO_2/UV/PS} - (k_{MnO_2/PS} + k_{UV/PS})}{k_{MnO_2/UV/PS}} \times 100 \quad (1)$$

#### 4.3.3.2 Contribution of ROS ( $\bullet OH$ , $SO_4^{\bullet -}$ , and $^1O_2$ )

To elucidate the ROS involved in the MnO<sub>2</sub>/PS, UV/PS, and MnO<sub>2</sub>/UV/PS processes for BPA degradation, quenching experiments using MeOH, TBA, and FFA were carried out. The UV/MnO<sub>2</sub> process was also tested as a control. The MeOH could rapidly react with both  $SO_4^{\bullet -}$  ( $k = 2.5 \times 10^7 \text{ M}^{-1}\text{s}^{-1}$ ) and  $\bullet OH$  ( $k = 9.7 \times 10^8 \text{ M}^{-1}\text{s}^{-1}$ ), and TBA could rapidly quench  $\bullet OH$  with a rate constant in the range of  $3.8\text{--}7.6 \times 10^8 \text{ M}^{-1}\text{s}^{-1}$  (Huang et al., 2019a). As the rate constant for TBA quenching of  $\bullet OH$  was 1,000 times higher than that with  $SO_4^{\bullet -}$ , it was frequently employed as a  $\bullet OH$  scavenger (Eslami et al., 2018). The FFA was confirmed to effectively quench  $^1O_2$  with a rate constant of  $1.2 \times 10^8 \text{ M}^{-1}\text{s}^{-1}$  (Li et al., 2019; Zhou et al., 2015). Therefore, in this study, MeOH (1 M), TBA (1 M), and FFA (5 mM) were used to distinguish between  $SO_4^{\bullet -}$ ,  $\bullet OH$ , and  $^1O_2$ , respectively. All the scavenger concentrations were excessive according to previous studies (Zhu et al., 2018). The dynamic performance of the above four BPA degradation processes was evaluated at the same conditions.

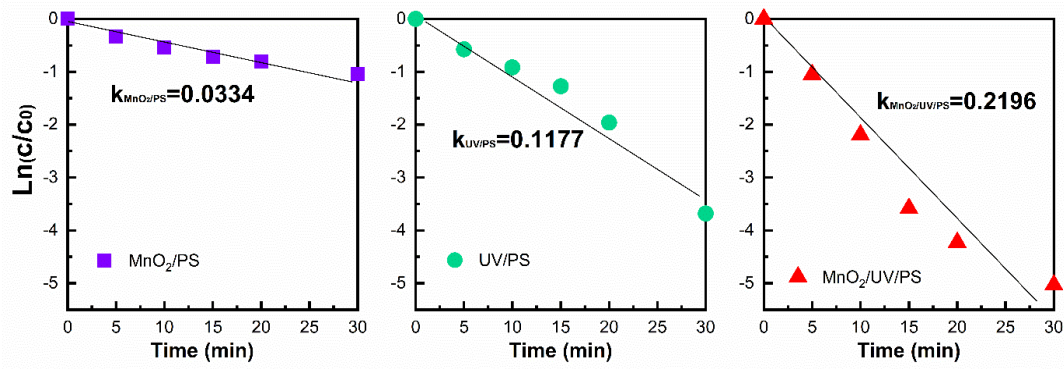
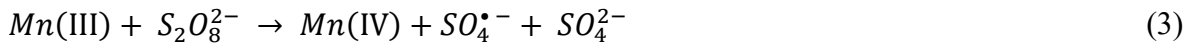


**Figure 4.4** BPA degradation using MnO<sub>2</sub>/PS, UV/PS, and MnO<sub>2</sub>/UV/PS processes over 30

min.  $k$  = rate constant of pseudo-first-order kinetics. Conditions at  $t = 0$  min: [BPA] = 30

mg/L, [PS] = 1 mM, [MnO<sub>2</sub>] = 0.25 g/L, pH = 6.5

The control test showed that only limited  $^1O_2$  and  $\bullet OH$  could be generated in the UV/MnO<sub>2</sub> process to degrade BPA (Fig. 4.5). In the MnO<sub>2</sub>/PS process (Fig. 4.6a), FFA slightly inhibited BPA degradation by decreasing BPA removal efficiency from 65.0 to 62.0%, while a 55.0% of removal rate was observed with TBA. However, MeOH showed the strongest inhibition effect by decreasing the BPA removal efficiency to 40.0%, indicating that  $SO_4^{\bullet -}$  had a significant contribution in the MnO<sub>2</sub>/PS process. Several chemical reactions generating ROS likely occurred. Initially, the  $SO_4^{\bullet -}$  species could be generated according to Eqs. 2 and 3 (Zhao et al., 2016b). Subsequently, more radicals were produced by the chain reactions initiated by  $SO_4^{\bullet -}$ , producing  $\bullet OH$  and  $^1O_2$  species (Eqs. 4–8) (Lu et al., 2017; Zhu et al., 2018). The quenching experiments proved that the ROS would attack and degrade BPA (Eq. 9).



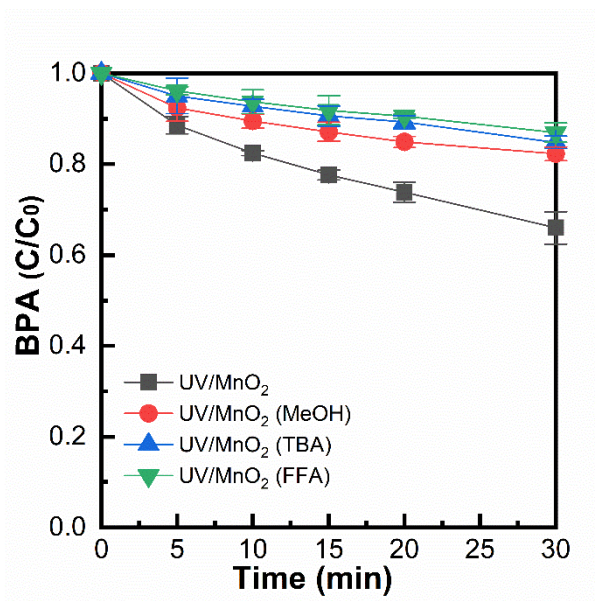


**Figure 4.5** Effects of radical inhibitors on BPA concentrations over 30 min for UV/MnO<sub>2</sub>.

Initial conditions: [BPA] = 30 mg/L, Ph = 6.5, [PS] = 1 mM, [MnO<sub>2</sub>] = 0.25 g/L. When

inhibitor is used, initial [MeOH] = 1 M or [TBA] = 1 M or [FFA] = 5 mM.

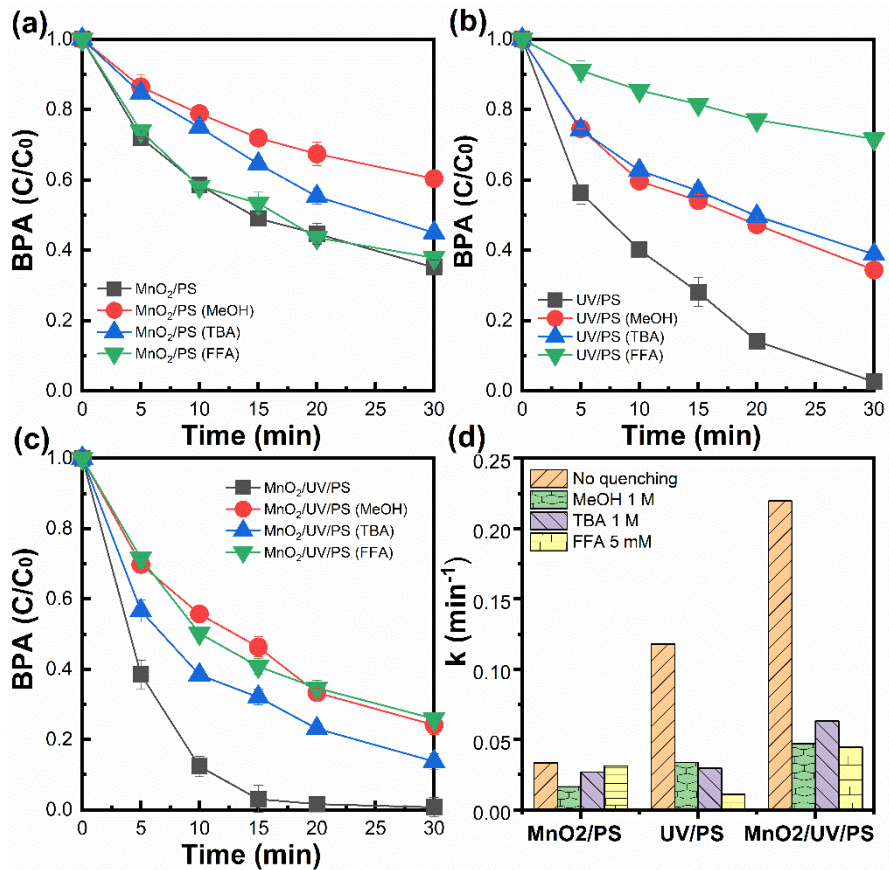
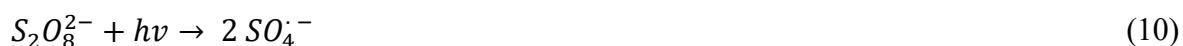


**Figure 4.6** Effects of radical inhibitors on BPA concentrations over 30 min for (a) MnO<sub>2</sub>/PS, (b) UV/PS, and (c) MnO<sub>2</sub>/UV/PS processes, and (d) effects these inhibitors on process rate constants. Initial conditions: [BPA] = 30 mg/L, pH = 6.5, [PS] = 1 mM, [MnO<sub>2</sub>] = 0.25 g/L.

When inhibitor is used, initial [MeOH] = 1 M or [TBA] = 1 M or [FFA] = 5 mM.

As shown in **Fig. 4.6b**, the removal efficiency of BPA in the UV/PS process decreased from 97.0% to 66.0%, 61.0%, and 28.0% after MeOH, TBA, and FFA were added, respectively. These results indicated that  $SO_4^{\bullet-}$ ,  $\bullet OH$ , and  $^1O_2$  were generated, and the  $^1O_2$  species played a crucial role, followed by  $SO_4^{\bullet-}$  and  $\bullet OH$ . Unlike in the  $MnO_2/PS$  process, upon irradiation with UV light, the peroxy acid O–O bond reportedly undergoes a cleavage reaction and generates two equivalents of  $SO_4^{\bullet-}$  (Eq. 10) (Liu et al., 2016). Consequently, radical conversion reactions and degradation of BPA also occurred in this process (Eqs. 4–8). Wang et al. (2016) confirmed that  $^1O_2$  was generated under UV irradiation, but that this reaction had little effect on organic species mineralization. Our study confirmed that the UV/PS process achieved a high BPA removal rate, albeit a lower TOC removal rate (**Fig. 4.1b**), in agreement with Wang et al. (2016).



The BPA removal efficiency of the  $MnO_2/UV/PS$  process decreased from 100.0% to 76.0%, 86.0%, and 74.0% in the presence of MeOH, TBA, and FFA, respectively (**Fig. 4.6c**). These findings indicated that plenty of  $SO_4^{\bullet-}$ ,  $\bullet OH$ , and  $^1O_2$  species were generated to enhance BPA decomposition (**Fig. 4.6d**). Among these ROS,  $^1O_2$  and  $SO_4^{\bullet-}$  played more critical roles than  $\bullet OH$ . All the above reactions (Eqs 2–10) could occur in the synergetic process. Given that  $^1O_2$  had little effect on the mineralization rate of organics, more robust degradation and mineralization occurred when  $SO_4^{\bullet-}$  attacked the BPA. The detailed parameters before and after quenching experiments were displayed in **Table 4.1**. To better understand the interaction between UV irradiation and  $MnO_2$ , more characterization analysis of  $MnO_2$  was discussed below.

**Table 4.1** Parameters of BPA degradation following the pseudo-first-order kinetics with and without quenching (reaction time: 30 min; D: degradation efficiency)

<b>Processes</b>	<b>Scavengers</b>	<b>k (min<sup>-1</sup>)</b>	<b>R<sup>2</sup></b>	<b>D (%)</b>
UV/MnO <sub>2</sub>	No quenching	0.0132	0.9724	34.0
	MeOH (1 M)	0.0061	0.9026	17.7
	TBA (1 M)	0.0051	0.9685	15.2
	FFA (5 mM)	0.0044	0.9732	13.1
MnO <sub>2</sub> /PS	No quenching	0.0333	0.946	64.9
	MeOH (1 M)	0.0164	0.9631	39.6
	TBA (1 M)	0.0268	0.9934	55.0
	FFA (5 mM)	0.0313	0.9321	62.2
UV/PS	No quenching	0.1178	0.9622	97.5
	MeOH (1 M)	0.0337	0.9723	65.7
	TBA (1 M)	0.0297	0.963	61.2
	FFA (5 mM)	0.0109	0.9701	28.4
MnO <sub>2</sub> /UV/PS	No quenching	0.2196	0.9471	99.3
	MeOH (1 M)	0.0469	0.9841	75.9
	TBA (1 M)	0.0631	0.9716	86.2
	FFA (5 mM)	0.0445	0.9547	74.1

#### 4.3.4 Infrared Spectra of MnO<sub>2</sub> and Mn leaching in different processes

The ATR-FTIR spectra of the MnO<sub>2</sub> particles (**Fig. 4.7a**) contained several distinct peaks that had different changes effected after 2 h of treatment in MnO<sub>2</sub>, UV/MnO<sub>2</sub>, MnO<sub>2</sub>/PS, and MnO<sub>2</sub>/UV/PS processes. The bands at around 720 and 650 cm<sup>-1</sup> were assigned to the Mn–O stretching and bending vibrations within a MnO<sub>6</sub> octahedral coordination environment (Ananth et al., 1998; Xie et al., 2016). The interactions between manganese and the constituent species were revealed in the range of 2500 to 1000 cm<sup>-1</sup> (Ananth et al., 1998). The band at around 1120 cm<sup>-1</sup> could be assigned to vibrations of Mn–OH bonds (Liu et al., 2009). A blue-shift of about 52 cm<sup>-1</sup> was observed in both UV/MnO<sub>2</sub> and MnO<sub>2</sub>/UV/PS processes, indicating UV irradiation could affect the bond between Mn and OH. Two bands at around 1653 and 1546 cm<sup>-1</sup> represented the vibrations related to the interactions between Mn centers with OH and related surface groups (Khan et al., 2017). A blue shift of about 48 cm<sup>-1</sup> at the peak position 1546 cm<sup>-1</sup> was observed in MnO<sub>2</sub>/PS and MnO<sub>2</sub>/UV/PS processes, which depicted the effects of MnO<sub>2</sub> surface by PS activation. A new peak appeared at around 3380 cm<sup>-1</sup> was only occurred in the MnO<sub>2</sub>/UV/PS process, attributing to the single bond –OH stretching vibration on the MnO<sub>2</sub> surface. For heterogeneous catalytic reactions, the degradation of organics mostly occurred on the surface of the catalyst. The –OH groups on the surface of metal oxides would enhance peroxide activation since they could make a bridge between peroxides and metal oxide surfaces (Dong et al., 2019; Ren et al., 2015). It has been confirmed the electron binding energies of both Mn and O on MnO<sub>2</sub> surface could be increased after UV irradiation (Blackburn et al., 1979; Yang et al., 2017). The results implied that UV irradiation could stimulate the surface

activity of  $\text{MnO}_2$  to generate  $-\text{OH}$  groups in the presence of PS, then facilitate more ROS generation, and thereby increase BPA degradation.

The ICP-OES was further applied to identify Mn leaching after 2 h of treatment in  $\text{MnO}_2$ , UV/ $\text{MnO}_2$ ,  $\text{MnO}_2/\text{PS}$ , and  $\text{MnO}_2/\text{UV}/\text{PS}$  processes (**Fig. 4.7b**). Limited Mn leached in  $\text{MnO}_2$  process indicated that only a small amount of  $\text{MnO}_2$  was involved in BPA oxidation, consisting with the BPA degradation experiments (**Fig. 4.1**). In contrast, in UV/ $\text{MnO}_2$  process, the Mn leaching was significantly increased to 8.71 mg/L. Therefore, UV irradiation could stimulate the surface of  $\text{MnO}_2$  to produce more Mn ions. The Mn leaching (3.21 mg/L) was relatively moderate in the  $\text{MnO}_2/\text{PS}$  process. Intriguingly, compared with the  $\text{MnO}_2/\text{PS}$  process, only 0.30 mg/L of Mn leaching was increased in the  $\text{MnO}_2/\text{UV}/\text{PS}$  process. In the UV/ $\text{MnO}_2$  process, high Mn leaching had little effect on BPA mineralization (**Fig. 4.1b**). Fortunately, in the UV/ $\text{MnO}_2/\text{PS}$  process, Mn leaching was greatly reduced, and BPA mineralization was significantly increased. When PS presented, UV irradiation might promote the formation of  $-\text{OH}$  groups on the surface of  $\text{MnO}_2$  to protect the structure of  $\text{MnO}_2$  and decrease Mn leaching.

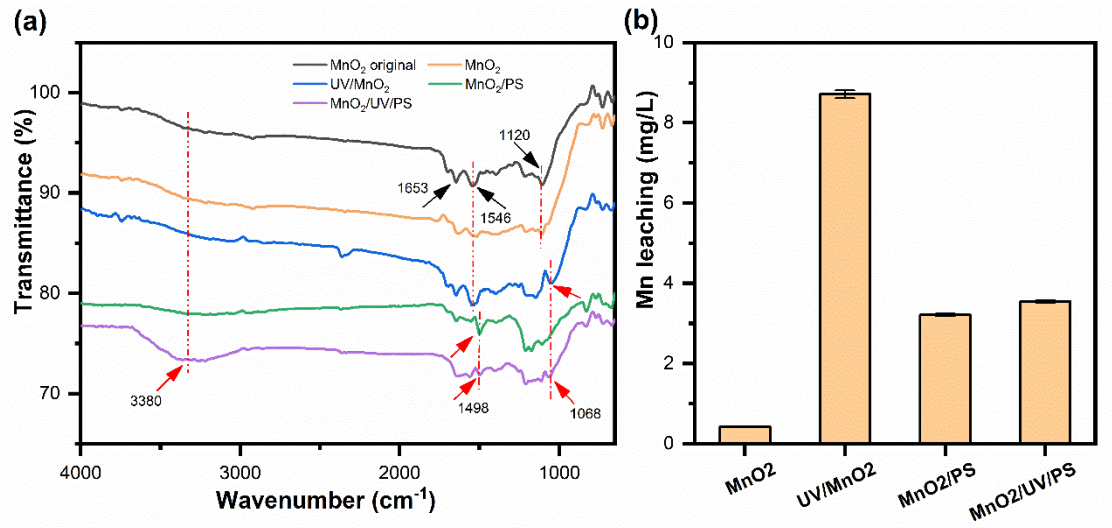
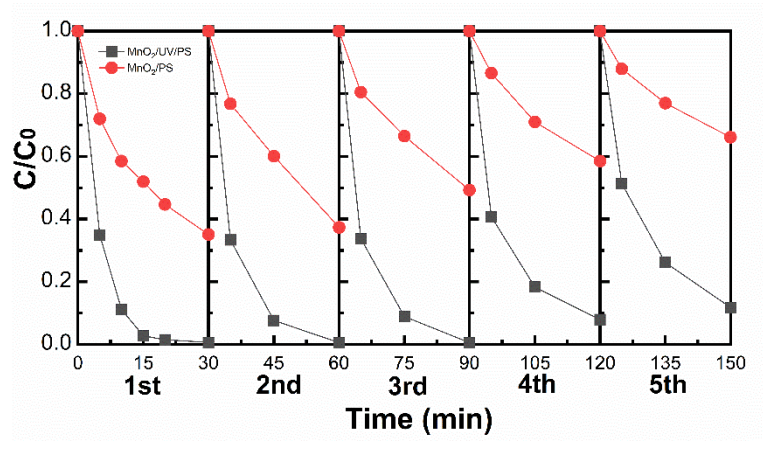


**Figure 4.7** ATR-FTIR spectra of MnO<sub>2</sub> particles (a) and the concentration of Mn leaching (b) after 2 h treatment via MnO<sub>2</sub> only, UV/MnO<sub>2</sub>, MnO<sub>2</sub>/PS, and MnO<sub>2</sub>/UV/PS processes

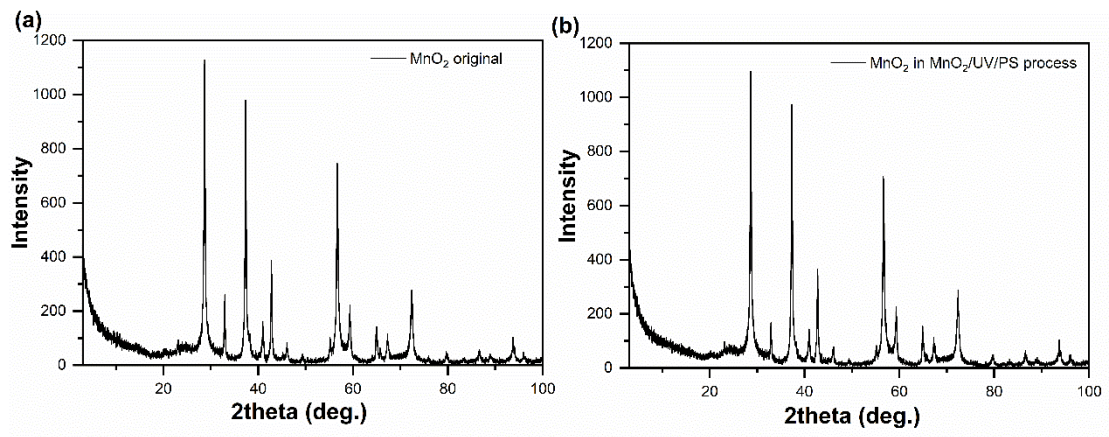
In our study, a relatively high concentration of Mn leaching was observed mainly due to the long reaction time of 2 h for organic mineralization (e.g., over 90.0% TOC removed). Relatively low concentrations of Mn leaching were reported given the short reaction time (less than 1 h), in which thorough mineralization of organics were not considered (Dong et al., 2019; Eslami et al., 2018; Huang et al., 2017). Our future research will further investigate how to decrease Mn leaching meanwhile maintaining high organic mineralization.

#### 4.3.5 Reusability of MnO<sub>2</sub>

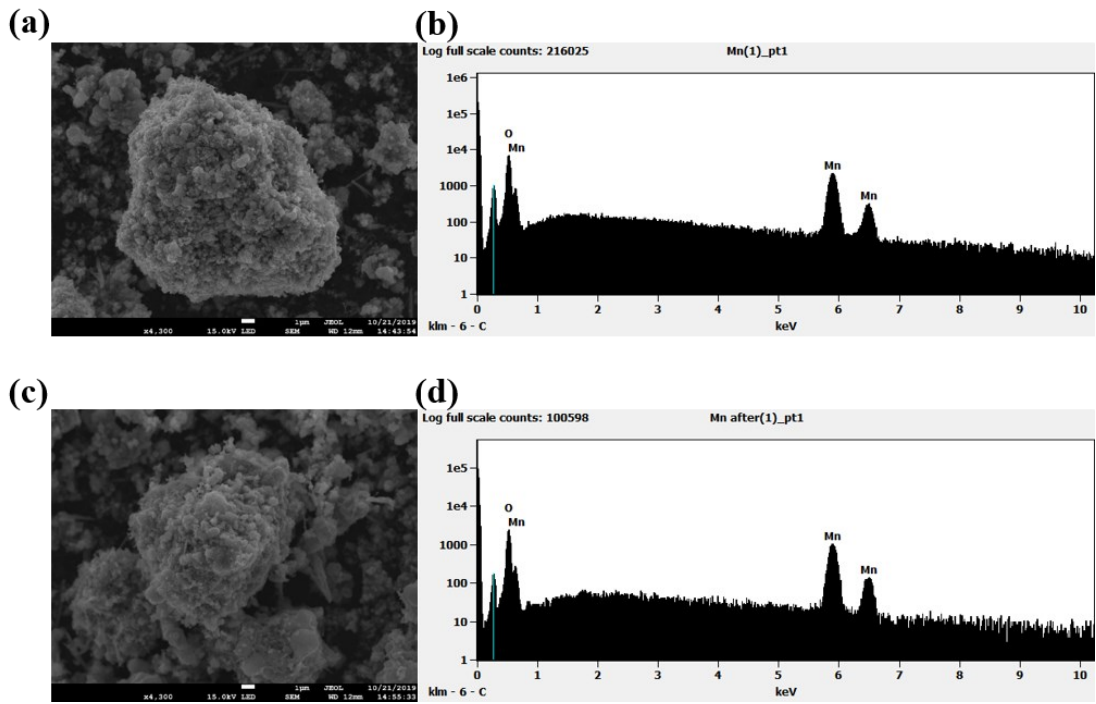
To test the reusability of MnO<sub>2</sub>, MnO<sub>2</sub> particles were recovered and reused five times with the same initial conditions in the MnO<sub>2</sub>/PS and MnO<sub>2</sub>/UV/PS processes. As shown in **Fig. 4.8**, the removal rate of BPA in the MnO<sub>2</sub>/UV/PS process kept 100.0% in the first three recycles and only decreased by 12.0% after five recycles. However, the removal rate of BPA continuously decreased from an initial 65.0% to 34.0% in the MnO<sub>2</sub>/PS process. The MnO<sub>2</sub> particles in the MnO<sub>2</sub>/UV/PS process showed excellent stability for BPA degradation. It might be because the surface hydroxyl groups were generated under UV irradiation that ATR-FTIR results confirmed (**Fig. 4.7a**). The recovered MnO<sub>2</sub> particles had obvious agglomeration from the fourth cycle, leading to decreased surface contact with PS and reduced BPA removal. In addition, both XRD (**Fig. 4.9**) and SEM (**Fig. 4.10**) results manifested no significant change of the crystal structure and morphology of MnO<sub>2</sub> was observed after reactions in the MnO<sub>2</sub>/UV/PS process.



**Figure 4.8**  $MnO_2$  recycles in  $MnO_2/PS$  and  $MnO_2/UV/PS$  processes



**Figure 4.9** XRD of MnO<sub>2</sub> before (a) and after (b) 2 h treatment in MnO<sub>2</sub>/UV/PS process

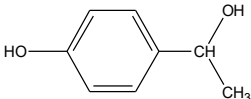
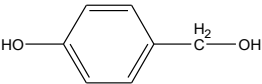
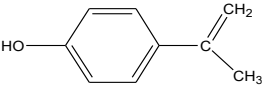
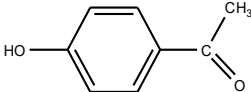
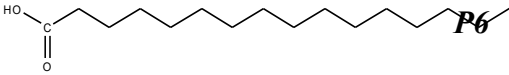
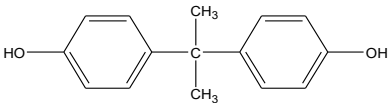


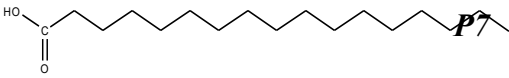
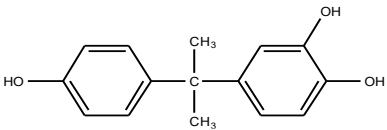
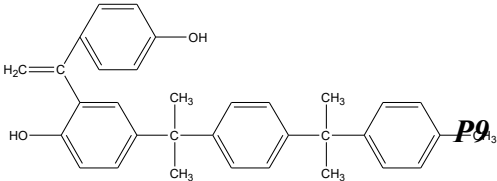
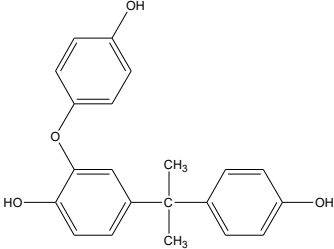
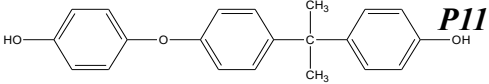
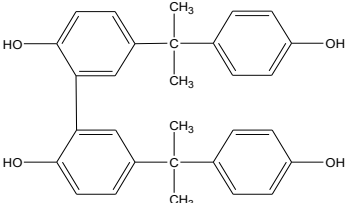
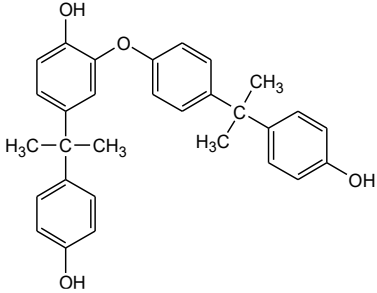
**Figure 4.10** SEM image and EDS analysis of MnO<sub>2</sub> before (a, b) and after (c, d) 2 h treatment in MnO<sub>2</sub>/UV/PS process

#### 4.3.6 Proposed degradation products and pathways

To determine the BPA degradation pathways and intermediates under the  $\text{MnO}_2/\text{UV}/\text{PS}$  process, the reaction solutions (after 5, 15, 30, 60, 90, and 120 min) were subjected to a GC-MS analysis after extraction and derivatization. As shown in **Table 4.2**, 13 products were identified as their silylated derivatives, some of which had been proposed in previous studies. The fragment ions for both BPA and intermediates were analyzed in detail. Some degradation products might remain unidentified in this study, as not all components could be effectively extracted into methylene chloride.

**Table 4.2** Degradation products of BPA under the MnO<sub>2</sub>/UV/PS process identified using GC-MS

Retention time (min)	Molecular weight	Proposed structure	No.	References
8.92	108		<b>P1</b>	—
9.65	138		<b>P2</b>	—
11.42	124		<b>P3</b>	—
16.63	134		<b>P4</b>	(de Freitas et al., 2017a; Guo et al., 2010; Lin et al., 2020; Liu et al., 2020a)
20.76	136		<b>P5</b>	(Inoue et al., 2008; Liu et al., 2020a)
41.32	256		<b>P6</b>	—
46.23	228		<b>BPA</b>	

47.12	280		<b>P7</b>	—
49.58	244		<b>P8</b>	(Lin et al., 2020; Liu et al., 2020a)
63.85	462		<b>P9</b>	—
65.03	336		<b>P10</b>	—
66.07	320		<b>P11</b>	(Sharma et al., 2015)
76.93	454		<b>P12</b>	(de Freitas et al., 2017a; Qi et al., 2017)
82.04	454		<b>P13</b>	(Divya et al., 2018; Yao et al., 2020)

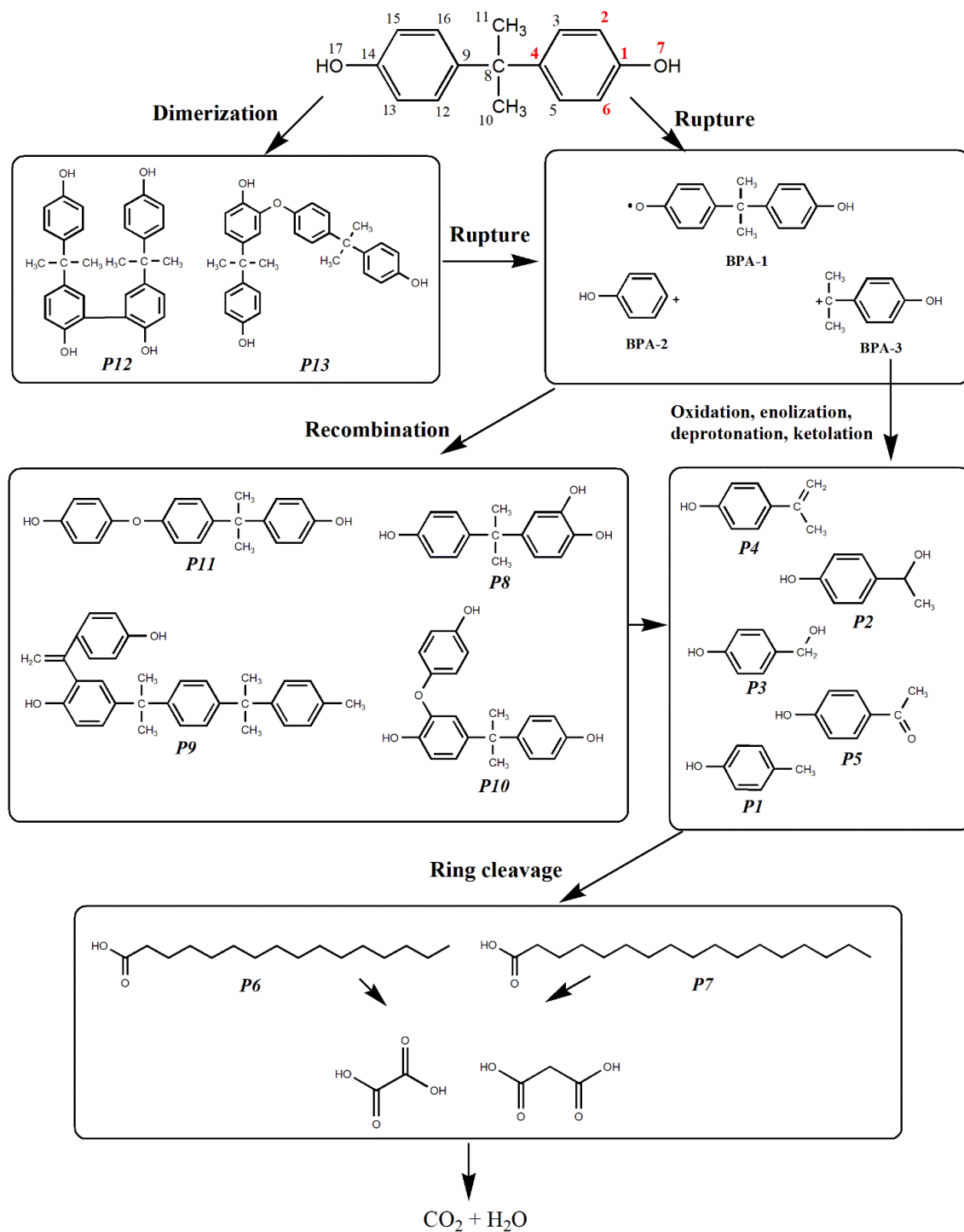


**Figure 4.11** Proposed main BPA degradation pathways with steps leading to the intermediates identified using GC-MS under the MnO<sub>2</sub>/UV/PS process

Based on the intermediates identified by GC-MS, BPA degradation via the MnO<sub>2</sub>/UV/PS process was proposed to occur in five steps (**Fig. 4.11**). Both charge and spin densities, calculated using density functional theory, indicated that the 1, 2, 4, 6, and 7 positions of BPA (shown in red in **Fig. 4.11** (top)) were most susceptible to free radical attacks (Lin et al., 2009; Yao et al., 2020). In the first step, attacks at positions 2 and 6 were considered, and the BPA oxidative condensation through C–C and ether bridges between two phenyl rings led to the formation of dimers, such as **P12** and **P13**. Previous studies confirmed that such condensation reactions commonly occurred upon the oxidation of phenolic compounds (de Freitas et al., 2017b; Zhang & Huang, 2005). It is worth noting that these dimers were very unstable and gradually decomposed, as the reaction proceeded (**Fig. 4.12**). In the second step, it was presumed that the free radicals attacked both BPA and the dimers formed in the first step at positions 1, 4, and 7. The rupture of phenolic C–O and O–H bonds, and the C–C bond (between phenyl and isopropyl groups) led to the formation of three active species containing phenol moieties of BPA, labeled BPA-1, BPA-2, and BPA-3. In the third step, a variety of rearrangement reactions was proposed to occur among these active species. For instance, the coupling reaction between BPA-1 and BPA-2 would generate **P11**. The BPA-2 was further oxidized, subsequently recombining with another molecule of BPA directly at the position of 2 to create the ether **P10**. The generation of **P8** was formed by hydroxylation that occurred when water molecules attacked the aromatic ring through electrophilic action (Lin et al., 2020). Meanwhile, multiple BPA intermediates were considered to undergo coupling and deprotonation reactions to generate **P9**. In the fourth step, the carbocation of BPA-3 could

trigger a suite of oxidation, substitution, or elimination reactions to yield *P1*, *P2*, *P3*, *P4*, and *P5*. In detail, the BPA-3 was subject to deprotonation to give *P4* or substitution by hydroxyl, yielding *P2*. The elimination reaction of *P2* produced *P3*. The BPA-3 could be subject to ketonization, generating *P5*, or elimination reaction, producing *P1*. Subsequently, the fifth step would take place with the cleavage of the phenyl rings by free radical attack. Long-chain carboxylic acids would be produced during this step by the combination of fragments (*P6* and *P7*) (de Freitas et al., 2017b; Molkenthin et al., 2013). Finally, these long-chain compounds would continue to be converted into small molecules, such as oxalic and malonic acids (Kusvuran & Yildirim, 2013) and ultimately into carbon dioxide and water.

#### **4.3.7 Acute toxicity evaluation**

The toxicity of the BPA solution in the MnO<sub>2</sub>/UV/PS process was monitored within 2 h with and without a buffer (pH 6.5). As shown in **Fig. 4.13**, the EC<sub>50</sub> value increased from 17.5% to 75.0% within 30 min, and then gradually decreased to 27.7% after 2 h without buffer. In the unbuffered process, the pH decreased from 6.5 for the initial BPA solution to 5.5 after 30 min, and to 2.9 after 120 min. Considering that luminescent bacterial metabolism is inhibited by overly acidic environments, as the pH value of the reaction mixture decreased, the increase in toxicity was observed by declining bioluminescence.

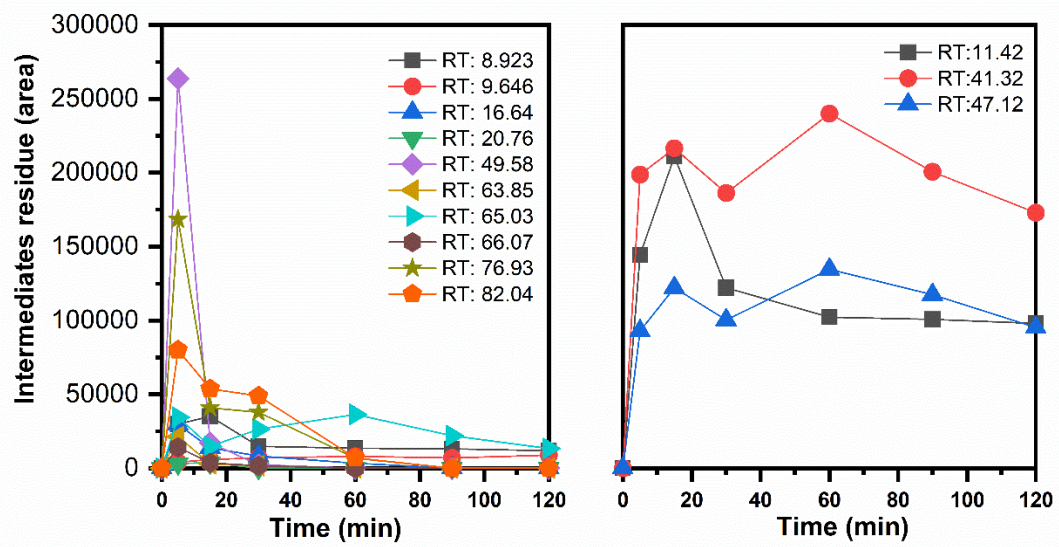
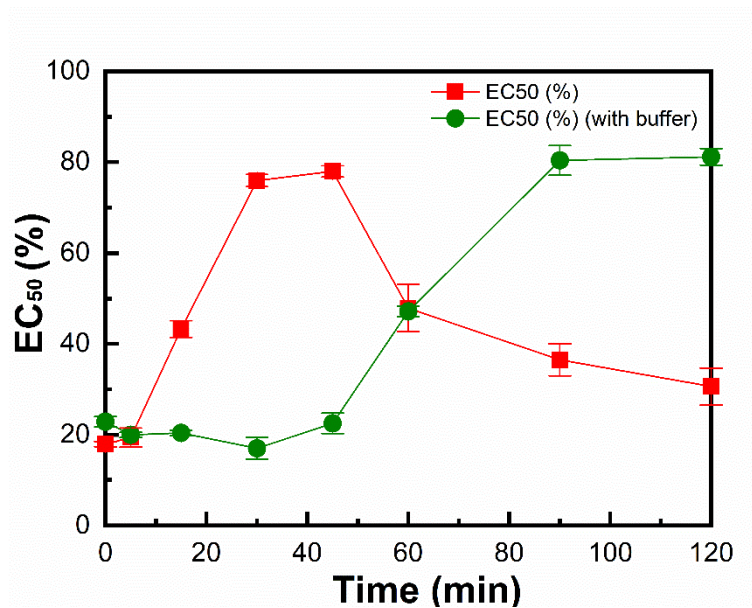


Figure 4.12 Intermediates residue in MnO<sub>2</sub>/UV/PS process



**Figure 4.13** EC<sub>50</sub> of MnO<sub>2</sub>/UV/PS process mixtures determined after 4-fold dilution with the Microtox® Basic test. Initial conditions: [BPA] = 30 mg/L, [PS] = 1 mM, [MnO<sub>2</sub>] = 0.25 g/L, with(out) phosphate buffer, pH = 6.5

In order to discern the effect of pH on the toxicity determination, phosphate buffer was used to maintain the pH of the reaction mixture at 6.5. We observed that the EC<sub>50</sub> value decreased slightly by 3.3% after the first 30 min of the process, followed by a substantial four-fold increase by 82.5% after 2 h. In the above discussion and **Fig. 4.1**, we confirmed that the concentration of BPA and TOC of the reaction mixture decreased rapidly, especially in the first 30 min. Therefore, the increased toxicity observed in the first 30 min could be caused by some BPA degradation intermediates. **Fig. 4.12** showed that the intermediates were observed after the first 30 min of the process, and that most of these gradually degraded at process times of between 30 and 120 min. These results were consistent with the toxicity test.

#### **4.4. Summary**

This study proposed an integrated MnO<sub>2</sub>/UV-activated PS process for BPA removal and demonstrated that the synergetic use of MnO<sub>2</sub> and UV is a more powerful hybrid activator of PS in this AOP. The mineralization of the MnO<sub>2</sub>/UV/PS process was significantly improved in comparison with MnO<sub>2</sub> or UV as a single activator. This process also showed a stable removal efficiency with a large variation of pH levels (3.6 to 10.0). The presence of SO<sub>4</sub><sup>•-</sup> and <sup>1</sup>O<sub>2</sub> were the key to the more rapid decomposition of BPA. Infrared spectra showed that UV irradiation could stimulate the generation of –OH groups on the MnO<sub>2</sub> surface, facilitating the PS activation in this process. The degradation pathways consisting of 5 steps and 13 intermediates were further studied by GC-MS. The acute toxicity of reaction mixtures during the process was evaluated, which confirmed the overall reduction by the proposed method. This study provides a new scientific knowledge to improve the understanding of the oxidation mechanism and

degradation pathways of emerging contaminant under the synergetic PS activation by UV/Metal oxide. The results indicated that the combination of  $\text{MnO}_2$  with UV improved PS activation as a more promising means of treating BPA and with the potential of applications in other emerging organic contaminants. Future effects are suggested to focus on controlling the Mn leaching, assessing the chronic toxicity of effluent as well as applying other water matrixes (like real wastewater) to evaluate the feasibility of this process.

# CHAPTER 5

## UV LED-BASED PS ACTIVATION BY TiO<sub>2</sub>/G-C<sub>3</sub>N<sub>4</sub> NANOSHEETS IN A MICROREACTOR FOR BPS DEGRADATION

---

The contents of this chapter are based on the following manuscript:

**Dong, G.**, Liu, B., Chen, X., Cao, Y., \*Stoyanov, S. R., Zhang, B & \*Chen, B. (2024). Degradation of bisphenol S in microreactor using UV LED-based persulfate activation by TiO<sub>2</sub>/g-C<sub>3</sub>N<sub>4</sub> nanosheet. (to be submitted)

**Authorship contribution statement:**

**Guihua Dong:** *Conceptualization, Methodology, Resources, Visualization, Writing – original draft.* **Bing Chen:** *Methodology, Supervision, Writing – review & editing.* **Bo Liu:** *Conceptualization, Methodology, Writing – original draft.* **Xiujuan Chen:** *Conceptualization, Methodology, Writing – original draft.* **Yiqi Cao:** *Writing – original draft.* **Stanislav R Stoyanov:** *Supervision, Writing – review & editing.* **Baiyu Zhang:** *Supervision, Writing – review & editing.*

## 5.1 Introduction

Due to the health concerns and restrictions by regulations worldwide, BPA has been removed from all food containers and thermal paper in the United States of America, Canada, France, and several other industrialized countries (Peillex et al., 2021). Bisphenol S (BPS), which is composed of two phenol groups on each side of a sulfonyl group, has been regarded safe and widely used as one of the main substitutes for BPA in various “BPA-free” consumer products, including food containers, baby bottles, beverages, and food can linings (Gao et al., 2015; Thoene et al., 2020). BPS is also found in thermal papers, including receipts, envelopes, and airline boarding passes, which protects the paper against overheating (Liu et al., 2021c). Recently, BPS has received significant attention because it is frequently detected in many environmental media, including foods, drinks, human urine, breastmilk, et al. (Liu et al., 2024; Thoene et al., 2020). Besides, it was reported that BPS has adverse effects on the endocrine system, and it has a longer half-time but lower biodegradability compared to BPA (Huang et al., 2019b). Therefore, it is critical to develop effective techniques to remove BPS from water and wastewater.

AOPs have been confirmed to be an effective solution for unselectively degrading recalcitrant organic pollutants in water and wastewater treatment. Persulfate-based AOPs have made many advances and attracted extensive attention due to the generation of  $\text{SO}_4^{\bullet-}$ , which has a higher selectivity, high redox potential, and longer half-life time (30–40  $\mu\text{s}$ ) in water compared with the conventional  $\bullet\text{OH}$  ( $10^{-3}$   $\mu\text{s}$ ) (Zhang et al., 2022). There are many methods to activate persulfate to produce  $\text{SO}_4^{\bullet-}$  such as heat, UV light, zero-valent iron (ZVI), transition

metal oxides, soil minerals, ultrasound, carbon-based materials (Wang & Wang, 2022). Carbon-based materials are usually preferred, as they are non-toxic, cost-effective, and have good chemical stability. Graphene carbon nitride ( $g\text{-C}_3\text{N}_4$ ) was considered an excellent option because of the strong covalent bonds between carbon and nitride atoms to make it stable under light irradiation in solutions with all pH ranges. However, the easy charge-carrier recombination limits its application in activating PS. This can be achieved by coupling two semiconductors with the different band gaps and suitable band edge positions. It has been confirmed that using  $g\text{-C}_3\text{N}_4$  combined with  $\text{TiO}_2$  to form a heterojunction is an efficient method (Troppová et al., 2018).

Even though AOPs are useful in organic decomposition, degradation at the trace concentration level requires high costs and energy consumption due to the application of expensive reagents and electric energy. Microreactors' interior structures exhibit high surface area-to-volume ratios, which reduce reactant diffusion distances, impart high process efficiencies, and reduce energy consumption. Recent studies have reported that AOPs in microreactors overcome the shortcomings of conventional reactors (Dong et al., 2022). However, the main influencing factors of AOP in microreactors and the comparison of conventional and micro reactors in terms of degradation, energy consumption, and effluent toxicity are still unknown. The research on the degradation of BPS in the AOP-microreactor system will fill this gap and provide technical support for the removal of emerging contaminants in the future.

Hence, in this study, we developed a UV LED based AOP-microreactor system for BPS

degradation. The TiO<sub>2</sub>/g-C<sub>3</sub>N<sub>4</sub> nanosheets were synthesized and applied to activate persulfate under UV LED. Factorial design methods were applied to find the critical impact factors in a microreactor. In addition, to help examine the advantages of microreactors, the same AOP system was set up in a conventional batch reactor for parallel testing. The degradation performance and acute toxicity of effluent from both the microreactor and conventional reactor were analyzed and compared. This work offers valuable insight into the future development of AOPs in microreactors for emerging contaminants treatment.

## **5.2 Materials and Methods**

### **5.2.1 Chemicals and materials**

The chemicals, including BPS, melamine, and sodium persulfate were purchased from Sigma-Aldrich (Canada). Aeroxide® P25 TiO<sub>2</sub> nanoparticles (anatase: rutile is 9:1, average particle size is around 21 nm) were purchased from Fisher Scientific (Canada).

### **5.2.2 Synthesis and characteristics of TiO<sub>2</sub>/g-C<sub>3</sub>N<sub>4</sub> nanosheets**

The synthesis of bulk g-C<sub>3</sub>N<sub>4</sub> followed a modified procedure previously reported (Lin et al., 2021a). Typically, 10 g of melamine was put into an alumina crucible with a cover, heated at a rate of 2.5 °C min<sup>-1</sup> to 550 °C in air atmosphere in a muffle furnace, and kept at 550 °C for 4 h. The obtained yellow bulk was ground into fine powder after cooling to ambient temperature. To synthesize the TiO<sub>2</sub>/g-C<sub>3</sub>N<sub>4</sub> nanosheets, the appropriate amounts of g-C<sub>3</sub>N<sub>4</sub> and commercial TiO<sub>2</sub> nanoparticles were added into methanol and sonicated separately for 30 min (Miranda et al., 2013). Then these two solutions were mixed and stirred at room temperature

for 24 h. Afterward, the composite photocatalysts were obtained by evaporating the methanol under a rotary evaporator at 80 °C. Carbon nitride content ranged from 1 to 5 wt% with respect to TiO<sub>2</sub>.

The morphology of the nanosheets was imaged by SEM equipped with EDS (Quanta 400 MLA). The XRD spectra were obtained by an X-ray diffractometer (Rigaku XtaLAB Synergy-S). The functional groups were characterized by ATR-FTIR. The spectra were taken in the range of 4000–400 cm<sup>-1</sup>.

### 5.2.3 System development and operations

The AOP-microreactor system consists of a commercial serpentine microreactor (1.7 ml in volume and 1 mm in diameter), which was purchased from Little Things Factory, a syringe pump, a 35 V DC power supply, and a UV-LED light (365 nm, 18.57 mw/cm<sup>2</sup>) with the cooling fan. **Fig. 5.1** shows the schematic diagram of the AOP-microreactor system. The prepared BPS solution with dispersed TiO<sub>2</sub>/g-C<sub>3</sub>N<sub>4</sub> nanosheets was evenly injected into the microreactor through the syringe pump. The tinfoil was used to cover the parts of the light source and the microreactor to ensure the efficient use of the light. Batch reactor experiments were performed by dosing nanosheets into a 250 mL beaker of contaminant solution with shaker stirring to reach adsorption equilibrium. All experiments were conducted in duplicate to ensure reproducibility.

### 5.2.4 Analysis of water samples

The concentration of BPS was determined by the UV spectrophotometer and the HPLC

system equipped with Symmetry C18 column (Agilent 1260 Infinity II) ( $4.6 \times 150$  mm,  $5 \mu\text{m}$  particle size) at UV wavelengths of 259 nm (Yang et al., 2019). The mobile phase consisted of 0.1% acetic acid and methanol at a ratio of 50:50 (v/v). The flow rate of the mobile phase was 1 mL/min. The TOC concentrations were measured by the burning oxidation-non-dispersive infrared absorption method using a Shimadzu TOC-L analyzer (Shimadzu, Tokyo, Japan). Before measuring TOC, few drops of phosphoric acid were added to maintain the sample pH  $< 1$ .

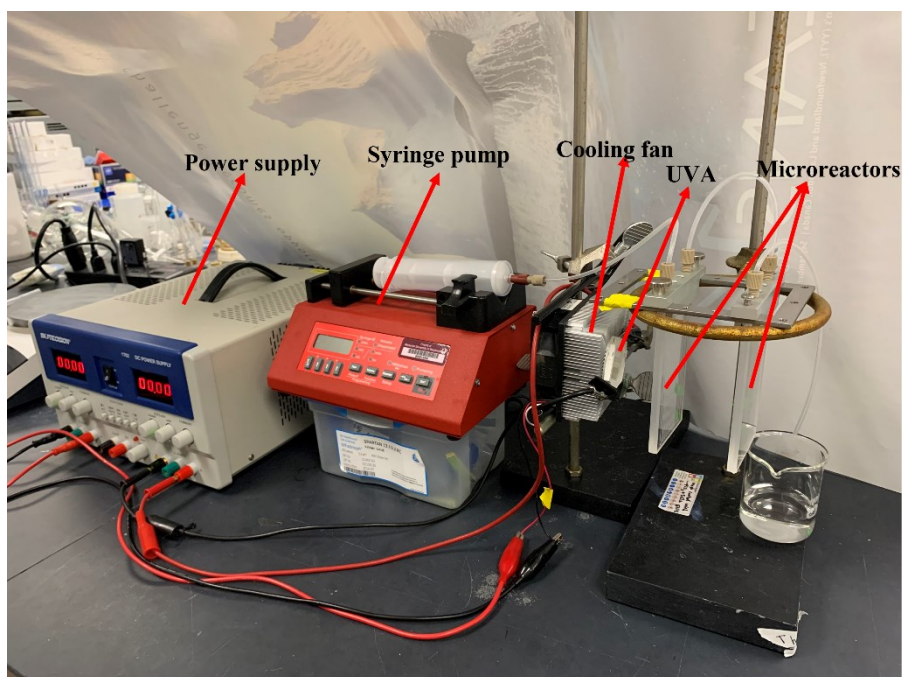


**Figure 5.1** Schematic diagram of the microfluidic reactor

### **5.2.5 Acute toxicity evaluation**

Acute toxicity tests of the influent and effluent were carried out using a Microtox® (Model 500) analyzer, whose primary indicator was the luminous bacterium (*Vibrio fischeri*). The acute toxicity test relied on bacterial luminescence via cellular respiration. Inhibition of cellular activity (caused by exposure to toxicants, acidic or alkaline conditions, etc.) decreased the respiratory rate, leading to a corresponding decrease in luminosity. EC<sub>50</sub> refers to the percentage of water samples that cause a 50% decrease in luminous intensity. The pH range of 6.0–8.5 was recommended as standard since *Vibrio fischeri* is pH-sensitive (Dong et al., 2021).

### **5.2.6 Statistical analysis**

The fractional-factorial design analysis was conducted using Design Expert® v12 and Minitab® 18 software. All experiments were performed in triplicate for quality control. The error bar and error area represented each standard deviation from the means of the independent experiments. The significant differences were determined by ANOVA with *F*-tests using Minitab® 18 software. The  $P < 0.05$  (\*) was considered statistically significant, and  $P < 0.001$  (\*\*) was statistically highly significant.

## 5.3 Results and Discussion

### 5.3.1 Nano photocatalysts characterization

To identify the crystallographic structure and phase characterization of g-C<sub>3</sub>N<sub>4</sub>, TiO<sub>2</sub>, and TiO<sub>2</sub>/g-C<sub>3</sub>N<sub>4</sub> nanosheets, the samples were examined by XRD. As shown in **Fig. 5.2a**, the XRD pattern of g-C<sub>3</sub>N<sub>4</sub> showed two typical diffraction peaks at 8.3° and 20.1°, corresponding to g-C<sub>3</sub>N<sub>4</sub>, which were attributed to the in-plane structure of tri-s-triazine units and the interlayer stacking of conjugated aromatic groups, respectively (Ren et al., 2018). The XRD pattern of TiO<sub>2</sub> showed evident peaks at 18.4°, 27.2°, 34.2°, 38.3°, 44.1°, and 52.4°, which corresponded to the crystal facet of anatase TiO<sub>2</sub>, respectively (**Fig. 5.2b**). The g-C<sub>3</sub>N<sub>4</sub> and anatase TiO<sub>2</sub> peaks could be observed in the g-C<sub>3</sub>N<sub>4</sub>/TiO<sub>2</sub> sample, thus indicating that the g-C<sub>3</sub>N<sub>4</sub>/TiO<sub>2</sub> composite was successfully synthesized (**Fig. 5.2c**). Furthermore, it is noteworthy that the diffraction peak of the g-C<sub>3</sub>N<sub>4</sub> plane overlapped the characteristic peak of the TiO<sub>2</sub> plane rutile phase. Compared with the diffraction peaks of pristine g-C<sub>3</sub>N<sub>4</sub> and TiO<sub>2</sub>, the diffraction peak corresponding to the g-C<sub>3</sub>N<sub>4</sub> crystal plane in the composite was relatively broader, and the intensity was weaker. This finding can be attributed to the reduced g-C<sub>3</sub>N<sub>4</sub> content in the composite. The internal figures in **Fig. 5.2a-c** showed the corresponding 2D-XRD, fully proving the authenticity of the above crystal structures.

The compositional information and chemical bonds of TiO<sub>2</sub>, g-C<sub>3</sub>N<sub>4</sub>, and g-C<sub>3</sub>N<sub>4</sub>/TiO<sub>2</sub> composite were analyzed by FT-IR spectroscopy. As shown in **Fig. 5.2d**, the broad peak at 3000–3300 cm<sup>-1</sup> for pristine g-C<sub>3</sub>N<sub>4</sub> corresponded to the stretching mode of the terminal NH<sub>2</sub> of the NH groups at the defect sites of the aromatic rings, whereas several peaks in the 1200–

1650  $\text{cm}^{-1}$  range were assigned to the typical stretching mode of C-N heterocycles. **Fig. 5.2e** shows the FTIR spectrum of  $\text{TiO}_2$  nanoparticles, Ti-O bending mode and deformative vibration of Ti-OH stretching could be observed at 483  $\text{cm}^{-1}$  and 1623  $\text{cm}^{-1}$ , respectively. Asymmetrical and symmetrical stretching vibrations of hydroxyl group (-OH) may be observed at 3400  $\text{cm}^{-1}$ . The 1623  $\text{cm}^{-1}$  band may be attributed to water adsorbed on the  $\text{TiO}_2$  surface. These results agree well with earlier reports (Chougala et al., 2017). **Fig. 5.2f** shows that, as expected, all the prominent absorption peaks of g- $\text{C}_3\text{N}_4$  and  $\text{TiO}_2$  appeared in the spectra of the  $\text{TiO}_2/\text{g-C}_3\text{N}_4$  nanosheets but in low intensity (Sun et al., 2015). The fingerprint area shows the different characteristic peaks of the nanosheets (**Fig. 5.3**). The pristine carbon nitride g- $\text{C}_3\text{N}_4$  exhibits the typical band at around 800  $\text{cm}^{-1}$  corresponding to the breathing mode of the heptazine arrangement (Wang et al., 2014a). For  $\text{TiO}_2$  and  $\text{TiO}_2/\text{g-C}_3\text{N}_4$ , the peak near 430  $\text{cm}^{-1}$  is the characteristic peak of  $\text{TiO}_2$ , which is related to the stretching vibration of Ti-O-Ti (Zhang et al., 2021a).

The morphology and microstructure as well as elemental analysis of as-synthesized samples were further investigated by SEM with EDS (**Figs. 5.2g-i**). **Fig. 5.2g** shows the crumpled layer structure of g- $\text{C}_3\text{N}_4$  nanoparticles, possibly containing several stacking layers, indicating the planar graphitic-like structure. The  $\text{TiO}_2$  nanoparticles showed the tendency of agglomeration under SEM because the  $\text{TiO}_2$  is unstable in its nanoparticle form, and they tend to join each other until they are relatively stable (**Fig. 5.2h**) (Diantoro et al., 2018). It can be seen that some of the surfaces of the  $\text{TiO}_2$  were wrapped by g- $\text{C}_3\text{N}_4$ , reflecting the strong aggregation interaction between  $\text{TiO}_2$  and g- $\text{C}_3\text{N}_4$  (**Fig. 5.2i**). All the morphology and structural

characterization results denoted that the  $\text{TiO}_2/\text{g-C}_3\text{N}_4$  nanosheets were synthesized by the impregnation method.

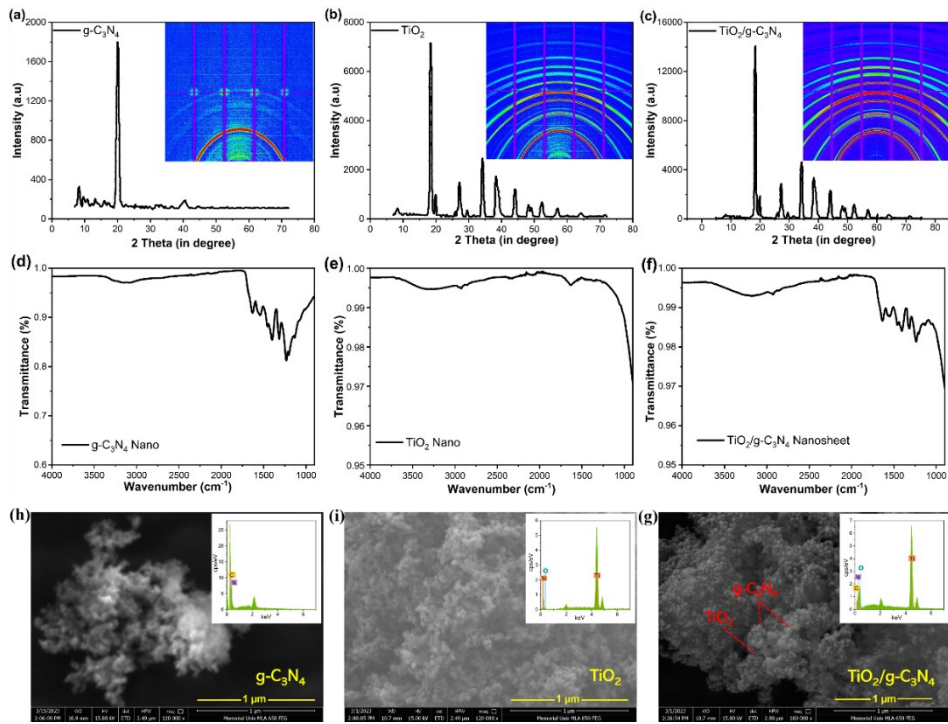


**Figure 5.2** Characterization of  $g\text{-C}_3\text{N}_4$ ,  $\text{TiO}_2$ , and  $\text{TiO}_2/g\text{-C}_3\text{N}_4$  nanosheets

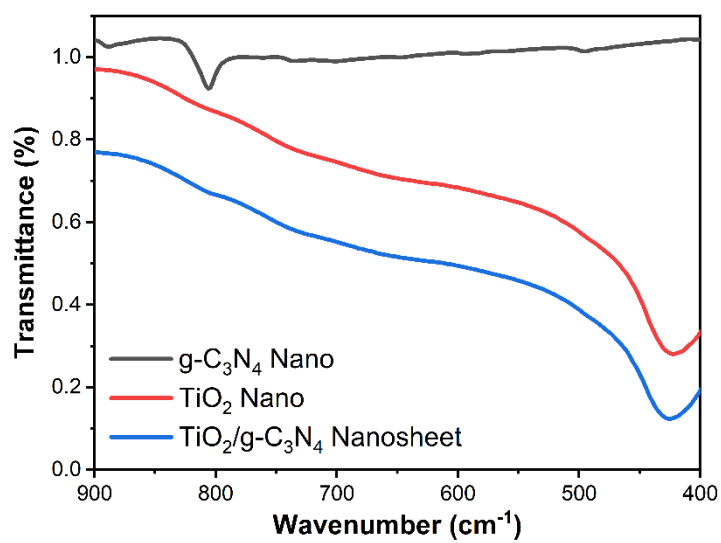


**Figure 5.3** FTIR fingerprint regions of g-C<sub>3</sub>N<sub>4</sub>, TiO<sub>2</sub>, and TiO<sub>2</sub>/g-C<sub>3</sub>N<sub>4</sub> nanosheets

### 5.3.2 Degradation performance in microreactor

To demonstrate the advantages of the synthesized  $\text{TiO}_2/\text{g-C}_3\text{N}_4$  nanosheets as the photocatalyst by activating PS with UV irradiation, the degradation of BPS in a microreactor under 1 ml/min of flow rate was studied using different catalysts. The results show that the degradation efficiency in no catalyst,  $\text{TiO}_2$ , and  $\text{TiO}_2/\text{g-C}_3\text{N}_4$  were 5.88%, 11.64%, and 17.62%, respectively. This indicated that the synthesized  $\text{TiO}_2/\text{g-C}_3\text{N}_4$  nanosheets have a significantly improved effect on BPS degradation.

The key influencing factors, including PS dose, catalyst ( $\text{TiO}_2/\text{g-C}_3\text{N}_4$ ) dose, flow rate, light distance, pH, and inorganic ions, were further investigated to explore their effect and optimize the process on the degradation of BPS in a microreactor (**Fig. 5.4**). The PS dosage should be appropriate since overdose can increase secondary pollution and cost. As shown in **Fig. 5.4a**, only 28.32% of BPS removal efficiency could be achieved after 17 min of reaction retention without any PS addition. It was found that the removal efficiency could be improved when PS was added, which was supported by the increased efficiency up to 62.91% with a PS concentration of 1 mM. Slightly improved removal efficiency (65.61%) was observed when further increasing the PS dose to 2 mM. The corresponding reaction rate constants were 0.02, 0.0384, 0.0598, and 0.0641  $\text{min}^{-1}$  when the PS dose was 0, 0.5, 1, and 2 mM, respectively. Considering that increasing the dose above 1 mM did not significantly improve the process efficiency, the PS concentration of 1 mM was then selected for the remaining study.

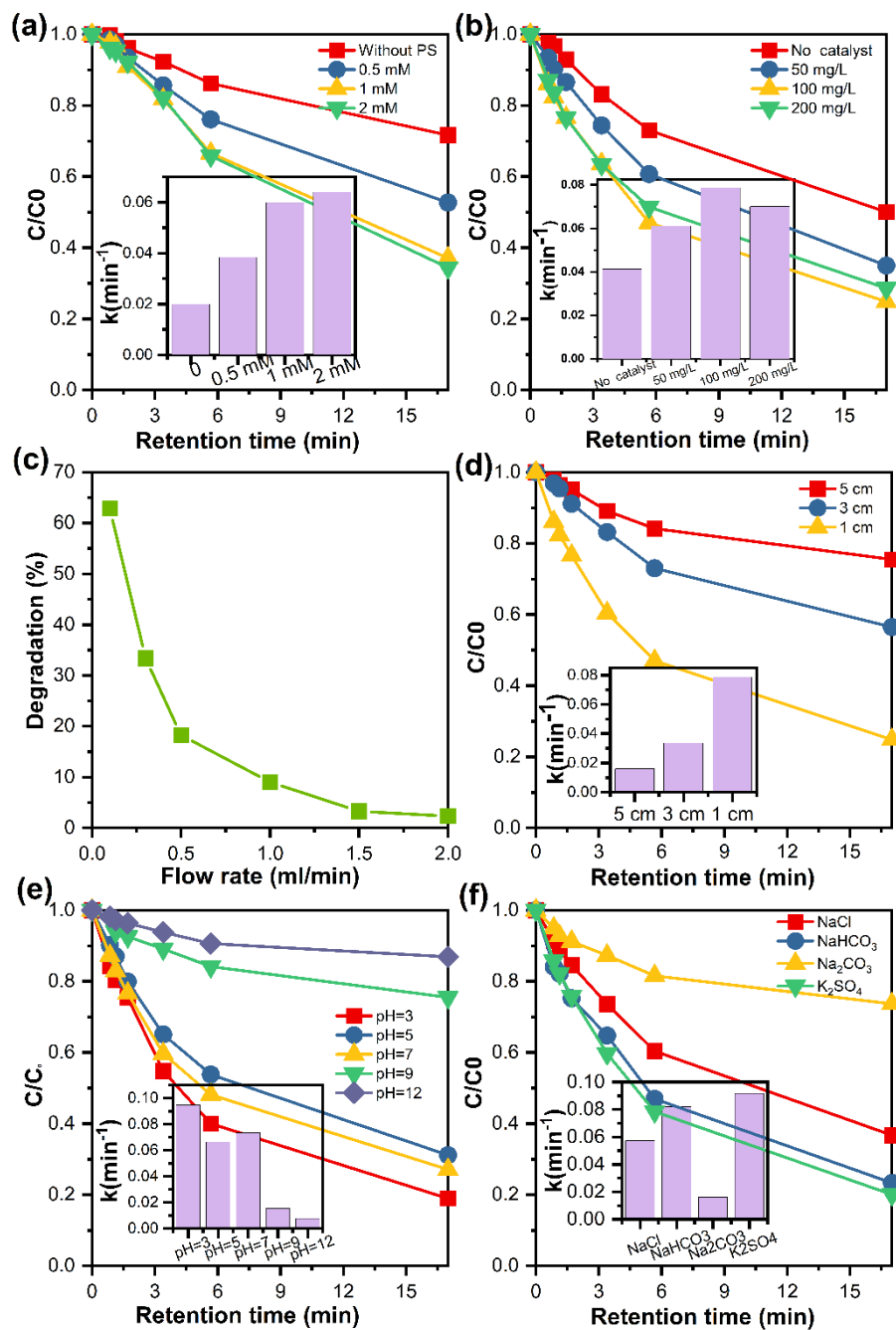


**Figure 5.4** Effects of parameters ((a) PS dose, (b) catalyst dose, (c) flow rate, (d) light distance, (e) pH level, and (f) inorganic salts) on BPS degradation in the microreactor (PS dose 1mM, catalyst 100 mg/L, light distance 3 cm if not mentioned)

Determining a suitable catalyst (dispersed) dosage is essential because an overdose could reduce degradation efficiency (Danyliuk et al., 2021). Without using the catalyst, around 50.00% of BPS were removed within 34 min of reaction in a microreactor (**Fig. 5.4b**). The addition of 50 mg/L of catalyst significantly enhanced the removal efficiency by up to 65.05% compared to that without catalyst. When the catalyst dose was increased to 100 mg/L, 75.20% of BPS could be removed. However, when the dose was further increased to 200 mg/L, the removal efficiency decreased to 71.38%. The calculated rate constant increased from 0.0414 to 0.0789  $\text{min}^{-1}$  when the catalyst doses were 0 and 100 mg/L, respectively, but decreased to 0.0701  $\text{min}^{-1}$  if the catalyst dose was 200 mg/L. This performance is due to the shielding effect of an overdosed photocatalyst, which reduced light penetration and the generation of reactive species for BPS degradation. Consequently, the best catalyst dose among the selected values was determined as 100 mg/L in this microreactor.

The effect of different flow rates (0.01, 0.05, 0.1, 0.5, 1, and 2 mL/min) on degradation performance in the microreactor were examined (**Fig. 5.4c**). As the flow rates were increased from 0.01 to 2 mL/min, the degradation rates of BPS decreased from 62.91% to 2.33% due to a shorter retention time. Any attempt to lower the flow rate, hence increasing residence time, resulted in a higher removal efficiency. However, the lower flow rate may result in a longer residence time and catalyst precipitation. Finding the optimal flow rate is one of the key points in the AOP-microreactor system.

The distance between the light source and the microreactor substantially affected the microfluidic system performance due to the light attenuation (**Fig. 5.4d**). The results showed

that the BPS removal efficiencies were 24.80%, 56.49%, and 75.48% when the light distances were set as 5, 3, and 1 cm, respectively. Correspondingly, the reaction rate constants were calculated as 0.0162, 0.0335, and 0.0787 min<sup>-1</sup>, respectively.

Solution pH significantly impacted the reaction kinetics. An investigation on the effect of pH on the degradation of BPS in microreactor was conducted at the pH values of 3, 5, 7, 9, and 12 (**Fig. 5.4e**). The BPS degradation efficiency gradually increased along with the decreased pH values. Significantly, the degradation efficiency was relatively high, reaching 81.03%, 72.87%, and 68.84%, under acidic and neutral conditions with pH of 3, 5, and 7, respectively. Only 25.48% and 13.12% of BPS could be removed when the pH values were 9 and 12, respectively, which indicated that the BPS degradation was strongly restricted in alkaline conditions. The calculated rate constants increased from 0.0077 to 0.0947 min<sup>-1</sup>, corroborating the important role of pH in this system. Previous studies indicated that both •OH and SO<sub>4</sub><sup>•-</sup> were the main contributors at acid and neutral pH while SO<sub>4</sub><sup>•-</sup> could react with HO<sup>-</sup> to form •OH at higher pH. Meanwhile, an alkaline environment not only increases PS consumption but also may capture free radicals and thus inhibit the degradation process (Guan et al., 2011; Waclawek et al., 2022).

The water matrix (e.g., various inorganic salts) may affect the process efficiency because matrix components could reduce light transmittance and/or scavenge radicals (Miklos et al., 2018). **Fig. 5.4f** presented the degradation of BPS at varied concentrations of inorganic salts in the microreactor system. The degradation efficiencies of BPS in the presence of NaCl, NaHCO<sub>3</sub>, Na<sub>2</sub>CO<sub>3</sub>, and K<sub>2</sub>SO<sub>4</sub> were 36.71%, 23.34%, 73.70%, and 20.09%, and the corresponding rate

constants were 0.0575, 0.0821, 0.0162, and 0.0917 min<sup>-1</sup>, respectively. The suppression of BPS degradation by these inorganic salts decreased in the order Na<sub>2</sub>CO<sub>3</sub> > NaCl > NaHCO<sub>3</sub> > K<sub>2</sub>SO<sub>4</sub>. The observation that Na<sub>2</sub>CO<sub>3</sub> inhibited the degradation of BPS more than the other salts may be attributed to the trapping of free radicals by carbonate ions.

**Table 5.1** A 2<sup>5</sup> full factorial design table

<b>StdOrder</b>	<b>RunOrder</b>	<b>Distance (cm)</b>	<b>Flow rate (<math>\mu</math>L/min)</b>	<b>Photocatalysts (mg/L)</b>	<b>PS dosage (mM)</b>	<b>NaCl (mM)</b>	<b>Removal efficiency (%)</b>
32	1	5	500	100	1	0.5	<b>10.33</b>
31	2	1	500	100	1	0.5	<b>30.98</b>
19	3	1	500	20	0.2	0.5	<b>23.15</b>
12	4	5	500	20	1	0	<b>8.44</b>
14	5	5	100	100	1	0	<b>59.40</b>
22	6	5	100	100	0.2	0.5	<b>49.47</b>
26	7	5	100	20	1	0.5	<b>51.77</b>
7	8	1	500	100	0.2	0	<b>44.01</b>
27	9	1	500	20	1	0.5	<b>34.29</b>
1	10	1	100	20	0.2	0	<b>63.98</b>
28	11	5	500	20	1	0.5	<b>19.44</b>
24	12	5	500	100	0.2	0.5	<b>27.67</b>
21	13	1	100	100	0.2	0.5	<b>64.19</b>
10	14	5	100	20	1	0	<b>69.38</b>
6	15	5	100	100	0.2	0	<b>64.93</b>
18	16	5	100	20	0.2	0.5	<b>62.16</b>
8	17	5	500	100	0.2	0	<b>35.97</b>
23	18	1	500	100	0.2	0.5	<b>46.91</b>
30	19	5	100	100	1	0.5	<b>77.55</b>
13	20	1	100	100	1	0	<b>83.29</b>
2	21	5	100	20	0.2	0	<b>60.95</b>
17	22	1	100	20	0.2	0.5	<b>63.71</b>
4	23	5	500	20	0.2	0	<b>31.65</b>
15	24	1	500	100	1	0	<b>52.98</b>
20	25	5	500	20	0.2	0.5	<b>27.13</b>
5	26	1	100	100	0.2	0	<b>68.10</b>
29	27	1	100	100	1	0.5	<b>83.63</b>
11	28	1	500	20	1	0	<b>52.17</b>
16	29	5	500	100	1	0	<b>41.91</b>
3	30	1	500	20	0.2	0	<b>42.93</b>
9	31	1	100	20	1	0	<b>82.95</b>
25	32	1	100	20	1	0.5	<b>82.61</b>

**Table 5.2** Significant factor effects and contributions

	<b>Term</b>	<b>F value</b>	<b>p-value</b>	<b>Standardized effect</b>	<b>Contribution (%)</b>
A	Distance	19.69	0.000	-14.07	<b>10.89</b>
B	Flow rate	123.64	0.000	-35.26	<b>68.40</b>
C	Catalyst dose	1.18	0.294	3.44	0.65
D	PS dose	2.16	0.161	4.67	1.20
E	NaCl	4.83	0.043	-6.97	2.67
AB	Distance & Flow rate	0.35	0.561	-1.88	0.20
AC	Distance & Catalyst dose	0.03	0.874	0.51	0.014
AD	Distance & PS dose	4.44	0.051	-6.68	2.46
AE	Distance & NaCl	0.05	0.823	0.72	0.03
BC	Flow rate & Catalyst dose	0.53	0.476	2.31	0.29
BD	Flow rate & PS dose	5.58	0.031	-7.49	3.08
BE	Flow rate & NaCl	2.13	0.164	-4.63	1.18
CD	Catalyst dose & PS dose	0.07	0.792	0.85	0.04
CE	Catalyst dose & NaCl	0.03	0.862	-0.56	0.01
DE	PS dose & NaCl	0.04	0.845	-0.63	0.02

### 5.3.3 Factorial-based performance analysis of microreactor

The factorial experiment was designed to identify the key factors influencing the process efficiency in the developed AOP-microreactor system. Based on the one-factor-a-time experiment for performance analysis in the above section, the five factors, including PS dose, catalyst dose, flow rate, light distance, and inorganic salts, were further investigated by the 2-level full factorial experiment design. The experimental arrangement of this 2<sup>5</sup> full factorial design was generated using the Design Expert® 12 software (**Table 5.1**).

The residual analysis was performed to determine the normal distribution probability (**Fig. 5.5**). The normal probability plot showed that the experimental points were reasonably aligned, suggesting normal distribution. The histogram of residuals showed an almost symmetrical distribution, meaning the errors were normally distributed with a mean of zero. The plot about residual versus fitted value showed the residuals were scattered randomly at about zero, which indicates that the errors had a constant variance. The plot of residuals versus run of experiments showed that the residuals appear to be randomly scattered about zero and almost all points were found to fall in the range of +10 to -10. The residual plots were verified to show that the full factorial design was sufficient for this study. This design aimed to ensure that the main effect of each individual factor is clear.

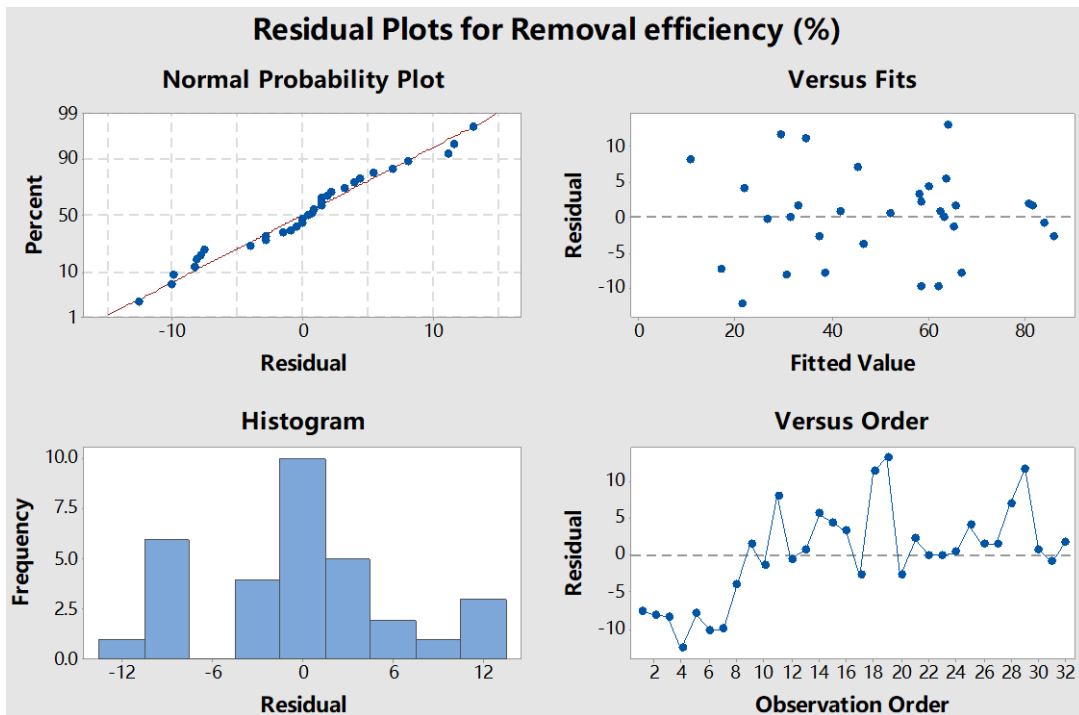


**Figure 5.5** Residual graphs (a) normal probability plot for residuals, (b) histograms of residuals, (c) residuals vs. fitted values, and (d) residual vs. the run of the experiments

In the main effects plot depicted in **Fig. 5.6a**, each factor was represented by a line connecting the average value of all observations at the low (left) and high (right) levels, with the vertical height of each line indicating the main effect (Jiang et al., 2017). This graph can visualize the influence of each factor on the response variable, in this case, the BPS removal efficiency. As detailed in **Table 5.2** and illustrated in **Fig. 5.6a**, the factor of flow rate exhibited the largest negative impact on BPS removal efficiency. Specifically, the reduction in flow rate contributed 68.40% to the improvement of BPS degradation efficiency. This significant effect is attributed to the enhanced mass transfer under slow flow conditions. The enhanced mass transfer facilitates better contact between the reactants and the catalytic surfaces, leading to more efficient degradation reactions. This was evidenced by the result of **Fig. 5.4c**, where the degradation rate increased dramatically from 2.33 to 62.91% when the flow rate decreased from 2 to 0.01 ml/min. The increased retention time at lower flow rates is expected to improve the interaction between BPS molecules and the active species, thereby enhancing the overall degradation process.

In addition to the flow rate, the distance between the light source and the microreactor played an important secondary role, contributing 10.89% to the degradation rate. According to the Beer-Lambert law, the intensity of UV radiation diminishes exponentially as the optical path length increases. This phenomenon was confirmed by the data in **Fig. 5.4d**, which demonstrated a decrease in the degradation rate from 75.48% to 24.80% as the optical path lengthened from 1 cm to 5 cm. The significant effect of light distance underscores the importance of optimizing the light source position to ensure adequate UV exposure for

effective photodegradation.

The presence of NaCl salt showed a minor effect, contributing 2.67% to the inhibition of BPS degradation. That may be because salts can influence degradation processes by affecting the ionic strength of the solution, which in turn can impact the behavior of charged species and radicals involved in the degradation reactions (Luo et al., 2022). The relatively minimal effect of NaCl in the microreactor is probably because of the low concentration of NaCl (0.5 mM) present in this system. Both catalyst and persulfate dosage had limited effects in this microreactor system, contributing 0.65% and 1.20%, respectively. This suggests that within the tested range, the microreactor system was not significantly sensitive to variations in these factors.

In half-normal probability plots further corroborated the significance of these factors. Factors of greater importance deviated more from the 'near-zero' line, providing additional evidence that flow rate and light distance were more significant compared to the other factors (**Fig. 5.6b**). All the 2-factor interaction plots are displayed in **Fig. 5.6c**. In factorial experiments, interactions between factors can give insights into how the effects of one factor might depend on the level of another. An interaction is considered significant if the p-value in the regression model is less than 0.05. From **Table 5.2**, we can conclude that the only significant 2-factor interaction was flow rate and PS dosage. It was interesting to note that a combination of a slow flow rate and a low level of PS dosage could enhance the BPS degradation rate. This synergistic effect might be due to the more efficient utilization of sulfate radicals at slower flow rates, where the longer residence time allows for more complete degradation. Overall, factorial

analysis revealed that flow rate and light distance were the dominant factors influencing BPS degradation in the developed AOP-microreactor system. The findings highlighted the importance of optimizing these parameters to achieve maximum degradation efficiency in practical applications.

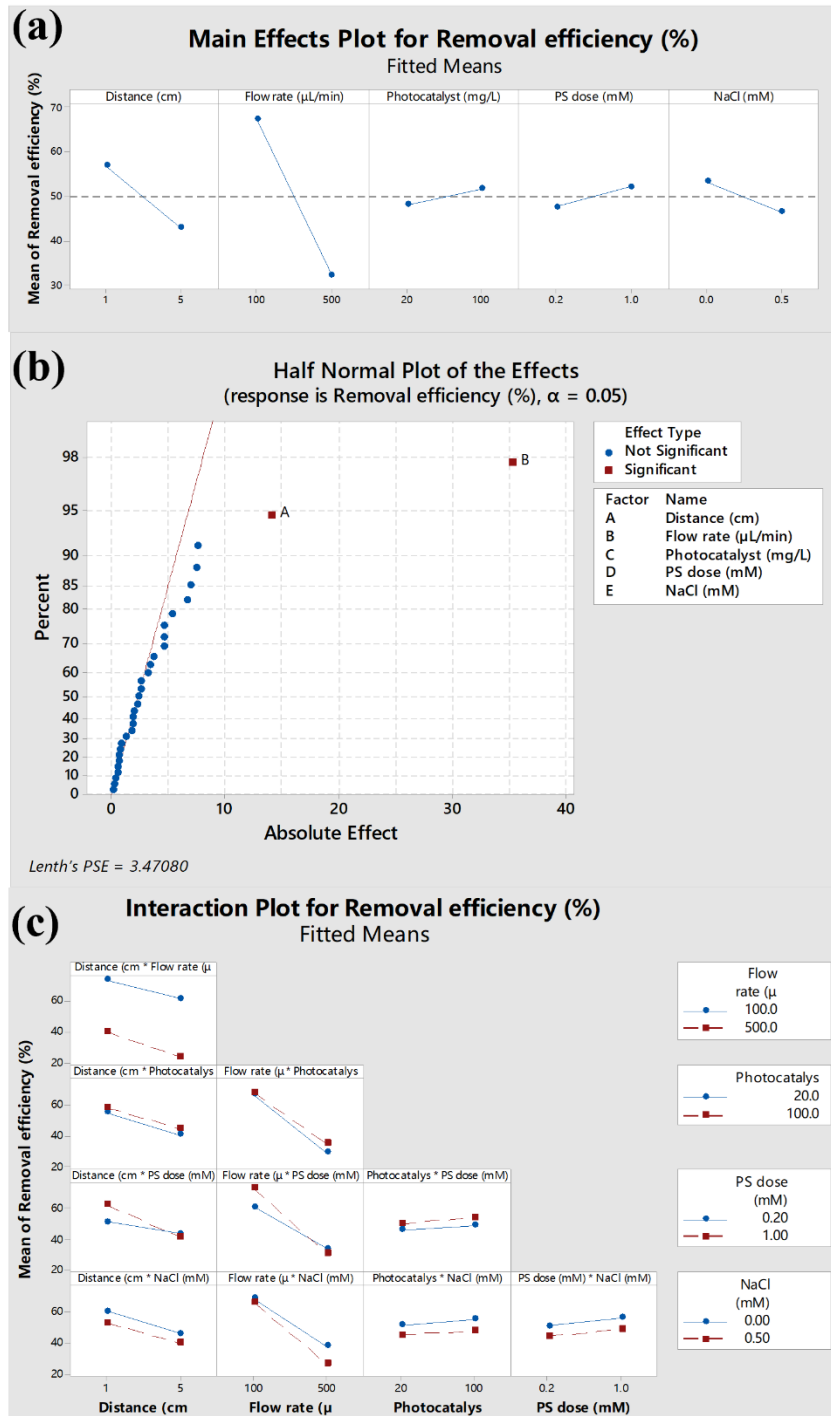


**Figure 5.6** (a) Main effect plot of impact factors in a microreactor, (b) Half-normal plot of effects to BPS degradation, and (c) 2-factor interaction plots for removal efficiency

### 5.3.4 Performance comparison between a microreactor vs. a batch reactor

#### 5.3.4.1 Comparison of degradation performance and mineralization

The BPS degradation and the mineralization in the developed microreactor under optimum conditions were thoroughly investigated. To verify the merits of the microreactor, water samples were also collected and tested from a batch reactor under the same residence time and reaction conditions. After 34 min of residence time, the BPS degradation rates in the batch reactor and microreactor were found to be 31.07% and 84.86%, respectively (**Fig. 5.7a**). This significant difference indicated the enhanced efficiency of the microreactor. Specifically, the reaction rate constant in the microreactor ( $0.0536 \text{ min}^{-1}$ ) was five times higher than that of the batch reactor ( $0.0116 \text{ min}^{-1}$ ), indicating a substantial improvement in treatment efficiency. Moreover, the BPS mineralization rates were also markedly different. In the batch reactor, the mineralization rate was 10.67%, whereas in the microreactor, it reached 41.09% (**Fig. 5.7b**). It's worth noting that the reaction rate constant in the microreactor ( $0.0156 \text{ min}^{-1}$ ) remained 5 times higher than that of the batch reactor ( $0.0032 \text{ min}^{-1}$ ). Overall, these results demonstrated that both the degradation and mineralization of BPS in the microreactor were five times more efficient than in the batch reactor. The enhanced performance can be attributed to the improved mass transfer and optimized reaction conditions inherent in the microreactor design, which facilitated more effective interaction between BPS and reactive species. This significant enhancement indicated the potential of microfluidic technology in advancing the efficiency of AOPs for emerging contaminant degradation and mineralization.

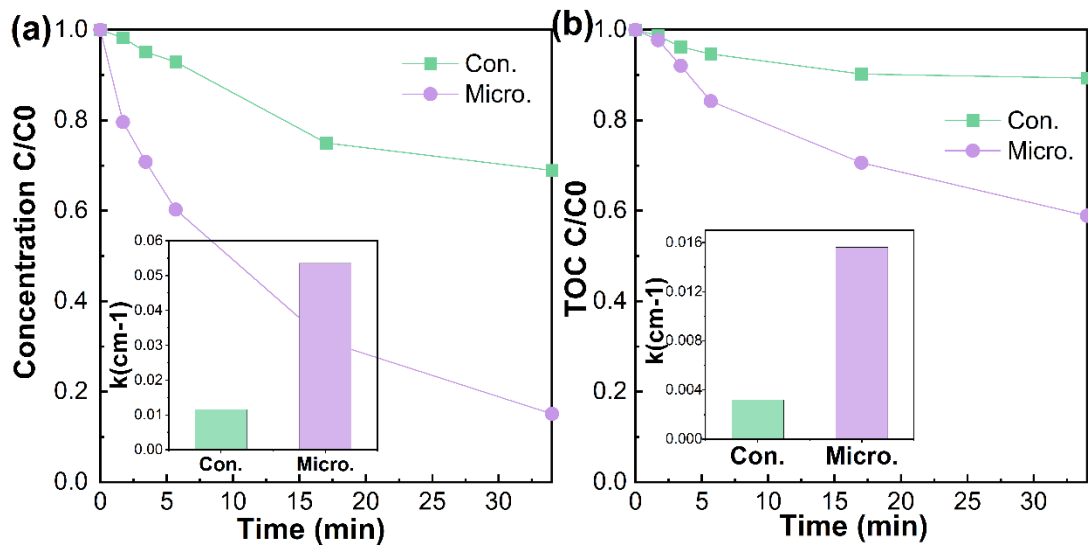


**Figure 5.7** Comparison of BPS and TOC removal in micro- and batch reactors

#### 5.3.4.2 Comparison of reaction rates

To obtain the reaction rate ( $r$ ) in both the microreactor and batch reactor from the first-order reaction model, we used the following equation (Ogbomo et al., 2024):

$$r = k * [A]$$

Where  $r$  is the instantaneous reaction rate,  $k$  is the rate constant, and  $[A]$  is the instant concentration of the BPS. Clearly, the instantaneous reaction rate  $r$  in both the batch reactor and microreactor was observed to decrease with time (**Fig. 5.8**). Initially, the reaction rate in the microreactor was approximately an order of magnitude higher than that in the batch reactor. Specifically, the reaction rate in the batch reactor exhibited a slight reduction from 0.250 to 0.172 s<sup>-1</sup> with time. Conversely, the reaction rate in the microreactor decreased more rapidly from 1.154 to 0.175 s<sup>-1</sup> as the retention time increased to 34 min, ultimately reaching the same value as in the batch reactor. This significantly high initial reaction rate in the microreactor could be attributed to the enhanced mass transfer and more efficient mixing conditions created by the microfluidic environment. The decline in the reaction rate over time in the microreactor indicated that the microfluidic device is highly effective at accelerating the reaction within a short retention time, making it particularly advantageous for processes requiring rapid degradation of contaminants. In general, the comparison of reaction rates highlighted the significant advantage of the microreactor in achieving higher reaction rates initially, which leads to more efficient and faster degradation of BPS compared to conventional reactors.

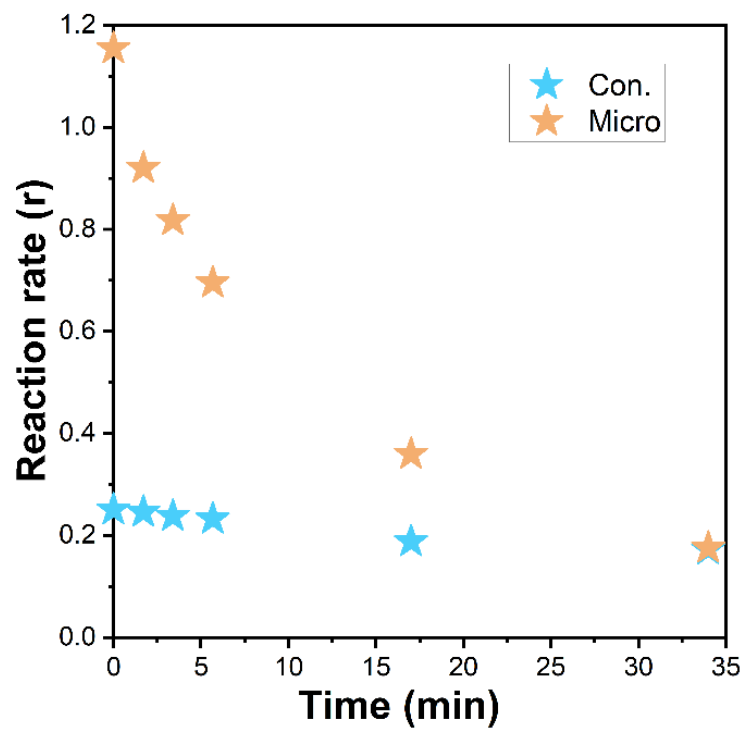


**Figure 5.8** Comparison of reaction rate under batch and micro-reactors

### 5.3.4.3 Comparison of energy consumption

Economics is a critical factor in selecting optimum treatment technologies, and energy consumption plays a major role in the overall operating cost, particularly for electricity-intensive processes. Bolton et al. (2001) developed the figures of merit for the comparison of AOPs. Electrical energy per order is applied to calculate the energy consumption required to remove a unit mass of contaminants using various electrical-driven AOPs. For batch and continuous reactors, the electrical energy per order is defined in the equations below:

$$\text{Electrical energy per order} = \frac{P \times t \times 1000}{V \times \lg \left( \frac{C_i}{C_f} \right)} \quad (\text{for a batch reactor}) \quad (5-1)$$

$$\text{Electrical energy per order} = \frac{P}{F \times \lg \left( \frac{C_i}{C_f} \right)} \quad (\text{for a continuous reactor}) \quad (5-2)$$

Where P is the total energy input of the processes (kW), V is the volume (L) of the water treated in time t (hour),  $C_i$  and  $C_f$  are the initial and final concentrations of organic contaminants (M or mol/L), and F is the flow rate ( $\text{m}^3/\text{h}$ ) for the water treated in a continuous flow system.

**Fig. 5.9a** illustrates the calculated BPS removal efficiency and energy consumption over time in the developed microreactor. The microreactor demonstrated an energy consumption of approximately 14 kWh/L while achieving over 80% removal efficiency. In stark contrast, the energy consumption rose up to 850 kWh/L with only 30% removal efficiency in the conventional reactor (**Fig. 5.9b**). This significant difference indicated that the microreactor offers a substantially higher removal efficiency of emerging contaminants such as BPS at a markedly lower energy consumption rate compared to the batch reactor. The enhanced mass transfer, improved light utilization rate, and efficient mixing within the microfluidic

environment contribute to this superior performance, making the microreactor a more economically viable option for large-scale applications in wastewater treatment.

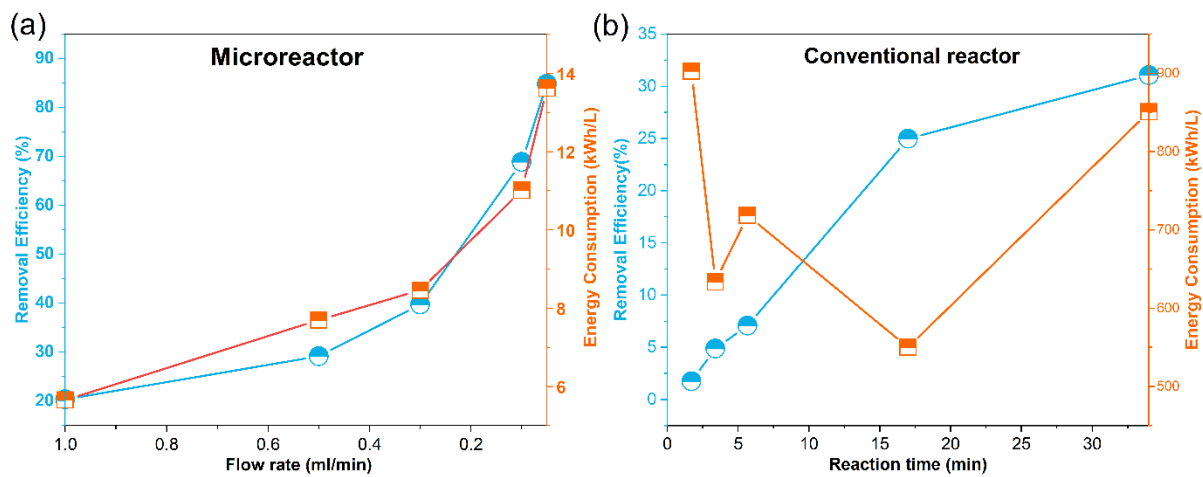


**Figure 5.9** Comparison of the energy consumption in the (a) microreactor and (b) conventional reactors

#### ***5.3.4.4 Acute toxicity evaluations of effluent from microreactor and conventional reactor***

The acute toxicity of the BPS solution before and after microfluidic AOP treatment was assessed by Microtox® bioassay under various flow rates (ranging from 2 to 0.01 ml/min), corresponding to different retention times (from 0.85 to 170 min). To provide a comparative analysis of toxicity trends in both the microreactor and conventional reactor under identical residence times, toxicity assessments were also performed on samples from the batch reactor using the same reaction conditions as the microreactor. The flow rates were converted into residence times in the microreactor (reactor volume 1.7 mL), allowing for the toxicity values to be plotted for both micro- and batch reactors on a single graph (**Fig. 5.10**).

The initial BPS solution exhibited moderate toxicity with an EC<sub>50</sub> value of 20.3%. In the conventional reactor, the EC<sub>50</sub> value decreased significantly from 20.3% to 0.26% within the first 34 min of reaction time, indicating an increase in acute toxicity. This initial increase was followed by a gradual decrease in toxicity, with the EC<sub>50</sub> value rising to 4.2% after 170 min of reaction time. This trend suggested that the degradation intermediates formed during the early stages of the reaction in the conventional reactor were more toxic than the parent compound BPS, but with extended reaction time, further degradation of these intermediates led to a reduction in overall toxicity. In contrast, the microreactor generally demonstrated a lower acute toxicity compared to the conventional reactor. When the residence time was 1.7 min, the toxicity in the microreactor reached its peak, with an EC<sub>50</sub> of 0.17%, after which the EC<sub>50</sub> increased to 6.821% at 170 min. This may be because the microreactor exhibited the ability to enhance mass transfer and provide more uniform irradiation, leading to more efficient

degradation of toxic intermediates, resulting in lower overall toxicity of the treated effluent over time. To confirm this hypothesis, future research aims to focus on the identification of intermediates over time in two reactors.

In summary, the microreactor not only improves the degradation and mineralization rates of BPS but also significantly reduces the energy consumption associated with the photocatalytic process, thereby presenting a more cost-effective and energy-efficient solution for the removal of emerging contaminants from wastewater. Additionally, the microreactor effectively controls and reduces the acute toxicity of the effluent more efficiently than the conventional reactor. This suggests that the microfluidic AOP system could offer significant advantages in terms of efficiency, safety, and operational costs for wastewater treatment applications.

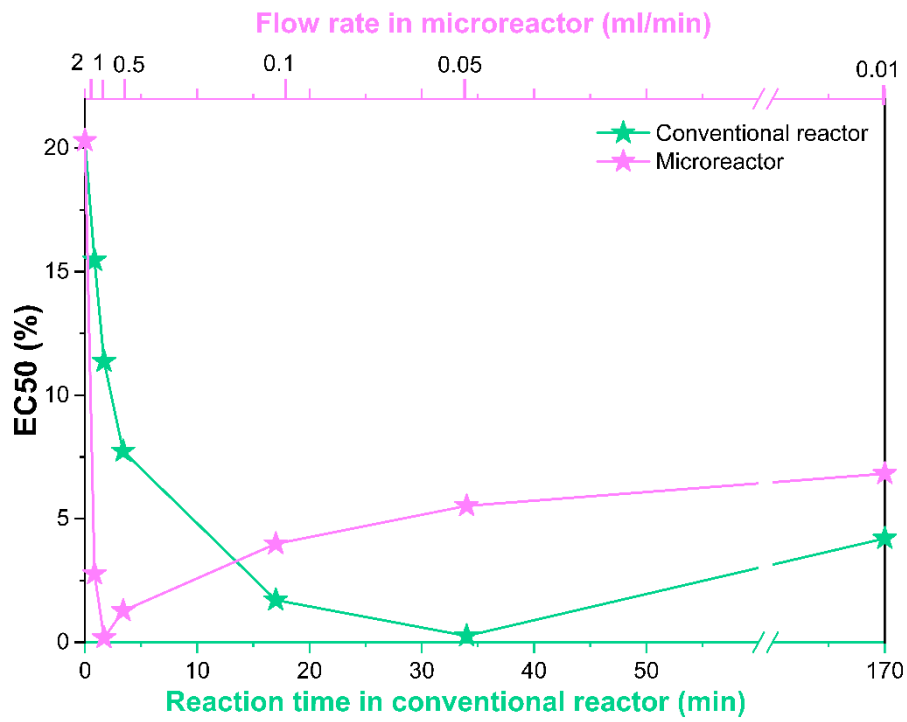


**Figure 5.10** Acute toxicity of effluent from conventional and micro-reactors

## 5.4 Summary

With their high internal specific surface areas, which impart high process efficiencies and minimal energy consumption, microreactors overcome many of the shortcomings of conventional reactors. This study innovatively developed a UV LED/composite nanosheet-based persulfate activation in a microfluidic system for BPS degradation. The  $\text{TiO}_2/\text{g-C}_3\text{N}_4$  nanosheets were synthesized and showed excellent photocatalytic performance in the microreactor over the conventional reactor. The factorial design analysis confirmed that the flow rate and light distance were the main factors affecting the performance of a microreactor. Comparative experiments between conventional reactors and microreactors have confirmed that microreactors can significantly improve emerging contaminants' removal efficiency, reduce energy consumption, and decrease the acute toxicity of effluent. This work offers valuable insight for the future development of AOPs in microreactors for emerging contaminants treatment.

**CHAPTER 6**  
**CONCLUSION AND RECOMMENDATIONS**

## 6.1 Conclusion

The ubiquitous occurrence of persistent and emerging contaminants such as PAHs and BPA and their substitutes (e.g., bisphenol S) in the environment and their adverse effects on both aquatic organisms and humans have attracted global concern. These contaminants are usually chemical stability and difficulty to be completely mineralized by traditional wastewater treatment. AOPs are considered an effective solution for the non-selective removal of persistent and emerging organic pollutants through the generation of reactive oxygen species. However, the limited process efficiency and high energy consumption are major concerns for the wide application of traditional AOPs.

To fill the gaps, the development of powerful treatment technologies to remove persistent and emerging contaminants is an urgent task that humanity is facing. This research, therefore, started by 1) reviewing the recent advances in AOP enhancement methods primarily focusing on synergetic persulfate activation and environmental microfluidics, followed by 2) developing a synergetic persulfate activation system by UV/O<sub>3</sub> process in a 1 L ozone reactor for the treatment of marine oily wastewater which includes various PAHs; and then 3) investigating UV/MnO<sub>2</sub> activated PS system for the BPA degradation; finally 4) designing a novel AOP-microreactor system to explore the degradation mechanism of BPS and the advantages of AOPs in microreactor over batch reactor.

Persulfate activation was recently demonstrated with enhanced contaminants removal in comparison with traditional hydroxyl radical-based AOPs. Various activation methods including physical methods (e.g., thermal, cavitation, electromagnetic radiation, and discharge

plasma) and chemical methods (e.g., alkaline, electrochemistry, and catalyst) were summarized in this work. Synergetic persulfate activation (a combination of some single activation methods) is believed to trend toward the direction of high efficiency, aiming to fully activate persulfate and minimize energy consumption and environmental effects. The key impact factors in those activation methods are discussed to help provide the technique support for practical application. The fast growth of the emerging area of environmental microfluidics has attracted public attention in the last decade. The hydrodynamic characteristics, designs, emerging applications, and challenges associated with applying AOP-microreactors were reviewed thoroughly. Several novel AOP-microreactor designs were exhibited to showcase the merits of microfluidic technology for AOP applications. Two scale-up strategies are recommended to maintain the microfluidic characteristics and achieve industry application by accelerating chemical processes with high-throughput reactors.

Synergetic persulfate activation by UV/O<sub>3</sub> process was investigated for the treatment of marine oily wastewater (including various PAHs). The degradation performance, toxicity assessment, and floc formation of three ozone-based processes (i.e., O<sub>3</sub> only, UV/O<sub>3</sub>, and UV/O<sub>3</sub>/PS) for light and heavy crude oils were investigated in this work. The results showed that, in comparison with O<sub>3</sub> and UV/O<sub>3</sub> processes, the addition of PS could achieve more than 90% of degradation efficiency for PAHs within 30 min. This provided evidence for the addition of PS in O<sub>3</sub>-based AOP to explore the optimal treatment conditions for scale-up to an operational system. Acute toxicity was significantly reduced in all three processes, confirming the significance of the treatment processes in reducing the negative ecological impacts of oily

wastewater. Another essential contribution of this study was to investigate the fate of flocs formed during O<sub>3</sub>-based treatments, which was rarely reported in the literature. The morphology and functional groups of flocs that formed during O<sub>3</sub>-based processes were characterized, showing that the floating flocs could be further degraded significantly in the UV/O<sub>3</sub>/PS process. Overall, the results developed and verified a more energy-effective and low environmental impact approach to treating PAHs containing wastewater by synergetic PS-based AOP.

The work in Chapter 4 focused on synergetic persulfate activation using transition metal oxide (i.e., MnO<sub>2</sub>) and UV as hybrid activators. A MnO<sub>2</sub>/UV/PS process was proposed for the efficient removal and mineralization of BPA from wastewater streams. The results showed that the synergistic use of MnO<sub>2</sub> and UV is a more powerful hybrid activator for PS activation, and it works in a large variation of pH levels (3.6 to 10.0). The presence of SO<sub>4</sub><sup>•-</sup> and <sup>1</sup>O<sub>2</sub> was the key to the more rapid decomposition of BPA. Infrared spectra showed that UV irradiation could stimulate the generation of –OH groups on the MnO<sub>2</sub> surface, facilitating PS activation in this process. The degradation pathways consisting of 5 steps and 13 intermediates were further investigated using GC-MS. The acute toxicity of reaction mixtures during the process confirmed the overall reduction by the proposed method. These findings indicated that the synergetic use of MnO<sub>2</sub> and UV improved PS catalytic activation, and this provides a more promising means of treating emerging organic contaminants such as BPA.

The main purpose of the study in Chapter 5 was to demonstrate the value of the introduction of environmental microfluidics into AOP as an effective way to improve

efficiency and reduce energy consumption and also gain an in-depth understanding of the mechanism and performance. A UV light/composite nanosheet-based persulfate activation was first developed and incorporated into a microfluidic AOP system, and then BPS degradation was examined, followed by comparative testing in a conventional batch reactor. The  $\text{TiO}_2/\text{g-C}_3\text{N}_4$  nanosheets were synthesized and showed excellent photocatalytic performance in the microreactor over the batch reactor. The factorial design analysis confirmed that the flow rate and light distance were the leading factors affecting the performance of the microreactor. The reaction rates were calculated, and the results showed that the initial reaction rate in the microreactor was around one order of magnitude higher than that in the batch reactor. The comparative experiments between the two systems demonstrated that the microreactors could significantly improve the removal efficiency for BPS and reduce the acute toxicity in the effluent. This work offers valuable insights for the future development of AOPs in microreactors for removal of emerging contaminants from wastewater streams.

## 6.2 Research Contributions

The main contributions of this dissertation can be summarized below:

1. A comprehensive review of the recent advances of AOPs focusing on synergetic persulfate and environmental microfluidics was completed. Various PS activation methods and their synergetic strategies were discussed. The advantages of synergetic persulfate activation, such as high efficiency and minimize energy consumption and environmental effects, made it the trend of PS-AOPs. The rapidly emerging area of environmental microfluidics was explored for the first time. The hydrodynamic

characteristics, fabrications, various AOP-microreactor designs, limitations, scale-up strategies, and cost-reduction of AOP-microreactor systems were discussed in detail. This work offers valuable insight for future research and development of AOPs in microreactors for environmental purposes.

2. A variety of PS-based AOP coupling enhancement systems were developed for the degradation of persistent organic pollutants such as PAHs and several emerging contaminants (i.e., BPA, BPS). The degradation mechanisms of these pollutants were disclosed and discussed in detail. Among them, the analysis of the different components degradation in marine oily wastewater (e.g., TPHs, PAHs) was the first time to demonstrate the effective degradation of this complex pollutant, which provided solid scientific evidence and technical solutions for removing oil from marine water. Particularly, it presented important practical values for improving the current practice in handling oily wastewater (i.e., decanting process) during marine oil spill responses. The degradation mechanism of synergetic PS-based AOP systems on pollutants, the degradation pathways under different conditions, and the change of acute toxicity before and after treatment were explored in-depth. Those developed AOP methods and findings could not only fill the knowledge gaps but also provide powerful tools for treatment of wastewater containing persistent and emerging contaminants.
3. The miniaturized system (a novel UV light-induced microreactor) has been developed to explore the mechanisms and feasibility of integration of AOP and microfluidics and evaluate the efficiency in pollutant removal and energy consumption. Significantly, the

new method could improve oxidation performance with less energy consumption, indicating a highly innovative and promising solution for removing traces of persistent organics and emerging contaminants (e.g., Bisphenols) from water in this study. To the candidate's best knowledge, this was the first attempt in the field. Furthermore, the integration of AOPs and microfluidics presented a bright future and the right direction for AOPs advancement, particularly in dealing with persistent and emerging contaminants. The comparison with the batch reactor further demonstrated the advantages of the developed microreactors. The study achieved the goal of advancing oxidation with fast mass transfer in the microreactors and recommended the optimum operational conditions to provide scientific evidence for industrial applications.

### **6.3 Recommendations for Future Research**

1. It is inspired by the synergistic persulfate activation methods to find more effective, robust, and energy-efficient methods, especially through the development of new carbon-based materials and their combined use with natural sunlight for AOPs. The dominant role of free radicals (e.g.,  $\bullet\text{OH}$ ,  $\text{SO}_4^{\bullet-}$ , and  $\bullet\text{O}_2^-$ ) during persulfate activation for degradation of emerging contaminants still needs to be further explored.
2. Future research on emerging contaminants removal by AOPs needs to be more thorough and in-depth in terms of reaction mechanisms and degradation pathways and associated toxicological effects, as well as feasibility studies on large-scale applications.

3. The scientific understanding of AOPs in micro-scale reactors is much desired. Although the hydrodynamic characteristics of microreactors have been well documented, the kinetic models of advanced oxidation processes in microreactors demand further development, verification, and applications.
4. An important goal of AOP-microreactor system development is to realize both high throughput and cost-efficiency for practical needs in the water and wastewater treatment sector. Maintaining microfluidic characteristics (advantages) while expanding throughput is a key challenge and worth pondering. Scale-up and feasibility studies are much desired for microreactor-inspired AOPs to support industrial applications.

## REFERENCES

- Ahmed, S. N., & Haider, W. 2018. Heterogeneous photocatalysis and its potential applications in water and wastewater treatment: a review. *Nanotechnology*, 29(34), 342001. <https://doi.org/10.1088/1361-6528/aac6ea>
- Akmaz, S., Iscan, O., Gurkaynak, M., & Yasar, M. 2011. The structural characterization of saturate, aromatic, resin, and asphaltene fractions of Batiraman crude oil. *Petroleum Science and Technology*, 29(2), 160-171. <https://doi.org/10.1080/10916460903330361>
- Alemu, Z. A., & Dioha, M. O. 2020. Modelling scenarios for sustainable water supply and demand in Addis Ababa city, Ethiopia. *Environmental Systems Research*, 9, 1-14. <https://doi.org/10.1186/s40068-020-00168-3>
- Ambade, B., Sethi, S. S., Giri, B., Biswas, J. K., & Baudh, K. 2022. Characterization, behavior, and risk assessment of polycyclic aromatic hydrocarbons (PAHs) in the estuary sediments. *Bulletin of environmental contamination and toxicology*, 108(2), 243-252. <https://doi.org/10.1007/s00128-021-03393-3>
- Ana, K. M. S., & Espino, M. P. 2020. Occurrence and distribution of hormones and bisphenol A in Laguna Lake, Philippines. *Chemosphere*, 256, 127122. <https://doi.org/10.1016/j.chemosphere.2020.127122>
- Ananth, M., Pethkar, S., & Dakshinamurthi, K. 1998. Distortion of MnO<sub>6</sub> octahedra and electrochemical activity of Nstutite-based MnO<sub>2</sub> polymorphs for alkaline electrolytes—an FTIR study. *Journal of power sources*, 75(2), 278-282. [https://doi.org/10.1016/S0378-7753\(98\)00100-1](https://doi.org/10.1016/S0378-7753(98)00100-1)
- Aran, H., Salamon, D., Rijnaarts, T., Mul, G., Wessling, M., & Lammertink, R. 2011. Porous

- photocatalytic membrane microreactor (P2M2): a new reactor concept for photochemistry. *Journal of Photochemistry and Photobiology A: Chemistry*, 225(1), 36-41. <https://doi.org/10.1016/j.jphotochem.2011.09.022>
- Asemani, M., & Rabbani, A. R. 2020. Detailed FTIR spectroscopy characterization of crude oil extracted asphaltene: Curve resolve of overlapping bands. *Journal of Petroleum Science and Engineering*, 185, 106618. <https://doi.org/10.1016/j.petrol.2019.106618>
- Ashikari, Y., Kawaguchi, T., Mandai, K., Aizawa, Y., & Nagaki, A. 2020. A Synthetic Approach to Dimetalated Arenes Using Flow Microreactors and the Switchable Application to Chemoselective Cross-Coupling Reactions. *Journal of the American Chemical Society*, 142(40), 17039-17047. <https://doi.org/10.1021/jacs.0c06370>
- Azzouz, I., Habba, Y. G., Capochichi-Gnambodoe, M., Marty, F., Vial, J., Leprince-Wang, Y., & Bourouina, T. 2018. Zinc oxide nano-enabled microfluidic reactor for water purification and its applicability to volatile organic compounds. *Microsystems & Nanoengineering*, 4(1), 1-7. <https://doi.org/10.1038/micronano.2017.93>
- Babuponnusami, A., & Muthukumar, K. 2014. A review on Fenton and improvements to the Fenton process for wastewater treatment. *Journal of Environmental Chemical Engineering*, 2(1), 557-572. <https://doi.org/10.1016/j.jece.2013.10.011>
- Baird, S. J., Bailey, E. A., & Vorhees, D. J. 2007. Evaluating human risk from exposure to alkylated PAHs in an aquatic system. *Human and Ecological Risk Assessment*, 13(2), 322-338. <https://doi.org/10.1080/10807030701226277>
- Banerjee, R., Kumar, S. J., Mehendale, N., Sevda, S., & Garlapati, V. K. 2019. Intervention of

microfluidics in biofuel and bioenergy sectors: Technological considerations and future prospects. *Renewable and Sustainable Energy Reviews*, 101, 548-558.

<https://doi.org/10.1016/j.rser.2018.11.040>

Blackburn, T. R., Holland, H. D., & Ceasar, G. P. 1979. Viking gas exchange reaction:

Simulation on UV-irradiated manganese dioxide substrate. *Journal of Geophysical Research: Solid Earth*, 84(B14), 8391-8394.

<https://doi.org/10.1029/JB084iB14p08391>

Bojang, A. A., & Wu, H.-S. 2020a. Design, fundamental principles of fabrication and

applications of microreactors. *Processes*, 8(8), 891. <https://doi.org/10.3390/pr8080891>

Bojang, A. A., & Wu, H.-S. 2020b. Design, Fundamental Principles of Fabrication, and

Applications of Microreactors. *Processes*, 8(8), 891.

<https://doi.org/10.3390/pr8080891>

Bolton, J. R., Bircher, K. G., Tumas, W., & Tolman, C. A. 2001. Figures-of-merit for the

technical development and application of advanced oxidation technologies for both electric-and solar-driven systems (IUPAC Technical Report). *Pure and Applied Chemistry*, 73(4), 627-637. <https://doi.org/10.1351/pac200173040627>

<https://doi.org/10.1351/pac200173040627>

Brillas, E., Sirés, I., & Oturan, M. A. 2009. Electro-Fenton process and related

electrochemical technologies based on Fenton's reaction chemistry. *Chemical reviews*, 109(12), 6570-6631. <https://doi.org/10.1021/cr900136g>

Bugden, J., Yeung, C., Kepkay, P., & Lee, K. 2008. Application of ultraviolet fluorometry and

excitation–emission matrix spectroscopy (EEMS) to fingerprint oil and chemically

dispersed oil in seawater. *Marine Pollution Bulletin*, 56(4), 677-685.

<https://doi.org/10.1016/j.marpolbul.2007.12.022>

Bumroongsakulsawat, P., Khongthon, W., & Pavarajarn, V. 2020. Degradation of diuron in water by electrochemical advanced oxidation in a microreactor: effects of anion contamination on degradation and toxicity. *Journal of Environmental Chemical Engineering*, 103824. <https://doi.org/10.1016/j.jece.2020.103824>

Cambié, D., Bottecchia, C., Straathof, N. J., Hessel, V., & Noel, T. 2016. Applications of continuous-flow photochemistry in organic synthesis, material science, and water treatment. *Chemical reviews*, 116(17), 10276-10341.

<https://doi.org/10.1021/acs.chemrev.5b00707>

Cao, E., Radhakrishnan, A. N., Hasanudin, R. b., & Gavriilidis, A. 2021a. Study of Liquid–Solid Mass Transfer and Hydrodynamics in Micropacked Bed with Gas–Liquid Flow. *Industrial & Engineering Chemistry Research*.

<https://doi.org/10.1021/acs.iecr.1c00089>

Cao, Q., Sang, L., Tu, J., Xiao, Y., Liu, N., Wu, L., & Zhang, J. 2020a. Rapid degradation of refractory organic pollutants by continuous ozonation in a micro-packed bed reactor. *Chemosphere*, 128621. <https://doi.org/10.1016/j.chemosphere.2020.128621>

Cao, Q., Sang, L., Tu, J., Xiao, Y., Liu, N., Wu, L., & Zhang, J. 2021b. Rapid degradation of refractory organic pollutants by continuous ozonation in a micro-packed bed reactor. *Chemosphere*, 270, 128621. <https://doi.org/10.1016/j.chemosphere.2020.128621>

Cao, Y., Kang, Q., Zhang, B., Zhu, Z., Dong, G., Cai, Q., Lee, K., & Chen, B. 2022. Machine

learning-aided causal inference for unraveling chemical dispersant and salinity effects on crude oil biodegradation. *Bioresource Technology*, 345, 126468.

<https://doi.org/10.1016/j.biortech.2021.126468>

Cao, Y., Zhang, B., Zhu, Z., Rostami, M., Dong, G., Ling, J., Lee, K., Greer, C. W., & Chen, B. 2021c. Access-dispersion-recovery Strategy for Enhanced Mitigation of Heavy Crude Oil Pollution Using Magnetic Nanoparticles Decorated Bacteria. *Bioresource Technology*, 125404. <https://doi.org/10.1016/j.biortech.2021.125404>

Cao, Y., Zhang, B., Zhu, Z., Song, X., Cai, Q., Chen, B., Dong, G., & Ye, X. 2020b. Microbial eco-physiological strategies for salinity-mediated crude oil biodegradation. *Science of the total environment*, 727, 138723.

<https://doi.org/10.1016/j.scitotenv.2020.138723>

Cao, Y., Zhang, B., Zhu, Z., Xin, X., Wu, H., & Chen, B. 2021d. Microfluidic Based Whole-Cell Biosensors for Simultaneously On-Site Monitoring of Multiple Environmental Contaminants. *Frontiers in Bioengineering and Biotechnology*, 9, 178.

<https://doi.org/10.3389/fbioe.2021.622108>

Cao, Y., Zhang, B., Zhu, Z., Xin, X., Wu, H., & Chen, B. 2021e. Microfluidic based whole-cell biosensors for simultaneously on-site monitoring of multiple environmental contaminants. *Frontiers in Bioengineering and Biotechnology*, 9, 622108.

<https://doi.org/10.3389/fbioe.2021.622108>

Castellanos, R. M., Bassin, J. P., Dezotti, M., Boaventura, R. A., & Vilar, V. J. 2020. Tube-in-tube membrane reactor for heterogeneous TiO<sub>2</sub> photocatalysis with radial addition of

H<sub>2</sub>O<sub>2</sub>. *Chemical Engineering Journal*, 395, 124998.

<https://doi.org/10.1016/j.cej.2020.124998>

Chaplin, B. P. 2014. Critical review of electrochemical advanced oxidation processes for water treatment applications. *Environmental Science: Processes & Impacts*, 16(6), 1182-1203. DOI: 10.1039/C3EM00679D

Charles, G., Roques-Carmes, T., Becheikh, N., Falk, L., Commenge, J.-M., & Corbel, S. 2011. Determination of kinetic constants of a photocatalytic reaction in micro-channel reactors in the presence of mass-transfer limitation and axial dispersion. *Journal of Photochemistry and Photobiology A: Chemistry*, 223(2-3), 202-211.

<https://doi.org/10.1016/j.jphotochem.2011.08.019>

Chen, F., Huang, X.-T., Bai, C.-W., Zhang, Z.-Q., Duan, P.-J., Sun, Y.-J., Chen, X.-J., Zhang, B.-B., & Zhang, Y.-S. 2024. Advancements in heterogeneous activation of persulfates: Exploring mechanisms, challenges in organic wastewater treatment, and innovative solutions. *Chemical Engineering Journal*, 148789.

<https://doi.org/10.1016/j.cej.2024.148789>

Chen, Y., Fang, J., Dai, B., Wei, H., Kou, J., & Lu, C. 2020a. Seaweed bio-inspired ZnO piezoelectric cilia array applied in microreactors for enhanced photocatalytic performance. *Catalysis Science & Technology*, 10(8), 2337-2342. DOI:

10.1039/C9CY02509J

Chen, Z., Zheng, Z., Li, D., Chen, H., & Xu, Y. 2020b. Continuous supercritical water oxidation treatment of oil-based drill cuttings using municipal sewage sludge as

diluent. *Journal of hazardous materials*, 384, 121225.

<https://doi.org/10.1016/j.jhazmat.2019.121225>

Chiang, K., Lim, T. M., Tsen, L., & Lee, C. C. 2004. Photocatalytic degradation and mineralization of bisphenol A by TiO<sub>2</sub> and platinized TiO<sub>2</sub>. *Applied Catalysis A: General*, 261(2), 225-237. <https://doi.org/10.1016/j.apcata.2003.11.004>

Chong, M. N., Jin, B., Chow, C. W., & Saint, C. 2010. Recent developments in photocatalytic water treatment technology: a review. *Water research*, 44(10), 2997-3027. <https://doi.org/10.1016/j.watres.2010.02.039>

Chougala, L., Yatnatti, M., Linganagoudar, R., Kamble, R., & Kadadevarmath, J. 2017. A simple approach on synthesis of TiO<sub>2</sub> nanoparticles and its application in dye sensitized solar cells. DOI: 10.21272/jnep.9(4).04005

Coha, M., Farinelli, G., Tiraferri, A., Minella, M., & Vione, D. 2021. Advanced oxidation processes in the removal of organic substances from produced water: Potential, configurations, and research needs. *Chemical Engineering Journal*, 128668. <https://doi.org/10.1016/j.cej.2021.128668>

Corbel, S., Charles, G., Becheikh, N., Roques-Carmes, T., & Zahraa, O. 2012. Modelling and design of microchannel reactor for photocatalysis: Here, the freedom of design and accuracy of the stereolithography technique were exploited to study the photolytic degradation of salicylic acid as a model water pollutant in stereolithography-fabricated microchannel reactors. *Virtual and physical prototyping*, 7(3), 203-209. <https://doi.org/10.1080/17452759.2012.708837>

Criquet, J., & Leitner, N. K. V. 2009. Degradation of acetic acid with sulfate radical generated by persulfate ions photolysis. *Chemosphere*, 77(2), 194-200.

<https://doi.org/10.1016/j.chemosphere.2009.07.040>

Da Silva, B., Habibi, M., Ognier, S., Schelcher, G., Mostafavi-Amjad, J., Khalesifard, H., Tatoulian, M., & Bonn, D. 2016. Silver nanocluster catalytic microreactors for water purification. *The European Physical Journal Special Topics*, 225(4), 707-714. DOI: 10.1140/epjst/e2015-50262-6

Danyliuk, N., Tatarchuk, T., Kannan, K., & Shyichuk, A. 2021. Optimization of TiO<sub>2</sub>-P25 photocatalyst dose and H<sub>2</sub>O<sub>2</sub> concentration for advanced photo-oxidation using smartphone-based colorimetry. *Water Science and Technology*, 84(2), 469-483.

<https://doi.org/10.2166/wst.2021.236>

Das, S., & Srivastava, V. C. 2016. Microfluidic-based photocatalytic microreactor for environmental application: a review of fabrication substrates and techniques, and operating parameters. *Photochemical & Photobiological Sciences*, 15(6), 714-730.

<https://doi.org/10.1039/C5PP00469A>

de Araujo, L. G., Prado, E. S. A. P., de Souza Miranda, F., Vicente, R., da Silva Sobrinho, A. S., Petraconi Filho, G., & Marumo, J. T. 2020. Physicochemical modifications of radioactive oil sludge by ozone treatment. *Journal of Environmental Chemical Engineering*, 8(5), 104128. <https://doi.org/10.1016/j.jece.2020.104128>

de Freitas, E., Bubna, G., Brugnari, T., Kato, C., Nolli, M., Rauen, T., Moreira, R., Peralta, R., Bracht, A., & de Souza, C. 2017a. Removal of bisphenol A and evaluation of

ecotoxicity of degradation products by laccases from *Pleurotus ostreatus* and

*Pleurotus pulmonarius*. *Chem. Eng. J.*, 330, 1361-1369.

<https://doi.org/10.1016/j.cej.2017.08.051>

de Freitas, E. N., Bubna, G. A., Brugnari, T., Kato, C. G., Nolli, M., Rauen, T. G., Moreira, R.

d. F. P. M., Peralta, R. A., Bracht, A., & de Souza, C. G. 2017b. Removal of bisphenol

A by laccases from *Pleurotus ostreatus* and *Pleurotus pulmonarius* and evaluation of

ecotoxicity of degradation products. *Chemical Engineering Journal*, 330, 1361-1369.

<https://doi.org/10.1016/j.cej.2017.08.051>

de Sá, D., Vasconcellos, L., de Souza, J., Marinkovic, B., Del Rosso, T., Fulvio, D., Maza, D.,

Massi, A., & Pandoli, O. 2018. Intensification of photocatalytic degradation of

organic dyes and phenol by scale-up and numbering-up of meso- and microfluidic

TiO<sub>2</sub> reactors for wastewater treatment. *Journal of Photochemistry and Photobiology*

*A: Chemistry*, 364, 59-75. <https://doi.org/10.1016/j.jphotochem.2018.05.020>

Dessimoz, A.-L., Cavin, L., Renken, A., & Kiwi-Minsker, L. 2008. Liquid–liquid two-phase

flow patterns and mass transfer characteristics in rectangular glass microreactors.

*Chemical Engineering Science*, 63(16), 4035-4044.

<https://doi.org/10.1016/j.ces.2008.05.005>

Devi, P., Das, U., & Dalai, A. K. 2016. In-situ chemical oxidation: principle and applications

of peroxide and persulfate treatments in wastewater systems. *Science of The Total*

*Environment*, 571, 643-657. <https://doi.org/10.1016/j.scitotenv.2016.07.032>

Deyris, P.-A., Pelissier, F., Grison, C. M., Hesemann, P., Petit, E., & Grison, C. 2023.

Efficient removal of persistent and emerging organic pollutants by biosorption using abundant biomass wastes. *Chemosphere*, 313, 137307.

<https://doi.org/10.1016/j.chemosphere.2022.137307>

Diantoro, M., Kusumaatmaja, A., & Triyana, K. (2018). *Study on photocatalytic properties of TiO<sub>2</sub> nanoparticle in various pH condition*. Paper presented at the Journal of Physics: Conference Series. DOI 10.1088/1742-6596/1011/1/012069

Díaz-Angulo, J., Cotillas, S., Gomes, A. I., Miranda, S. M., Mueses, M., Machuca-Martínez, F., Rodrigo, M. A., Boaventura, R. A., & Vilar, V. J. 2021. A tube-in-tube membrane microreactor for tertiary treatment of urban wastewaters by photo-Fenton at neutral pH: A proof of concept. *Chemosphere*, 263, 128049.

<https://doi.org/10.1016/j.chemosphere.2020.128049>

Ding, J., Bu, L., Zhao, Q., Kabutey, F. T., Wei, L., & Dionysiou, D. D. 2020. Electrochemical activation of persulfate on BDD and DSA anodes: Electrolyte influence, kinetics and mechanisms in the degradation of bisphenol A. *Journal of hazardous materials*, 388, 121789. <https://doi.org/10.1016/j.jhazmat.2019.121789>

Divya, L. M., Prasanth, G. K., Arun, K. G., & Sadasivan, C. 2018. Bisphenol-A carbonate dimer is a more preferred substrate for laccase mediated degradation than the Biphenol-A in its monomeric and dimeric forms. *International Biodeterioration & Biodegradation*, 135, 19-23. <https://doi.org/10.1016/j.ibiod.2018.09.006>

Dłuska, E., Wroński, S., & Ryszczuk, T. 2004. Interfacial area in gas–liquid Couette–Taylor flow reactor. *Experimental thermal and fluid science*, 28(5), 467-472.

<https://doi.org/10.1016/j.expthermflusci.2003.06.003>

- Dong, G., Chen, B., Liu, B., Hounjet, L. J., Cao, Y., Stoyanov, S. R., Yang, M., & Zhang, B. 2022. Advanced Oxidation Processes in Microreactors for Water and Wastewater Treatment: Development, Challenges, and Opportunities. *Water research*, 118047. <https://doi.org/10.1016/j.watres.2022.118047>
- Dong, G., Chen, B., Liu, B., Stoyanov, S. R., Cao, Y., Yang, M., & Zhang, B. 2021. UV stimulated manganese dioxide for the persulfate catalytic degradation of bisphenol A. *Catalysts*, 11(4), 502. <https://doi.org/10.3390/catal11040502>
- Dong, G., Huang, L., Wu, X., Wang, C., Liu, Y., Liu, G., Wang, L., Liu, X., & Xia, H. 2018. Effect and mechanism analysis of MnO<sub>2</sub> on permeable reactive barrier (PRB) system for the removal of tetracycline. *Chemosphere*, 193, 702-710. <https://doi.org/10.1016/j.chemosphere.2017.11.085>
- Dong, Z., Zhang, Q., Chen, B.-Y., & Hong, J. 2019. Oxidation of bisphenol A by persulfate via Fe<sub>3</sub>O<sub>4</sub>- $\alpha$ -MnO<sub>2</sub> nanoflower-like catalyst: mechanism and efficiency. *Chemical Engineering Journal*, 357, 337-347. <https://doi.org/10.1016/j.cej.2018.09.179>
- Elvira, K. S., i Solvas, X. C., Wootton, R. C., & Demello, A. J. 2013. The past, present and potential for microfluidic reactor technology in chemical synthesis. *Nature chemistry*, 5(11), 905. <https://doi.org/10.1038/nchem.1753>
- Eskandarloo, H., & Badiiei, A. 2015. Fabrication of an inexpensive and high efficiency microphotoreactor using CO<sub>2</sub> laser technique for photocatalytic water treatment applications. *Environmental technology*, 36(8), 1063-1073.

<https://doi.org/10.1080/09593330.2014.974681>

Eskandarloo, H., Badiei, A., Behnajady, M. A., & Ziarani, G. M. 2015. UV-LEDs assisted preparation of silver deposited TiO<sub>2</sub> catalyst bed inside microchannels as a high efficiency microphotoreactor for cleaning polluted water. *Chemical Engineering Journal*, 270, 158-167. <https://doi.org/10.1016/j.cej.2015.01.117>

Eslami, A., Hashemi, M., & Ghanbari, F. 2018. Degradation of 4-chlorophenol using catalyzed peroxymonosulfate with nano-MnO<sub>2</sub>/UV irradiation: Toxicity assessment and evaluation for industrial wastewater treatment. *Journal of Cleaner Production*, 195, 1389-1397. <https://doi.org/10.1016/j.jclepro.2018.05.137>

Falk, L., & Commenge, J.-M. 2010. Performance comparison of micromixers. *Chemical Engineering Science*, 65(1), 405-411. <https://doi.org/10.1016/j.ces.2009.05.045>

Fang, C., & Huang, Q. 2018. Dielectric barrier discharge plasma activates persulfate to degrade norfloxacin: mechanism and degradation pathways. *Plasma Medicine*, 8(4). DOI: 10.1615/PlasmaMed.2018028857

Fang, Z., Huang, R., Chelme-Ayala, P., Shi, Q., Xu, C., & El-Din, M. G. 2019. Comparison of UV/Persulfate and UV/H<sub>2</sub>O<sub>2</sub> for the removal of naphthenic acids and acute toxicity towards *Vibrio fischeri* from petroleum production process water. *Science of the total environment*, 694, 133686. <https://doi.org/10.1016/j.scitotenv.2019.133686>

Fath, V., Szmaiz, S., Lau, P., Kockmann, N., & Röder, T. 2019. Model-Based Scale-Up Predictions: From Micro-to Millireactors Using Inline Fourier Transform Infrared Spectroscopy. *Organic Process Research & Development*, 23(9), 2020-2030.

<https://doi.org/10.1021/acs.oprd.9b00265>

Fischer, J., Lange, T., Boehling, R., Rehfinger, A., & Klemm, E. 2010. Uncatalyzed selective oxidation of liquid cyclohexane with air in a microcapillary reactor. *Chemical Engineering Science*, 65(16), 4866-4872. <https://doi.org/10.1016/j.ces.2010.05.028>

Fisher, B., Thankamony, A., Mendiola, J., Petry, C., Frederiksen, H., Andersson, A., Juul, A., Ong, K., Dunger, D., & Hughes, I. 2020. Maternal serum concentrations of bisphenol A and propyl paraben in early pregnancy are associated with male infant genital development. *Human Reproduction*, 35(4), 913-928.  
<https://doi.org/10.1093/humrep/deaa045>

Foster, J. E. 2017. Plasma-based water purification: Challenges and prospects for the future. *Physics of Plasmas*, 24(5), 055501. <https://doi.org/10.1063/1.4977921>

Frontistis, Z., Daskalaki, V. M., Hapeshi, E., Drosou, C., Fatta-Kassinou, D., Xekoukoulotakis, N. P., & Mantzavinos, D. 2012. Photocatalytic (UV-A/TiO<sub>2</sub>) degradation of 17 $\alpha$ -ethynylestradiol in environmental matrices: Experimental studies and artificial neural network modeling. *Journal of Photochemistry and Photobiology A: Chemistry*, 240, 33-41. <https://doi.org/10.1016/j.jphotochem.2012.05.007>

Gao, M., Zeng, Z., Sun, B., Zou, H., Chen, J., & Shao, L. 2012. Ozonation of azo dye Acid Red 14 in a microporous tube-in-tube microchannel reactor: Decolorization and mechanism. *Chemosphere*, 89(2), 190-197.  
<https://doi.org/10.1016/j.chemosphere.2012.05.083>

Gao, X., Ma, J., Chen, Y., & Wang, H.-S. 2015. Rapid responses and mechanism of action for

- low-dose bisphenol S on ex vivo rat hearts and isolated myocytes: evidence of female-specific proarrhythmic effects. *Environmental health perspectives*, 123(6), 571-578. DOI: 10.1289/ehp.1408679
- Gao, Y., Cong, S., He, Y., Zou, D., Liu, Y., Yao, B., & Sun, W. 2020. Study on the mechanism of degradation of tetracycline hydrochloride by microwave-activated sodium persulfate. *Water Science and Technology*, 82(9), 1961-1970.  
<https://doi.org/10.2166/wst.2024.004>
- Gassie, L. W., & Englehardt, J. D. 2019. Mineralization of greywater organics by the ozone-UV advanced oxidation process: Kinetic modeling and efficiency. *Environmental Science: Water Research & Technology*, 5(11), 1956-1970.  
<https://doi.org/10.1039/C9EW00653B>
- Geng, Y., Ling, S., Huang, J., & Xu, J. 2020. Multiphase microfluidics: Fundamentals, fabrication, and functions. *Small*, 16(6), 1906357.  
<https://doi.org/10.1002/sml.201906357>
- Ghauch, A., & Tuqan, A. M. 2012. Oxidation of bisoprolol in heated persulfate/H<sub>2</sub>O systems: kinetics and products. *Chemical Engineering Journal*, 183, 162-171.  
<https://doi.org/10.1016/j.cej.2011.12.048>
- Gheraout, D., & Elboughdiri, N. 2020. Advanced oxidation processes for wastewater treatment: facts and future trends. *Open Access Library Journal*, 7(2), 1-15. DOI: 10.4236/oalib.1106139
- Gioria, E., Signorini, C., Wisniewski, F., & Gutierrez, L. 2020a. Green synthesis of time-

- stable palladium nanoparticles using microfluidic devices. *Journal of Environmental Chemical Engineering*, 8(5), 104096. <https://doi.org/10.1016/j.jece.2020.104096>
- Gioria, E., Signorini, C., Wisniewski, F., & Gutierrez, L. 2020b. Green synthesis of time-stable palladium nanoparticles using microfluidic devices. *Journal of Environmental Chemical Engineering*, 104096. <https://doi.org/10.1016/j.jece.2020.104096>
- Gorges, R., Meyer, S., & Kreisel, G. 2004. Photocatalysis in microreactors. *Journal of Photochemistry and Photobiology A: Chemistry*, 167(2-3), 95-99. <https://doi.org/10.1016/j.jphotochem.2004.04.004>
- Guan, Y.-H., Ma, J., Li, X.-C., Fang, J.-Y., & Chen, L.-W. 2011. Influence of pH on the formation of sulfate and hydroxyl radicals in the UV/peroxymonosulfate system. *Environmental science & technology*, 45(21), 9308-9314. <https://doi.org/10.1021/es2017363>
- Gujar, S. K., Divyapriya, G., Gogate, P. R., & Nidheesh, P. V. 2023. Environmental applications of ultrasound activated persulfate/peroxymonosulfate oxidation process in combination with other activating agents. *Critical Reviews in Environmental Science and Technology*, 53(6), 780-802. DOI:10.1080/10643389.2022.2085965
- Guo, C., Ge, M., Liu, L., Gao, G., Feng, Y., & Wang, Y. 2010. Directed synthesis of mesoporous TiO<sub>2</sub> microspheres: catalysts and their photocatalysis for bisphenol A degradation. *Environmental Science & Technology*, 44(1), 419-425. <https://doi.org/10.1002/chem.201801933>
- Guo, H., Pan, S., Hu, Z., Wang, Y., Jiang, W., Yang, Y., Wang, Y., Han, J., Wu, Y., & Wang, T.

- 2023a. Persulfate activated by non-thermal plasma for organic pollutants degradation: A review. *Chemical Engineering Journal*, 144094.  
<https://doi.org/10.1016/j.nanoms.2019.02.004>
- Guo, J., Wen, X., Yang, J., & Fan, T. 2020. Removal of benzo (a) pyrene in polluted aqueous solution and soil using persulfate activated by corn straw biochar. *Journal of Environmental Management*, 272, 111058.  
<https://doi.org/10.1016/j.jenvman.2020.111058>
- Guo, Y., Shi, W., Liu, Z., Sun, X., Wu, J., & Wu, Y. 2023b. Bisphenol A alternatives continuously contribute to the endocrine disruption in cetaceans. *Environment international*, 171, 107679. <https://doi.org/10.1016/j.envint.2022.107679>
- Hafeez, A., Shezad, N., Javed, F., Fazal, T., ur Rehman, M. S., & Rehman, F. 2021a. Developing multiplexed plasma micro-reactor for ozone intensification and wastewater treatment. *Chemical Engineering and Processing-Process Intensification*, 162, 108337. DOI:10.1016/J.CEP.2021.108337
- Hafeez, A., Shezad, N., Javed, F., Fazal, T., ur Rehman, M. S., & Rehman, F. 2021b. Synergetic effect of packed-bed corona-DBD plasma micro-reactor and photocatalysis for organic pollutant degradation. *Separation and Purification Technology*, 269, 118728. DOI:10.1016/J.SEPPUR.2021.118728
- Hao, N., Nie, Y., Xu, Z., Jin, C., Fyda, T. J., & Zhang, J. X. 2020. Microfluidics-enabled acceleration of Fenton oxidation for degradation of organic dyes with rod-like zero-valent iron nanoassemblies. *Journal of colloid and interface science*, 559, 254-262.

<https://doi.org/10.1016/j.jcis.2019.10.042>

He, L., Fan, Y., Luo, L., Bellettre, J., & Yue, J. 2020. Preparation of Pt/ $\gamma$ -Al<sub>2</sub>O<sub>3</sub> catalyst coating in microreactors for catalytic methane combustion. *Chemical Engineering Journal*, 380, 122424. DOI:10.1016/J.CEJ.2019.122424

He, X., Chen, R., Zhu, X., Liao, Q., An, L., Cheng, X., & Li, L. 2016. Optofluidics-based membrane microreactor for wastewater treatment by photocatalytic ozonation. *Industrial & Engineering Chemistry Research*, 55(31), 8627-8635.  
<https://doi.org/10.1021/acs.iecr.6b00562>

He, Z., Li, Y., Zhang, Q., & Wang, H. 2010. Capillary microchannel-based microreactors with highly durable ZnO/TiO<sub>2</sub> nanorod arrays for rapid, high efficiency and continuous-flow photocatalysis. *Applied Catalysis B: Environmental*, 93(3-4), 376-382.  
<https://doi.org/10.1016/j.apcatb.2009.10.011>

Heggo, D., & Ookawara, S. 2017. Multiphase photocatalytic microreactors. *Chemical Engineering Science*, 169, 67-77. <https://doi.org/10.1016/j.ces.2017.01.019>

Honarmandrad, Z., Sun, X., Wang, Z., Naushad, M., & Boczkaj, G. 2023. Activated persulfate and peroxymonosulfate based advanced oxidation processes (AOPs) for antibiotics degradation—A review. *Water Resources and Industry*, 29, 100194.  
<https://doi.org/10.1016/j.wri.2022.100194>

Hou, X., Dong, H., Li, Y., Xiao, J., Dong, Q., Xiang, S., & Chu, D. 2023. Activation of persulfate by graphene/biochar composites for phenol degradation: Performance and nonradical dominated reaction mechanism. *Journal of Environmental Chemical*

*Engineering*, 11(2), 109348. <https://doi.org/10.1016/j.jece.2023.109348>

Huang, G.-X., Wang, C.-Y., Yang, C.-W., Guo, P.-C., & Yu, H.-Q. 2017. Degradation of bisphenol A by peroxymonosulfate catalytically activated with  $Mn_{1.8}Fe_{1.2}O_4$  nanospheres: synergism between Mn and Fe. *Environmental science & technology*, 51(21), 12611-12618. <https://doi.org/10.1021/acs.est.7b03007>

Huang, J., Dai, Y., Singewald, K., Liu, C.-C., Saxena, S., & Zhang, H. 2019a. Effects of  $MnO_2$  of different structures on activation of peroxymonosulfate for bisphenol A degradation under acidic conditions. *Chemical Engineering Journal*, 370, 906-915. <https://doi.org/10.1016/j.cej.2019.03.238>

Huang, J., & Zhang, H. 2019. Mn-based catalysts for sulfate radical-based advanced oxidation processes: A review. *Environment international*, 133, 105141. <https://doi.org/10.1016/j.envint.2019.105141>

Huang, R., Gao, P., Zhu, J., Zhang, Y., Chen, Y., Huang, S., Wang, G., Yu, Z., Zhao, S., & Zhou, S. 2022. Insights into the pollutant electron property inducing the transformation of peroxymonosulfate activation mechanisms on manganese dioxide. *Applied Catalysis B: Environmental*, 317, 121753. <https://doi.org/10.1016/j.apcatb.2022.121753>

Huang, W.-C., Jia, X., Li, J., & Li, M. 2019b. Dynamics of microbial community in the bioreactor for bisphenol S removal. *Science of The Total Environment*, 662, 15-21. DOI:10.1016/j.scitotenv.2019.01.173

Huang, W., & Fan, Y. 2020. Management of Contaminated Drinking Water Source in Rural

Communities. *JOURNAL OF ENVIRONMENTAL INFORMATICS*. DOI:

10.3808/jei.202000431

Hurtado, L., Solís-Casados, D., Escobar-Alarcón, L., Romero, R., & Natividad, R. 2016.

Multiphase photo-capillary reactors coated with TiO<sub>2</sub> films: Preparation, characterization and photocatalytic performance. *Chemical Engineering Journal*, 304, 39-47. <https://doi.org/10.1016/j.cej.2016.06.003>

Ike, I. A., Linden, K. G., Orbell, J. D., & Duke, M. 2018. Critical review of the science and sustainability of persulphate advanced oxidation processes. *Chemical Engineering Journal*, 338, 651-669. <https://doi.org/10.1016/j.cej.2018.01.034>

Inoue, M., Masuda, Y., Okada, F., Sakurai, A., Takahashi, I., & Sakakibara, M. 2008.

Degradation of bisphenol A using sonochemical reactions. *Water Research*, 42(6-7), 1379-1386. DOI:10.1016/J.WATRES.2007.10.006

Isaacson, A. (1979). *Shipboard Oily Water Pollution-A Practical Guide For The Owner And Designer*. Paper presented at the Offshore Technology Conference.

<https://doi.org/10.4043/3608-MS>

Izadifard, M., Achari, G., & Langford, C. H. 2017. Degradation of sulfolane using activated persulfate with UV and UV-Ozone. *Water research*, 125, 325-331.

<https://doi.org/10.1016/j.watres.2017.07.042>

Javornik, G., Basso, A., Padoin, N., & Soares, C. An investigation of scale effect and applicability of compact light sources in microchannel reactors applied to pollutant abatement. *Environmental Science and Pollution Research*, 1-12. DOI:

10.1007/s11356-020-12099-8

- Jayamohan, H., Smith, Y. R., Gale, B. K., Mohanty, S. K., & Misra, M. 2016. Photocatalytic microfluidic reactors utilizing titania nanotubes on titanium mesh for degradation of organic and biological contaminants. *Journal of Environmental Chemical Engineering*, 4(1), 657-663. <https://doi.org/10.1016/j.jece.2015.12.018>
- Ji, H., Gong, Y., Duan, J., Zhao, D., & Liu, W. 2018. Degradation of petroleum hydrocarbons in seawater by simulated surface-level atmospheric ozone: reaction kinetics and effect of oil dispersant. *Marine Pollution Bulletin*, 135, 427-440.  
DOI:10.1016/j.marpolbul.2018.07.047
- Ji, Z., Zhang, N., Huang, C., Duan, X., Ren, D., & Huo, Z. 2024. The degradation of polycyclic aromatic hydrocarbons (PAHs) by ozone-based advanced oxidation processes: A review. *Ozone: Science & Engineering*, 46(1), 26-42.  
<https://doi.org/10.1080/01919512.2023.2192751>
- Jiang, B., Zheng, J., Qiu, S., Wu, M., Zhang, Q., Yan, Z., & Xue, Q. 2014. Review on electrical discharge plasma technology for wastewater remediation. *Chemical Engineering Journal*, 236, 348-368. <https://doi.org/10.1016/j.cej.2013.09.090>
- Jiang, Y., Zhang, Y., Banks, C., Heaven, S., & Longhurst, P. 2017. Investigation of the impact of trace elements on anaerobic volatile fatty acid degradation using a fractional factorial experimental design. *Water research*, 125, 458-465. DOI: 10.1016/j.watres.2017.09.010
- Jing, L., Chen, B., Zhang, B., & Li, P. 2015. Process simulation and dynamic control for

- marine oily wastewater treatment using UV irradiation. *Water research*, 81, 101-112.  
<https://doi.org/10.1016/j.watres.2015.03.023>
- Jing, L., Chen, B., Zhang, B., & Ye, X. 2018a. Modeling marine oily wastewater treatment by a probabilistic agent-based approach. *Marine Pollution Bulletin*, 127, 217-224.  
<https://doi.org/10.1016/j.marpolbul.2017.12.004>
- Jing, L., Chen, B., Zheng, J., Liu, B., & Zhang, B. 2018b. Ozonation of offshore produced water: kinetic study and fuzzy inference system modeling. *Environmental monitoring and assessment*, 190(3), 1-14. DOI: 10.1007/s10661-018-6508-7
- John, A., Brookes, A., Carra, I., Jefferson, B., & Jarvis, P. 2020. Microbubbles and their application to ozonation in water treatment: A critical review exploring their benefit and future application. *Critical Reviews in Environmental Science and Technology*, 1-43. <https://doi.org/10.1080/10643389.2020.1860406>
- Johnson, B. T. (2005). Microtox® acute toxicity test *Small-scale freshwater toxicity investigations* (pp. 69-105): Springer. <http://dx.doi.org/10.1007/1-4020-3120-3>
- Kakaç, S., Kosoy, B., Li, D., & Pramuanjaroenkij, A. (2010). *Microfluidics based microsystems: fundamentals and applications*: Springer.
- Karim, A. V., Jiao, Y., Zhou, M., & Nidheesh, P. 2021. Iron-based persulfate activation process for environmental decontamination in water and soil. *Chemosphere*, 265, 129057. <https://doi.org/10.1016/j.chemosphere.2020.129057>
- Kasiri, M., Aleboyeh, H., & Aleboyeh, A. 2008. Degradation of Acid Blue 74 using Fe-ZSM5 zeolite as a heterogeneous photo-Fenton catalyst. *Applied Catalysis B: Environmental*,

84(1-2), 9-15. <https://doi.org/10.1016/j.apcatb.2008.02.024>

Kayahan, E., Urbani, D., Dambruoso, P., Massi, A., Braeken, L., Van Gerven, T., & Leblebici,

M. E. 2021. Overcoming mass and photon transfer limitations in a scalable reactor:

Oxidation in an aerosol photoreactor. *Chemical Engineering Journal*, 408, 127357.

<https://doi.org/10.1016/j.cej.2020.127357>

Khalifa, O., Banat, F., Srinivasakannan, C., AlMarzooqi, F., & Hasan, S. W. 2021. Ozonation-

assisted electro-membrane hybrid reactor for oily wastewater treatment: A

methodological approach and synergy effects. *Journal of Cleaner Production*, 289,

125764. <https://doi.org/10.1016/j.jclepro.2020.125764>

Khan, A., Liao, Z., Liu, Y., Jawad, A., Ifthikar, J., & Chen, Z. 2017. Synergistic degradation

of phenols using peroxymonosulfate activated by CuO-Co<sub>3</sub>O<sub>4</sub>@ MnO<sub>2</sub> nanocatalyst.

*Journal of hazardous materials*, 329, 262-271.

<https://doi.org/10.1016/j.jhazmat.2017.01.029>

Khan, S., Sohail, M., Han, C., Khan, J. A., Khan, H. M., & Dionysiou, D. D. 2021.

Degradation of highly chlorinated pesticide, lindane, in water using UV/persulfate:

kinetics and mechanism, toxicity evaluation, and synergism by H<sub>2</sub>O<sub>2</sub>. *Journal of*

*hazardous materials*, 402, 123558. <https://doi.org/10.1016/j.jhazmat.2020.123558>

Khongthong, W., Jovanovic, G., Yokochi, A., Sangvanich, P., & Pavarajarn, V. 2016.

Degradation of diuron via an electrochemical advanced oxidation process in a

microscale-based reactor. *Chemical Engineering Journal*, 292, 298-307.

<https://doi.org/10.1016/j.cej.2016.02.042>

- Khoshnood, R., Jaafarzadeh, N., Jamili, S., Farshchi, P., & Taghavi, L. 2017. Acute toxicity of TiO<sub>2</sub>, CuO and ZnO nanoparticles in brine shrimp, *Artemia franciscana*.  
DOI:10.22092/IJFS.2018.114738
- Kies, F. K., Benadda, B., & Otterbein, M. 2004. Experimental study on mass transfer of a co-current gas–liquid contactor performing under high gas velocities. *Chemical Engineering and Processing: Process Intensification*, 43(11), 1389-1395.  
<https://doi.org/10.1016/j.cep.2003.12.009>
- Kim, H., Kwon, H., Song, R., Shin, S., Ham, S.-Y., Park, H.-D., Lee, J., Fischer, P., & Bodenschatz, E. 2022. Hierarchical optofluidic microreactor for water purification using an array of TiO<sub>2</sub> nanostructures. *npj Clean Water*, 5(1), 62.  
<https://doi.org/10.1038/s41545-022-00204-y>
- Kim, S., Kim, D. H., Kim, W., Cho, Y. T., & Fang, N. X. 2020. Additive manufacturing of functional microarchitected reactors for energy, environmental, and biological applications. *International Journal of Precision Engineering and Manufacturing-Green Technology*, 1-24. <https://doi.org/10.1007/s40684-020-00277-5>
- Kim, S., Kim, D. H., Kim, W., Cho, Y. T., & Fang, N. X. 2021. Additive manufacturing of functional microarchitected reactors for energy, environmental, and biological applications. *International Journal of Precision Engineering and Manufacturing-Green Technology*, 8, 303-326. <https://doi.org/10.1007/s40684-020-00277-5>
- Kockmann, N. (2007). *Transport phenomena in micro process engineering*: Springer Science & Business Media.

- Kockmann, N., Kiefer, T., Engler, M., & Woias, P. 2006. Convective mixing and chemical reactions in microchannels with high flow rates. *Sensors and Actuators B: Chemical*, 117(2), 495-508. <https://doi.org/10.1016/j.snb.2006.01.004>
- Kponee, K. Z., Chiger, A., Kakulu, I. I., Vorhees, D., & Heiger-Bernays, W. 2015. Petroleum contaminated water and health symptoms: a cross-sectional pilot study in a rural Nigerian community. *Environmental Health*, 14(1), 1-8. <https://doi.org/10.1186/s12940-015-0073-0>
- Krivec, M., Dillert, R., Bahnemann, D. W., Mehle, A., Štrancar, J., & Dražić, G. 2014. The nature of chlorine-inhibition of photocatalytic degradation of dichloroacetic acid in a TiO<sub>2</sub>-based microreactor. *Physical Chemistry Chemical Physics*, 16(28), 14867-14873. <https://doi.org/10.1039/C4CP01043D>
- Krivec, M., Žagar, K., Suhadolnik, L., Čeh, M., & Dražić, G. 2013. Highly efficient TiO<sub>2</sub>-based microreactor for photocatalytic applications. *ACS Applied Materials & Interfaces*, 5(18), 9088-9094. <https://doi.org/10.1021/am402389t>
- Kusvuran, E., & Yildirim, D. 2013. Degradation of bisphenol A by ozonation and determination of degradation intermediates by gas chromatography–mass spectrometry and liquid chromatography–mass spectrometry. *Chemical Engineering Journal*, 220, 6-14. <https://doi.org/10.1016/j.cej.2013.01.064>
- Lebik-Elhadi, H., Frontistis, Z., Ait-Amar, H., Madjene, F., & Mantzavinos, D. 2020. Degradation of pesticide thiamethoxam by heat–activated and ultrasound–activated persulfate: effect of key operating parameters and the water matrix. *Process Safety*

*and Environmental Protection*, 134, 197-207.

<https://doi.org/10.1016/j.psep.2019.11.041>

Lee, C.-Y., Chang, C.-L., Wang, Y.-N., & Fu, L.-M. 2011. Microfluidic mixing: a review.

*International journal of molecular sciences*, 12(5), 3263-3287.

<https://doi.org/10.3390/ijms12053263>

Lee, H., Lee, H.-J., Jeong, J., Lee, J., Park, N.-B., & Lee, C. 2015. Activation of persulfates by carbon nanotubes: oxidation of organic compounds by nonradical mechanism.

*Chemical Engineering Journal*, 266, 28-33. <https://doi.org/10.1016/j.cej.2014.12.065>

Lee, J., Von Gunten, U., & Kim, J.-H. 2020. Persulfate-based advanced oxidation: critical assessment of opportunities and roadblocks. *Environmental science & technology*,

54(6), 3064-3081. <https://doi.org/10.1021/acs.est.9b07082>

Lee, K., Wohlgeschaffen, G., Tremblay, G. H., Johnson, B. T., Sergy, G. A., Prince, R. C.,

Guénette, C. C., & Owens, E. H. 2003. Toxicity evaluation with the Microtox® test to assess the impact of in situ oiled shoreline treatment options: natural attenuation and sediment relocation. *Spill Science & Technology Bulletin*, 8(3), 273-284.

[https://doi.org/10.1016/S1353-2561\(03\)00039-2](https://doi.org/10.1016/S1353-2561(03)00039-2)

Lee, Y.-C., Lo, S.-L., Kuo, J., & Huang, C.-P. 2013. Promoted degradation of

perfluorooctanic acid by persulfate when adding activated carbon. *Journal of*

*hazardous materials*, 261, 463-469. <https://doi.org/10.1016/j.jhazmat.2013.07.054>

Lei, J., Duan, P., Liu, W., Sun, Z., & Hu, X. 2020. Degradation of aqueous cefotaxime in electro-oxidation—electro-Fenton—persulfate system with Ti/CNT/SnO<sub>2</sub>–Sb–Er

anode and Ni@ NCNT cathode. *Chemosphere*, 250, 126163.

<https://doi.org/10.1016/j.chemosphere.2020.126163>

Lei, L., Wang, N., Zhang, X., Tai, Q., Tsai, D. P., & Chan, H. L. 2010. Optofluidic planar reactors for photocatalytic water treatment using solar energy. *Biomicrofluidics*, 4(4), 043004. <https://doi.org/10.1063/1.3491471>

Li, C., Wu, J., Peng, W., Fang, Z., & Liu, J. 2019. Peroxymonosulfate activation for efficient sulfamethoxazole degradation by Fe<sub>3</sub>O<sub>4</sub>/β-FeOOH nanocomposites: coexistence of radical and non-radical reactions. *Chemical Engineering Journal*, 356, 904-914. <https://doi.org/10.1016/j.cej.2018.09.064>

Li, J., Yang, L., Lai, B., Liu, C., He, Y., Yao, G., & Li, N. 2021. Recent progress on heterogeneous Fe-based materials induced persulfate activation for organics removal. *Chemical Engineering Journal*, 414, 128674. <https://doi.org/10.1016/j.cej.2021.128674>

Li, L., Chen, R., Zhu, X., Wang, H., Wang, Y., Liao, Q., & Wang, D. 2013. Optofluidic microreactors with TiO<sub>2</sub>-coated fiberglass. *ACS Applied Materials & Interfaces*, 5(23), 12548-12553. <https://doi.org/10.1021/am403842b>

Li, L., Tang, D., Song, Y., & Jiang, B. 2018. Dual-film optofluidic microreactor with enhanced light-harvesting for photocatalytic applications. *Chemical Engineering Journal*, 339, 71-77. <https://doi.org/10.1016/j.cej.2018.01.074>

Li, L., Wang, G., Chen, R., Zhu, X., Wang, H., Liao, Q., & Yu, Y. 2014. Optofluidics based micro-photocatalytic fuel cell for efficient wastewater treatment and electricity

- generation. *Lab on a Chip*, 14(17), 3368-3375. <https://doi.org/10.1039/C4LC00595C>
- Li, N., Wu, S., Dai, H., Cheng, Z., Peng, W., Yan, B., Chen, G., Wang, S., & Duan, X. 2022. Thermal activation of persulfates for organic wastewater purification: Heating modes, mechanism and influencing factors. *Chemical Engineering Journal*, 450, 137976. <https://doi.org/10.1016/j.cej.2022.137976>
- Li, P., Cai, Q., Lin, W., Chen, B., & Zhang, B. 2016. Offshore oil spill response practices and emerging challenges. *Marine Pollution Bulletin*, 110(1), 6-27. <https://doi.org/10.1016/j.marpolbul.2016.06.020>
- Li, R., Hu, H., Ma, Y., Liu, X., Zhang, L., Zhou, S., Deng, B., Lin, H., & Zhang, H. 2020. Persulfate enhanced photocatalytic degradation of bisphenol A over wasted batteries-derived ZnFe<sub>2</sub>O<sub>4</sub> under visible light. *Journal of Cleaner Production*, 276, 124246. <https://doi.org/10.1016/j.jclepro.2020.124246>
- Li, X., Wang, H., Inoue, K., Uehara, M., Nakamura, H., Miyazaki, M., Abe, E., & Maeda, H. 2003. Modified micro-space using self-organized nanoparticles for reduction of methylene blue. *Chemical communications*(8), 964-965. <https://doi.org/10.1039/B300765K>
- Liang, J.-P., Zhou, X.-F., Zhao, Z.-L., Yang, D.-Z., & Wang, W.-C. 2021. Degradation of trimethoprim in aqueous by persulfate activated with nanosecond pulsed gas-liquid discharge plasma. *Journal of Environmental Management*, 278, 111539. <https://doi.org/10.1016/j.jenvman.2020.111539>
- Liao, W., Wang, N., Wang, T., Xu, J., Han, X., Liu, Z., Zhang, X., & Yu, W. 2016.

Biomimetic microchannels of planar reactors for optimized photocatalytic efficiency of water purification. *Biomicrofluidics*, 10(1), 014123.

<https://doi.org/10.1063/1.4942947>

Lin, C., Liu, B., Pu, L., Sun, Y., Xue, Y., Chang, M., Li, X., Lu, X., Chen, R., & Zhang, J.

2021a. Photocatalytic oxidation removal of fluoride ion in wastewater by gC<sub>3</sub>N<sub>4</sub>/TiO<sub>2</sub> under simulated visible light. *Advanced composites and hybrid materials*, 4, 339-349. <https://doi.org/10.1007/s42114-021-00228-x>

Lin, C., Zhang, W., Yuan, M., Feng, C., Ren, Y., & Wei, C. 2014. Degradation of polycyclic

aromatic hydrocarbons in a coking wastewater treatment plant residual by an

O<sub>3</sub>/ultraviolet fluidized bed reactor. *Environmental Science and Pollution Research*, 21(17), 10329-10338. <https://doi.org/10.1007/s11356-014-3034-1>

Lin, J., Hu, Y., Wang, L., Liang, D., Ruan, X., & Shao, S. 2020. M88/PS/Vis system for

degradation of bisphenol A: Environmental factors, degradation pathways, and

toxicity evaluation. *Chemical Engineering Journal*, 382, 122931.

<https://doi.org/10.1016/j.cej.2019.122931>

Lin, K., Liu, W., & Gan, J. 2009. Oxidative removal of bisphenol A by manganese dioxide:

efficacy, products, and pathways. *Environmental science & technology*, 43(10), 3860-

3864. <https://doi.org/10.1021/es900235f>

Lin, L., Pho, H. Q., Zong, L., Li, S., Pourali, N., Rebrov, E., Tran, N. N., Ostrikov, K. K., &

Hessel, V. 2021b. Microfluidic Plasmas: Novel Technique for Chemistry and

Chemical Engineering. *Chemical Engineering Journal*, 129355.

<https://doi.org/10.1016/j.cej.2021.129355>

Lin, L., Pho, H. Q., Zong, L., Li, S., Pourali, N., Rebrov, E., Tran, N. N., Ostrikov, K. K., & Hessel, V. 2021c. Microfluidic plasmas: Novel technique for chemistry and chemical engineering. *Chemical Engineering Journal*, 417, 129355.

<https://doi.org/10.1016/j.cej.2021.129355>

Lin, Y.-T., Chiu, Y.-T., Ciou, C., & Liang, C. 2019. Natural organic activator quercetin for persulfate oxidative degradation of halogenated hydrocarbons. *Environmental Science: Water Research & Technology*, 5(6), 1064-1071.

<https://doi.org/10.1039/C9EW00178F>

Lindstrom, H., Wootton, R., & Iles, A. 2007. High surface area titania photocatalytic microfluidic reactors. *AIChE Journal*, 53(3), 695-702.

<https://doi.org/10.1002/aic.11096>

Liu, B., Chen, B., Ling, J., Ye, X., Dong, G., Matchinski, E. J., & Zhang, B. 2022a. Ecotoxicity Studies for Onsite Disposal of Decant Water during Oil Spills: A Review. *Frontiers in Environmental Science*, 1002. <https://doi.org/10.3389/fenvs.2022.944010>

Liu, B., Chen, B., Zhang, B., Song, X., Zeng, G., & Lee, K. 2021a. Photocatalytic ozonation of offshore produced water by TiO<sub>2</sub> nanotube arrays coupled with UV-LED irradiation. *Journal of hazardous materials*, 402, 123456.

<https://doi.org/10.1016/j.jhazmat.2020.123456>

Liu, B., Zhang, B., Dong, G., Wu, F., & Chen, B. 2023. A UVA light-emitting diode microreactor for the photocatalytic degradation of humic acids and the control of

- disinfection by-products formation potential. *Journal of Cleaner Production*, 429, 139395. <https://doi.org/10.1016/j.jclepro.2023.139395>
- Liu, G., Wu, K., Zhang, C., Ji, Y., Lu, J., Chen, J., & Kong, D. 2024. Efficient degradation of bisphenol S by ultraviolet/persulfate oxidation in fresh and saline waters: Effects of operating conditions and reaction mechanism. <https://doi.org/10.21203/rs.3.rs-3420886/v1>
- Liu, H., Gao, Y., Wang, J., Ma, D., Wang, Y., Gao, B., Yue, Q., & Xu, X. 2021b. The application of UV/O<sub>3</sub> process on ciprofloxacin wastewater containing high salinity: Performance and its degradation mechanism. *Chemosphere*, 276, 130220. <https://doi.org/10.1016/j.chemosphere.2021.130220>
- Liu, J., Zhang, L., Lu, G., Jiang, R., Yan, Z., & Li, Y. 2021c. Occurrence, toxicity and ecological risk of Bisphenol A analogues in aquatic environment—A review. *Ecotoxicology and environmental safety*, 208, 111481. <https://doi.org/10.1016/j.ecoenv.2020.111481>
- Liu, L., Xu, X., Li, Y., Su, R., Li, Q., Zhou, W., Gao, B., & Yue, Q. 2020a. One-step synthesis of “nuclear-shell” structure iron-carbon nanocomposite as a persulfate activator for bisphenol A degradation. *Chemical Engineering Journal*, 382, 122780. <https://doi.org/10.1016/j.cej.2019.122780>
- Liu, Q., Yao, Y., Wei, J., & Huang, W. 2020b. Removal of Phenol from Wastewater Using Micellar-Enhanced Ultrafiltration with Quaternary Ammonium Salt Cationic Gemini Surfactants. *JOURNAL OF ENVIRONMENTAL INFORMATICS LETTERS*, 4(1), 40-

47. doi:10.3808/jeil.202000039

Liu, R., Liu, H., Qiang, Z., Qu, J., Li, G., & Wang, D. 2009. Effects of calcium ions on surface characteristics and adsorptive properties of hydrous manganese dioxide. *Journal of Colloid and Interface Science*, 331(2), 275-280.

<https://doi.org/10.1016/j.jcis.2008.11.051>

Liu, S., Lai, C., Li, B., Liu, X., Zhou, X., Zhang, C., Qin, L., Li, L., Zhang, M., & Yi, H. 2022b. Heteroatom doping in metal-free carbonaceous materials for the enhancement of persulfate activation. *Chemical Engineering Journal*, 427, 131655.

<https://doi.org/10.1016/j.cej.2021.131655>

Liu, Y., He, X., Fu, Y., & Dionysiou, D. D. 2016. Kinetics and mechanism investigation on the destruction of oxytetracycline by UV-254 nm activation of persulfate. *Journal of hazardous materials*, 305, 229-239. <https://doi.org/10.1016/j.jhazmat.2015.11.043>

Loeb, B. L., Thompson, C. M., Drago, J., Takahara, H., & Baig, S. 2012. Worldwide ozone capacity for treatment of drinking water and wastewater: a review. *Ozone: Science & Engineering*, 34(1), 64-77. <https://doi.org/10.1080/01919512.2012.640251>

Lominchar, M., Santos, A., De Miguel, E., & Romero, A. 2018. Remediation of aged diesel contaminated soil by alkaline activated persulfate. *Science of the total environment*, 622, 41-48. <https://doi.org/10.1016/j.scitotenv.2017.11.263>

Losey, M. W., Schmidt, M. A., & Jensen, K. F. 2001. Microfabricated multiphase packed-bed reactors: characterization of mass transfer and reactions. *Industrial & Engineering Chemistry Research*, 40(12), 2555-2562. <https://doi.org/10.1021/ie000523f>

- Lu, X., Li, Z., Liu, Y. a., Tang, B., Zhu, Y., Razal, J. M., Pakdel, E., Wang, J., & Wang, X. 2020. Titanium dioxide coated carbon foam as microreactor for improved sunlight driven treatment of cotton dyeing wastewater. *Journal of Cleaner Production*, 246, 118949. <https://doi.org/10.1016/j.jclepro.2019.118949>
- Lu, X., Shao, Y., Gao, N., Chen, J., Zhang, Y., Xiang, H., & Guo, Y. 2017. Degradation of diclofenac by UV-activated persulfate process: Kinetic studies, degradation pathways and toxicity assessments. *Ecotoxicology and environmental safety*, 141, 139-147. <https://doi.org/10.1016/j.ecoenv.2017.03.022>
- Ludmerczki, R., Mura, S., Carbonaro, C. M., Mandity, I. M., Carraro, M., Senes, N., Garroni, S., Granozzi, G., Calvillo, L., & Marras, S. 2019. Carbon dots from citric acid and its intermediates formed by thermal decomposition. *Chemistry—A European Journal*, 25(51), 11963-11974. <https://doi.org/10.1002/chem.201902497>
- Lumbaue, E. C., Lüdtke, D. S., Dionysiou, D. D., Vilar, V. J., & Sirtori, C. 2021. Tube-in-tube membrane photoreactor as a new technology to boost sulfate radical advanced oxidation processes. *Water research*, 191, 116815. <https://doi.org/10.1016/j.watres.2021.116815>
- Lundstedt, S., White, P. A., Lemieux, C. L., Lynes, K. D., Lambert, I. B., Öberg, L., Haglund, P., & Tysklind, M. 2007. Sources, fate, and toxic hazards of oxygenated polycyclic aromatic hydrocarbons (PAHs) at PAH-contaminated sites. *AMBIO: A Journal of the Human Environment*, 36(6), 475-485. [https://doi.org/10.1579/0044-7447\(2007\)36\[475:SFATHO\]2.0.CO;2](https://doi.org/10.1579/0044-7447(2007)36[475:SFATHO]2.0.CO;2)

- Luo, R., Wang, C., Yao, Y., Qi, J., & Li, J. 2022. Insights into the relationship of reactive oxygen species and anions in persulfate-based advanced oxidation processes for saline organic wastewater treatment. *Environmental Science: Water Research & Technology*, 8(3), 465-483. <https://doi.org/10.1039/D1EW00731A>
- Ma, L., Zhou, M., Ren, G., Yang, W., & Liang, L. 2016. A highly energy-efficient flow-through electro-Fenton process for organic pollutants degradation. *Electrochimica acta*, 200, 222-230. <https://doi.org/10.1016/j.electacta.2016.03.181>
- Ma, P., Ma, H., Sabatino, S., Galia, A., & Scialdone, O. 2018. Electrochemical treatment of real wastewater. Part 1: effluents with low conductivity. *Chemical Engineering Journal*, 336, 133-140. <https://doi.org/10.1016/j.cej.2017.11.046>
- Malik, M. A. 2010. Water purification by plasmas: Which reactors are most energy efficient? *Plasma Chemistry and Plasma Processing*, 30(1), 21-31. <https://doi.org/10.1007/s11090-009-9202-2>
- Mani, P., Kim, Y., Lakhera, S. K., Neppolian, B., & Choi, H. 2021. Complete arsenite removal from groundwater by UV activated potassium persulfate and iron oxide impregnated granular activated carbon. *Chemosphere*, 277, 130225. <https://doi.org/10.1016/j.chemosphere.2021.130225>
- Martin, M. V., Alfano, O. M., & Satuf, M. L. 2019. Cerium-doped TiO<sub>2</sub> thin films: Assessment of radiation absorption properties and photocatalytic reaction efficiencies in a microreactor. *Journal of Environmental Chemical Engineering*, 7(6), 103478. <https://doi.org/10.1016/j.jece.2019.103478>

- Martínez-Huitle, C. A., Rodrigo, M. A., Sires, I., & Scialdone, O. 2015. Single and coupled electrochemical processes and reactors for the abatement of organic water pollutants: a critical review. *Chemical reviews*, *115*(24), 13362-13407.  
<https://doi.org/10.1021/acs.chemrev.5b00361>
- Matsushita, Y., Ohba, N., Kumada, S., Sakeda, K., Suzuki, T., & Ichimura, T. 2008. Photocatalytic reactions in microreactors. *Chemical Engineering Journal*, *135*, S303-S308. <https://doi.org/10.1016/j.cej.2007.07.045>
- Matzek, L. W., & Carter, K. E. 2016. Activated persulfate for organic chemical degradation: a review. *Chemosphere*, *151*, 178-188.  
<https://doi.org/10.1016/j.chemosphere.2016.02.055>
- Mazloomi, S., Nasser, S., Nabizadeh, R., Yaghmaeian, K., Alimohammadi, K., Nazmara, S., & Mahvi, A. H. 2016. Remediation of fuel oil contaminated soils by activated persulfate in the presence of MnO<sub>2</sub>. *Soil and Water Research*, *11*(2), 131-138. DOI: 10.17221/39/2015-SWR
- McBean, E. 2019. Removal of emerging contaminants: the next water revolution. *Journal of Environmental Informatics Letters*, *1*(1), 1-7. doi:10.3808/jeil.201900001
- Mehrjouei, M., Müller, S., & Möller, D. 2015. A review on photocatalytic ozonation used for the treatment of water and wastewater. *Chemical Engineering Journal*, *263*, 209-219.  
<https://doi.org/10.1016/j.cej.2014.10.112>
- Meng, Z., Zhang, X., & Qin, J. 2013. A high efficiency microfluidic-based photocatalytic microreactor using electrospun nanofibrous TiO<sub>2</sub> as a photocatalyst. *Nanoscale*, *5*(11),

4687-4690. <https://doi.org/10.1039/C3NR00775H>

Miklos, D. B., Remy, C., Jekel, M., Linden, K. G., Drewes, J. E., & Hübner, U. 2018.

Evaluation of advanced oxidation processes for water and wastewater treatment—A critical review. *Water research*, 139, 118-131.

<https://doi.org/10.1016/j.watres.2018.03.042>

Miranda, C., Mansilla, H., Yáñez, J., Obregón, S., & Colón, G. 2013. Improved

photocatalytic activity of g-C<sub>3</sub>N<sub>4</sub>/TiO<sub>2</sub> composites prepared by a simple impregnation method. *Journal of Photochemistry and Photobiology A: Chemistry*, 253, 16-21.

<https://doi.org/10.1016/j.jphotochem.2012.12.014>

Miruka, A. C., Zhang, A., Wang, Q., Zhu, D., Wang, Z., Sun, Z., Héroux, P., & Liu, Y. 2021.

Degradation of glucocorticoids in water by a synergistic system of peroxymonosulfate, microbubble and dielectric barrier discharges. *Journal of Water Process Engineering*, 42, 102175. <https://doi.org/10.1016/j.jwpe.2021.102175>

<https://doi.org/10.1016/j.jwpe.2021.102175>

Molkenthin, M., Olmez-Hanci, T., Jekel, M. R., & Arslan-Alaton, I. 2013. Photo-Fenton-like

treatment of BPA: effect of UV light source and water matrix on toxicity and transformation products. *Water Research*, 47(14), 5052-5064.

<https://doi.org/10.1016/j.watres.2013.05.051>

Mook, W., Aroua, M., & Issabayeva, G. 2014. Prospective applications of renewable energy

based electrochemical systems in wastewater treatment: A review. *Renewable and Sustainable Energy Reviews*, 38, 36-46. <https://doi.org/10.1016/j.rser.2014.05.042>

Mousset, E., Puce, M., & Pons, M. N. 2019. Advanced Electro-Oxidation with Boron-Doped

- Diamond for Acetaminophen Removal from Real Wastewater in a Microfluidic Reactor: Kinetics and Mass-Transfer Studies. *ChemElectroChem*, 6(11), 2908-2916.  
<https://doi.org/10.1002/celec.201900182>
- Munirathinam, R., Huskens, J., & Verboom, W. 2015. Supported catalysis in continuous-flow microreactors. *Advanced synthesis & catalysis*, 357(6), 1093-1123.  
<https://doi.org/10.1002/adsc.201401081>
- Najam, L., & Alam, T. (2023). Occurrence, distribution, and fate of emerging persistent organic pollutants (POPs) in the environment *Emerging contaminants and plants: interactions, adaptations and remediation technologies* (pp. 135-161): Springer.  
[https://doi.org/10.1007/978-3-031-22269-6\\_6](https://doi.org/10.1007/978-3-031-22269-6_6)
- Neta, P., Madhavan, V., Zemel, H., & Fessenden, R. W. 1977. Rate constants and mechanism of reaction of sulfate radical anion with aromatic compounds. *Journal of the American Chemical Society*, 99(1), 163-164. <https://doi.org/10.1021/ja00443a030>
- Nge, P. N., Rogers, C. I., & Woolley, A. T. 2013. Advances in microfluidic materials, functions, integration, and applications. *Chemical reviews*, 113(4), 2550-2583.  
<https://doi.org/10.1021/cr300337x>
- Nidheesh, P., & Gandhimathi, R. 2012. Trends in electro-Fenton process for water and wastewater treatment: an overview. *Desalination*, 299, 1-15.  
<https://doi.org/10.1016/j.desal.2012.05.011>
- Nieves-Remacha, M. J., Kulkarni, A. A., & Jensen, K. F. 2013. Gas-liquid flow and mass transfer in an advanced-flow reactor. *Industrial & Engineering Chemistry Research*,

52(26), 8996-9010. <https://doi.org/10.1021/ie4011707>

Ogbomo, E., Bhuiyan, F. H., Latorre, C. A., Martini, A., & Ewen, J. P. 2024. Effects of surface chemistry on the mechanochemical decomposition of tricresyl phosphate.

*Physical Chemistry Chemical Physics*, 26(1), 278-292.

<https://doi.org/10.1039/D3CP05320B>

Ouada, S. B., Ali, R. B., Leboulanger, C., Ouada, H. B., & Sayadi, S. 2018. Effect of Bisphenol A on the extremophilic microalgal strain *Picocystis* sp.(Chlorophyta) and its high BPA removal ability. *Ecotoxicology and environmental safety*, 158, 1-8.

<https://doi.org/10.1016/j.ecoenv.2018.04.008>

Özbakır, Y., Jonáš, A., Kiraz, A., & Erkey, C. 2021. An aerogel-based photocatalytic microreactor driven by light guiding for degradation of toxic pollutants. *Chemical Engineering Journal*, 409, 128108. <https://doi.org/10.1016/j.cej.2020.128108>

Pan, X., Yan, L., Li, C., Qu, R., & Wang, Z. 2017. Degradation of UV-filter benzophenone-3 in aqueous solution using persulfate catalyzed by cobalt ferrite. *Chemical Engineering Journal*, 326, 1197-1209. <https://doi.org/10.1016/j.cej.2017.06.068>

Pan, Y., Zhang, Y., Zhou, M., Cai, J., & Tian, Y. 2019. Enhanced removal of emerging contaminants using persulfate activated by UV and pre-magnetized Fe<sup>0</sup>. *Chemical Engineering Journal*, 361, 908-918. <https://doi.org/10.1016/j.cej.2018.12.135>

Parsons, S. (2004). *Advanced oxidation processes for water and wastewater treatment*: IWA publishing. <https://doi.org/10.2166/9781780403076>

Patinglag, L., Melling, L. M., Whitehead, K. A., Sawtell, D., Iles, A., & Shaw, K. J. 2021.

- Non-thermal plasma-based inactivation of bacteria in water using a microfluidic reactor. *Water research*, 117321. <https://doi.org/10.1016/j.watres.2021.117321>
- Patinglag, L., Sawtell, D., Iles, A., Melling, L. M., & Shaw, K. J. 2019. A microfluidic atmospheric-pressure plasma reactor for water treatment. *Plasma Chemistry and Plasma Processing*, 39(3), 561-575. <https://doi.org/10.1007/s11090-019-09970-z>
- Peillex, C., Kerever, A., Lachhab, A., & Pelletier, M. 2021. Bisphenol A, bisphenol S and their glucuronidated metabolites modulate glycolysis and functional responses of human neutrophils. *Environmental Research*, 196, 110336. <https://doi.org/10.1016/j.envres.2020.110336>
- Pérez, J., Llanos, J., Sáez, C., López, C., Cañizares, P., & Rodrigo, M. 2018. Development of an innovative approach for low-impact wastewater treatment: A microfluidic flow-through electrochemical reactor. *Chemical Engineering Journal*, 351, 766-772. <https://doi.org/10.1016/j.cej.2018.06.150>
- Pérez, J., Llanos, J., Sáez, C., López, C., Cañizares, P., & Rodrigo, M. 2019. On the design of a jet-aerated microfluidic flow-through reactor for wastewater treatment by electro-Fenton. *Separation and Purification Technology*, 208, 123-129. <https://doi.org/10.1016/j.seppur.2018.04.021>
- Pérez, J. F., Llanos, J., Sáez, C., López, C., Cañizares, P., & Rodrigo, M. A. 2017. A microfluidic flow-through electrochemical reactor for wastewater treatment: a proof-of-concept. *Electrochemistry communications*, 82, 85-88. <https://doi.org/10.1016/j.elecom.2017.07.026>

- Pervez, M. N., He, W., Zarra, T., Naddeo, V., & Zhao, Y. 2020. New sustainable approach for the production of Fe<sub>3</sub>O<sub>4</sub>/graphene oxide-activated persulfate system for dye removal in real wastewater. *Water*, 12(3), 733. <https://doi.org/10.3390/w12030733>
- Petala, A., Arvaniti, O. S., Christofili, M., Safakas, A., Frontistis, Z., & Mantzavinos, D. 2020. Lanthanum nickel oxide: an effective heterogeneous activator of sodium persulfate for antibiotics elimination. *Catalysts*, 10(12), 1373. <https://doi.org/10.3390/catal10121373>
- Qi, C., Liu, X., Li, Y., Lin, C., Ma, J., Li, X., & Zhang, H. 2017. Enhanced degradation of organic contaminants in water by peroxydisulfate coupled with bisulfite. *Journal of hazardous materials*, 328, 98-107. <https://doi.org/10.1016/j.jhazmat.2017.01.010>
- Qi, F., Zeng, Z., Wen, Q., & Huang, Z. 2021. Enhanced organics degradation by three-dimensional (3D) electrochemical activation of persulfate using sulfur-doped carbon particle electrode: The role of thiophene sulfur functional group and specific capacitance. *Journal of hazardous materials*, 416, 125810. <https://doi.org/10.1016/j.jhazmat.2021.125810>
- Qiao, J., Luo, S., Yang, P., Jiao, W., & Liu, Y. 2019. Degradation of Nitrobenzene-containing wastewater by ozone/persulfate oxidation process in a rotating packed bed. *Journal of the Taiwan Institute of Chemical Engineers*, 99, 1-8. <https://doi.org/10.1016/j.jtice.2019.02.015>
- Qin, W., Lin, Z., Sun, L., Yuan, X., & Xia, D. 2020. A preliminary study on the integrated UV/ozone/persulfate process for efficient abatement of atrazine. *Ozone: Science &*

*Engineering*, 42(6), 558-564. <https://doi.org/10.1080/01919512.2020.1746631>

Radjenovic, J., & Sedlak, D. L. 2015. Challenges and opportunities for electrochemical processes as next-generation technologies for the treatment of contaminated water.

*Environmental science & technology*, 49(19), 11292-11302.

<https://doi.org/10.1021/acs.est.5b02414>

Rahimi, M., Aghel, B., Sadeghi, M., & Ahmadi, M. 2014. Using Y-shaped microreactor for continuous decolorization of an Azo dye. *Desalination and Water Treatment*, 52(28-30), 5513-5519. doi: 10.1080/19443994.2013.807471

Rajasekhar, B., Nambi, I. M., & Govindarajan, S. K. 2021. Investigating the degradation of nC12 to nC23 alkanes and PAHs in petroleum-contaminated water by electrochemical advanced oxidation process using an inexpensive Ti/Sb-SnO<sub>2</sub>/PbO<sub>2</sub> anode. *Chemical Engineering Journal*, 404, 125268. <https://doi.org/10.1016/j.cej.2020.125268>

Ramos, B., Ookawara, S., Matsushita, Y., & Yoshikawa, S. 2014a. Intensification of photochemical wastewater decolorization process using microreactors. *Journal of Chemical Engineering of Japan*, 47(2), 136-140. <https://doi.org/10.1252/jcej.13we025>

Ramos, B., Ookawara, S., Matsushita, Y., & Yoshikawa, S. 2014b. Low-cost polymeric photocatalytic microreactors: catalyst deposition and performance for phenol degradation. *Journal of Environmental Chemical Engineering*, 2(3), 1487-1494. <https://doi.org/10.1016/j.jece.2014.06.022>

Ramos, B., Ookawara, S., Matsushita, Y., & Yoshikawa, S. 2014c. Photocatalytic decolorization of methylene blue in a glass channel microreactor. *Journal of Chemical*

*Engineering of Japan*, 47(10), 788-791. <https://doi.org/10.1252/jcej.14we040>

Rao, A. N. S., & Venkatarangiah, V. T. 2014. Metal oxide-coated anodes in wastewater treatment. *Environmental Science and Pollution Research*, 21(5), 3197-3217. <https://doi.org/10.1007/s11356-013-2313-6>

Ren, B., Wang, T., Qu, G., Deng, F., Liang, D., Yang, W., & Liu, M. 2018. In situ synthesis of gC<sub>3</sub>N<sub>4</sub>/TiO<sub>2</sub> heterojunction nanocomposites as a highly active photocatalyst for the degradation of Orange II under visible light irradiation. *Environmental Science and Pollution Research*, 25, 19122-19133. <https://doi.org/10.1007/s11356-018-2114-z>

Ren, Y., Lin, L., Ma, J., Yang, J., Feng, J., & Fan, Z. 2015. Sulfate radicals induced from peroxymonosulfate by magnetic ferrosinell MFe<sub>2</sub>O<sub>4</sub> (M= Co, Cu, Mn, and Zn) as heterogeneous catalysts in the water. *Applied Catalysis B: Environmental*, 165, 572-578. <https://doi.org/10.1016/j.apcatb.2014.10.051>

Renault, C., Colin, S., Orioux, S., Cognet, P., & Tzédakis, T. 2012. Optimal design of multi-channel microreactor for uniform residence time distribution. *Microsystem Technologies*, 18(2), 209-223. <https://doi.org/10.1007/s00542-011-1334-7>

Russo, D. 2021. Kinetic Modeling of Advanced Oxidation Processes Using Microreactors: Challenges and Opportunities for Scale-Up. *Applied Sciences*, 11(3), 1042. <https://doi.org/10.3390/app11031042>

Russo, D., Cochran, K. H., Westerman, D., Puma, G. L., Marotta, R., Andreozzi, R., & Richardson, S. D. 2020. Ultrafast photodegradation of isoxazole and isothiazolinones by UV254 and UV254/H<sub>2</sub>O<sub>2</sub> photolysis in a microcapillary reactor. *Water research*,

169, 115203. <https://doi.org/10.1016/j.watres.2019.115203>

Russo, D., Spasiano, D., Vaccaro, M., Cochran, K. H., Richardson, S. D., Andreozzi, R., Puma, G. L., Reis, N. M., & Marotta, R. 2016. Investigation on the removal of the major cocaine metabolite (benzoylecgonine) in water matrices by UV254/H<sub>2</sub>O<sub>2</sub> process by using a flow microcapillary film array photoreactor as an efficient experimental tool. *Water research*, 89, 375-383.

<https://doi.org/10.1016/j.watres.2015.11.059>

Sabatino, S., Galia, A., & Scialdone, O. 2016. Electrochemical Abatement of Organic Pollutants in Continuous-Reaction Systems through the Assembly of Microfluidic Cells in Series. *ChemElectroChem*, 3(1), 83-90.

<https://doi.org/10.1002/celec.201500409>

Saber, M., Commenge, J., & Falk, L. 2010. Microreactor numbering-up in multi-scale networks for industrial-scale applications: impact of flow maldistribution on the reactor performances. *Chemical Engineering Science*, 65(1), 372-379.

<https://doi.org/10.1016/j.ces.2009.06.010>

Saha, S., & Bagdi, A. K. 2022. Visible light-promoted photocatalyst-free activation of persulfates: a promising strategy for C–H functionalization reactions. *Organic & Biomolecular Chemistry*, 20(16), 3249-3262. <https://doi.org/10.1039/D2OB00109H>

Saien, J., Soleymani, A. R., & Bayat, H. 2012. Modeling Fenton advanced oxidation process decolorization of Direct Red 16 using artificial neural network technique. *Desalination and Water Treatment*, 40(1-3), 174-182.

<https://doi.org/10.1080/19443994.2012.671165>

- Sang, L., Tu, J., Cheng, H., Luo, G., & Zhang, J. 2020. Hydrodynamics and mass transfer of gas–liquid flow in micropacked bed reactors with metal foam packing. *AIChE Journal*, 66(2), e16803. <https://doi.org/10.1002/aic.16803>
- Santana, H., Silva, J., Aghel, B., & Ortega-Casanova, J. 2020a. Review on microfluidic device applications for fluids separation and water treatment processes. *SN Applied Sciences*, 2(3), 1-19. <https://doi.org/10.1007/s42452-020-2176-7>
- Santana, H., Silva Jr, J., Aghel, B., & Ortega-Casanova, J. 2020b. Review on microfluidic device applications for fluids separation and water treatment processes. *SN Applied Sciences*, 2(3), 395. <https://doi.org/10.1007/s42452-020-2176-7>
- Santos, A., Fernandez, J., Rodriguez, S., Dominguez, C., Lominchar, M., Lorenzo, D., & Romero, A. 2018. Abatement of chlorinated compounds in groundwater contaminated by HCH wastes using ISCO with alkali activated persulfate. *Science of The Total Environment*, 615, 1070-1077. <https://doi.org/10.1016/j.scitotenv.2017.09.224>
- Saththasivam, J., Loganathan, K., & Sarp, S. 2016. An overview of oil–water separation using gas flotation systems. *Chemosphere*, 144, 671-680. <https://doi.org/10.1016/j.chemosphere.2015.08.087>
- Sattari-Najafabadi, M., Esfahany, M. N., Wu, Z., & Sunden, B. 2018. Mass transfer between phases in microchannels: A review. *Chemical Engineering and Processing-Process Intensification*, 127, 213-237. <https://doi.org/10.1016/j.cep.2018.03.012>
- Satuf, M. L., Macagno, J., Manassero, A., Bernal, G., Kler, P. A., & Berli, C. L. A. 2019.

Simple method for the assessment of intrinsic kinetic constants in photocatalytic microreactors. *Applied Catalysis B: Environmental*, 241, 8-17.

<https://doi.org/10.1016/j.apcatb.2018.09.015>

Scialdone, O., Corrado, E., Galia, A., & Sirés, I. 2014a. Electrochemical processes in macro and microfluidic cells for the abatement of chloroacetic acid from water.

*Electrochimica acta*, 132, 15-24. <https://doi.org/10.1016/j.electacta.2014.03.127>

Scialdone, O., Galia, A., Guarisco, C., & La Mantia, S. 2012. Abatement of 1, 1, 2, 2-tetrachloroethane in water by reduction at silver cathode and oxidation at boron doped diamond anode in micro reactors. *Chemical Engineering Journal*, 189, 229-236.

<https://doi.org/10.1016/j.cej.2012.02.062>

Scialdone, O., Galia, A., & Sabatino, S. 2013. Electro-generation of H<sub>2</sub>O<sub>2</sub> and abatement of organic pollutant in water by an electro-Fenton process in a microfluidic reactor.

*Electrochemistry communications*, 26, 45-47.

<https://doi.org/10.1016/j.elecom.2012.10.006>

Scialdone, O., Galia, A., & Sabatino, S. 2014b. Abatement of Acid Orange 7 in macro and micro reactors. Effect of the electrocatalytic route. *Applied Catalysis B: Environmental*, 148, 473-483. <https://doi.org/10.1016/j.apcatb.2013.11.005>

Scialdone, O., Guarisco, C., & Galia, A. 2011. Oxidation of organics in water in microfluidic electrochemical reactors: Theoretical model and experiments. *Electrochimica acta*, 58, 463-473. <https://doi.org/10.1016/j.electacta.2011.09.073>

Scialdone, O., Guarisco, C., Galia, A., Filardo, G., Silvestri, G., Amatore, C., Sella, C., &

- Thouin, L. 2010. Anodic abatement of organic pollutants in water in micro reactors. *Journal of Electroanalytical Chemistry*, 638(2), 293-296.  
<https://doi.org/10.1016/j.jelechem.2009.10.031>
- Shao, N., Gavriilidis, A., & Angeli, P. 2010. Mass transfer during Taylor flow in microchannels with and without chemical reaction. *Chemical Engineering Journal*, 160(3), 873-881. <https://doi.org/10.1016/j.cej.2010.02.049>
- Sharma, J., Mishra, I., Dionysiou, D. D., & Kumar, V. 2015. Oxidative removal of Bisphenol A by UV-C/peroxymonosulfate (PMS): kinetics, influence of co-existing chemicals and degradation pathway. *Chemical Engineering Journal*, 276, 193-204.  
<https://doi.org/10.1016/j.cej.2015.04.021>
- Sharma, S., & Ruparelia, J. 2017. SYNERGISTIC EFFECT OF O<sub>3</sub>/UV/PS PROCESS FOR OXIDATION OF REACTIVE DYES: EFFECTS OF OPERATING PARAMETERS.  
<https://doi.org/10.1007/s40030-023-00735-8>
- Sheng, J. J. 2015. Investigation of alkaline–crude oil reaction. *Petroleum*, 1(1), 31-39.  
<https://doi.org/10.1016/j.petlm.2015.04.004>
- Shilin, S., Huang, Y., Yansheng, D., Sisi, X., Song, H., Kun, H., Zhang, H., Huijuan, W., Chundu, W., & Qiong, A. 2023. Oxidation of ciprofloxacin by the synergistic effect of DBD plasma and persulfate: reactive species and influencing factors analysis. *Plasma Science and Technology*, 25(2), 025505. DOI 10.1088/2058-6272/ac8dd4
- Shinozawa, Y., Heggo, D., Ookawara, S., & Yoshikawa, S. 2019. Photo-Fenton Degradation of Carbofuran in Helical Tube Microreactor and Kinetic Modeling. *Industrial &*

*Engineering Chemistry Research*, 59(9), 3811-3819.

<https://doi.org/10.1021/acs.iecr.9b04213>

Shirke, A., Li, S., Ebeling, D., Carter, M. T., & Stetter, J. R. 2014. Integrated Ozone Microreactor Technology for Water Treatment. *ECS Transactions*, 58(35), 11. DOI 10.1149/05835.0011ecst

Shukla, K., Agarwalla, S., Duraiswamy, S., & Gupta, R. K. 2021a. Recent advances in heterogeneous micro-photoreactors for wastewater treatment application. *Chemical Engineering Science*, 116511. <https://doi.org/10.1016/j.ces.2021.116511>

Shukla, K., Agarwalla, S., Duraiswamy, S., & Gupta, R. K. 2021b. Recent advances in heterogeneous micro-photoreactors for wastewater treatment application. *Chemical Engineering Science*, 235, 116511. <https://doi.org/10.1016/j.ces.2021.116511>

Siguemoto, É. S., Leite Reche, L., Gut, J. A., & Palma, M. S. 2020. Residence time distribution of a capillary microreactor used for pharmaceutical synthesis. *Chemical Engineering & Technology*, 43(3), 429-435. <https://doi.org/10.1002/ceat.201900478>

Sirés, I., Brillas, E., Oturan, M. A., Rodrigo, M. A., & Panizza, M. 2014. Electrochemical advanced oxidation processes: today and tomorrow. A review. *Environmental Science and Pollution Research*, 21(14), 8336-8367. <https://doi.org/10.1007/s11356-014-2783-1>

Sohrabi, S., Moraveji, M. K., & Iranshahi, D. 2020. A review on the design and development of photocatalyst synthesis and application in microfluidic reactors: Challenges and opportunities. *Reviews in Chemical Engineering*, 36(6), 687-722.

<https://doi.org/10.1515/revce-2018-0013>

Song, X., Chen, B., Liu, B., Lye, L. M., Ye, X., Nyantekyi-Kwakye, B., & Zhang, B. 2021a.

Impacts of frazil ice on the effectiveness of oil dispersion and migration of dispersed oil. *Environmental science & technology*, 56(2), 835-844.

<https://doi.org/10.1021/acs.est.1c04014>

Song, X., Chen, B., Liu, B., Lye, L. M., Ye, X., Nyantekyi-Kwakye, B., & Zhang, B. 2021b.

Impacts of Frazil Ice on the Effectiveness of Oil Dispersion and Migration of Dispersed Oil. *Environmental science & technology*.

<https://doi.org/10.1021/acs.est.1c04014>

Song, Y., Cheng, D., & Zhao, L. (2018a). *Microfluidics: Fundamentals, Devices, and*

*Applications*: John Wiley & Sons. DOI:10.1002/9783527800643

Song, Y., Zhao, X., Tian, Q., & Liang, H. 2018b. Fundamental concepts and physics in microfluidics. *Microfluidics: Fundamentals, Devices, and Applications*.

<https://doi.org/10.1002/9783527800643.ch2>

Soriano Jr, N. U., Migo, V. P., & Matsumura, M. 2003. Functional group analysis during

ozonation of sunflower oil methyl esters by FT-IR and NMR. *Chemistry and Physics of Lipids*, 126(2), 133-140. <https://doi.org/10.1016/j.chemphyslip.2003.07.001>

Soubh, A., & Mokhtarani, N. 2016. The post treatment of composting leachate with a

combination of ozone and persulfate oxidation processes. *RSC advances*, 6(80), 76113-76122. <https://doi.org/10.1039/C6RA09539A>

Stasinakis, A. S., Thomaidis, N. S., Arvaniti, O. S., Asimakopoulos, A. G., Samaras, V. G.,

- Ajibola, A., Mamais, D., & Lekkas, T. D. 2013. Contribution of primary and secondary treatment on the removal of benzothiazoles, benzotriazoles, endocrine disruptors, pharmaceuticals and perfluorinated compounds in a sewage treatment plant. *Science of the total environment*, 463, 1067-1075.  
<https://doi.org/10.1016/j.scitotenv.2013.06.087>
- Su, Y., Song, Y., & Xiang, L. (2020). Continuous-flow microreactors for polymer synthesis: engineering principles and applications *Accounts on Sustainable Flow Chemistry* (pp. 147-190): Springer. <https://doi.org/10.1007/s41061-018-0224-1>
- Su, Y., Straathof, N. J., Hessel, V., & Noël, T. 2014. Photochemical transformations accelerated in continuous-flow reactors: basic concepts and applications. *Chemistry–A European Journal*, 20(34), 10562-10589. <https://doi.org/10.1002/chem.201400283>
- Suhadolnik, L., Krivec, M., Žagar, K., Dražić, G., & Čeh, M. 2017. A TiO<sub>2</sub>-nanotubes-based coil-type microreactor for highly efficient photoelectrocatalytic degradation of organic compounds. *Journal of industrial and engineering chemistry*, 47, 384-390.  
<https://doi.org/10.1016/j.jiec.2016.12.009>
- Suhadolnik, L., Pohar, A., Novak, U., Likozar, B., Mihelič, A., & Čeh, M. 2019. Continuous photocatalytic, electrocatalytic and photo-electrocatalytic degradation of a reactive textile dye for wastewater-treatment processes: batch, microreactor and scaled-up operation. *Journal of industrial and engineering chemistry*, 72, 178-188.  
<https://doi.org/10.1016/j.jiec.2018.12.017>
- Sun, B., Gao, M., Arowo, M., Wang, J., Chen, J., Meng, H., & Shao, L. 2014. Ozonation of

- acid red 14 in the presence of inorganic salts in a microporous tube-in-tube microchannel reactor. *Industrial & Engineering Chemistry Research*, 53(49), 19071-19076. <https://doi.org/10.1021/ie801424r>
- Sun, Q., Lv, K., Zhang, Z., Li, M., & Li, B. 2015. Effect of contact interface between TiO<sub>2</sub> and g-C<sub>3</sub>N<sub>4</sub> on the photoreactivity of g-C<sub>3</sub>N<sub>4</sub>/TiO<sub>2</sub> photocatalyst:(0 0 1) vs (1 0 1) facets of TiO<sub>2</sub>. *Applied Catalysis B: Environmental*, 164, 420-427. <https://doi.org/10.1021/ie801424r>
- Sun, Z., Xia, F., Lou, Z., Chen, X., Zhu, N., Yuan, H., & Shen, Y. 2020. Innovative process for total petroleum hydrocarbons reduction on oil refinery sludge through microbubble ozonation. *Journal of Cleaner Production*, 256, 120337. <https://doi.org/10.1016/j.jclepro.2020.120337>
- Suryawanshi, P. L., Gumfekar, S. P., Bhanvase, B. A., Sonawane, S. H., & Pimplapure, M. S. 2018. A review on microreactors: Reactor fabrication, design, and cutting-edge applications. *Chemical Engineering Science*, 189, 431-448. <https://doi.org/10.1016/j.ces.2018.03.026>
- Takei, G., Kitamori, T., & Kim, H.-B. 2005. Photocatalytic redox-combined synthesis of L-pipecolic acid with a titania-modified microchannel chip. *Catalysis Communications*, 6(5), 357-360. <https://doi.org/10.1016/j.catcom.2005.02.010>
- Tanimu, A., Jaenicke, S., & Alhooshani, K. 2017. Heterogeneous catalysis in continuous flow microreactors: A review of methods and applications. *Chemical Engineering Journal*, 327, 792-821. <https://doi.org/10.1016/j.cej.2017.06.161>

- Thoene, M., Dzika, E., Gonkowski, S., & Wojtkiewicz, J. 2020. Bisphenol S in food causes hormonal and obesogenic effects comparable to or worse than bisphenol A: a literature review. *Nutrients*, 12(2), 532. <https://doi.org/10.3390/nu12020532>
- Troppová, I., Šihor, M., Reli, M., Ritz, M., Praus, P., & Kočí, K. 2018. Unconventionally prepared TiO<sub>2</sub>/g-C<sub>3</sub>N<sub>4</sub> photocatalysts for photocatalytic decomposition of nitrous oxide. *Applied Surface Science*, 430, 335-347. <https://doi.org/10.1016/j.apsusc.2017.06.299>
- Tsuchiya, N., Kuwabara, K., Hidaka, A., Oda, K., & Katayama, K. 2012. Reaction kinetics of dye decomposition processes monitored inside a photocatalytic microreactor. *Physical Chemistry Chemical Physics*, 14(14), 4734-4741. <https://doi.org/10.1039/C2CP23979E>
- Tu, J., Sang, L., Cheng, H., Ai, N., & Zhang, J. 2019. Continuous Hydrogenolysis of N-Diphenylmethyl Groups in a Micropacked-Bed Reactor. *Organic Process Research & Development*, 24(1), 59-66. <https://doi.org/10.1021/acs.oprd.9b00416>
- Vilar, V. J., Alfonso-Muniozguren, P., Monteiro, J. P., Lee, J., Miranda, S. M., & Boaventura, R. A. 2020. Tube-in-tube membrane microreactor for photochemical UVC/H<sub>2</sub>O<sub>2</sub> processes: A proof of concept. *Chemical Engineering Journal*, 379, 122341. <https://doi.org/10.1016/j.cej.2019.122341>
- Waclawek, S., Lutze, H. V., Sharma, V. K., Xiao, R., & Dionysiou, D. D. 2022. Revisit the alkaline activation of peroxydisulfate and peroxymonosulfate. *Current Opinion in Chemical Engineering*, 37, 100854. <https://doi.org/10.1016/j.coche.2022.100854>

- Wang, A., Teng, Y., Hu, X., Wu, L., Huang, Y., Luo, Y., & Christie, P. 2016. Photodegradation of diphenylarsinic acid by UV-C light: Implication for its remediation. *Journal of hazardous materials*, 308, 199-207. <https://doi.org/10.1016/j.jhazmat.2016.01.049>
- Wang, B., Fu, T., An, B., & Liu, Y. 2020a. UV light-assisted persulfate activation by Cu<sub>0</sub>-Cu<sub>2</sub>O for the degradation of sulfamerazine. *Separation and Purification Technology*, 251, 117321. <https://doi.org/10.1016/j.seppur.2020.117321>
- Wang, B., & Wang, Y. 2022. A comprehensive review on persulfate activation treatment of wastewater. *Science of The Total Environment*, 831, 154906. <https://doi.org/10.1016/j.scitotenv.2022.154906>
- Wang, H., Wu, Y., Deng, N., Li, B., Li, F., & He, J.-B. 2020b. Development of a bipolar electrochemical flow microreactor for recovery of valuable metals from mixed solutions. *Chemical Engineering Journal*, 382, 121907. <https://doi.org/10.1016/j.cej.2019.121907>
- Wang, J., & Chen, H. 2020. Catalytic ozonation for water and wastewater treatment: Recent advances and perspective. *Science of the total environment*, 704, 135249. <https://doi.org/10.1016/j.cej.2019.121907>
- Wang, J., Huang, J., Xie, H., & Qu, A. 2014a. Synthesis of g-C<sub>3</sub>N<sub>4</sub>/TiO<sub>2</sub> with enhanced photocatalytic activity for H<sub>2</sub> evolution by a simple method. *International Journal of Hydrogen Energy*, 39(12), 6354-6363. <https://doi.org/10.1016/j.ijhydene.2014.02.020>
- Wang, J., & Wang, S. 2018. Activation of persulfate (PS) and peroxymonosulfate (PMS) and application for the degradation of emerging contaminants. *Chemical Engineering*

*Journal*, 334, 1502-1517. <https://doi.org/10.1016/j.cej.2017.11.059>

Wang, N., Chan, N. Y., To, C. H., Tan, F., & Zhang, X. (2013a). *Photocatalytic microreactors for water purification: Selective control of oxidation pathways*. Paper presented at the The 8th Annual IEEE International Conference on Nano/Micro Engineered and Molecular Systems. DOI: 10.1109/NEMS.2013.6559753

Wang, N., Chelme-Ayala, P., Perez-Estrada, L., Garcia-Garcia, E., Pun, J., Martin, J. W., Belosevic, M., & Gamal El-Din, M. 2013b. Impact of ozonation on naphthenic acids speciation and toxicity of oil sands process-affected water to *Vibrio fischeri* and mammalian immune system. *Environmental science & technology*, 47(12), 6518-6526. <https://doi.org/10.1021/es4008195>

Wang, N., Lei, L., Zhang, X., Tsang, Y., Chen, Y., & Chan, H. L. 2011. A comparative study of preparation methods of nanoporous TiO<sub>2</sub> films for microfluidic photocatalysis. *Microelectronic engineering*, 88(8), 2797-2799. <https://doi.org/10.1016/j.mee.2010.12.051>

Wang, N., Tan, F., Tsoi, C. C., & Zhang, X. 2017. Photoelectrocatalytic microreactor for seawater decontamination with negligible chlorine generation. *Microsystem Technologies*, 23(10), 4495-4500. <https://doi.org/10.1007/s00542-016-3193-8>

Wang, N., Tan, F., Wan, L., Wu, M., & Zhang, X. 2014b. Microfluidic reactors for visible-light photocatalytic water purification assisted with thermolysis. *Biomicrofluidics*, 8(5), 054122. <https://doi.org/10.1063/1.4899883>

Wang, N., Tan, F., Wan, L., Wu, M., & Zhang, X. 2014c. Microfluidic reactors for visible-

- light photocatalytic water purification assisted with thermolysis. *Biomicrofluidics*, 8(5). <https://doi.org/10.1063/1.4899883>
- Wang, N., Zhang, X., Chen, B., Song, W., Chan, N. Y., & Chan, H. L. 2012. Microfluidic photoelectrocatalytic reactors for water purification with an integrated visible-light source. *Lab on a Chip*, 12(20), 3983-3990. <https://doi.org/10.1039/C2LC40428A>
- Wang, N., Zhang, X., Wang, Y., Yu, W., & Chan, H. L. 2014d. Microfluidic reactors for photocatalytic water purification. *Lab on a Chip*, 14(6), 1074-1082. <https://doi.org/10.1039/C3LC51233A>
- Wang, Q., Zhang, A., Li, P., Héroux, P., Zhang, H., Yu, X., & Liu, Y. 2021. Degradation of aqueous atrazine using persulfate activated by electrochemical plasma coupling with microbubbles: removal mechanisms and potential applications. *Journal of hazardous materials*, 403, 124087. <https://doi.org/10.1016/j.jhazmat.2020.124087>
- Wang, T., Yu, C., & Xie, X. 2020c. Microfluidics for Environmental Applications. [https://doi.org/10.1007/10\\_2020\\_128](https://doi.org/10.1007/10_2020_128)
- Wang, X., Wang, Y., Li, F., Li, L., Ge, X., Zhang, S., & Qiu, T. 2020d. Scale-up of microreactor: Effects of hydrodynamic diameter on liquid–liquid flow and mass transfer. *Chemical Engineering Science*, 226, 115838. <https://doi.org/10.1039/C8EE02656D>
- Wang, Y., Huang, J., Guo, H., Puyang, C., Han, J., Li, Y., & Ruan, Y. 2022. Mechanism and process of sulfamethoxazole decomposition with persulfate activated by pulse dielectric barrier discharge plasma. *Separation and Purification Technology*, 287,

120540. <https://doi.org/10.1016/j.seppur.2022.120540>

- Wang, Y., Li, H., Yi, P., & Zhang, H. 2019. Degradation of clofibric acid by UV, O<sub>3</sub> and UV/O<sub>3</sub> processes: performance comparison and degradation pathways. *Journal of hazardous materials*, 379, 120771. <https://doi.org/10.1016/j.jhazmat.2019.120771>
- Wang, Y., Wang, R., Yu, L., Wang, Y., Zhang, C., & Zhang, X. 2020e. Efficient reactivity of LaCu<sub>0.5</sub>Co<sub>0.5</sub>O<sub>3</sub> perovskite intercalated montmorillonite and g-C<sub>3</sub>N<sub>4</sub> nanocomposites in microwave-induced H<sub>2</sub>O<sub>2</sub> catalytic degradation of bisphenol A. *Chemical Engineering Journal*, 401, 126057. <https://doi.org/10.1016/j.cej.2020.126057>
- Wang, Y., Zu, M., Zhou, X., Lin, H., Peng, F., & Zhang, S. 2020f. Designing efficient TiO<sub>2</sub>-based photoelectrocatalysis systems for chemical engineering and sensing. *Chemical Engineering Journal*, 381, 122605. <https://doi.org/10.1016/j.cej.2019.122605>
- Wen, D., Chen, B., & Liu, B. 2022. An ultrasound/O<sub>3</sub> and UV/O<sub>3</sub> process for atrazine manufacturing wastewater treatment: a multiple scale experimental study. *Water Science and Technology*, 85(1), 229-243. <https://doi.org/10.2166/wst.2021.633>
- Wong, V.-L., Ng, C.-A. I., Teo, L.-R. I., & Lee, C.-W. (2020). Microfluidic Synthesis of Functional Materials as Potential Sorbents for Water Remediation and Resource Recovery *Advances in Microfluidic Technologies for Energy and Environmental Applications* (pp. 39): IntechOpen. DOI: 10.5772/intechopen.89302
- Wu, L., Wu, T., Liu, Z., Tang, W., Xiao, S., Shao, B., Liang, Q., He, Q., Pan, Y., & Zhao, C. 2022. Carbon nanotube-based materials for persulfate activation to degrade organic

- contaminants: Properties, mechanisms and modification insights. *Journal of hazardous materials*, 431, 128536. <https://doi.org/10.1016/j.jhazmat.2022.128536>
- Wu, S., & Hu, Y. H. 2020. A comprehensive review on catalysts for electrocatalytic and photoelectrocatalytic degradation of antibiotics. *Chemical Engineering Journal*, 127739. <https://doi.org/10.1016/j.cej.2020.127739>
- Wu, W., Huang, Z.-H., & Lim, T.-T. 2014. Recent development of mixed metal oxide anodes for electrochemical oxidation of organic pollutants in water. *Applied Catalysis A: General*, 480, 58-78. <https://doi.org/10.1016/j.apcata.2014.04.035>
- Xiao, C., Wang, L., Zhou, Q., & Huang, X. 2020. Hazards of bisphenol A (BPA) exposure: A systematic review of plant toxicology studies. *Journal of hazardous materials*, 384, 121488. <https://doi.org/10.1016/j.jhazmat.2019.121488>
- Xie, J., Chen, L., Zhou, W.-F., Au, C.-T., & Yin, S.-F. 2016. Selective oxidation of p-chlorotoluene to p-chlorobenzaldehyde over metal-modified OMS-2 molecular sieves. *Journal of Molecular Catalysis A: Chemical*, 425, 110-115. <https://doi.org/10.1016/j.molcata.2016.09.038>
- Xu, L., Srinivasakannan, C., Peng, J., Zhang, L., & Zhang, D. 2017. Synthesis of Cu-CuO nanocomposite in microreactor and its application to photocatalytic degradation. *Journal of Alloys and Compounds*, 695, 263-269. <https://doi.org/10.1016/j.jallcom.2016.10.195>
- Xu, Y., Wu, Y., Zhang, W., Fan, X., Wang, Y., & Zhang, H. 2018. Performance of artificial sweetener sucralose mineralization via UV/O<sub>3</sub> process: Kinetics, toxicity and

intermediates. *Chemical Engineering Journal*, 353, 626-634.

<https://doi.org/10.1016/j.cej.2018.07.090>

Yamamoto, T., Yasuhara, A., Shiraishi, H., & Nakasugi, O. 2001. Bisphenol A in hazardous waste landfill leachates. *Chemosphere*, 42(4), 415-418. [https://doi.org/10.1016/S0045-6535\(00\)00079-5](https://doi.org/10.1016/S0045-6535(00)00079-5)

Yan, H., Lai, C., Liu, S., Wang, D., Zhou, X., Zhang, M., Li, L., Li, X., Xu, F., & Nie, J. 2023. Metal-carbon hybrid materials induced persulfate activation: Application, mechanism, and tunable reaction pathways. *Water Research*, 119808. <https://doi.org/10.1016/j.watres.2023.119808>

Yang, M., Chen, B., Xin, X., Song, X., Liu, J., Dong, G., Lee, K., & Zhang, B. 2021. Interactions between microplastics and oil dispersion in the marine environment. *Journal of hazardous materials*, 403, 123944. <https://doi.org/10.1016/j.jhazmat.2020.123944>

Yang, T., Wang, L., Liu, Y., Huang, Z., He, H., Wang, X., Jiang, J., Gao, D., & Ma, J. 2019. Comparative study on ferrate oxidation of BPS and BPAF: Kinetics, reaction mechanism, and the improvement on their biodegradability. *Water research*, 148, 115-125. <https://doi.org/10.1016/j.watres.2018.10.018>

Yang, X., Chen, Z., Zhao, W., Liu, C., Qian, X., Zhang, M., Wei, G., Khan, E., Ng, Y. H., & Ok, Y. S. 2020. Recent advances in photodegradation of antibiotic residues in Water. *Chemical Engineering Journal*, 126806. <https://doi.org/10.1016/j.cej.2020.126806>

Yang, Y., Ji, Y., Yang, P., Wang, L., Lu, J., Ferronato, C., & Chovelon, J.-M. 2018. UV-

- activated persulfate oxidation of the insensitive munitions compound 2, 4-dinitroanisole in water: kinetics, products, and influence of natural photoinducers. *Journal of Photochemistry and Photobiology A: Chemistry*, 360, 188-195.  
<https://doi.org/10.1016/j.jphotochem.2018.04.044>
- Yang, Y., Li, Y., Mao, M., Zeng, M., & Zhao, X. 2017. UV–visible–infrared light driven thermocatalysis for environmental purification on ramsdellite MnO<sub>2</sub> hollow spheres considerably promoted by a novel photoactivation. *ACS Applied Materials & Interfaces*, 9(3), 2350-2357. <https://doi.org/10.1021/acsami.6b12819>
- Yang, Z., Liu, M., & Lin, C. 2016. Photocatalytic activity and scale-up effect in liquid–solid mini-fluidized bed reactor. *Chemical Engineering Journal*, 291, 254-268.  
<https://doi.org/10.1016/j.cej.2016.01.050>
- Yao, J., Qu, R., Wang, X., Sharma, V. K., Shad, A., Dar, A. A., & Wang, Z. 2020. Visible light and fulvic acid assisted generation of Mn (III) to oxidize bisphenol A: The effect of tetrabromobisphenol A. *Water Research*, 169, 115273.  
<https://doi.org/10.1016/j.watres.2019.115273>
- Yao, X., Zhang, Y., Du, L., Liu, J., & Yao, J. 2015. Review of the applications of microreactors. *Renewable and Sustainable Energy Reviews*, 47, 519-539.  
<https://doi.org/10.1016/j.rser.2015.03.078>
- Yew, M., Ren, Y., Koh, K. S., Sun, C., & Snape, C. 2019. A Review of State-of-the-Art Microfluidic Technologies for Environmental Applications: Detection and Remediation. *Global challenges*, 3(1), 1800060.

<https://doi.org/10.1002/gch2.201800060>

- Yin, H., Wang, Y., Yang, Y., Huang, J., & Xu, Z. 2020. Tryptophan-like fluorescence as a fingerprint of dry-weather misconnections into storm drainage system. *Environmental Sciences Europe*, 32(1), 1-14. <https://doi.org/10.1186/s12302-020-00336-3>
- Yoon, T.-H., Hong, L.-Y., & Kim, D.-P. 2011. Photocatalytic reaction using novel inorganic polymer derived packed bed microreactor with modified TiO<sub>2</sub> microbeads. *Chemical Engineering Journal*, 167(2-3), 666-670. <https://doi.org/10.1016/j.cej.2010.08.090>
- Yu, G., & Wang, N. 2020. Gas-Liquid-Solid interface enhanced photocatalytic reaction in a microfluidic reactor for water treatment. *Applied Catalysis A: General*, 591, 117410. <https://doi.org/10.1016/j.apcata.2020.117410>
- Yuan, R., Jiang, Z., Wang, Z., Gao, S., Liu, Z., Li, M., & Boczkaj, G. 2020. Hierarchical MnO<sub>2</sub> nanoflowers blooming on 3D nickel foam: a novel micro-macro catalyst for peroxymonosulfate activation. *Journal of colloid and interface science*, 571, 142-154. <https://doi.org/10.1016/j.jcis.2020.03.041>
- Yue, J., Chen, G., Yuan, Q., Luo, L., & Gonthier, Y. 2007. Hydrodynamics and mass transfer characteristics in gas–liquid flow through a rectangular microchannel. *Chemical Engineering Science*, 62(7), 2096-2108. <https://doi.org/10.1016/j.ces.2006.12.057>
- Yusuf, A., & Palmisano, G. 2021. Three-dimensional CFD modelling of a photocatalytic parallel-channel microreactor. *Chemical Engineering Science*, 229, 116051. <https://doi.org/10.1016/j.ces.2020.116051>
- Zawadzki, P. 2022. Persulfate activation by organic compounds: advancements and

challenges. *Current Opinion in Chemical Engineering*, 37, 100837.

<https://doi.org/10.1016/j.coche.2022.100837>

Zhang, B.-T., Zhang, Y., Teng, Y., & Fan, M. 2015. Sulfate radical and its application in decontamination technologies. *Critical Reviews in Environmental Science and Technology*, 45(16), 1756-1800. <https://doi.org/10.1080/10643389.2014.970681>

Zhang, H., & Huang, C.-H. 2005. Reactivity and transformation of antibacterial N-oxides in the presence of manganese oxide. *Environmental Science & Technology*, 39(2), 593-601. <https://doi.org/10.1021/es048753z>

Zhang, H., Xie, C., Chen, L., Duan, J., Li, F., & Liu, W. 2022. Different reaction mechanisms of  $\text{SO}_4^{\bullet-}$  and  $\bullet\text{OH}$  with organic compound interpreted at molecular orbital level in Co (II)/peroxymonosulfate catalytic activation system. *Water research*, 119392. <https://doi.org/10.1016/j.watres.2022.119392>

Zhang, J., Teixeira, A. R., & Jensen, K. F. 2018. Automated measurements of gas-liquid mass transfer in micropacked bed reactors. *AIChE Journal*, 64(2), 564-570. <https://doi.org/10.1002/aic.15941>

Zhang, J., Wang, K., Teixeira, A. R., Jensen, K. F., & Luo, G. 2017. Design and scaling up of microchemical systems: a review. *Annual review of chemical and biomolecular engineering*, 8, 285-305. <https://doi.org/10.1146/annurev-chembioeng-060816-101443>

Zhang, J., Yan, S., Yuan, D., Alici, G., Nguyen, N.-T., Warkiani, M. E., & Li, W. 2016. Fundamentals and applications of inertial microfluidics: a review. *Lab on a Chip*, 16(1), 10-34. <https://doi.org/10.1039/C5LC01159K>

- Zhang, M.-h., Dong, H., Zhao, L., Wang, D.-x., & Meng, D. 2019. A review on Fenton process for organic wastewater treatment based on optimization perspective. *Science of the total environment*, 670, 110-121. <https://doi.org/10.1016/j.scitotenv.2019.03.180>
- Zhang, M., Feng, Y., Zhang, K., Wang, Y., & Pan, X. 2020. Impact of salinity on colloidal ozone aphrons in removing phenanthrene from sediments. *Journal of hazardous materials*, 384, 121436. <https://doi.org/10.1016/j.jhazmat.2019.121436>
- Zhang, M., Han, N., Fei, Y., Liu, J., Xing, L., Núñez-Delgado, A., Jiang, M., & Liu, S. 2021a. TiO<sub>2</sub>/g-C<sub>3</sub>N<sub>4</sub> photocatalyst for the purification of potassium butyl xanthate in mineral processing wastewater. *Journal of Environmental Management*, 297, 113311. <https://doi.org/10.1016/j.jenvman.2021.113311>
- Zhang, Q., Zhang, Q., Wang, H., & Li, Y. 2013. A high efficiency microreactor with Pt/ZnO nanorod arrays on the inner wall for photodegradation of phenol. *Journal of hazardous materials*, 254, 318-324. <https://doi.org/10.1016/j.jhazmat.2013.04.012>
- Zhang, W., He, Y., Li, C., Hu, X., Yang, S., You, X., & Liang, W. 2021b. Persulfate activation using Co/AC particle electrodes and synergistic effects on humic acid degradation. *Applied Catalysis B: Environmental*, 285, 119848. <https://doi.org/10.1016/j.apcatb.2020.119848>
- Zhang, Z., Hu, D., Chen, H., Chen, C., Zhang, Y., He, S., & Wang, J. 2021c. Enhanced degradation of triclosan by gamma radiation with addition of persulfate. *Radiation Physics and Chemistry*, 180, 109273. <https://doi.org/10.1016/j.radphyschem.2020.109273>

- Zhang, Z., Wu, H., Yuan, Y., Fang, Y., & Jin, L. 2012. Development of a novel capillary array photocatalytic reactor and application for degradation of azo dye. *Chemical Engineering Journal*, 184, 9-15. <https://doi.org/10.1016/j.cej.2011.02.057>
- Zhao, D., He, Z., Wang, G., Wang, H., Zhang, Q., & Li, Y. 2016a. A novel efficient ZnO/Zn(OH) F nanofiber arrays-based versatile microfluidic system for the applications of photocatalysis and histidine-rich protein separation. *Sensors and Actuators B: Chemical*, 229, 281-287. <https://doi.org/10.1016/j.snb.2016.01.125>
- Zhao, Y., Zhao, Y., Zhou, R., Mao, Y., Tang, W., & Ren, H. 2016b. Insights into the degradation of 2, 4-dichlorophenol in aqueous solution by  $\alpha$ -MnO<sub>2</sub> nanowire activated persulfate: catalytic performance and kinetic modeling. *RSC advances*, 6(42), 35441-35448. <https://doi.org/10.1039/C6RA00008H>
- Zheng, J., Liu, B., Ping, J., Chen, B., Wu, H., & Zhang, B. 2015. Vortex-and shaker-assisted liquid–liquid microextraction (VSA-LLME) coupled with gas chromatography and mass spectrometry (GC-MS) for analysis of 16 polycyclic aromatic hydrocarbons (PAHs) in offshore produced water. *Water, Air, & Soil Pollution*, 226(9), 1-13. <https://doi.org/10.1007/s11270-015-2575-3>
- Zheng, X., Niu, X., Zhang, D., Lv, M., Ye, X., Ma, J., Lin, Z., & Fu, M. 2022. Metal-based catalysts for persulfate and peroxymonosulfate activation in heterogeneous ways: A review. *Chemical Engineering Journal*, 429, 132323. <https://doi.org/10.1016/j.cej.2021.132323>
- Zhou, Y., Jiang, J., Gao, Y., Ma, J., Pang, S.-Y., Li, J., Lu, X.-T., & Yuan, L.-P. 2015.

Activation of peroxymonosulfate by benzoquinone: a novel nonradical oxidation process. *Environmental Science & Technology*, 49(21), 12941-12950.

<https://doi.org/10.1021/acs.est.5b03595>

Zhou, Z., Guo, L., Shiller, A. M., Lohrenz, S. E., Asper, V. L., & Osburn, C. L. 2013.

Characterization of oil components from the Deepwater Horizon oil spill in the Gulf of Mexico using fluorescence EEM and PARAFAC techniques. *Marine Chemistry*,

148, 10-21. <https://doi.org/10.1016/j.marchem.2012.10.003>

Zhu, D., & Zhou, Q. 2019. Action and mechanism of semiconductor photocatalysis on degradation of organic pollutants in water treatment: A review. *Environmental*

*Nanotechnology, Monitoring & Management*, 12, 100255.

<https://doi.org/10.1016/j.enmm.2019.100255>

Zhu, S., Dai, H., Jiang, B., Shen, Z., & Chen, X. 2016. Efficient microfluidic photocatalysis in a symmetrical metal-cladding waveguide. *Physical Chemistry Chemical Physics*,

18(6), 4585-4588. <https://doi.org/10.1039/C5CP06813D>

Zhu, S., Li, X., Kang, J., Duan, X., & Wang, S. 2018. Persulfate activation on

crystallographic manganese oxides: mechanism of singlet oxygen evolution for

nonradical selective degradation of aqueous contaminants. *Environmental science & technology*, 53(1), 307-315. <https://doi.org/10.1021/acs.est.8b04669>

Zhu, Z., Merlin, F., Yang, M., Lee, K., Chen, B., Liu, B., Cao, Y., Song, X., Ye, X., & Li, Q.

K. 2022. Recent Advances in Chemical and Biological Degradation of Spilled Oil: A Review of Dispersants Application in the Marine Environment. *Journal of hazardous*

*materials*, 129260. <https://doi.org/10.1016/j.jhazmat.2022.129260>

Zou, L., Wang, Y., Huang, C., Li, B., Lyu, J., Wang, S., Lu, H., & Li, J. 2021. Meta-cresol degradation by persulfate through UV/O<sub>3</sub> synergistic activation: contribution of free radicals and degradation pathway. *Science of The Total Environment*, 754, 142219. <https://doi.org/10.1016/j.scitotenv.2020.142219>

# APPENDIX

## 1) First-authored work

### Peer reviewed journal publications:

1. **Dong, G.**, Chen, B., Liu, B., Cao, Y., de Jourdan, B., Stoyanov, S. R., Ling, J., Ye, X., Lee, K., & Zhang, B. (2022). Comparison of O<sub>3</sub>, UV/O<sub>3</sub>, and UV/O<sub>3</sub>/PS Processes for Marine Oily Wastewater Treatment: Degradation Performance, Toxicity Evaluation, and Flocc Analysis. *Water Research*, 119234. <https://doi.org/10.1016/j.watres.2022.119234>
2. **Dong, G.**, Chen, B., Liu, B., Hounjet, L., Cao, Y., Stoyanov, S. R., Yang, M., & Zhang, B. (2022). Advanced Oxidation Processes in Microreactors for Water and Wastewater Treatment: Development, Challenges, and Opportunities. *Water Research*, 118047. <https://doi.org/10.1016/j.watres.2022.118047>
3. **Dong, G.**, Chen, B., Liu, B., Stoyanov, S. R., Cao, Y., Yang, M., & Zhang, B. (2021). UV Stimulated Manganese Dioxide for the Persulfate Catalytic Degradation of Bisphenol A. *Catalysts*, 11(4), 502. <https://doi.org/10.3390/catal11040502>
4. **Dong, G.**, Chen, B., Liu, B., Chen, X., Cao, Y., Stoyanov, S. R. & Zhang, B. (2024). Degradation of bisphenol S in microreactor using visible light-based persulfate activation by TiO<sub>2</sub>/g-C<sub>3</sub>N<sub>4</sub> nanosheet. (*To be submitted*)

### Conference abstract and oral presentations (°Presenter):

1. ° **Dong, G.H.**, Chen, B., Stoyanov, S., Benjaminde Jourdan<sup>3</sup>, Kenneth Lee<sup>4</sup>, and Zhang, B.Y. Sulfate Radical-based Advanced Oxidation Process for Decanting Water On-site Treatment in Oil Spill Response. (**Persistent, Emerging, and Organic Pollution in Environments (PEOPLE Conference)**, Montreal, Aug. 4-11, 2023)

2. ° **Dong, G.H.**, Chen, B., Stoyanov, S., Benjaminde Jourdan<sup>3</sup>, Kenneth Lee<sup>4</sup>, and Zhang, B.Y. Persulfate-based AOP for decanting water treatment during oil spill response. (the **45<sup>th</sup> Arctic and Marine Oilspill Program (AMOP)** Jun 7-8, 2023)
3. ° **Dong, G.H.**, Chen, B., Liu, B., Cao, Y.Q., Lee, K., and Zhang, B.Y. Ozonation-based advanced oxidation processes for onsite treatment of marine oily wastewater. (**International Oil Spill Science Conference (IOSSC)**, Halifax, Oct. 4-7, 2022).
4. ° **Dong, G.H.**, Chen, B., Liu, B., Honjet, L., Stoyanov, S., and Zhang, B.Y. Microfluidic-based advanced oxidation processes for environmental application: state-of-art, current challenges, and future trends. (**Persistent, Emerging, and Organic Pollution in Environments (PEOPLE Conference)**, Prince Edward Island, Aug. 23-26, 2022)
5. Liu, B., Chen, B., Ling, J., ° **Dong G.**, Matchinski. E., Wu, F., & Zhang, B. Evaluation of Gravity Settling on Crude Oil-Water Emulsion Separation (**Canadian Association on Water Quality (CAWQ Conference)**, Nov 2-3, 2021)
6. ° **Dong, G.**, Chen, B., Liu, B., Stoyanov, S., Lee, K., & Zhang, B. Effects of persulfate on UV/O<sub>3</sub> System for On-site Decanting Water Treatment during Marine Oil Spill Responses. (**Multi-Partner Research Initiative (MPRI) Student Research Forum**, Sep. 23-24, 2021)
7. ° **Dong, G.**, Chen, B., Liu, B., Stoyanov, S., Song, X., Lee, K., & Zhang, B. Persulfate based Advanced Oxidation for Onsite Wastewater Treatment in Marine Oil Spill. (**LEADERS & PEOPLE Virtual Symposium**, Jul. 20-22, 2021)

8. ° **Dong, G.**, Chen, B., Liu, B., Stoyanov, S., Cao, Y., Lee, K., & Zhang, B. A Photo-Ozonation based Decanting Water Onsite Treatment System for Marine Oil Spill Response. **(the 43rd Arctic and Marine Oil spill Program (AMOP) (virtual) Jun 8-10, 2021)**
9. ° **Dong, G.**, Chen, B., Liu, B., Stoyanov, S., Cao, Y., Lee, K., & Zhang, B. A New UV/Ozonation-based Decanting Water Onsite Treatment System for Marine Oil Spill Response. **(Multi-Partner Research Initiative (MPRI) Student Research Forum. Nov 13, 2020)**
10. ° **Dong, G.**, Chen, B., Liu, B., Stoyanov, S., Cao, Y., & Zhang, B. An Integrated MnO<sub>2</sub>/UV-Activated Persulfate Process for the Removal of Bisphenol A from Water. **(LEADERS & PEOPLE Virtual Symposium, Aug 31– Sep 1, 2020)**

Poster presentations:

1. **Dong, G.**, Huang, L., Chen, B., & Zhang, B. Manganese Electroplated Zero-Valent Iron in Permeable Reactive Barrier for Removal of Emerging Pollutants in Groundwater. **The International Water Association (IWA) Water and Development Congress & Exhibition (Dec 1-4, 2019)**

## 2) Co-authored work

*My contributions:*

*Experiments, Writing-original draft, Visualization, Review and editing.*

*Peer reviewed journal publications:*

1. Liu, B., Chen, B., **Dong, G.**, Wu, F., & Zhang, B. (2023). A UVA-LED microreactor for photocatalytic degradation of humic acids and control of disinfection by-products production. *Journal of Cleaner Production*, 139395. <https://doi.org/10.1016/j.jclepro.2023.139395>
2. Liu, B., Chen, B., Ling, J., Matchinski, E. J., **Dong, G.**, Ye, X., ... & Zhang, B. (2022). Development of advanced oil/water separation technologies to enhance the effectiveness of mechanical oil recovery operations at sea: potential and challenges. *Journal of Hazardous Materials*, 129340. <https://doi.org/10.1016/j.jhazmat.2022.129340>
3. Zhang, Y., Cao, Y., Chen, B., **Dong, G.**, Zhao, Y., & Zhang, B. (2024). Marine biodegradation of plastic films under various ambient temperatures: Bacterial enrichment, morphology alteration, and release of degradation products. *Science of the Total Environment*, 917, 170527. <https://doi.org/10.1016/j.scitotenv.2024.170527>
4. Liu, B., Chen, B., Ling, J., Ye, X., **Dong, G.**, Matchinski, E. J., & Zhang, B. (2022). Ecotoxicity Studies for Onsite Disposal of Decant Water during Oil Spills: A Review. *Frontiers in Environmental Science*, 1002. <https://doi.org/10.3389/fenvs.2022.944010>
5. Cao, Y., Zhang, B., **Dong, G.**, & Chen, B. (2023). Blue economy: A new era of petroleum microbiology in a changing climate. *National Science Open*.

<https://doi.org/10.1360/nso/20230024>

6. Cao, Y., Zhang, B., Cai, Q., Zhu, Z., Liu, B., **Dong, G.**, Greer, C., Lee, K. & Chen, B. (2022). Responses of Alcanivorax species to marine alkanes and polyhydroxybutyrate plastic pollution: Importance of the ocean hydrocarbon cycles. *Environmental Pollution*, 120177. <https://doi.org/10.1016/j.envpol.2022.120177>
7. Cao, Y., Kang, Q., Zhang, B., Zhu, Z., **Dong, G.**, Cai, Q., Lee, K., & Chen, B. (2022). Unveiling the complicated biodegradation process of chemically dispersed oil under various salinities using machine learning added causal effect analysis. *Bioresource Technology*, 345, 126468. <https://doi.org/10.1016/j.biortech.2021.126468>
8. Cao, Y., Yu, M., **Dong, G.**, Chen, B., & Zhang, B. (2020). Digital PCR as an emerging tool for monitoring of microbial biodegradation. *Molecules*, 25(3), 706. <https://doi.org/10.3390/molecules25030706>
9. Yang, M., Zhang, B, Xin, X., Liu, B., Zhu, Z., **Dong, G.**, Zhao, Y., Lee, K. & Chen, B. (2021). Microplastics-Oil-Dispersant Agglomerates in the Marine Environment: Formation Mechanism and Impact on Oil Dispersion. *Journal of Hazardous Materials*, 127825. <https://doi.org/10.1016/j.jhazmat.2021.127825>
10. Cao, Y., Zhang, B., Zhu, Z., Rostami, M., **Dong, G.**, Ling, J., Lee, K., Greer, C., & Chen, B. (2021). Access-dispersion-recovery Strategy for Enhanced Mitigation of Heavy Crude Oil Pollution Using Magnetic Nanoparticles Decorated Bacteria. *Bioresource Technology*, 125404. <https://doi.org/10.1016/j.biortech.2021.125404>
11. Yang, M., Chen, B., Xin, X., Song, X., Liu, J., **Dong, G.**, Lee, K. & Zhang, B. (2021).

Interactions between microplastics and oil dispersion in the marine environment. *Journal of Hazardous Materials*, 403, 123944. <https://doi.org/10.1016/j.jhazmat.2020.123944>

12. Cao, Y., Zhang, B., Greer, C., Lee, K., Cai, Q., Song, X., Tremblay, J., Zhu, Z., **Dong, G.** & Chen, B. (2022). Metagenomic and Metatranscriptomic Responses of Chemical Dispersant Application during a Marine Dilbit Spill. *Applied and Environmental Microbiology*, aem-02151. <https://doi.org/10.1128/aem.02151-21>
13. Cao, Y., Zhang, B., Zhu, Z., Song, X., Cai, Q., Chen, B., **Dong, G.**, & Ye, X. (2020). Microbial eco-physiological strategies for salinity-mediated crude oil biodegradation. *Science of The Total Environment*, 727, 138723. <https://doi.org/10.1016/j.scitotenv.2020.138723>

Conference proceedings:

Liu, B., Chen, B., **Dong, G. H.**, Wu, F., & Zhang, B. Y. (2023). Development of Microfluidic Photocatalytic Oxidation System for Drinking Water Treatment. In *Canadian Society of Civil Engineering Annual Conference* (pp. 413-418). Springer, Singapore.